University of Strathclyde
Design, Manufacture and Engineering Management

Online Defect Detection using a Highspeed Multi-sensor Data Fusion System for Laser Metal Deposition

Ahmed Murtaza Qureshi

A thesis presented in fulfilment of the requirements for the degree of Doctor of Philosophy.

December 2021

Table of Contents

Table of Contents 2

Chapter 1: Introduction 1

1.1. What is Laser Metal Deposition? 2

1.2. Applications of LMD 3

1.3. Problems and State of the Art Solutions 4

1.4. Research Aims and Questions 6

1.5. Significance of this Research 7

1.6. Scope and Limitations 8

1.7. Thesis Structure 9

Chapter 2: Defects in LMD 10

2.1. Cracks 11

2.2. Pores and Porosity 17

2.3. Other Defects 23

2.4. Influence of Machine Parameters on defects 25

2.5. Discussion 29

Chapter 3: Process monitoring, Defect Detection Methodologies and Systems in LMD ... 33

3.1. Optical Camera Defect Detection and LMD Monitoring Systems 34

3.2. Thermal Camera Defect Detection and LMD Monitoring Systems 39

3.3. Acoustic Emission Defect Detection and LMD Monitoring Systems 41

3.4. Pyrometers Defect Detection and LMD Monitoring Systems 42

3.5. Ultrasonics Defect Detection and LMD Monitoring Systems 43

3.6. Data Fusion Architectures and Models 44

3.7. Multisensory and Data Fusion systems in LMD 48

3.8. “High Speed” measurement systems and “Online” monitoring 50

3.9. Discussion 51

Chapter 4: Research Design and Methodology 57

4.1. Specific gaps and Objectives 58

4.2. Research Methodology 59

4.2.1. Development of System Architecture 60

4.2.2. Collecting Training Data 63

4.2.3. Training the System 66

4.2.4. Testing the System 74

4.3. Discussion 76

Chapter 5: System Architecture and Development 79

5.1. Sensors Specifications 80

5.2. Hardware Architecture 85

5.3. Software Architecture 89

5.4. Discussion 95

Chapter 6: Experimentation 99

6.1. Defect Provocation Experiments 100

6.1.1. Contaminated Powder Experiment 102

6.1.2. Surface Finish Experiment 103

6.1.3. Machine Deformities Experiment 105

6.1.4. Machine Process Parameters 106

6.2. Experimental Setup 109

6.3. Discussion 111

Chapter 7: Data Analysis 115

7.1. Data Processing 117

7.1.1. Machine Parameters 118

7.1.2. Physical Measurements 118

7.1.3. X-Ray Computed Tomography (XCT) Data Analysis 119
7.1.3.1. Detected Defect Types 120
7.1.4. High Speed Optical Sensor Data Processing & Feature Extraction 129
7.1.5. Thermal Sensor Data Processing & Feature Extraction 135
7.1.6. Acoustic Emission Sensor Data Processing & Feature Extraction 140
7.2. Machine Learning 149
7.2.1. Scaling Data 149
7.2.2. K-means Clustering 152
7.3. Defect Detection Algorithm 159
7.3.1. Feature Range Prediction 160
7.3.2. Percentage Confidence 167
7.4. Discussion 175
Chapter 8: Statistical Analysis and Verification 181
8.1. Feature Prediction 182
8.1.1. Feature Range Prediction 182
8.1.2. Single Feature Value Prediction 184
8.1.3. Feature Prediction for an entire sample 186
8.2. Total Number of Defects 188
8.2.1. Precision Calculation 188
8.2.2. Linear Regression Model 188
8.2.3. Wilcoxon Signed Rank test for Total Defects Accuracy 190
8.2.4. Binomial Test for Total Defects Range Accuracy 191
8.3. Defect Classification 193
8.4. Defect size and total Defected Area 196
8.4.1. Binomial Test for Max Defect Size and Total Defected Area Range Accuracy 196
8.5. Discussion 197

Chapter 9: Conclusion and Further works. 200

References 207

Figure 1: a) LMD Process b) LMD Laser Head (Gibson I., 2015) 3

Figure 2: Classification of Cracks 12

Figure 3: a) Slag Cracks b) Structural Segregation Cracks c) the cracks caused by thermal stress d) Cracks caused by machining (Wang, 2008) 13

Figure 4: Vertical Cracks in Laser clad layer using 75%WC+25%Ni (Barun Haldara, 2018) ... 13

Figure 5: Cracking in Ti-6Al-4V and H13 tool steel LMD Deposit (Gaja & Liou, 2017) 14

Figure 6: a) Typical Gas Pore Shape & Size b) Ti-6Al-4V and H13 powder shape and size (Gaja & Liou, 2017) 18

Figure 7: a) Porosity and Crack features (John A. Slotwinski & E.J. Garboczii, 2014) b) Surface Porosity in LMD Sample (Barun Haldara, 2018) 19

Figure 8: Transverse cross section of laser deposit using Inconel 718 powder over steel plates that shows Gas Porosity. (Gary K.L. Ng, 2008) 20

Figure 9: a) Pore formation due to Depression Collapse b) Pore formation due to Vortex (Saad A. Khairallah, 2020) 22

Figure 10: Defect Classification as per ISO 13919-2 24

Figure 11: Average Porosity and pore size reduction thought LMD parameter manipulation (Rasheedat M. Mahamood, 2014) 25

Figure 12: Effect of LMD parameters on a) Gas Porosity Defects, b) Lack of Fusion and c) build height (Gary K.L. Ng, 2008) 26

Figure 13: Grading Criteria for Solidification Defects (C Y Kong, 2010) 26

Figure 14: a) Machine Feed Rate and Powder Flow Rate effects on Lack of Fusion and Cracking as predicted by Design Expert Software b) Machine Feed Rate and Powder Flow Rate effects on Porosity and Penetration as predicted by Design Expert Software (C Y Kong, 2010) 27

Figure 15: (a) Relation between Cooling Rate and Scanning Speed (b) Relation between Meltpool Temprature and Scanning Speed (Mohammad H. Farshidianfar, 2016) 28

Figure 16: Spectral Radiance at unity emissivity derived from Planck's equation 35

Figure 17: a) A schematic representation of directional emittance from a flat surface. b) Directional emittance of a blackbody and real body. (Robert Sampson, 2020) 38
Figure 18: a) Melt pool particle Monitoring. b) Microstructure shows unmelted powder. c) particle ignited when entering laser beam zone. d) Particle landing and solidifying on the surface (James C. Haley, 2018) 39
Figure 19: Joint Directors of Laboratories (JDL) architecture (White, 1991) 45
Figure 20: Luo and Kay's Architecture (Luo & Kay, 1989) 46
Figure 21: Dasarathy's architecture (Meng, Jing, & Zheng Yan, 2020) 47
Figure 22: Water Fall Model (Esteban, Starr, Willetts, & Hannah, 2005) 48
Figure 23:Physical Phenomenon that occur due to defects 51
Figure 24: Observation Window of different sensors during the LMD process 54
Figure 25: Overall Research Methodology... 60
Figure 26: General System Architecture 62
Figure 27:Method of measuring physical width 64
Figure 28: XCT deposit Identification Method 65
Figure 29: Defect Position and sizing method 66
Figure 30: System Training Data Fusion Methodology 68
Figure 31: Optical Event and its features 71
Figure 32:Thermal Event and its features.. 71
Figure 33: AE Event and its features 71
Figure 34: Box and Whisker plot working (Galarnyk, 2018) 72
Figure 35: Data Fusion algorithm 74
Figure 36: Online Data Fusion Methodology 75
Figure 37:HS Camera Calibration method 83
Figure 38: Ideal Hardware Architecture... 86
Figure 39: System Architecture Parts... 87
Figure 40:Hardware Architecture 88
Figure 41: Highspeed Multisensory System.. 89
Figure 42: Software Architecture 90
Figure 43:Acquisition VI 91
Figure 44:Acquisition Flow Chart 91
Figure 45:Universal Timer Script Flow Chart 92
Figure 46: High-Speed Camera SDK VI 93

Figure 47: High Speed VI Flow Chart.. 93
Figure 48: NIT Tachyon Application Software... 94
Figure 49: Thermal Script Flow Chart.. 94
Figure 50: Workings of DMA Engine in LabView... 95
Figure 51: All Software Scripts during deposition... 95
Figure 52: a) Electromagnetic Spectrum b) Spectral Response c) Specteral Response Photron FASTCAM SA-X2 98
Figure 53: Deposition Tracks.. 102
Figure 54: Deposition Diagram 102
Figure 55: Contaminated Powder Experiment 103
Figure 56: a) Surface Finish EDM b) Surface Finish Milled...................................... 104
Figure 57: Surface Finish Experiment 105
Figure 58: Machined Deformities 106
Figure 59: Influence of Machine Parameter 107
Figure 60:Powder Feed Rate and Laser Power Sample 108
Figure 61: Experimental Setup diagram.. 109
Figure 62: Calibration and Paper 110
Figure 63: (a) AE Clamping (b) LMD Head... 110
Figure 64: Experimentation Setup 111
Figure 65: Defect Provocation Experiments 112
Figure 66: Work Piece with deposits 113
Figure 67: Samples cut to thickness.. 114
Figure 68: Data Processing and Event Extraction Method 117
Figure 69: (a) Deposited tracks (b) Measurements Diagram..................................... 119
Figure 70: (a) XCT Imaging method (Kastner J., 2018) (b) XCT Image Slice 120
Figure 71: (a) Pores Identified in XCT Images (b) Cracks in XCT Images (c) Other Defects in XCT Images.. 121
Figure 72: a) Cracks causing Pores b) Pores causing other pores............................. 122
Figure 73: a) Edge Detection for feature recognition b) Deposit width measurement....... 122
Figure 74: a) Laser On Images b) Laser Off Images.. 124
Figure 75: Defect Origin with respect to deposition length 124
Figure 76: Defect Type and Size Spatial Domain.. 126
Figure 77: Defect Size and Type in Time Domain 127

Figure 78: a) Stable Melt pool b) Segregated Small Events c) Big Event. 129
Figure 79: a) Powder Impact Event, b) Powder Particle Rejection, c) Powder Particle Clean Fuse 130
Figure 80: a) Z Projection b) Angle Correction c) Image Sharpening d) ROI 131
Figure 81: a) 3D Surface Intensity Plot b) 2D Intensity Profile Plot 132
Figure 82: HS data stitched onto Defect data in Spatial Domain.. 133
Figure 83: HS Data stitched on to Defect data in Time Domain 133
Figure 84: a) Raw Thermal Image b) Raw Thermal Profile 135
Figure 85: Raw Data for a defect free deposition Track 137
Figure 86: Thermal Data in Time Domain 137
Figure 87: Thermal Data in Spatial Domain 138
Figure 88: Cooling rates being affected due to large defect 139
Figure 89: a) Machine Only AE FFT and Spectrogram b) Powder only AE FFT and Spectrogram c) Track Deposition AE FFT and Spectrogram 141
Figure 90: a) AE Event Features b) AE Events 144
Figure 91: Signal Event Analysis.. 145
Figure 92: AE Source Position Calculation 147
Figure 93: AE Data stitched onto Defect Data in Time Domain.. 148
Figure 94: AE Sources Stitched onto Defect Data in Spatial Domain.................................. 148
Figure 95: Machine Learning Procedure.. 149
Figure 96: K-means Clustering Algorithm 153
Figure 97: a) Calinski-Harabasz Index for HS data Events, b) Calinski-Harabasz Index for Thermal data Events, c) Calinski-Harabasz Index for AE data Events................................. 154
Figure 98: a) HS Data Clustering plot in 3D b) XY Projection HS Data Clustering, c) XZ Projection HS Data Clustering, b) YZ Projection HS Data Clustering................................... 157
Figure 99: Thermal Data Clustering 158
Figure 100: AE Data Clustering 158
Figure 101: Data Fusion Algorithm 160
Figure 102: Box and Whiskers plot for Total Defects for a) HS Cluster Events, b) Thermal Cluster Events, c) AE Cluster Events.. 161
Figure 103: Box and Whiskers plot for Total Pores for a) HS Cluster Events, b) Thermal Cluster Events, c) AE Cluster Events.. 162

Figure 104: Box and Whiskers plot for Total Cracks for a) HS Cluster Events, b) Thermal Cluster Events, c) AE Cluster Events.. 163
Figure 105: Box and Whiskers plot for Max Defect Size for a) HS Cluster Events, b) Thermal Cluster Events, c) AE Cluster Events.. 164
Figure 106: Box and Whiskers plot for Total Defected Area for a) HS Cluster Events, b) Thermal Cluster Events, c) AE Cluster Events 165
Figure 107: HS Cluster 1 Variance vs Distance from Cluster Centroid................................ 167
Figure 108: HS Cluster 2 Variance vs Distance from Cluster Centroid................................ 168
Figure 109: Thermal Cluster 1 Variance vs Distance from Cluster Centroid........................ 168
Figure 110: Thermal Cluster 2 Variance vs Distance from Cluster Centroid........................ 169
Figure 111: AE Cluster 1 Variance vs Distance from Cluster Centroid................................ 169
Figure 112: AE Cluster 2 Variance vs Distance from Cluster Centroid................................ 170
Figure 113: Confidence Interval Range based on "3 sigma rule" 172
Figure 114: Normality Test for Euclidian Distances 173
Figure 115: % Confidence Scale 174
Figure 116:Avg Defect Size in defect provocation Experiments... 176
Figure 117: Avg Defect Size compared to Avg size found in literature............................... 177
Figure 118: a) Frame by Frame overlap using z projection b) Image reconstruction retaining high intensity pixel positions 178
Figure 119: Method of intensity profile construction... 179
Figure 120: Future Works (HMDF stands for High Speed Data Fusion System) 206

Table 1: Percentage Cracking in Temperature Ranges (Wang, 2008) 11
Table 2: The composition of Laser Cladding Materials in Table 1 (Fujun Wang, 2008)......... 11
Table 3: Total Crack Length (TCL) for set parameters (Segerstark, 2017) 14
Table 4: Machine Parameter Setting (Segerstark, 2017)... 15
Table 5: Sulphur, Phosphorus, Silicon and Nitrogen Content effect on cracking (J.Yu, 2013) 16
Table 6: Porosity Geometry and Dimensions (John A. Slotwinski & E.J. Garboczii, 2014) 19
Table 7: ISO 13919-2 standards for Pores and Porosity 24
Table 8: Pore and Cracks classification in LMD research 29

Table 9: Scanning Window Example 73
Table 10: Best, Average and Worst-Case values 81
Table 11: Sensor Best, Average and Worst Case 85
Table 12: List of Hardware Modules 89
Table 13: Summary of Experiments 101
Table 14: Machine Process Parameters 107
Table 15: Defect Provocation using Machine Parameters experimental Runs 108
Table 16: Software Used for Data Processing and Extraction 118
Table 17: Laser Metal Deposition Machine Parameters 118
Table 18: XCT Machine Parameters 120
Table 19: Defect Classification Criterion 121
Table 20: Defect Size Statistic 128
Table 21: HS Data Event Feature Extraction 134
Table 22: Thermal Data Event Feature Extraction 139
Table 23: Frequency and Power Comparison 140
Table 24: AE event Feature Extraction 145
Table 25: Z-Score Scaling of Event Features 152
Table 26: Smallest Distortion for each sensor for K means runs 153
Table 27: Optimal Number of K Cluster for all sensors 154
Table 28: Predictive Ranges for Sensor Clusters 166
Table 29: Individual Scoring System 174
Table 30: Binary Output Look Up Table 182
Table 31: Binary Accuracy Data fused Predictions for a random Sample 183
Table 32: Data Variables used to create single value predictions 184
Table 33: Accuracy for single value prediction using Multiple Regression Model 185
Table 34: Range of Each Sensor Data when calculating for entire sample 187
Table 35: Results for Feature Prediction for an entire sample 187
Table 36: Output of the Linear Regression Model 190
Table 37: Wilcoxon Signed Rank test for one Sample 191
Table 38: Binomial Test for total Defects 192
Table 39: Logistic Regression Model Output 194
Table 40: Accuracy of Max Defect Size and Total Defect Size for training data 196
Table 41: Hypothesis Testing for Max Defect Size and Total Defected Area 197

Table 42: Methodologies and their Accuracies ... 198
Table 43: Statistical Tests ... 199

(Equation 1: Chemical Reactions that produce gases) ... 21
(Equation 2: Planck equation for spectral radiance) ... 34
(Equation 3: First Radiation Constant) ... 34
(Equation 4: Second Radiation Constant) ... 34
Equation 5: Wave speed and porosity relationship ... 44
(Equation 6: Total Length of the Deposition in frames) ... 123
(Equation 7: Depth each frame represents in mm) ... 123
(Equation 8: Total Laser On Frames) ... 125
(Equation 9: Experimentally calculated Total Laser On Time) ... 125
(Equation 10: Total Deposition Time) ... 125
(Equation 11: Error between Laser On Time Calculated from HS Frames and Laser On Time calculated from Laser Scan Speed) ... 125
(Equation 12: Defect Position in Time Domain) ... 126
(Equation 13: Weighted Average Coefficient Matrix) ... 131
(Equation 14: Total Frames for the deposition of a single track) ... 136
(Equation 15: Total Deposition time for a single Track) ... 136
(Equation 16: Thermal and Acoustic signal Time Difference) ... 142
(Equation 17: Time at which deposition Starts) ... 142
(Equation 18: Time at which deposition Ends) ... 143
(Equation 19: Time Synced Deposition Start time) ... 143
(Equation 20: Time Synced Deposition End time) ... 143
(Equation 21: AE Source Position using TOA method.) ... 146
(Equation 22: AE Source Position along the length of deposition) ... 147
(Equation 23: Z-Score Calculation) ... 149
(Equation 24: Cost Function) ... 155
(Equation 25: Predicted Feature Max Value) ... 166
(Equation 26: Predicted Feature Min Value) ... 166
(Equation 27: Predicted Feature Range) ... 166

(Equation 28: Collective Confidence Score) 174
(Equation 29: % Confidence Score) 174
(Equation 30: Avg Feature Value Calculation) 184
(Equation 31: Average Actual Defect Value Calculation) 184
(Equation 32: Single Value Predictor Model using Multiple variable Regression) 185
(Equation 33: Overlap Compensation Calculations) 186
(Equation 34: Calculating the feature for an entire sample) 186
(Equation 35: Accuracy Verification Method by (Khanzadeh & Bian, 2016)) 188
(Equation 36: Precision Verification using predicted total defects) 188
(Equation 37: Binomial Probability Formula) 191
(Equation 38: Generic Logistic Regression Model) 193
… (Equation 39: Logistic Regression Model developed by (Gaja & Liou, 2018)) 193
… (Equation 40: Pore Prediction Accuracy) 194
… (Equation 41: Crack Prediction Accuracy) 195

Declaration of author’s rights

Ahmed Murtaza Qureshi

December 2021

Abstract

Laser metal deposition (LMD) is an advanced additive manufacturing technology that is also known as metal 3D printing. It has many industrial applications which include building parts with complex geometry from scratch, Remanufacturing, and coating parts with a variety of materials. It is being adopted by the industry at a very quick rate, however quality assurance is still a hurdle that is being investigated. Defects are an inherent part of the process and are caused by many factors which may be unacceptable to industries like the Aerospace industry. For this the state of the art presents many NDT solutions to detect defects during the deposition process however, these methods have limitations due to the type of sensor being used, the high rate of change of the phenomenon the sensor is observing, the level of information that can be extracted from the sensor data about the defects and obviously the accuracy of the extracted information. This research investigates and develops a defect detection methodology that uses a multisensory array in collaboration with a custom data fusion algorithm that allows for the detection of defects and predicts features of the detected defects. This includes total number of defects, types and quantity of the defect, Max defect size and total defected area. This is achieved by first designing and developing a multisensory architecture capable of monitoring different parts of the defect development cycle at high enough sampling speeds so that information that indicates defects can be effectively captured. This is followed by monitoring defect provocation experiments to capture signals from a defected sample and training the system on these signals. In the training run the system takes the signals from these defect provocation experiments and stiches them onto defect information extracted from the XCT scans from the provocation experiments. From the stitched data sets events that exhibit anomalous behavior which might indicate the presence of a defect are extracted and plugged into a K means clustering algorithm which sorts them into clusters. For every cluster a predictor table is formed which are used to predict defect features for any new event that is assigned to that cluster. The online data fusion algorithm takes in values from the predictor table once a new defect is introduced and outputs a predicted range between which the actual value of the defect feature lies in. The reliability of the range is also quantified using another value called % confidence which is formed using a unique scoring system. The results of this system show a relatively higher accuracy than solutions that use a single sensor approach and predicts further information about the defects.

Acknowledgements

First and foremost, I would like to thank God almighty, the most gracious and merciful without whose permission nothing is possible.

I would like to thank my supervisor Paul Xirouchakis without whose wisdom, guidance and support I would have never been able to complete this piece of work. I would then like to thank Abdul Ahmad who was always a source of support and always there to help.

I want to thank my father Dr Haroon Javed Qureshi who has been my source of wisdom, knowledge, and my rock through this PhD Journey. I would like to thank my (late) Mother Seema Farheen Qureshi who taught me to persevere and made be believe that my place lies beyond the stars and all I would have to do is work for it.

I acknowledge the assistance and facilitation that James, Dino, Duncan have provided during this project. I would like to thank Dorothy Evans who helped me out in times of need whether it was funding or guidance.

I would also like to thank my loving wife Noor Mahmood for bearing with me for these tough past few years. To my brother Muhammad Mustafa Qureshi, my sister Khadijah Hameeda Qureshi, my two best friend Ayaz and Azmar, I thank you for the love and support you have shown me and for keeping me up when I was down.

I would like to thank National Instruments for their collaboration during this project and NIT Europe for providing us with their sensory equipment.

Chapter 1: Introduction

1.1. What is Laser Metal Deposition?

Laser metal deposition or LMD is an additive manufacturing technique through which structures can be formed by melting metal powder or metal wire (depending on the type of LMD process) using a laser source (Sibisi, Popoola, Arthur, & Pityana, 2020). Among other LMD techniques Direct Energy Deposition or DED is a process by which energy is focused onto a very narrow area to melt a substrate and the material being deposited on the substrate to form a melt pool. When the energy source moves off the melt pool at that point, the melt pool cools down forming a solid or deposit (Kai Zhang, 2007). Continuously laying down a length of these deposits can be called a track and each track that is overlayed over each other is known as a layer Figure 1 a. A common DED system is a Laser-based Metal Deposition or LBMD system which comprises of a deposition head, Powder Feed System and robotic arm or/and rotary table that moves the laser head and/or the table relative to each other. As shown in Figure 1 b, A typical deposition head for LBMD which uses powder material contains Laser Optics that focuses the laser on to a spot, powder feed nozzles, shield gas nozzle and at times sensors. The powder feed system jets metal powder through the nozzles onto the melt pool created by the laser and the shield gas controls the spread of the powder along with controlling the oxidation of the melt pool in the presence of air. The laser head is usually mounted on a 3 to 5 axis CNC that can enable manufacturers to create complex 3D shapes with the aid of CAD software’s (Gibson I., 2015).

The LMD machine has the following basic machine parameters, Laser Power, Laser Spot Size, Powder Feed Rate and Scanning Speed. Laser Power is the actual power of the laser which increases the intensity of the energy source while spot size is the area of the laser on the substrate focused using the laser optics installed in the head. The Powder feed rate is the flow of powder delivered into the melt pool and the scanning speed is the speed at which the Laser head moves over the surface.

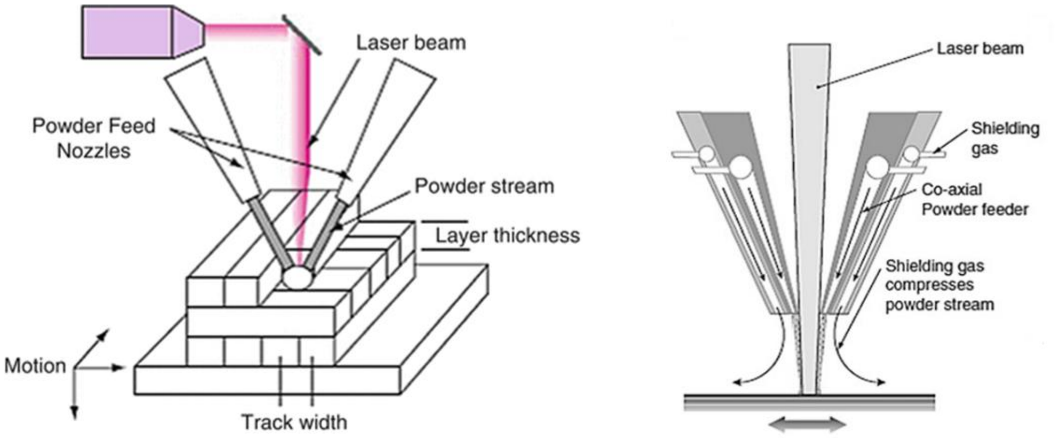

a) b)

Figure 1: a) LMD Process b) LMD Laser Head (Gibson I., 2015)

1.2. Applications of LMD

Laser metal deposition has found its applications in multiple major industries like Aerospace, Medical, Oil & Gas, Automotive and Tooling. (John H. Martin, 2017) (Torsten Petrat, 2016) (Markus Franz, 2014)

The Medical industry uses LMD specifically due to its ability to create custom complex shapes and the large range of powder materials that can be used in the process. Most alloys are used to create custom implants and prostheses like bone replacements, orthopedic implants, and dental implants. Some structures take advantage of the porosity or lattice structures to improve osteoconductivity[1] in bone implants and scaffolding structures. Different powder mixes can be used to enhance bioactivity[2], osseointegration[3], antibacterial and antimicrobial[4] characteristics in the LMD component. LMD can also be used to manufacture complex bioresorbable implants that dissolves with the growth of the bone (Kim Vanmeensel, 2018).

In Aerospace industry LMD is used in rapid prototyping, rapid tooling, direct part production and part repair of metal material components. The characteristics of Aerospace components fit well with the capabilities of the laser metal deposition specifically because they have a

---

[1] "Osteoconduction is the ability of bone-forming cells in the grafting area to move across a scaffold and slowly replace it with new bone over time. Osteoconductive materials serve as a scaffold onto which bone cells (osteoblasts and osteoclasts) can attach, migrate, grow and/or divide."

[2] "Bioactivity is defined as the property of materials to develop a direct, adherent, and strong bonding with the bone tissue."

[3] Osseointegration is the scientific term for bone ingrowth into a metal implant.

[4] "An antimicrobial agent is defined as a natural or synthetic substance that kills or inhibits the growth of microorganisms such as bacteria, fungi and algae."

large volume envelope to volume ratio, aerospace parts are difficult to machine and have high buy to fly ratios, parts have small production runs, parts that need quick turnaround time and parts need to be high performance. Specific applications for LMD include aero engine parts manufacturing, utilization of functional graded materials, mold and die repair casting and turbine blade repair. Examples can be found of parts like helicopter engine combustion chambers, turbine housing chambers, gas turbine exhaust, blisks, impellers and shafts being build using LMD. LMD systems display unique capabilities like low heat input during repair, small heat affected zone during repair, the mixture of powder allows superior mechanical properties of the build piece and complex shapes can be re-created during repair etc. In re-manufacturing and repair it is found that a blisks suffering erosion was repaired using LMD. Another interesting example is where the bearing seating area that was worn out in a gas turbine engine was repaired using LMD (R.Liu, 2017). One of the highlights in the aerospace industry of LMD would be Relativity Spaces' 3D printed Space rockets that have drastically changed the time in which rockets can be built. Relativity Space claims their rockets have fewer parts, their production time is 10 times faster and they do not need fixed tooling using this manufacturing technique (RelativitySpace, n.d.).

The Oil and Gas industry are mainly interested in LMD for the cladding purposes for wear resistant coating on components in offshore and onshore oil drilling. Particularly in TRUMF (TrumpF, n.d.) case study it is found that the metallurgical bond formed using LMD for cladding is far more superior than the conventional thermal spray process (A.J.Pinkerton, 2010).

1.3. Problems and State of the Art Solutions

The industries mentioned above have recognized LMD as a future technology and have invested in purchasing LMD technology. Even though these industries are currently utilizing LMD for specific but limited tasks, they still have not completely overcome the issues that are inherent to this process. These issues can hinder the progress Laser Metal Deposition is making in terms of a reliable and controllable manufacturing process that can produce high quality products with reliability. The two major types of defects that seems to be of paramount interest are cracks and pores. Even though there are other kinds of defects that are produced during the LMD process (ISO13919-2, 2001) cracks and pores seem to be the most important since they can affect the functionality and operational capabilities of the part being manufactured. For example, the parts manufactured in the Aerospace industry do not have a tolerance for porosity (Slotwinski, 2014) while certain parts in the medical industry prefer a certain level of porosity (Kim Vanmeensel, 2018).

Most researchers are nearly in agreement on the general types of Porosity seen in LMD parts, namely Gas Porosity and Lack of fusion porosity. Gas porosity is where any type of gas is trapped within the deposit during the cooldown of the deposit while lack of fusion porosity is incomplete bonding between any two points in the deposit. The researchers also seem to agree with the theories of mechanisms that cause these pores. The nomenclature of the types of Porosity however depends on the perspective on how they are being observed e.g., Pinkerton defines porosity based on the regions it is found in of the deposition (inter track, inter layer lack of fusion and interlayer porosity) (A.J.Pinkerton, 2010).

Cracks on the other hand are undesirable in all industrial applications due to the serious ramifications of cracks and micro cracks on the structural integrity and life span of the product. There is a good amount of study on the types of cracks that prop up during the LMD process and how they are propagated in the material. According to (Wang, 2008) the mechanism to crack generation are well understood and cracks can be classified as Structural Segregation Cracks, Thermal Stress Cracks, Cracks due to post machining and Slag cracks.

Whilst there is information on the mechanisms of LMD physics including its Thermodynamic and Geometric models and the phenomenon that causes defects in the laser metal deposition (A.J.Pinkerton, 2010), there is limited amounts of research found on how to effectively monitor, detect defects, and control the process. The general motivation of researchers is developing a system that utilizes non-destructive testing or NDT to detect defects during the LMD process. The state of the art involves solutions that use different types of Sensors and methodologies which take advantage of the change in thermal((Ulf Hassler, 2016), optical (Wei He, 2019), morphological (Khanzadeh & Bian, 2016), and acoustic (Gaja & Liou, 2017) signatures generated when an anomaly occurs in the deposit. A common trend in research is to train the machine on bad and good signatures. The good and bad signatures are determined through some form metallurgical post analysis of the sample upon which the data was collected.

There is plenty of literature present on the multisensory data fusion solutions to solve precision and accuracy problems with control systems in LMD. The goal objective of (Vandone & Stefano Baraldo, 2018) and (Song, Bagavath-Singh, Dutta, & Mazumder, 2012) is to control build height and dimensions and to do this they use very similar sensors and observe nearly the same phenomenon as in Defect detection solutions. It is ironic that even though they use similar monitoring methods the data fusion and multi sensor methodology approach is not utilized for defect detection research to improve precision and accuracy of detecting defects.

1.4. Research Aims and Questions

As discussed in the section the goal of the current state of the art research and the need of the industry is of a solution capable of monitoring, detecting, and preventing or correcting defects. Critical analysis reveals, each research approach has its limitations and different target goals. These goals vary from detection of specific type of Defect, Number of defects, Position of defects and Size of Defects. Each of the mentioned features is very important as they reveal vital information which determines the quality of the deposition as well as information required to take corrective action. However, each method seems to be observing different phenomenon's which occur at different stages of the defect development (The phases in which the defect starts to develop and then stops developing or comes into its final form) with different sensors and processing hardware which have varying sampling speeds and working principles. The trend analysis for the data collected also varies and each method uses different defect provocation techniques to carry out their experiments which might provoke different types of defects. Post metallurgical procedures and analysis techniques to which collected sensor data is compared to are also different. It can be assumed just based on the varying methodologies and approaches even before further investigation is revealed that each approach has its advantages as well as limitations in detecting and predicting the features of the defects. However, one thing is evident; research does not provide a singular solution that would be capable of painting a more complete picture of the state of the sample i.e., detecting position, type, size, and total number of defects which is more in line with the actual need of the industry.

Considering the need of the industry and the general motivation of the research, the different goals and limitations of the current research pose some very important questions regarding the current state of the art and require further investigation so that a more complete solution may be developed. The following is the overarching research question along with its sub questions:

Research Question: *"How can a multisensory data fusion approach overcome the limitations of the state-of-the-art Single Sensor Defect Detection solutions for Laser Metal Deposition? "*

a) *What are the prominent types of defects in LMD including their source mechanisms that give rise to these defects, their sizes, types, their developmental time, and the phases during which they are formed? (This should give a more complete picture of the entire defect development cycle.)*

b) *What are the possible provocation techniques (including influence of machine parameters on defects) that could give rise to different types of defects?*

c) *What are the state of the art in-situ defect detection solutions for laser metal deposition, including the phenomenon they observe, the hardware utilized to observe this phenomenon and its limitations with respect to the laser metal deposition process and lastly the data analysis/processing methodologies including their post/offline analysis techniques which are used to verify/ train their system?*

d) *At what part of the defect development cycle does a specific sensor pick up a specific type of defect? What specific information regarding a defect does a particular Sensor and hardware reveal effectively? What data analysis processing and training method used to predict the features of a defect is most effective?*

e) *What data fusion methodologies in industrial manufacturing could help formulate a possible fusion algorithm for defect detection in LMD that utilizes data from multiple sensors?*

This investigation will layout a road map on how to design a singular solution capable of effectively detecting and predicting useful information regarding those defects. Developing this solution is the goal of this research and the specific objectives of this goal are formulated after the above-mentioned investigations are carried out. These objectives are explained in detail in Chapter 4.

1.5. Significance of this Research

According to (Wohlers, 2008), from 2004 to 2007 Additive Manufacturing products and services have grown by 116% i.e., $612 million. According to (Lang, 2017), experts have predicted AM to become a 20-billion-dollar industry by 2020. It goes on to further explain that reports published by Gartner shows that by 2020, 10% of the applications in the industry will integrate robotic AM technologies in their manufacturing operations. This will cause product release timelines to be reduce by 25% and 75% of all global manufacturers will be using some tooling made with AM manufacturing.

Major industrial giants like SIEMENS (SIEMENS, n.d.) and Rolls Royce (Royce, n.d.) are now heavily invested in Metal 3D printing and are either providing services or creating commercial product parts using LMD. Due to the growing market and such heavy players adopting/investing in LMD, there is a natural need for quality assurance systems. The BigDataLMD project (3dpbm, n.d.) aims to improve the process stability of the LMD process by developing a quality assurance tool for Siemens IIoT platform Mind-Sphere. This project involves a partnership between Fraunhofer IAPT and Siemens AG ,BeAM/AddUP S.A.S, MT Aerospace AG, Safran S.A., ArianeGroup SAS, Precitec GmbH & Co. KG and New Infrared Technologies S.L. EU-funded project Innovative inspection techniques for laser powder deposition quality control (INTRAPID, n.d.) has developed NDT methods for inspection of parts manufactured using LMD. It is very evident that quality assurance tools in LMD are an ongoing effort and there is a serious amount of investment and interest in the endeavor.

A Quality assurance tool/ method capable of monitoring the process, detecting defects and their features will accelerate the acceptability of LMD as a mainstream manufacturing technology. Also, A Highspeed, multisensory, Data fusion approach will further open opportunities to study the LMD process in detail and through the lens of multiple sensors but in correlation to each other.

1.6. Scope and Limitations

The main output of the research is to develop a Multisensory data fusion methodology capable of detecting defects and predicting their features in LMD. The scope of the research is limited to exploring, evaluating, and implementing the most suitable sensor, hardware and methodology combination that can detect defects and predict features for these defects (Quantity, Type, Size, and defected Area) using a custom sensor fusion algorithm. Inevitably, it also involves the development of a hardware and software architecture to handle high speed multi-sensory input. This includes designing experiments to provoke a variety of defects so that signatures of multiple defects can be collected for training data. The findings of this thesis will result in a system capable of detecting multiple phenomenon that indicate defect development at high enough speeds so that they can catch the change in these phenomena with relatively high accuracy. The signals captured during the LMD monitoring should allow for events that indicate the presence or development of defects to be extracted which can be used in a data fusion algorithm capable of predicting defect features. Compared to the state-of-the-art single sensor approach the high speed, multisensory and data fusion approach should allow for more information to be collected and the fusion of data should increase the accuracy of detection of defects.

Consequently, the research has its limitations. The solution does not aim to create a control system that would allow for corrective action to be taken from the predicted results. The system does not output single values for a predicted feature instead, it outputs a range in which the feature value lies. The research heavily relies on the previous literature and does not establish the relation between the sensor signals and the phenomenon being observed. The research does not aim to establish which sensor is better at observing what and instead relies on literature for that.

1.7. Thesis Structure

Chapter 1 introduces the reader to the LMD technologies, its problems, and the current state of the art solutions. It also explains the Research Questions and Aims and the Significance of the study in the greater picture along with the Scope and limitations of the study. Chapter 2 and Chapter 3 aim to investigate in detail the defects in LMD, their source mechanisms along with the technologies and methodologies that were used to detect these defects. Chapter 4 discusses the Specifics of the Knowledge Gap discovered and Objectives of the research. It goes on to explain the Methodology of the research i.e., how the research is carried out. Chapter 5 goes through the development of the custom multi sensor defect detection platform and Chapter 6 explains the experimental design and the experimentation to collect training and test data using the custom platform. Chapter 7 goes in details on how the data is processed and how the defect detection algorithm is developed. Chapter 8 discusses the test runs of the Defect detection Data fusion algorithm along with putting it through a range of statistical tests and its performance in comparison to other researchers. Chapter 9 Summarizes and discusses the entire thesis and puts forth a discussion of further works.

Chapter 2: Defects in LMD

2.1. Cracks

According to (Wang, 2008) there are basically two types of cracks: Cold Cracks (400 to 600°C) and Hot Cracks (800°C to 1000°C). 75% of these cracks are reported to be cold cracks which further enforce the fact that the cooling rates must be lowered to avoid crack generation. Here the researcher has established that the cooling rate can go up to 10^4 °C/s. Below 200°C crack generation is relatively lower however crack expansion is comparatively higher due to contraction tension. The research mainly observes cracks as a function of Temperature instead of time e.g., For Ni45 material, the time taken for the deposit to cooldown from 600°C to 400°C is the time in which 54.3% of cracks are created in their experiment. Table 1 shows the % cracks generated at different temperature intervals during their experiment in different material types.

Temp(°C)	1000-1200	800-1000	600-800	400-600	200-400	0-200
Ni60 % Cracks	1.1%	23.1%	15.4%	42.7%	12.5%	5.2%
Ni45 % Cracks	0	12.2%	16.5%	54.3%	15.6%	2.4%
Co02 % Cracks	2.3%	17.2%	22.2%	49.6%	10.5%	2.2%

Table 1: Percentage Cracking in Temperature Ranges (Wang, 2008)

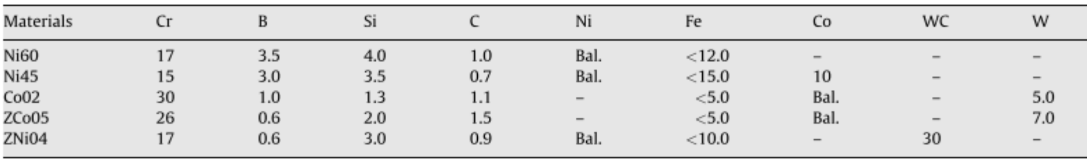

Materials	Cr	B	Si	C	Ni	Fe	Co	WC	W
Ni60	17	3.5	4.0	1.0	Bal.	<12.0	–	–	–
Ni45	15	3.0	3.5	0.7	Bal.	<15.0	10	–	–
Co02	30	1.0	1.3	1.1	–	<5.0	Bal.	–	5.0
ZCo05	26	0.6	2.0	1.5	–	<5.0	Bal.	–	7.0
ZNi04	17	0.6	3.0	0.9	Bal.	<10.0	–	30	–

Table 2: The composition of Laser Cladding Materials in Table 1 (Fujun Wang, 2008)

The above mentioned are of 4 Forms of Cracks; Slag Cracks, Cracks caused by Structural Segregation, Cracks caused by thermal stresses and cracks caused by post machining *Figure 1*. Slag Cracks are created by the slag produced in the melt pool due to impurities which are usually caused at the grain boundaries. Impurities here are defined as slagging elements or oxides generated during the process due to reactions. Structural segregation cracks are caused at the combining sites of coating and substrate. This happens due to both the thermal and structural stresses[5]. Thermal stress are mechanical stresses created due to the change in

---

[5] "Local stress which occurs immediately in front of the weld toe or weld end notch (or on the inside of the plate in front of the weld spot) is designated structural stress."

temperature. Cracks caused by high thermal stresses are mainly due to the difference in the thermal expansion coefficients of the substrate and cladding materials. The last kind of cracks (Post machining) are caused due to the post deposition grinding that is used to smooth out the irregularities in the surface which can cause other internal cracks to rise to the surface.

Figure 2: Classification of Cracks

The study also examines what they call extended forms of crack or what is generally called crack propagation. This is where cracks will extend further to become further elongated or grow is different directions. They find cracks that extend along the direction of maximal shearing stress, extend towards the substrate, extending towards the overlapping cladding and cracks that extend in multiple directions. The study theorizes that the cracks that extends towards the substrate is due to residual stress and the cracks in the overlapping cladding are extended parallel to the cladding. Lastly the cracks that extend in multiple directions are the ones caused due to various stress states of the cladding.

(Wu, Cui, & Xiao, 2020) establishes through their experiments that there is a proportional relationship between the depth of the crack and the peak temperature observed over the crack. This is usually a larger temperature compared to the rest of the melt pool or sample. These observations were made over cracks with widths that ranged from 120µm to 399µm and depths that ranged from 122.71µm to 280.13µm.

(Barun Haldara, 2018) also concludes that Cracks and Spalling are created by thermal stresses developed due to rapid solidification. The study goes on to explain the nature of these stresses to be compressive and tensile however tensile stresses are what the study holds responsible for the cracking. Spallings are where the material breaks down into smaller bits or spalls from the larger body. Spallings are created due to cracks in the LMD coating that are parallel to the surface. As per the definition spallings visually look like Slag Cracks in Figure 3(a). The research classifies the observed cracks as two types: Vertical Hair Cracks(Figure 4) and Segmented Cracks. Both these cracks are created to accommodate strain that is mainly a product of the thermal cycling in the deposition of multiple layers. Thermal Cycling in the

LMD process is where the material goes through two extreme temperatures usually at a very rapid rate. Crevices are formed due to lack of fusion between two adjacent overlapping layers.

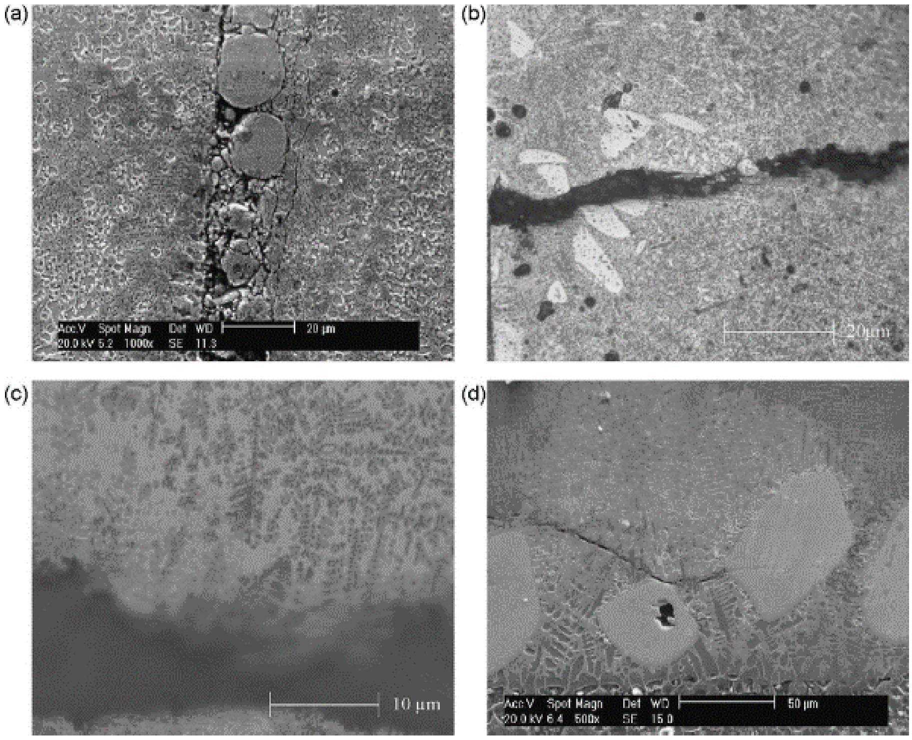

Figure 3: a) Slag Cracks b) Structural Segregation Cracks c) the cracks caused by thermal stress d) Cracks caused by machining (Wang, 2008)

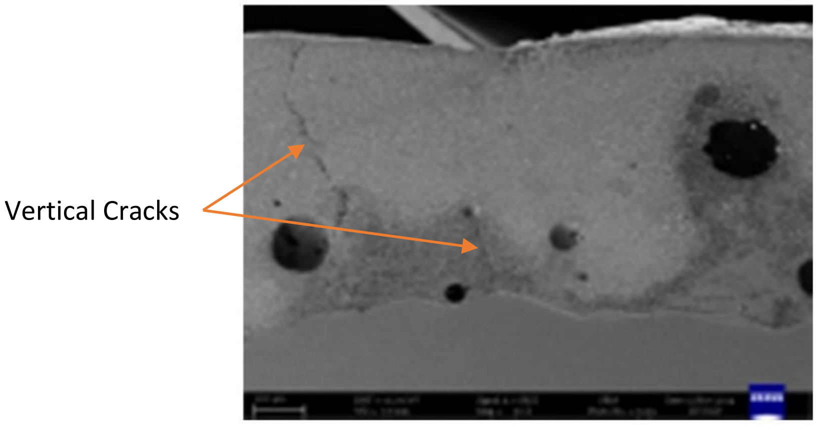

Figure 4: Vertical Cracks in Laser clad layer using 75%WC+25%Ni (Barun Haldara, 2018)

(Gaja & Liou, 2017) classify their defects as cracks and pores which are simulated by mixing two powders namely, Ti-6Al-4V and H13 tool steel. The mentioned powder mixture has a non-uniform shape and size and different thermal coefficients of expansion which should most definitely cause cracks to occur during the process due to high level of thermal stresses. Optical Image (Figure 5) shown in the research infers that crack widths maybe as small as approximately 1µm width and of a length of over 500µm.

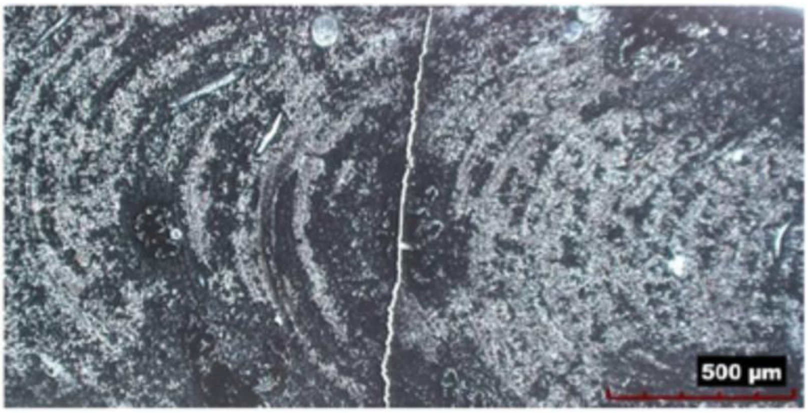

Figure 5: Cracking in Ti-6Al-4V and H13 tool steel LMD Deposit (Gaja & Liou, 2017)

(Segerstark, 2017) research creates cracks by using high laser power, high scanning speed and low powder feed rate. When the defect samples are observed under SEM it is discovered that all cracks observed were Heat Affected Zone Liquation Cracks and formed during re-solidification phase or when liquid metal was still present. This observation suggests that re-melting and re-solidification under certain LMD machine parameter settings may cause cracks. In their Samples total crack lengths or TCL measured from 60µm to 2350µm as shown in Table 3 & the machine parameter for these run are given in Table 4 where $\mathrm{L_p}$, $\mathrm{V_s}$,$\mathrm{M_p}$ and $\mathrm{P_{foc}}$ are the laser power, Laser Scanning speed, powder feed rate and Powder standoff distance respectively.

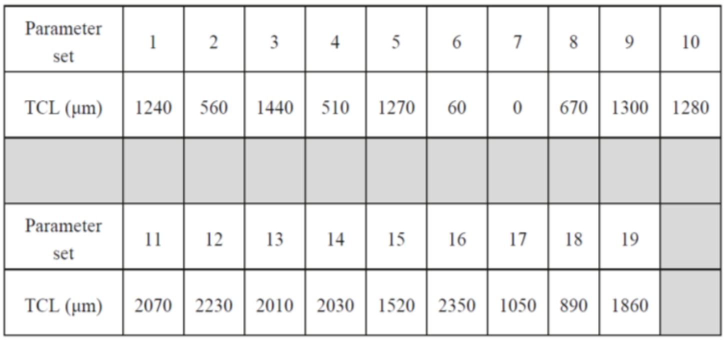

Parameter set	1	2	3	4	5	6	7	8	9	10
TCL (µm)	1240	560	1440	510	1270	60	0	670	1300	1280
Parameter set	11	12	13	14	15	16	17	18	19	
TCL (µm)	2070	2230	2010	2030	1520	2350	1050	890	1860	

Table 3: Total Crack Length (TCL) for set parameters (Segerstark, 2017)

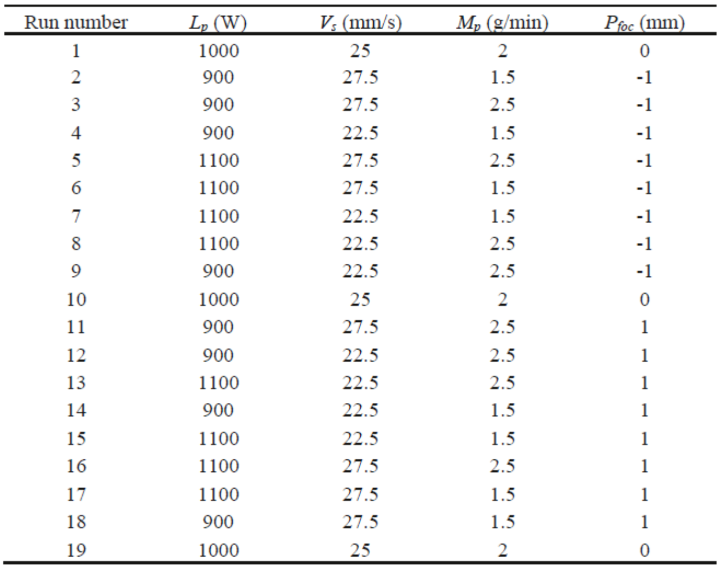

Run number	L_p (W)	V_s (mm/s)	M_p (g/min)	P_{foc} (mm)
1	1000	25	2	0
2	900	27.5	1.5	-1
3	900	27.5	2.5	-1
4	900	22.5	1.5	-1
5	1100	27.5	2.5	-1
6	1100	27.5	1.5	-1
7	1100	22.5	1.5	-1
8	1100	22.5	2.5	-1
9	900	22.5	2.5	-1
10	1000	25	2	0
11	900	27.5	2.5	1
12	900	22.5	2.5	1
13	1100	22.5	2.5	1
14	900	22.5	1.5	1
15	1100	22.5	1.5	1
16	1100	27.5	2.5	1
17	1100	27.5	1.5	1
18	900	27.5	1.5	1
19	1000	25	2	0

Table 4: Machine Parameter Setting (Segerstark, 2017)

(J.Yu, 2013) experiments give insight on how certain chemical composition in LMD powder can cause the final product to be more sensitive to cracking. The research specifies that cracks are formed in interdendritic regions. The experiment establishes that Sulphur, Silicone, Phosphorus and Nitrogen content in the powder influences susceptibility to cracking in the product of LMD. Silicon can form low melting eutectic phases in the interdendritic region and along the grain boundaries which is why it increases crack susceptibility in the work piece. Grain boundaries are the juncture between two gain structures or crystals in the material. Eutectic point is the lowest melting point between a mixture of the composition of the solids. This can be seen in a Eutectic phase diagrams (A. Ramakrishnan, 2020). Interdendric regions are between the dendrites. Dendrites are tree like structures of crystals growing as the material solidifies. Table 5 shows that crack susceptibility increases or decreases with the content of S + P +Si in the powder. The experiment also shows that the nitrogen content is detrimental to the crack solidification resistance of the work piece which can also be seen in Table 5.

Powder Number	S+ P+ Si (wt.%)	S+P (wt.%)	N Content (wt.%)	Cracking	Fabrication Method
1	2.25	0.02	0.047	Yes	Water Atomized
2	1.445	0.125	-	Yes	Water Atomized
3	0.553	0.023	0.062	No	Gas Atomized
4	0.541	0.041	0.09	Yes	Gas Atomized
5	0.475	0.035	-	No	Gas Atomized
6	0.384	0.044	-	No	Gas Atomized

Table 5: Sulphur, Phosphorus, Silicon and Nitrogen Content effect on cracking (J.Yu, 2013)

2.2. Pores and Porosity

(A.J.Pinkerton, 2010) classifies defects as 3 types: inter-track, interlayer, and intra-layer porosity. Inter track porosity is caused by horizontally aligned tracks and form at the base of the tracks. Inter layer porosity is caused by the lack of fusion between vertically aligned deposits while an intra layer porosity corresponds to is spherical pores within the deposition layers. These kinds of pores are said to be caused by trapped gas or moisture and can go on to produce larger voids. Lack of fusion which leads to porosity can be caused by low or improper specific energy provided during the bonding process in the sample, misplaced tracks and the existence or formation of oxide layer which can hinder fusion.

(Gaja & Liou, 2017) in their research induce pores by mixing 6Al-4V and H13 tool steel powder. The pores generated in the process are due to surface powder contamination, gasses trapped due to difference in physical size of the two powders as shown in Figure 6 (b) and due to the oxidation effect as the experiment is carried out in a non-enclosed environment. These surface oxides stay in solid state which causes incomplete melting and induces voids. The gas pores detected are spherical in shape and the inferred size is approximately 125µm as shown in Figure 6 (a).

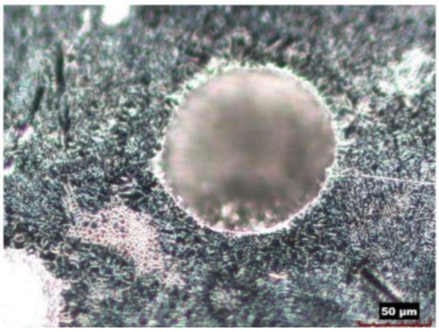

a)

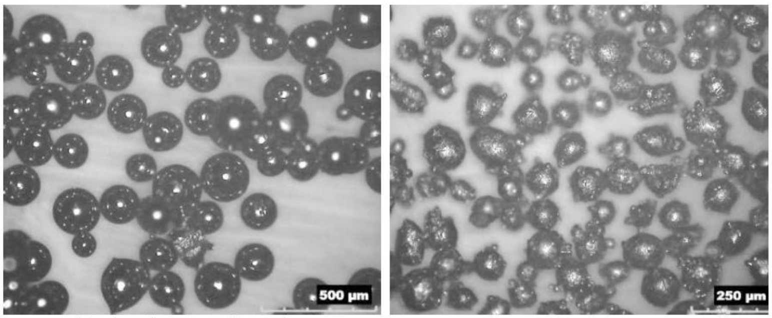

(a) Ti-6Al-4V Metal Powder (b) H13 Metal Powder

b)

Figure 6: a) Typical Gas Pore Shape & Size b) Ti-6Al-4V and H13 powder shape and size (Gaja & Liou, 2017)

(John A. Slotwinski & E.J. Garboczii, 2014) measure and analyse porosity in samples produce by Laser Additive Manufacturing using different techniques. In their experiment the level of porosity increases in their samples with increase in hatch speed or spacing. Both bulk porosities and local porosities were observed in the samples. Observation showed that pores are often not perfectly spherical in shape, hence, to measure their size in 3D and shape the researchers have employed the following technique: For each pore the largest length in the x, y and z directions were averaged over the entire pores samples and weighted by pore volume. Table 6 shows the average length and standard deviation of pores in x, y and z directions along with resolution of XCT scans used to measure the pores. The standard deviation was calculated in all directions so that an understanding of width distribution can be obtained.

Sample	Resolution (µm/voxel)	X-Direction Porosity Average & Standard Deviation (µm)	Y-Direction Porosity Average & Standard Deviation (µm	Z-Direction Porosity Average & Standard Deviation (µm)
1-2	0.82	89.7 ± 73.9	92.8 ± 72.0	73.2 ± 40.6
1-2	2.54	70.4 ± 49.0	70.6 ± 50.9	62.6 ± 33.1

Table 6: Porosity Geometry and Dimensions (John A. Slotwinski & E.J. Garboczii, 2014)

The research also mentions that sometimes pore may be joined/ connected in multiple directions across different layers. There is also a mention that where there are large amounts of Porosity, cracks are also present as shown in Figure 7(a).

(Barun Haldara, 2018) suggest pores are either created by entrapped gases or gases released due to oxidation. Gas entrapment is caused due to moisture in the oxide layer, or the shielding gas being trapped or even due to grease on the surface of the work piece. The gas pores are also created when gases like hydrogen released during oxidation and get trapped during solidification. These may be reduced if the process is held in thermal vacuum chamber, by adding Freon to the shielding gas to reduce hydrogen, addition of Li which promotes formation of Lithium hydride which may absorb hydrogen, or the proper laser power may also reduce holes and porosity. Figure 7(b) taken from the research show pores in a cross-section of the sample and the max inferred size from the scale of a single pore seems to approximately 200µm.

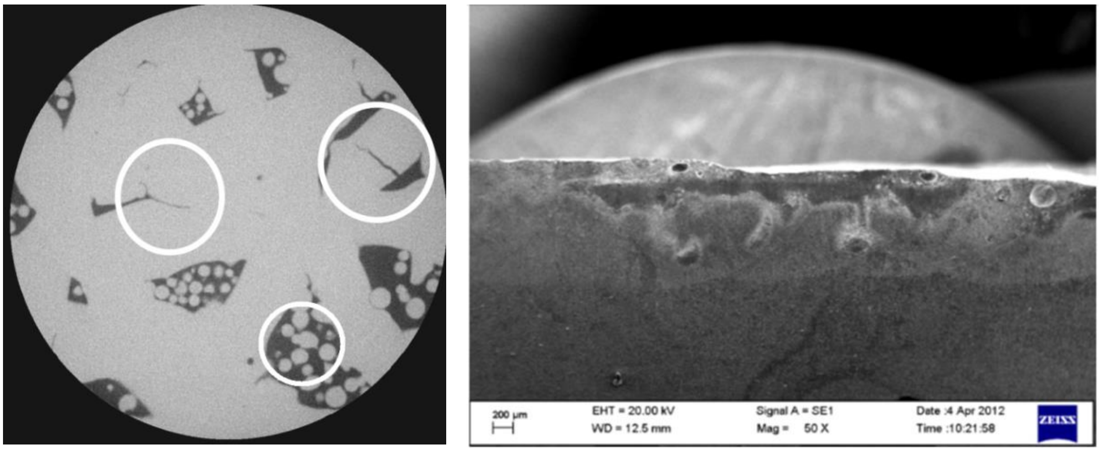

a) b)

Figure 7: a) Porosity and Crack features (John A. Slotwinski & E.J. Garboczii, 2014) b) Surface Porosity in LMD Sample (Barun Haldara, 2018)

(Gary K.L. Ng, 2008) states in his research that the two kind of porosities that are seen in LMD can be classified as Gas Porosity and Lack of fusion porosity. The research claims that gas porosity is caused by gas entrapment in the deposit be it due to oxidation or the inability of shielding gas to escape before the deposit solidifies. He describes the shape of these gas pores to be spherical and that they are not confined to any location in the deposit. Lack of fusion porosity as the name suggest is caused when the two materials surfaces do not fuse completely due to which a void is left in between them. The geometry of lack of fusion porosity is irregular and can usually be found at intersections of the deposited tacks. Garry also explains that like lack of fusion porosity, gas porosity may not be eliminated by optimizing machine parameters however it can be greatly reduced to a very minute amount (0.037%). Figure 8 shows an image of high-level gas porosity and in their research, it is mentioned that pores as small as 6µm have been observed.

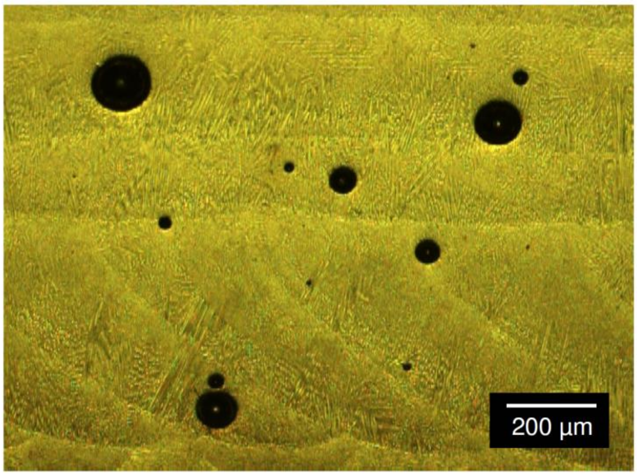

Figure 8: Transverse cross section of laser deposit using Inconel 718 powder over steel plates that shows Gas Porosity. (Gary K.L. Ng, 2008)

(Tiangang Zhang & Ronglu Sun, 2015) In Zhang's study they too attribute pores to gas entrapment and oxidation gas produced in the process. The research establishes that gas bubbles remain trapped as porosity in a sample because the solidification rate which is (dependent on cooling rate) is greater than the escape velocity of the gas bubbles. The samples show that the majority of the pores in the binding region (fusion zone) and pore size is usually greater than 30µm. The research also shows that pores generated are a result of free sulphur and oxygen which combine to form SO_2. The gasses produced are the following:

$$2MoS_2 + 7O_2 \rightarrow 2MoO_3 + 4SO_2$$ (Equation 1: Chemical Reactions that produce gases)

(Jon Iñaki Arrizubieta, 2018) study develops a model which amongst other features of the LMD sample can predict pore generation. The mechanisms of trapped gas during the deposition process and the mechanisms of shrinkage cavities generated due to the contraction of the material are used as the basis for their its porosity prediction model. To predict the occurrence of Gas porosity in a certain region the model calculates the amount of time each element is in liquid state. If the region has a higher time for which it is liquid than the threshold time it has a higher probability of trapping gas. As far as porosity due to shrinkage cavity is concerned; if a region is liquid and is surrounded by solidified material it has a higher probability of pores. This is because of contraction of material in the liquid solid-state change may cause voids.

(Saad A. Khairallah, 2020) uses models to study the pore formation phenomenon and dynamics of the melt pool that causes these defects. The study goes on to classify defects as depression collapse, lateral pores, open pores, and trapped pores. Figure 9 explains the formation of a pore of the defect development phases where pores are created due to depression collapse. Lateral Pores are pores caused by un-melted powder particles that don't merge with the melt pool. Open pores are causes by incomplete remelting of the pervious layers and trapped pores are large ellipsoidal pores that get trapped beneath the surface due to the fast laser ramp down time (Shut off time). From the study pores generation times are also observed to be as low as 11us and 85us.

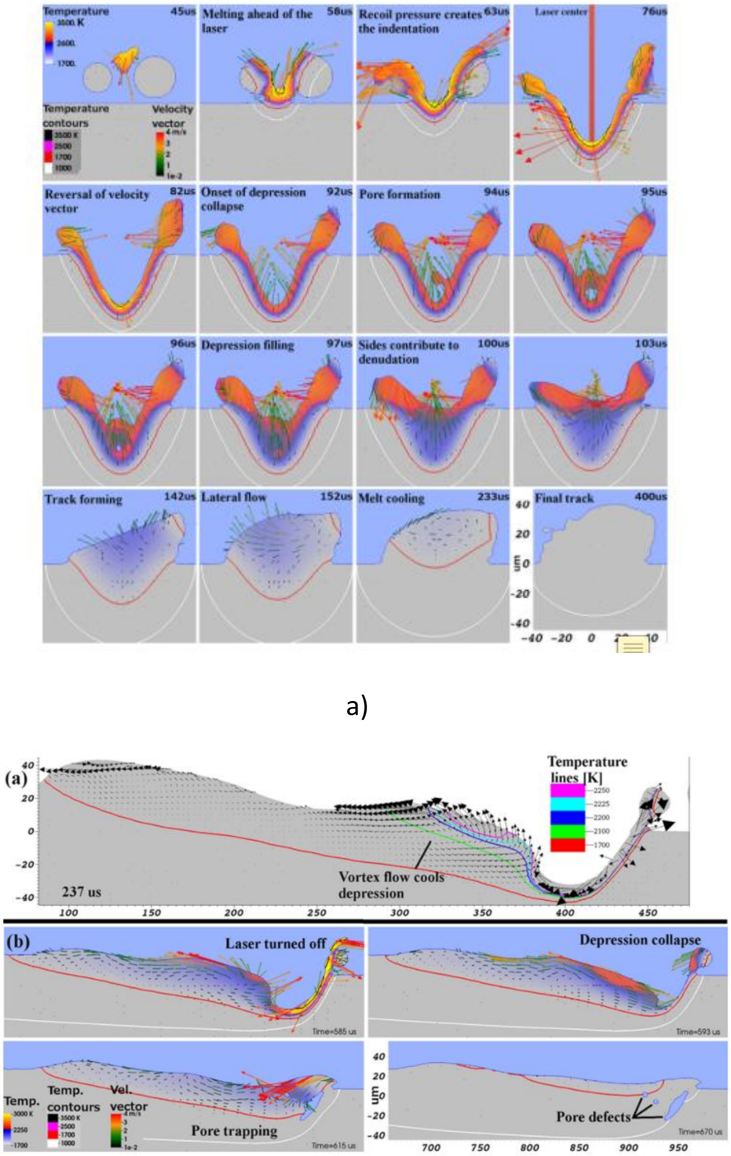

a)

b)

Figure 9: a) Pore formation due to Depression Collapse b) Pore formation due to Vortex (Saad A. Khairallah, 2020)

2.3. Other Defects

The (ISO 13919-2, 2001) classifies defects and their acceptability standards in laser welding which is the closest standard to the Laser Metal Deposition process available. The standards document classifies the kind of defects observed Figure 10 and shows the level of acceptability on three quality levels: Moderate(D), Intermediate(C) and Stringent(B). (Verhaeghe & Hilton, 2004)

The Standards show that in Class B or Stringent Quality Levels Cracks of any kind are not allowed however Pores, Porosity and Localised Porosity are allowed given that they meet a certain criterion. For example, Gas Pores and Porosity is allowed as far as the pore length (l) in any direction is less than 0.3 times the thickness (max 4mm) of the deposit (t) and for laser beam welding it must be smaller than 3% of the projected area(f). The projected area here is calculated by multiplying the thickness of the workpiece by the length of the weld. Weld length being the actual length of weld or 100mm whichever is smaller. For clustered porosity or localised linear porosity, the previous above rules apply but along with that, the inter-distance between any two single pores (ΔL) determines if they are considered as combined or clustered porosity and for clustered porosity the outer inner distance (L_c) is considered as the criteria for quality standard. Table 7 shows the acceptability criterion for Clustered Porosity, Porosity and Gas pores in intermediate, moderate, and stringent standards. The levels here refer to production quality and not for the fitness for purpose of the product manufactured.

The defects mentioned in Figure 10 are caused by porosity, thermal stresses, incorrect machining or machining setup, high cooling rates and impurities in the substrate. Crater Pipe defects are similar to craters in physical feature and are caused by gas pores that escape to the surface. Shrinkage cavities are caused by high cooling rates which cause materials to contract/shrink which ends up creating a cavity at the surface. Solid inclusions may occur due to impurities in powder or powder that is not melted completely. Lack of fusion as discussed usually occurs due to difference in thermal gradient of high cooling rate. Sagging again is caused by large porosity escaping during the cooling process causing the deposition to sag and weld splatter is common due high powder feed rate but can be machined off later. Incomplete Penetration, Undercut, Access weld metal, Linear Misalignment, Incomplete fillet grove Deviation from specified axis is more of welding problems but hardly occur in the LMD process with the advancement in terms of the precision of LMD machines.

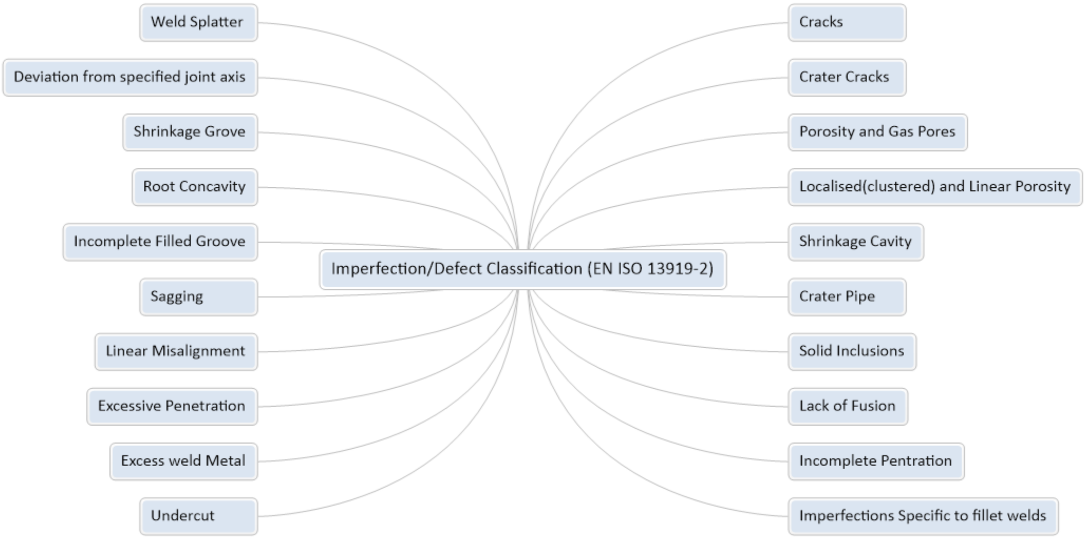

Figure 10: Defect Classification as per ISO 13919-2

Type of Defect	Diagrams	Standard B	Standard C	Standard D
Porosity & Gas Pores	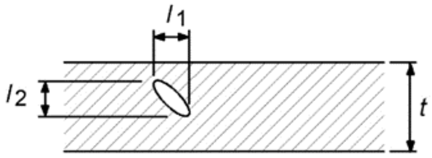	$f \le 3\%$ $l \le 0.3t$	$f \le 6\%$ $l \le 0.4t$	$f \le 10\%$ $l \le 0.5t$
Clustered Porosity	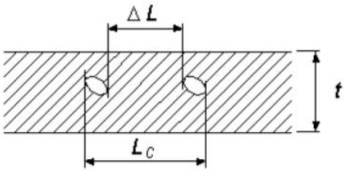	$f \le 2\%$ $l \le 0.3t$ (Max 4mm) $\Delta L = 5t$ (Max 5mm) $L_c \le t$	$f \le 5\%$ $l \le 0.4t$ (Max 5mm) $\Delta L = 5\%$ (Max 10mm) $L_c \le t$	$f \le 15\%$ $l \le 0.5t$ (Max 6mm) $\Delta L = 25t$ (Max 15mm) $L_c \le 2t$

Table 7: ISO 13919-2 standards for Pores and Porosity

2.4. Influence of Machine Parameters on defects

(Rasheedat M. Mahamood, 2014) investigates the relation of porosity to Laser Power and Scanning Speed experimentally using Ti6Al4V powder on a hot rolled Ti6Al4V plate. Particularly average porosity and average pore size in samples were observed. It is observed that with Laser Power increasing from 400W at 800W the average porosity was significantly reduced from 18% to 8.5%. However average pore size increased significantly with the same scanning speed at higher Laser Power (800W). When scanning speed was decreased the average pore size decreased which explains that even though porosity decreases at higher laser power due to more energy being provided to the system which causes a more complete melting of the powder, a higher scanning speed does not allow sufficient time for trapped gas to escape before the deposit solidifies. This shows that Laser power and Scanning Velocity are inversely regarding the formation of pores. By tuning the machine parameters, they were able to achieve a completely porosity free sample as shown in Figure 11.

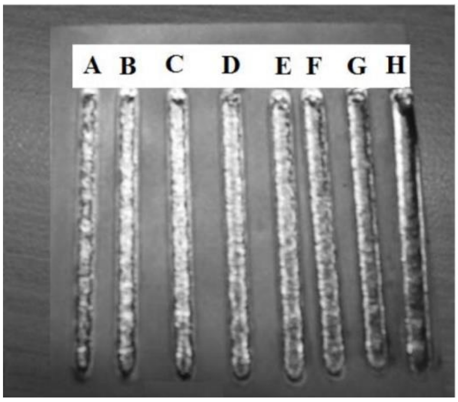

Sample Designation	Average porosity (%)	Average pore size (μm)
A	19.28	12.84
B	11.15	10.05
C	5.14	6.11
D	1.28	1.55
E	8.53	84.11
F	3.98	78.67
G	0.90	7.31
H	No porosity	-

Figure 11: Average Porosity and pore size reduction thought LMD parameter manipulation (Rasheedat M. Mahamood, 2014)

(Gary K.L. Ng, 2008) establishes in his experiment the relation of Laser Power, Scanning Speed, Powder Feed rate, Shielding Gas, Percentage overlap with build height, Porosity and Lack of Fusion using Inconel 718 powder on steel plates as shown in Figure 12. The results show that Laser Power and Powder feed-rate has a significant influence on Gas Porosity but Shielding Gas rate seem to have the most influence due to gas entrapment. Lack of fusion is heavily influenced by the combination of Laser Power and Scanning Speed. As far as build height is concerned Shielding gas rate and scanning speed are inversely proportional to build height whereas all other parameters have a direct relation with build height.

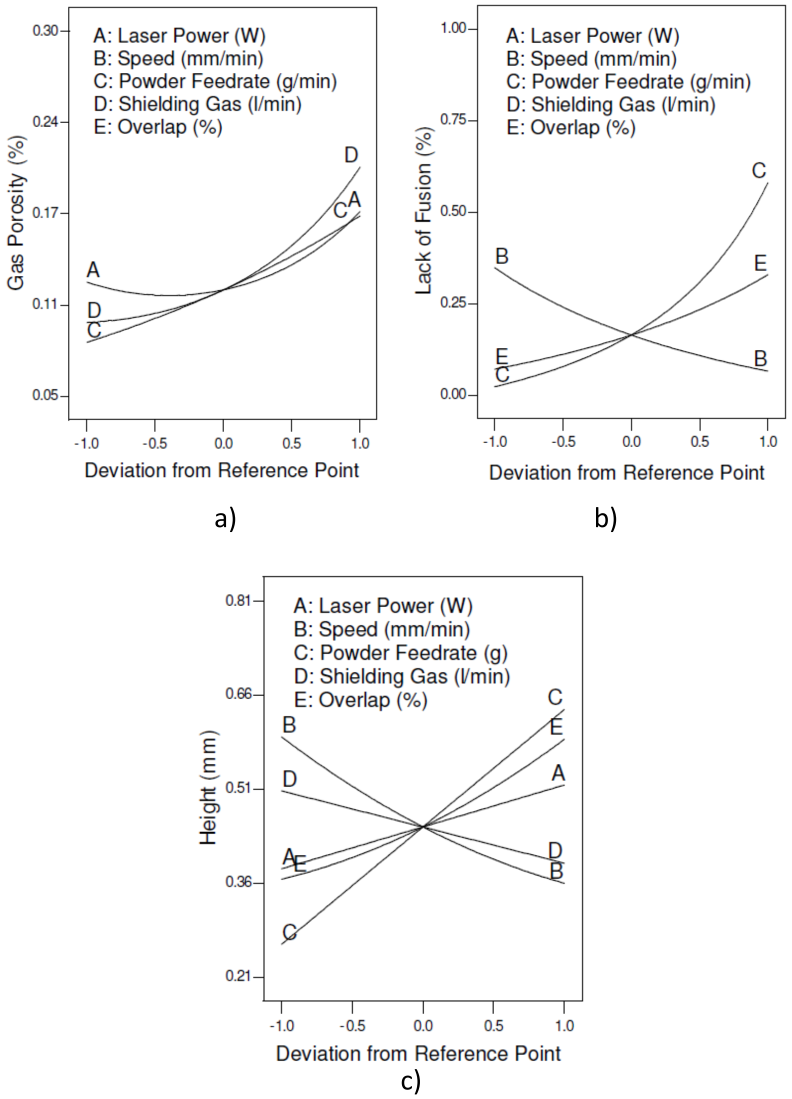

a)

b)

c)

Figure 12: Effect of LMD parameters on a) Gas Porosity Defects, b) Lack of Fusion and c) build height (Gary K.L. Ng, 2008)

(C Y Kong, 2010) deposit Inconel 718 powder on to Inconel 718 plates and in their experiments discover optimised process parameters to get a high-quality product. The criteria established for the grade of the product by the researchers is shown in Figure 13.

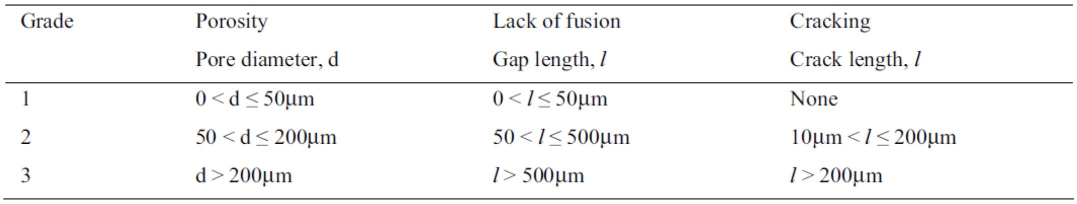

Grade	Porosity Pore diameter, d	Lack of fusion Gap length, *l*	Cracking Crack length, *l*
1	$0 < d \leq 50\mu m$	$0 < l \leq 50\mu m$	None
2	$50 < d \leq 200\mu m$	$50 < l \leq 500\mu m$	$10\mu m < l \leq 200\mu m$
3	$d > 200\mu m$	$l > 500\mu m$	$l > 200\mu m$

Figure 13: Grading Criteria for Solidification Defects (C Y Kong, 2010)

All samples had a porosity of less than $50\mu m$ and an overall low level of porosity which was achieved by machine feed rates (scanning speed) of less that 1000mm per minute. The only porosity seen in the samples is attributed to powder quality and high Shielding gas rates. With high laser power of 1400W and high powder feed rate, cracks are less likely to occur. It is also stated that cracks are not significantly influenced by beam spot Size and machine feed rate. Lack of fusion can be minimised by ramping up the spot size of the Laser. Figure 14 shows machine feed rate and powder flow rate influence on Porosity, Lack of Fusion, Cracking and root Penetration predicted by Design Expert Software for 1400W and beam spot size 1.5mm.

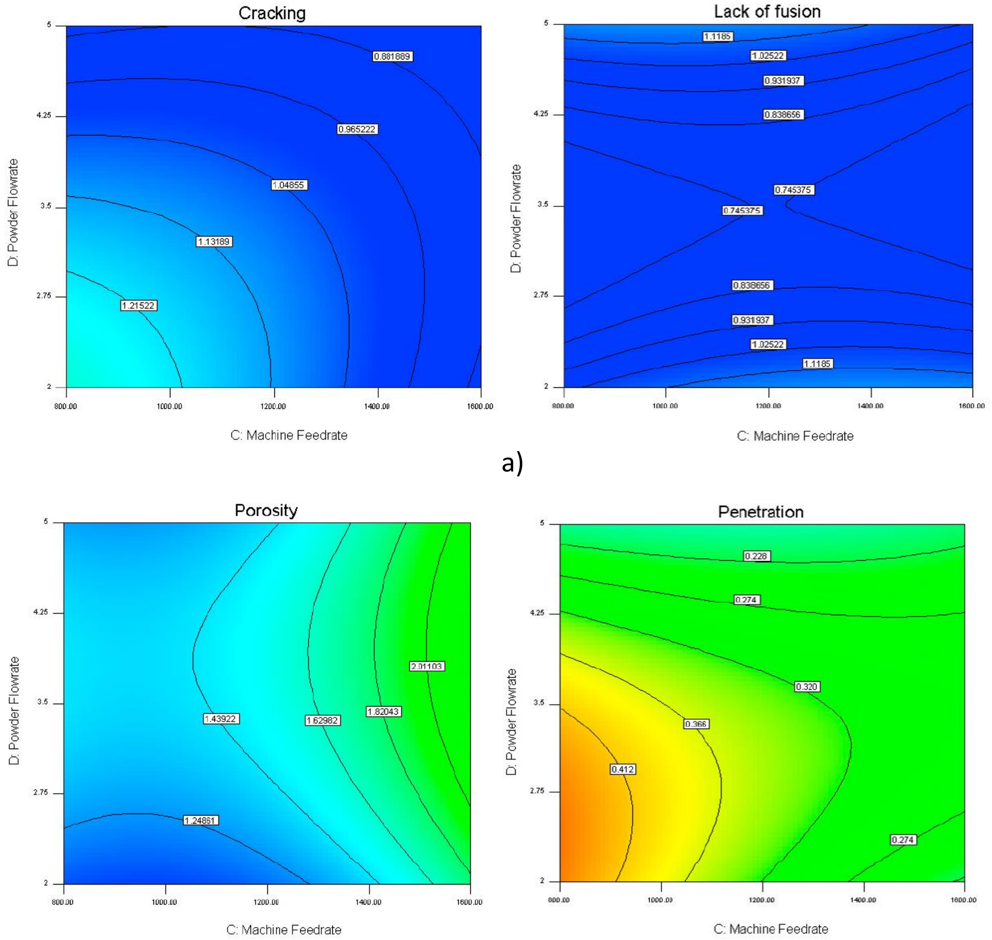

a)

b)

Figure 14: a) Machine Feed Rate and Powder Flow Rate effects on Lack of Fusion and Cracking as predicted by Design Expert Software b) Machine Feed Rate and Powder Flow Rate effects on Porosity and Penetration as predicted by Design Expert Software (C Y Kong, 2010)

Even though the purpose of the study by (Mohammad H. Farshidianfar, 2016) was to monitor cooling rates and not the defects generated in LMD, the study gives an insight on how cooling rates is affected by scanning speed. The cooling rates govern the time it takes for material to solidify and from the literature in this chapter it is well established that the quick solidification of the material can cause defects like porosity and cracks to be formed. Using 316L stainless steel the study observes the cooling rate in relation to machine parameters and this indirectly indicates a relation of scanning speed with defect generation. Figure 15 shows the effect of scanning speed on melt pool temperature and cooling rate. The higher the cooling rate the more likely it is that defects will occur.

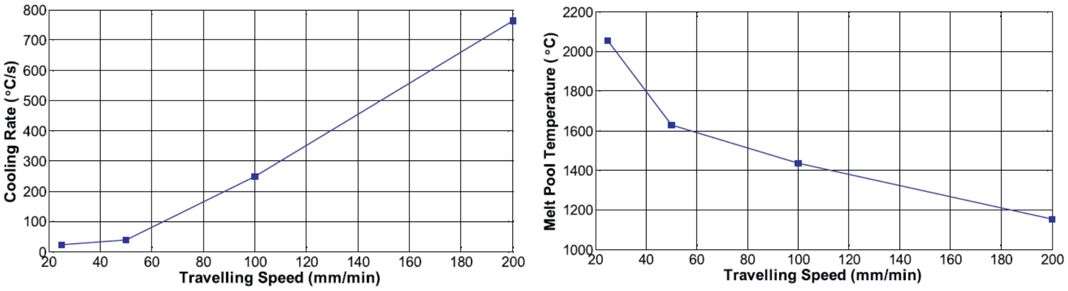

Figure 15: (a) Relation between Cooling Rate and Scanning Speed (b) Relation between Meltpool Temprature and Scanning Speed (Mohammad H. Farshidianfar, 2016)

On the matter of cooling rate (Zavala-Arredondo & Haider Ali, 2018) state that typical cooling rates can be as low as 10^3 °C/s and go up to 10^7 °C/s. The study suggests that very high cooling rates may cause cracking in brittle materials since cooling rates and residual stress have a direct correlation.

2.5. Discussion

The majority researchers are at a consensus that cracks, and pores or porosity are an inherent problem in Laser Metal Deposition. However, how these defects are classified is slightly different depending on the researcher and reference to which these defects are being observed. Mostly these are classified by the source mechanism responsible for them or the temperature region they are found in or the location in the deposit they are found in. Table 8 shows how Pores and Cracks are classified in LMD research.

Classification Bases	**Defect Type**	**Classification**
Temperature Region	Crack	Hot and Cold Cracks
Source Mechanism	Crack	Slag Cracks, Structural Segregation Cracks, Thermal Stress Cracks, Post Machining Cracks
Physical Appearance	Crack	Vertical Hair Cracks, Segmented Cracks
Region of Deposit	Porosity	Inter-layer Porosity, Intra-Layer Porosity and inter track porosity
Source Mechanism	Porosity	Gas Porosity and Lack of Fusion Porosity, Depression Collapse Pores, Lateral Pores, Open Pores and Trapped Pores
Measurement Criterion	Porosity	Bulk Porosity and Local Porosity

Table 8: Pore and Cracks classification in LMD research

The experimentation reviewed in this thesis shows that crack length can range from anywhere between $60\mu m$ to $2350\mu m$, crack width can range from $1\mu m$ to $399\mu m$ and crack depth $122.71\mu m$ to $280.13\mu m$. Research also reveals a relationship between Temperature measured over cracks and the crack depth. The relation of crack depth would show that a thermal sensor could be used to reliably capture cracks and their depths.

General cooling rates can range from 10^{3}°C/s to 10^{7}°C/s depending on material and machine parameters etc. The approximate time for a single crack can be calculated using cooling rates based on the number of cracks generated in a specific temperature interval however, this approximate might not be very reliable. It is however known that the majority (75%) cracks develop and expand at the lower temperatures (600°C to 0°C). This means that if you want to catch a crack being generated, the observation of the cooling phases should be given more weightage than the heating stages.

As far as cracks are concerned most research agrees that cracking across different materials is caused by high thermal stresses, high cooling rates, powder chemical composition, powder thermal coefficient, powder quality (Uniformity, shape, and size) and machine parameters (Scanning Speed, Laser Power and Powder Feed Rate). A good understanding of how to avoid cracking or even eliminating it is found in the literature. A widely suggested technique to avoid cracking is to pre-heat the powder before the deposition process which should also slightly help in melting the powder quicker. Cooling rate seems to be key in controlling the generation of cracks and can range from $10^3\ {}^oC/s$ all the way up to $10^7\ {}^oC/s$. Hence controlling or having the knowledge of cooling rates of a certain material in LMD is essential to predict if a defect will occur. It is also important to lay emphasis on the fact that inside the melt-pool, different regions may have different cooling rates which is why it is correct to assume that a stable melt pool is one where its temperature distribution is relatively uniform. A stable melt pool is less likely to have cracks or even other defects. Post machining may also cause crack or existing cracks to extend. When a high level of strain is built up inside the material and further stress is added through post machining, crack extension/propagation is a way for the material to relieve built up strain. A lot of current LMD machines utilize hybrid manufacturing methods where first LMD is carried out and any imperfections are smoothed out by subtractive tools. Another way of avoiding cracks is the right combination of relatively high laser power, relatively low scanning speed and to some extent relatively high powder feed-rate. Lastly powder quality in terms of its shape and size, impurities, and the content of Silicon, Phosphorous Sulphur and Nitrogen increases the crack susceptibility in a material. Where all the above information provides techniques to avoid cracks, it also provides vital information on how to provoke cracks.

Porosity is one of the more important defects to be controlled and identified since at times it is a desirable feature and at times it is partially accepted and at times it is completely unacceptable in certain LMD applications. It is clear from the research that porosity levels can be controlled but it is not clear to what extent. Some researchers even claim that porosity may not be eliminated but reduced to an insignificant amount. This is probably why the EN ISO 13919-2 standards allow a certain amount of porosity, given that they meet specific quality criterion.

The reviewed literature show that pores come in different shapes and sizes. Gas pores are spherical in shape and lack of fusion pores have a more irregular shape but are still round. However, there is a distinction made between voids and pores based on shape. The general projected or 2D size from microscopic or XCT images is $6\mathrm{\mu m}$ to $200\mathrm{\mu m}$ for spherical pores or ellipsoidal pores and for non-spherical pores in x, y, and z direction $x = 74.4\mathrm{\mu m}\ \mathrm{to}\ 89.7\mathrm{\mu m}\,, y = 70.6\mathrm{\mu m}\ \mathrm{to}\ 92.8\mathrm{\mu m}\ and\ z = 62.6\mathrm{\mu m}\ to\ 73.2\mathrm{\mu m}$.

Once again there is only a slight difference in classification of pores between researchers however it seems that they all agree upon the reason's pores are generated in the LMD process. It seems that porosity is caused by entrapped gases be it from oxidation, by product of chemical impurities or the shielding gas or even moisture. Most researchers consider the defects created by lack of fusion to be pores too but there are few who have not classified it as a pore. Gas often gets trapped due to the quick cooling of the deposit in LMD and are often seen in regions where both solid and liquid of the material exist at the same time. Un-melted powder is also given attributes to causing pores.

The interesting attribute about pores as a defect is they are acceptable even in the most stringent quality standards given that they pass a certain dimensional criterion. Hence it might be more important to figure out the level of porosity than just simply find out if a piece has pores or not.

There is no empirical evidence on the timing of pore generation because the LMD process is very quick. However, from certain models the plausible times for a pore to be generated can be found. According to the model presented by (Saad A. Khairallah, 2020), gas pores or entrapped pores development time can be as low as 11 µs and 85 µs.

Porosity can be significantly reduced by optimising machine parameters. Basically, giving the gas bubbles enough time to escape the melt pool before solidification is the objective. By decreasing scanning speed and increasing laser power this can be achieved however this means increased build height which can be mainly controlled using powder-feed-rate. Hence, when controlling porosity using machine parameters it is important to observe the build height too.

A conclusion can be drawn from the influence of machine parameters study that Pore Sizes increase with Laser Power and reduce with reduction in scanning speed. General Porosity decreases with increase of laser power and General Porosity increases with increase in powder feed rate and shielding gas rate. Cooling Rate however is heavily influence by Scanning speed i.e., as scanning speed increases so does the cooling rate and the average temperature of the melt pool decreases with higher cooling rates. Lack of fusion increases with powder feed rate and decreases with scanning speed. All these relationships can be used to decrease defects or if need provoke them.

EN ISO 13919-2 mentions a few other defects, but they all seem to be caused by the same source mechanisms; pre-existing porosity, thermal stresses, incorrect machining or machining setup, high cooling rates and impurities in the substrate. However, since they aren't many of these other type of defects in LMD it would be sensible to just focus on Cracks and Pores.

In conclusion it is learnt the typical sizes and shapes of Cracks and Pores that are observed in LMD. These features should help identify these defects when observed in the experiments for this research. It can also be concluded that since the other type of defects are not as much in quantity it would be better to concentrate on cracks and pores and classify all other defects as "other defects". From the literature the knowledge of defect generation time, the temperature zones, and geometric regions that the majority defects appear in, and the cooling rates at which they are generated is also gathered. This should help identify the specification of sensors and systems that can be used to observe these defects. Understanding the source mechanisms for the defects can also help design experiments to provoke a variety of these defects.

Chapter 3: Process monitoring, Defect Detection Methodologies and Systems in LMD

The major focus of this chapter is to investigate the LMD technologies and methodologies used to monitor and detect defects online. The aim is to discover the physical phenomena that occur during the LMD process which can be leveraged to effectively indicate defects. Consequently, the state of the art is studied to discover hardware that is typically used to detect these phenomena and the specifications of the hardware necessary to effectively pick up these defects. The investigation will also aim to study the methodologies researchers employ to monitor the LMD process and detect defects. This will include the defect provocation techniques, post analysis methods, any modeling or machine learning techniques employed as well as any signal transformation and processing techniques utilized in their methodology.

The last part of this chapter also looks at the Multisensory systems and data fusion methodologies in the state of the art that are used to monitor the LMD process or detect defects in an LMD sample. A study of popular data fusion architectures employed in manufacturing is also carried out to understand and possibly design a customized data fusion method.

3.1. Optical Camera Defect Detection and LMD Monitoring Systems

(Barua & Frank Liou, 2014) uses vision-based technique to detect defects like cracks and porosity based on the cooling curve generated by the deposit. The experimentation employs a SLR Camera[6] fitted with Macro lens for zoom and a neutral density filter to observe the entire deposit. The concept is to observe the spectral radiance of the deposit and as result observe the intensity of the image pixels of the deposit. The relation between the spectral radiance of ideal black body in vacuum and temperature and wavelength is given by Plank's equation ((Equation 2).

$$L_\lambda = \frac{C_1}{\lambda^5 . (e^{\left(\frac{C_2}{\lambda T}\right)} - 1)}$$ (Equation 2: Planck equation for spectral radiance)

$$C_1 = 2hc^2$$ (Equation 3: First Radiation Constant)

$$C_2 = \frac{hc}{k}$$ (Equation 4: Second Radiation Constant)

---

[6] SLR(Single-Lens reflex Camera)

$L_\lambda = Spectral\ Radiance\ \left(\frac{W}{sr\ m^2 m}\right)$

$\lambda = Wavelength\ of\ body\ in\ vaccum(m)$

$C_1 \&\ C_2 = Radiation\ Constants$

$T = surface\ Temperature\ (K)$

$\mathrm{h} = \mathrm{Planck's\ constant}(6.63\ \mathrm{x}\ 10^{-34}\ \mathrm{J\ s})$

$\mathrm{c} = Speed\ of\ Light(2.99\ \mathrm{x}\ 10^{-8}\ \mathrm{m\ s^{-1}})$

$\mathrm{k} = Boltzmann's\ constant(1.38\mathrm{x}10^{-23}\ \mathrm{J\ {}^{\circ}K^{-1}})$

Figure 16 Shows that at higher temperatures the wavelength decreases and however with increase in wavelength spectral radiance decreases after certain temperature points. According to measurements made by the pyrometer the highest temperature range recorded for their experiment was 2700K (2426.85°C) and hence the magnitude of spectral radiance of an ideal body would correspond to 0.5µm -0.8µm.

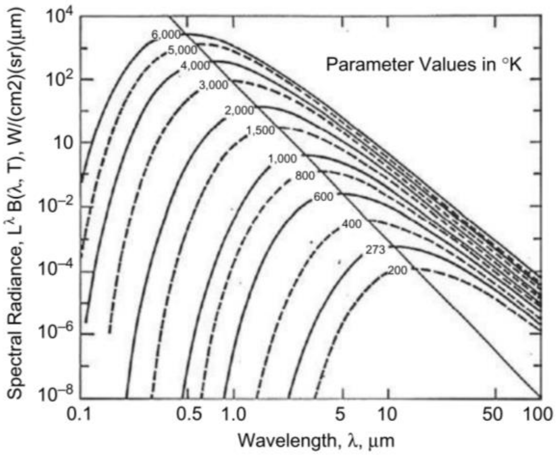

Figure 16: Spectral Radiance at unity emissivity derived from Planck's equation

The heat flow of the melt pool acts as an indicator of whether a defect is present in the object or not. In a normal or ideal case when the melt pool is generated the rest of the substrate acts as a heat sink and allows the heat to dissipate uniformly into the substrate. Heat flow is disrupted in the presence of defects such as porosity or cracks and hence high temperature regions form around these defects in the melt pool (Liu, Kumar, Bukkapatnam, &

Kuttolamadom, 2021). This leads to sudden temperature deviations from the normal temperature gradient hence creating an opportunity for the observer to identify the presence of a defect. Because there is a relation between temperature and spectral radiance an optical camera can be said to be suitable to indirectly pick up temperature. Using the images obtained with a SLR camera the author creates temperature gradient curves by associating the Incandescence of the deposited material to RGB values associated with temperatures which are calibrated using a pyrometer beforehand. Incandescence is the emission of electromagnetic radiation from a heated body because of temperature. A non-defected deposit temperature curve is compared to defected deposit temperature curves to determine if the sample is defected. The research points out that emissivity can affect the sensor readings but since their study is observing patterns of temperature gradient and not the actual temperature intensity to be an indicator of defect, emissivity may not make a big difference in the defect detection process.

(Tao Liu, 2019) manages to achieve real time defect detection system using an imaging system that utilizes Principal Component Analysis or PCA and support vector machine or SVM to detect and classify defects. The research uses a CCD[7] camera mounted inside the laser head which takes images of the melt pool and extracts the following features of the melt pool: Area, Perimeter, Compactness, Centroid x, Centroid y, Height, Width, Average Grayscale values, Number of Pixels and Average Temperature. The camera captures RGB images, each image is filtered and then turned into a grey scale image. Using thresholding the gray scale image is then converted into a binary image to establish a region of interest or ROI. A PCA analysis (Gawade, Singh, & Guo, 2022) is applied to these features to reduce the dimension of the set and then their PCA coefficients are used to establish the strength of the relationship between the principal components generated. The defect detection principle remains the same i.e., heat flow is interrupted due to the presence of defects and shape and size of the melt pool changes to accommodate to the necessary heat flow of the system. The first 2 PCA components are used to build an SVM classifier (Gaikwada, Yavaria, Montazeria, & Kevin Colea, 2020) for slag inclusion type of defect and the first 3 PCA components are used to build the SVM classifier for bulge type of defect. Since PCA reduces the dimension of the entire set only inferences can be made about which one of the Principal Component represents what part of the original features set. According to the author the first Principal

---

[7] CCD(Charged-Coupled Device)

component in their experiment represents the composition of the Melt pool size, the second one represents the cooling rate and the third one represents shape. The author concludes that the PCA components relation to the accuracy of the classifier is complex, given that if the right components are not chosen it reduces or increases accuracy of the system.

(Liu, Farahmand, & Kovacevic, 2014) use a Charged Couple Device or CCD Camera to observe the powder particle flight in the LMD process. The powder particles are illuminated by a 532nm green laser light and the reflection from the particles was picked up with a camera with an exposure time of 0.02s. From the max frame rate the exposure time is calculated to be 50fps $(FPS^{8} = \frac{1}{Exposure})$. An average of 25 images is taken to compensate for motion blur. The study aimed to observe particle velocity, powder concentration distribution, intersection position of the powder streams, and intersection position of the powder streams and laser beam. The CCD camera is picking up the luminance intensity of the particles which is explained by “Mie’s theory” or “Mie’s Scattering”. (Lockwood, 2016) (Liu, Farahmand, & Kovacevic, 2014). Luminance intensity is the measure of the wavelength-weighted power emitted by a light source in certain direction. Mie theory explains the scattering and absorption of light by a spherical particle of arbitrary size and refractive index. From this research it derives that the luminance intensity is proportional to the number of particles irradiated per unit area. Particle velocities are calculated to be from 2.4m/s to 4.9m/s. Even though the Laser beam and particle interaction is measured using thermal camera, the researcher reveals that thermal emission of particles is affected by the concentration of the powder in the area being observed and hence might not be the best way for quantitative measures. This means for low concentration areas the optical camera method of observations might be the best to study powder interaction. The study points out that Optical Sensors can pick up important information about the powder interactions with LMD.

(Robert Sampson, 2020) uses a Complementary Metal Oxide Sensor or CMOS camera and develops an improved image processing technique to observe the melt pool geometry. They use NIR COMS machine vision camera which is coaxially installed into the laser metal deposition camera. The camera is installed with an optical density filter for wavelengths of 200 -750nm which allows only to view light of certain wavelengths. The algorithm uses the directional emittance phenomenon to calculate melt pool dimensions which they found to

---

[8] FPS (Frames Per Second)

be a much more accurate method than the commonly used emissivity-based technique. Directional emittance is due to grey body radiation not emitting equally in all directions hence part of the substrate might be emitting strong radiation due to the angle it is being observed at even though, the temperature might be lower. The research points out that commonly used emissivity based binary threshold method (pixel intensity values are correlated to materials melting temperature) is often subject to erosion and dilation (in the image) therefore are unreliable in measuring melt pool dimensions.

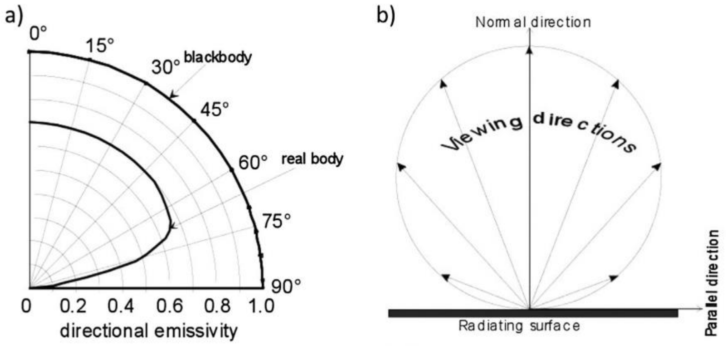

Figure 17: a) A schematic representation of directional emittance from a flat surface. b) Directional emittance of a blackbody and real body. (Robert Sampson, 2020)

(James C. Haley, 2018) study the powder particle interaction with the melt pool using 4 different highspeed cameras at 200 000 FPS. Particle speed was recorded depending on the direction and it was found to be 2-5m/s. The research found particles to impact of the melt pool surface and cause a ripple, float on the surface and then being observed into the melt pool. The time a particle stays on the melt pool before being absorbed is called residence time. It also states that the lowest residence time of a particle on the melt pool can range from 32µs to 1210µs and average time of 370µs. The study was able to observe the exact process of how the melt pool solidifies around the unmolten particles found on the surface of the LMD sample. The study shows that the radiance of these particles can be detected hence their state of interaction with the melt pool can be observed too.

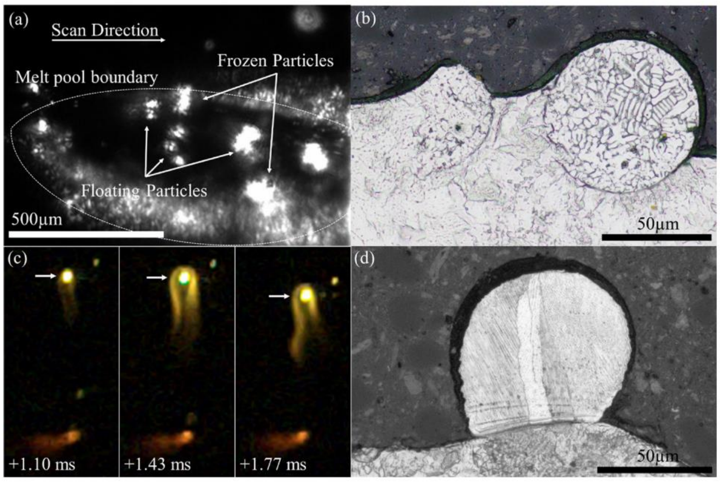

Figure 18: a) Melt pool particle Monitoring. b) Microstructure shows unmelted powder. c) particle ignited when entering laser beam zone. d) Particle landing and solidifying on the surface (James C. Haley, 2018)

3.2. Thermal Camera Defect Detection and LMD Monitoring Systems

(Ulf Hassler, 2016) presents an in-situ defect detection system that utilizes a high-speed thermographic sensor and optical 3D scanning. Initially using the Comsol Multipysics software package was used to estimate the temperatures and thermal contrast signatures at different diameter thickness and depths and dimension defects. This also gave them in an approximate way that the thermal camera frame rate must be 0.5 to 1kHz since that max thermal contrast is reached within 0.2ms after excitation. During their experimental phase they simulate defects using two methods a) A combination of machine parameters that yield suboptimal properties which lead to defects like porosity and b) creating physical deformities like drilled and punched holes on the material upon which the deposition is supposed to take place. The research uses an IRCAM Equus 327k SM equipped with M25 focus lens which is producing a 128 by 128-pixel thermal image. The Camera has a frame rate 1Khz and measures temperatures from 300 to 1500 °C. The captured image intensity is converted to temperature by using a data base on given black body calibration for the material. The image segments spots based on temperature threshold is decided by the researchers. An interesting exception in this process is that the start and end of the weld process is not recorded. Each frame is compared to the reference image by overlaying them over each other and subtracting the image from the reference image. This yields the difference in characteristics of the reference and current thermal image in the form of deviations. The results show that deviations of certain magnitudes can be found in the thermal images of samples that contain defects up to a certain size. As a result, this method can also be related to invalid machine parameters which implies they could be used for tuning the machine parameters.

(Khanzadeh & Bian, 2016) use an advanced infrared thermal imaging system to capture high speed melt pool data streams. They use Self Organizing maps or SOM to cluster the melt pool based on their morphology and link the patterns in these clusters to different type of porosities. The results are validated using X-Ray tomography of the sample after it is deposited. The process involves first Identifying the boundary of the melt pool based on temperature which should allow the extraction of the contour of the melt pool. Once this is done the contour is now transformed from the cartesian coordinate space to polar space to be represented as a function. A non-parametric curve fitting called the cubic spline is applied to this function to interpolate and form a curve. This is done because different melt pools may yield different points when their contour is converted to the polar coordinate system, hence after the cubic spline method is applied the same number of points can be evaluated. The points after interpolation are known as the features of the melt pool morphology. After this the melt pool shape are put through unsupervised machine learning methodology called SOM. This converts the higher dimensional space data to two-dimensional space and as a result uses the features to cluster different melt pool shapes based on their similarities. The Clusters that are not like others are interpreted as anomalies. Along with the difference in shape and size of morphology the defects can be classified using average peak temperature. The location is extracted using the SOM method (Zhengtao Gan, 2019) and compared with X ray CT and found that the systems accuracy was 62.75%. The system successfully captures pores, geometric inaccuracies, lack of fusion defects and unmelted areas.

(Liu, Farahmand, & Kovacevic, 2014) in their study uses optical camera to observe the powder flight path but uses Thermal Camera in collaboration with a pyrometer to observe the melt pool. The pyrometer is used to measure the emissivity of the melt pool since the material does not act as a perfect black body. This emissivity value is used to calibrate the thermal camera which observes the overall melt pool temperature distribution or thermal distribution, melt pool size and cooling rates. The research found that along the head of the melt pool the thermal gradient is sharp due to the heat sink effect but in contrast the temperature on the sides is slightly higher due to unmelted particles and oxides formed at the edges. Even though thermocouples were used in their study they were embedded into the substrate and were are only successful at giving temperature trends but not the correct temperature. The research discovers that the melt pool temperatures range from 1420 °C to 1750 °C and the cooling rates were from 7 $x10^3$ °C to 1.2 $x10^4$ °C/s.

3.3. Acoustic Emission Defect Detection and LMD Monitoring Systems

(Gaja & Liou, 2017) used acoustic emission sensors to detect and classify pores and cracks by employing PCA and K-means clustering technique. Acoustic emission sensors are basically piezo electric transducers that generate signals based on the elastic waves that travel through the material due to a change in the material or a sudden release in energy. Hence AE sensors pick up the signals release when cracks and pores are formed. The setup involves a single (Kistler's 8152B211) AE sensor attached to Picoscope 2205A oscilloscope to capture the AE signal stream and then forward it to a computer. The experimenters use powder contamination and non-uniform shape and size of the powder as a provocation technique to produce defects like pores and cracks. The signals generated by the defects are known in this research as Events. Events are AE signals whose amplitudes cross a specified threshold and then eventually return below threshold. From each one of these events features like amplitude kurtosis, energy number of counts, duration and rise are extracted. The research claims that no AE noise was detected from the CNC or the noise level was much smaller than the signal of interest and only signals between 100kHz to 1 MHz were allowed through the frequency filter. The data shows that all features were normalized and PCA was implemented for the dimensionality reduction tool and since the first two PCA components explained the majority of the variance they are selected for the K means Clustering algorithm (Hossein Taheri, 2019). The author does mention that once PCA is implemented and the chosen components are used in the K means clustering algorithm, the result of the K means clustering will not reflect the features in their original dimensions i.e., PCA reduces the dimension of the original feature set to a smaller dimension or principal components which are then used in the K means algorithm. The K means clustering algorithm is an unsupervised machine learning algorithm that groups similar data points based on their features. The K means requires the "K" value or number of clusters to be generated to be given to the algorithm in the beginning and hence an extra step to discover the optimal K for the data set must be carried out. This research uses the silhouette method to calculate optimal K values and the method reveals that the optimal K value for this data set was 2. Two very distinct clusters are generated and an Analysis of Variance or ANOVA on the cluster centers reveals that the means of features of two clusters are significantly different and hence the researcher concludes that the source mechanisms of the two signals are also different. The events in both clusters are analyzed and two major finds are made: a) The porosities produce shorter decay time and less amplitude and b) cracks produce shorter duration and high amplitude signals. Observation of the sample under a microscope shows that the number of cracks and pores are strongly correlated with the number of events found in both clusters.

(Fujun Wang, 2008) proposes a novel method of crack detection using acoustic emission sensors. The setup uses two acoustic sensors attached to a cuboid specimen upon which laser metal deposition is carried out. The specimen has two holes through which a water input pipe passes through to control its cooling. As signal processing and conditioning unit a PAC Spartan AT/72 acoustic emission detection device is used which calculates the position and time of the crack generation and extension. Two sensors are used so that the position can be calculated. In conjunction with these signals an FEA or Finite Element Analysis in ANSYS software is carried out and from this analysis the corresponding temperature ranges can be calculated. Water cooling is use in this experiment as crack controlling and provocation technique. Using this method, the authors were able to classify the type of cracks and the temperature interval in which they are generated.

(Gaja & Liou, 2018) use acoustic data to develop a Logistic Regression or LR Model and Artificial Neural Network ANN to evaluate their performance against the K means Clustering method for defect classification. The means squared error for the LR model and the error from the 3 layered ANN have a very little difference between them, but the ANN performed slightly better. The author says both methods can be used as a successful classification method to classify defects.

3.4. Pyrometers Defect Detection and LMD Monitoring Systems

(Wu, Cui, & Xiao, 2020) use an Infrared Monochrome Pyrometer or IMP to detect cracks, their depth and position during the laser metal deposition process. The IMP is mounted on one side of the nozzle head and can measure temperatures up to 150-1200 ^{o}C in an extremely small spot size. During defected sample run, the IMP device detected significantly high peaks over the defects and no peaks were detected by the IMP during the non-defected sample run. Hence the author concludes the sensor display high sensitivity. The temperature peaks coincide with the position of the defects and the crack depth is proportional to the temperature at the peak observed. The research implies that stable trends in temperatures with smaller changes shows that the sample is possibly defect free.

(Jon Iñaki Arrizubieta, 2018) develops a numerical model that uses the heat and mass transfer equations in LMD and based on the thermal fields predicts the probability of pore formations among other things. The experiment uses two color pyrometers with a range of 550 °C to 2500 °C to compare the model results to experimental temperatures.

Pyrometers are often not found to be used on their own in LMD experiments instead they are used either in conjunction with other sensors like thermal cameras or optical cameras. As mentioned above (Liu, Farahmand, & Kovacevic, 2014) also use a pyrometer along with a thermal camera for temperature measurement but the pyrometer is specifically focused on the center of the LMD machines laser spot. The pyrometer seems to measure temperatures up to 470–3000 °C with sampling time of 0.5s and a spot size of diameter 0.25mm.

(Song, Bagavath-Singh, Dutta, & Mazumder, 2012) also develops a closed loop control system that controls the melt pool temperature and build height using three CCD cameras and one two color pyrometer. The camera is used to monitor the build height while the pyrometer is used to measure temperature of the melt pool. As far as the melt pool is concerned the pyrometers data is used as an input for the temperature controller. The pyrometer measures temperatures from 1,000°C to 3,000°C with an accuracy of ±10°C and measured wavelengths were set 1.3µm and 1.63µm. Even though the study of control systems are not the interest of this investigation, the researchers successfully demonstrate the deposition on a turbine blade with varying widths.

3.5. Ultrasonics Defect Detection and LMD Monitoring Systems

(Cerniglia, Scafidi, Pantano, & Lopatka, 2013) uses Laser Interferometry to detect sub surface and surface defects in LMD samples. The system basically picks up the ultrasonic waves generated by the pulsating laser. This ultrasonic signal is disturbed in the presence of defects and its Time of flight or TOF i.e., the time the wave takes to travel from the position of origin to the sensor changes. An FE model is used to recognize the wave propagation patterns in un-defected pieces so than during actual experiments defected wave propagation can be recognized. On the Experimental work piece physical defects of different sizes are generated using laser machining and Electro Discharge Machining. Certain characteristics of the ultrasonic waves like width and TOF of the generated Wave front can be used to calculate the size and depth of the defect. The defect detection algorithm however utilized the characteristics of the hyperbolic shape of the ultrasonic reflections. The system successfully identifies defects up to 100 µm and a depth of up to 700 µm. The author says the technique does have inherent issues like large signal to noise ratio and selection of optimum parameter for analysis which requires further work.

(John A. Slotwinski & E.J. Garboczii, 2014) carries out an extensive study on how ultrasonic sensor can be used to determine the level of porosity in a sample. The system uses longitudinal wave pulse-echo time-of-flight measurements using 5Mhz ultrasonic transducer with an element of 12.7mm diameter. The shock impulse excitation is generated, and its ultrasonic reflections are picked by a commercial 30Mhz pulse reviver system. Ultrasonic echoes are read by 300 Mhz digital oscilloscope that was sampling data 2.5GS/s. The research establishes a linear relationship between bulk porosity and wave speed using Equation 5.

$$v = v_o + \beta\phi$$

Equation 5: Wave speed and porosity relationship

$$v = Wave\ speed\ in\ the\ sample\ , v_o = wave\ speed\ in\ a\ fully\ dense\ material, \beta = \mathrm{slope}\ , \phi = \mathrm{measured\ porosity}$$

3.6. Data Fusion Architectures and Models

(White, 1991)’s Joint Directors of laboratories or JDL architecture Figure 19 is one of the oldest data fusion architectures present. Even though it was originally made for military usage it is used and adapted for many non-military applications. JDL presents 5 levels of data fusion: Source processing, Object refinement, Situation Refinement, Threat Refinement and Process refinement. The Sources component of the JDL architecture is the live information while the Human Computer interaction HCI component is where the data fusion results are used to make decisions. Important part of the Data fusion Architecture is the data base management system that manages the source data base and fusion data base. Level 0 is where the lowest level or Raw data is processed or transformed into a form that will be processable by the next data fusion components. Level 1 then uses process or transformed data to identify the entities, their state, location, direction etc. Level 2 is where based on an entities state, predictions or estimations are made about its relation to other entities in its environment. Level 3 is where based on the relations of the entities calculated in step 2, risks, vulnerabilities, and operational probabilities are predicted. Level 4 is the process refinement step where information that was lacking is identified so that results can be improved. If all these steps were to be applied to let's say a vision-based system that predicts defects based on anomalous geometric features observed, the following is how the system would work; level 0 - Input raw data and process it for noise and combine into data which can be understood i.e. image in with a bunch of pixels. Level 1 – Use image processing to identify shapes and boundaries of geometries in the image. Level 2 – where do these shapes lie within boundaries. Level 3 -Do the geometry match the defected ones in the data bases or are these other features? Level 4 is to identify if the results were accurate and which part of the information was lacking.

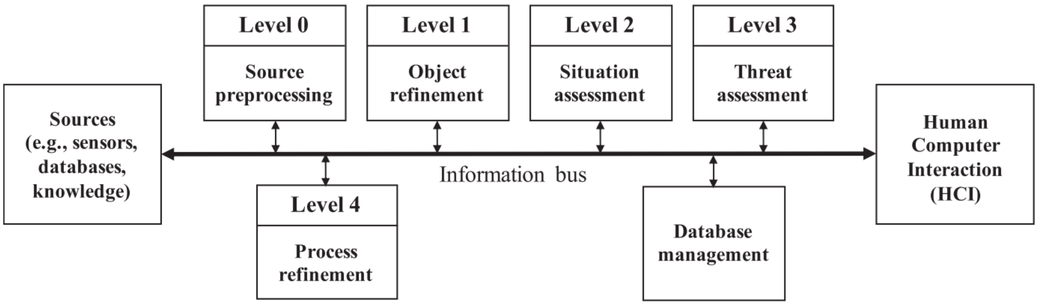

Figure 19: Joint Directors of Laboratories (JDL) architecture (White, 1991)

(Luo & Kay, 1989) developed a data fusion architecture (Figure 20) that handles multi sensor integration. The data is taken from multiple sources (S_n) at different levels (Signal, Pixel, Feature and Symbol) and used for data fusion at each level. The data representation levels go from low level to high level. The outputs of the fusion centers or Nodes ($X_{n,n+1}$) at each level are used as an input in the fusion center on the level above it. Signal level data is the lowest level data or raw data or even conditioned data, Pixel level is where data is still lower-level data but in a relatively more useful form like a pixel image, feature level data is where data represent specific features or characteristic from signal or pixels and symbol level data is decisions or logic from signals. (Esteban, Starr, Willetts, & Hannah, 2005) clearly points out that in Luo and Kays architecture a clear distinction is made between multi sensor integration and multi sensor data fusion. Multi sensor integration is where information from multiple sensors is used for a particular task whereas multi sensor data fusion is what is happening at the Fusion Centers i.e., actual combination of data.

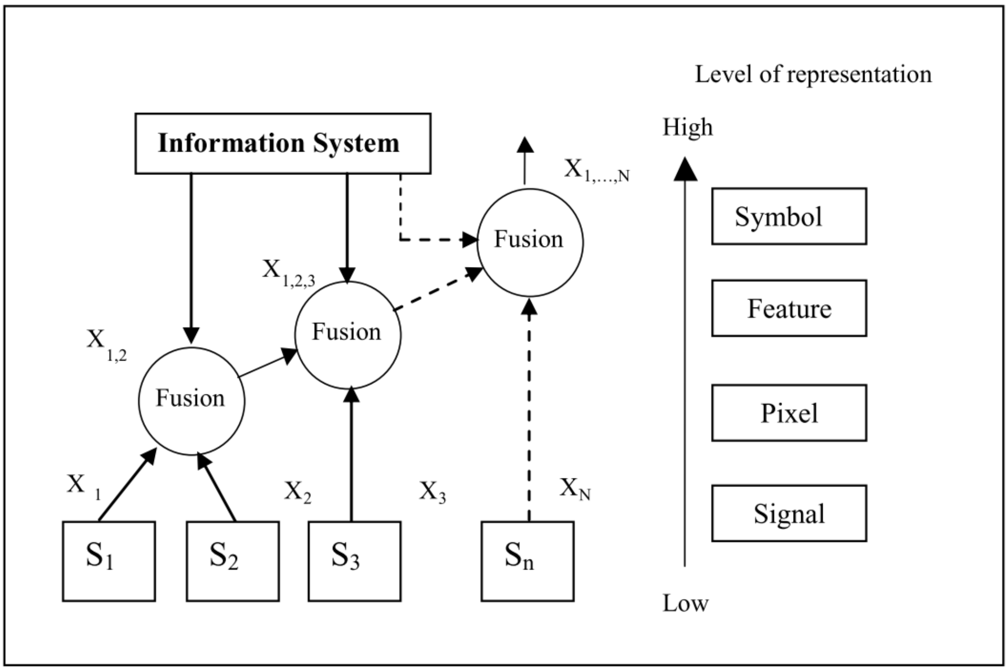

Figure 20: Luo and Kay's Architecture (Luo & Kay, 1989)

Dasrathay’s Architecture (Figure 21) is mentioned in a review paper by (Meng, Jing, & Zheng Yan, 2020). The architecture mentions 5 fusion processes in terms of input and output data. First is DAI-DAO (data in data out fusion) in which raw data inputs are refined using a fusion process. Second is DAI-FEO (data in feature out) is where some abstract information is extracted from processed data which can be called a feature. Third is FEI-FEO (feature in feature out fusion) where a multiple feature would yield another feature through the fusion process. An example of this could be where two boundary features in image processing could be used in a data fusion algorithm to form a shape. Second last is the FEI-DEO (feature in decision out fusion) where based on features a logical conclusion is made. Lastly is DEI-DEO (decision in and decision out) where based on multiple decisions an output decision is yielded by the fusion algorithm.

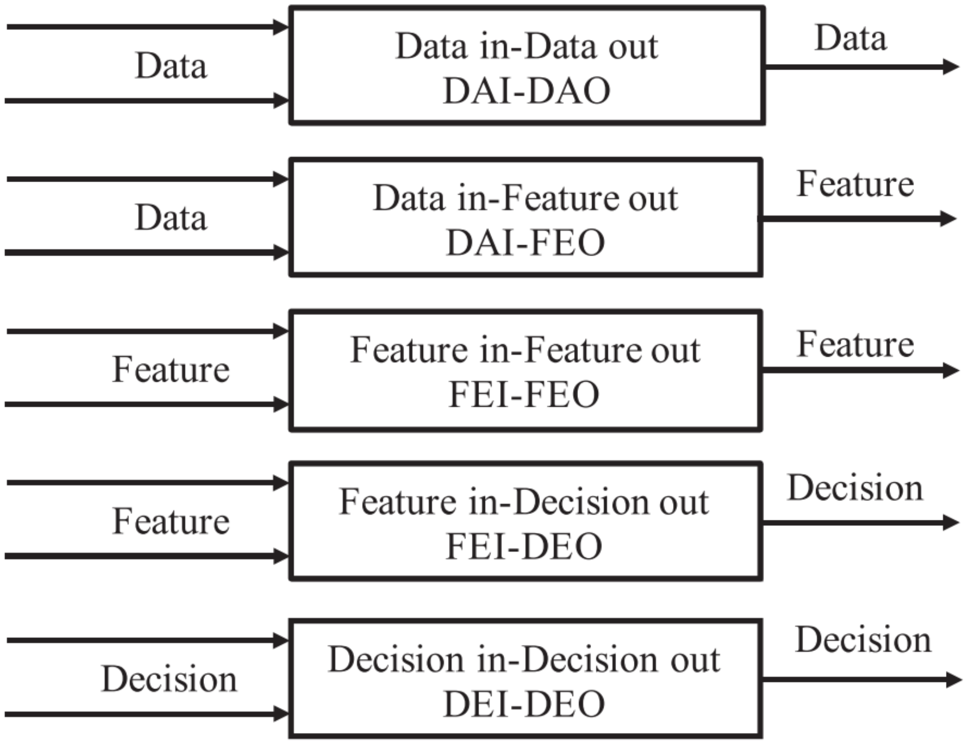

Figure 21: Dasarathy's architecture (Meng, Jing, & Zheng Yan, 2020)

(Esteban, Starr, Willetts, & Hannah, 2005) mentions the water fall fusion model (Figure 22) in their review. The model is where data fusion happens at different level of data however it is also continuously receiving feedback at signal level and being fused with the input signal to generate a more accurate decision-making output. Level 1 is where signal level data fusion happens and level 2 is where features are extracted, and these features are fused to output predictions about the state of the system. Level 3 is where predictions are evaluated, and a decision is outputted based on them. The model can be used for multiple or single data inputs because at level 1 the feedback from the controls will always be the second input.

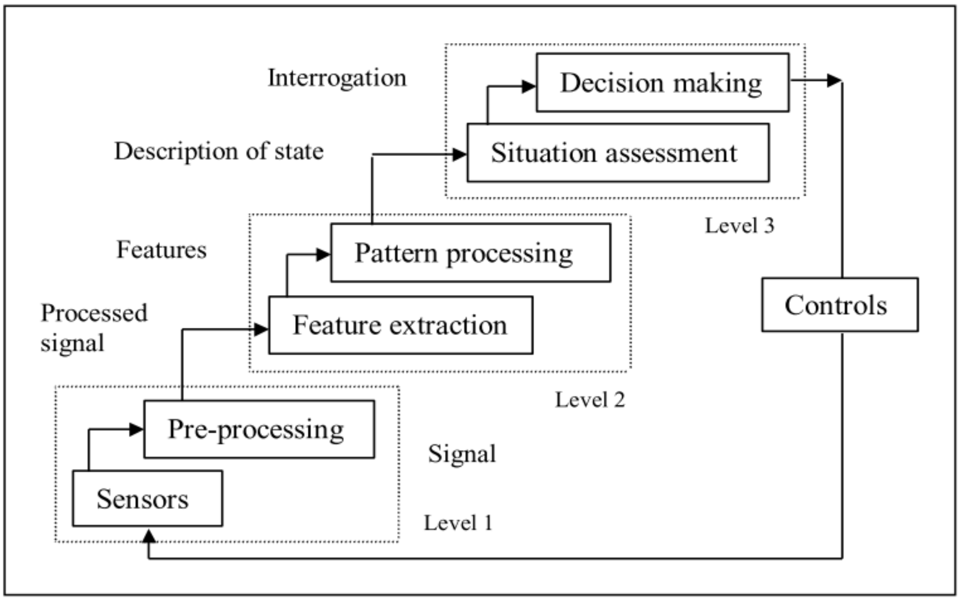

Figure 22: Water Fall Model (Esteban, Starr, Willetts, & Hannah, 2005)

3.7. Multisensory and Data Fusion systems in LMD

(Vandone & Stefano Baraldo, 2018) use data fusion to develop a control system that is capable of monitoring and controlling the width and the height of the deposit. The data fusion approach utilizes features extracted from online thermal camera data, online optical camera data, machine parameter data and offline data from the 3D surface reconstruction of the deposit developed using stereoscopic cameras. The data fusion process is used to build a mathematical process model which can be used to predict and hence control the dimensions of the deposit. The data is time synced using the laser on time as a start marker which is recorded by all three input sources. Thermal and optical images are used to extract the brightness of the melt pool along with its width. The offline machine data is used to extract the position and time of the laser during the deposition. The offline 3D scan study reveals details about the geometry. As mentioned all this data is used to construct a model.

(Song, Bagavath-Singh, Dutta, & Mazumder, 2012) develop a control system to monitor and control the built height of the deposit. The system employs a two-color pyrometer to measure melt pool temperature and three CCD cameras in triangulation set up to monitor the build height. This paper has been mentioned in parts in section 3.4 however here it is being mentioned for its multisensory approach and fusion algorithm. Two controllers; a master height controller and slave temperature controller are deployed in series to control the melt pool temperature and height and growth. Even though it is not labeled as a fusion algorithm in the grand scheme of the design, the system is fusing data from different sources at two points in the research. First point is where to the three cameras where image processing is applied to decipher height which is a feature, Height calculated according to each camera is then fused to calculate the decision of whether it has crossed a threshold or not. In the grand scheme of the system, data fusion is taking place from sensor data to predict the output by both controllers and based on this the laser power is being controlled. It's important to mention that due to the nature of this system it is a closed loop system. This is because the sensor input is in fact feedback from the corrective action that was made by the control system.

(Clijsters, Craeghs, & S. Buls, 2014) use a high-speed multisensory approach (Christopher B. Stutzman, 2018) (Renken & Stephan Albinger, 2017) (Jungeon Lee, 2021) to monitor the melt pool using custom hardware and software. The researchers emphasize how important the custom high speed hardware setup is in the context of implementing their mapping algorithm which not only allows melt pool monitoring but also allows for the detection of variations in the melt pool which can be linked to porosity. The need for the high-speed system is because the variations in the melt pool are very quick as a response to the development of defects. If the system is not fast enough it will miss out on essential modeling data. The system uses a FPGA as DAQ unit which collects and processes data from the two sensors at a very high sampling rate (10KHz to 20Khz). Melt pool intensity, area, length, and width is then calculated and compared to the reference data of a steady state melt pool which is then used to calculate estimates for the quality of the layer. These estimates are used to develop a 2D map of the layer using a mapping algorithm. The defected quality maps are verified by cutting up the sample and then studying them under XCT. This is one of the very few research papers which touches upon defect detection using data fusion even though positioning of defects seems to be incorrect in their results as per their own claim.

(Chabot, Rauch, & Hascoët, 2019) presents a feasibility study for a proposed control system model that utilizes multiple sensors with data fusion to monitor and control build height in LMD. The system monitors the LMD system including machine parameters to calculate scanning speed, Flow Rate, Temperature, Geometry, and leaves room within their architecture for any other monitoring strategy. All this data is fed into a controller that also takes in values from a process model and based on the set values and then manipulates power, flowrate, scanning speed and stick out (nozzle standoff distance) to control the LMD process.

3.8. “High Speed” measurement systems and “Online” monitoring

High speed is a relative term with no unified definition at a systems level and often associated with systems that collect data at very high sampling rates or have high data transfer rates (Hult, 2020) (JRPANEL, 2020). In the world of data acquisition systems, the term high speed is inherited by the entire system due to the high-speed semiconductor electronics that it utilizes. This electronics is usually the high-speed analog to digital converter (ADC) electronics or the high-speed system clock both of which are integral parts of a data acquisition system. As far as ADCs are concerned anything above 1 Mega Samples Per Second (MSPS) is considered High Speed and can go all the way up to 1 Giga Samples per second (Drachler & Murphy, 1995) (Yun-Jeong Kim, 2004).

In the realm of Imaging systems and Cameras any device that records video above 60 frames per second can be considered high speed (Bridges, 2021). These Cameras are often used to record quick events like Vehicle Impact Testing, Projectile Tracking, Flow Visualization, Material Testing, Vibration, Crack Propagation etc (Manin, Skeen, & Pickett, 2018). Modern high speed thermal imagers start at 1000 FPS and can go up to 30000 FPS and frame rates (Richards, 2021).

Some LMD systems or other measurement systems will use the terminology online or offline to describe their process monitoring methodology (Vandone & Stefano Baraldo, 2018) (Wang, 2008) (Tang, Wang, Zhang, & Wang, 2017) (Zhang, 2019) (Fang, et al., 1998).The term “Online” is most often seen to represent the systems that collect data while the process is ongoing and is quite often used in systems that utilize online machine learning but is not necessarily exclusive to machine learning. In an online system the sequence of data captured is critical. The purpose of an online systems and online data analysis is to draw conclusions or derive predictions based on the data available at that current point in time relative to the process or position being monitored during the process. This becomes even more clear when it offline data analysis is understood which is processing of data collected as a batch after the process has been completed. A simple example of an online system would be (Wei Feng, 2022) study where an online method of data collection in which the temperature distribution of the melt pool is measured using a thermal camera. Based on the difference between the temperature distribution of a non-defected melt pool and the temperature distribution of the melt pool at a given point in time or position during the LMD process a prediction can be made on the existence of a defect at that point in time or position.

3.9. Discussion

From the above investigation of the state of the art it is evident that elaborate work has been done on single sensor LMD process monitoring and LMD defect detection using different approaches and different hardware. Critical analysis reveals that two major phenomena of the LMD process are monitored using Nondestructive testing technologies: The heat flow of the melt pool and the geometry of the melt pool. These two-reveal information about the stability of the melt pool. Defects create disturbances in the Heat flow around the defect which causes high temperature zones. This may also affect cooling rates in that region and as a result in the entire melt pool. The spectral radiance of the melt pool is dependent on its temperature and as a result it can be seen those sudden changes in the temperatures will cause sudden changes in spectral radiance. The defects also cause a change in the materials internal structure because of which acoustic emission waves are propagated in the material. The formation of physical defects and disturbances in the heat flow can cause the melt pool to change in shape and size. Figure 23 shows how defects can cause changes in certain phenomenon of the melt pool which as a result can be observed through changes in certain properties and resultant phenomenon.

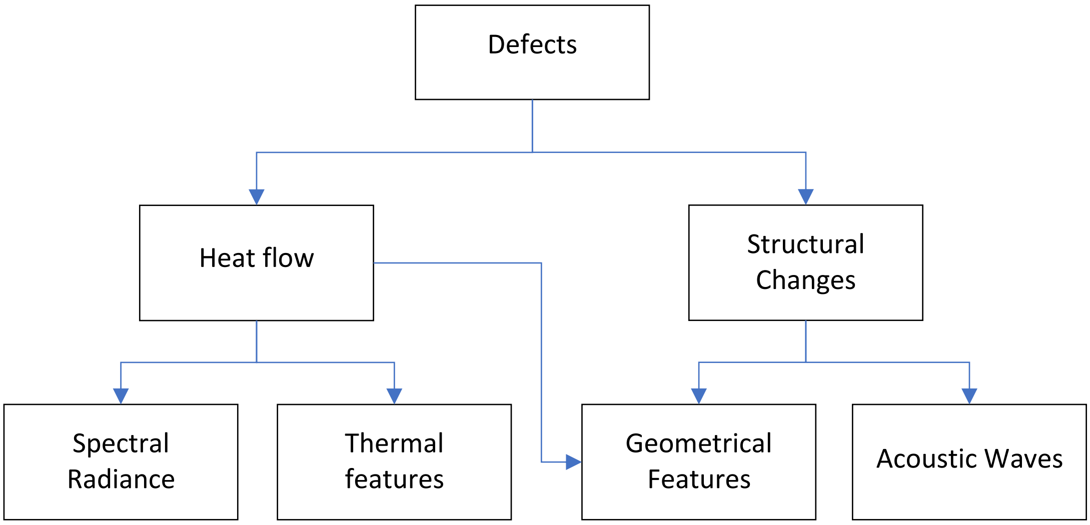

Figure 23:Physical Phenomenon that occur due to defects

In state of the art of the research it is found that different types of Thermal Cameras, Optical Cameras, Pyrometers, Ultrasonic and Acoustic emission sensors are used for in situ monitoring of the changes in the above-mentioned properties and phenomenon. The thermal features and Spectral Radiance are often measured using cameras that operate within a wavelength region of (as per the literature) 200nm all the way up to 890nm. This is deciphered from the hardware specifications and Natural Density Filters used on the cameras. Cameras that operate in the visible range (approx. 400nm-750nm) are often used to observe the spectral radiance or the geometry of the melt pool and in some cases used to track the powder particles interaction with the melt pool. Thermal Camera depending on the type of thermal camera usually observe the IR range (approx. 750nm- 1000nm). The problem in measuring temperature using thermal cameras is that the emissivity values must be fed into the thermal camera to convert the IR intensity to Temperature. In a chaotic (uneven temperature distributions with different materials in different phases existing at one time and quickly changing states) melt pool is that emissivity of certain regions might be different to others hence incorrect or anomalous temperature may be shown in thermal image. This problem can be managed by using a pyrometer to calculate the emissivity that most accurately represents most of the melt pool. Likewise, the issue with visual cameras are that they cannot detect IR spectrum of the electromagnetic radiation and to observe the melt pool the right level Density Filter must be applied otherwise reflections and excessive light saturate the optical sensor. Temperature ranges of the overall melt pool depends on the material and its melting temperature. In this literature study max temperatures observed depending on the study were from 1750^{o}C to 2426.85°C. Thermal Cameras compared to Pyrometers however have lower overall temperature ranges but thermal Imagers provide a lot more information in terms of thermal distribution of the melt pool. For image sensors there is ample amount of inference and evidence that they need to be of a high sampling rate to capture the quick change in observable phenomenon. The defect development time frame has been discussed in the previous chapter, but some researchers will decide the sampling rate of their system based on the excitation time (time it takes for the laser to raise the melt pool to max temperature). However, this time does not account for the time it takes for a change in the observation phenomenon due to a defect. For example, the time it can take for a floating particle to melt completely into the melt pool at an average is 370µs. And if moving particles are observed, the max speed of a particle recorded is 4.9m/s and to view its movement per 1 mm would take approx. 205 µs. In research the sampling rates of high-speed cameras are a lot more (up to 200000FPS) than thermal Cameras (Up to 1000 FPS).

2D Geometrical measurements are usually made by using image processing and at times stereoscopic calculations are made to get build height of the deposit. (Robert Sampson, 2020) shows that the directional emittance phenomenon causes the uneven radiance of light due to the angle it is being observed. By using this phenomenon instead of using usual emissivity-based approach a more accurate methodology of image processing could possibly be developed to get a more accurate geometric reading of the melt pool. The features of an Acoustic emission signal can reveal a lot about the nature of the wave and if these features are clustered, they can be used to classify defects. As per theory, acoustic waves can be created by cracks or pores or even by thermal and mechanical changes in the material. Not only can Acoustic waves be used to detect cracks at the point of generation but are also capable of revealing information about crack propagation.

Based on the phenomenon used to detect defects and the sensors used to detect them, acoustic emissions occur while the defect is developing. The disruption of heat flow is detected during and after the defect has developed although the maximum effect should be seen after the defect has occurred. Lastly the powder flight and interaction with melt pool and the residence time (time particle stays un-melted on or in the melt pool) for a particle can be considered a precursor to a defect since the longer the particles stay on the surface of the melt pool the more chances are of it staying un-melted. The physical geometry of the melt pool is also an after effect of defects being generated and hence can be said to occur after a defect has occurred. This information may help build a timeline for which phenomenon and property change in relation to the defects generated. These can be known as the observation windows of each sensor as seen in Figure 24.

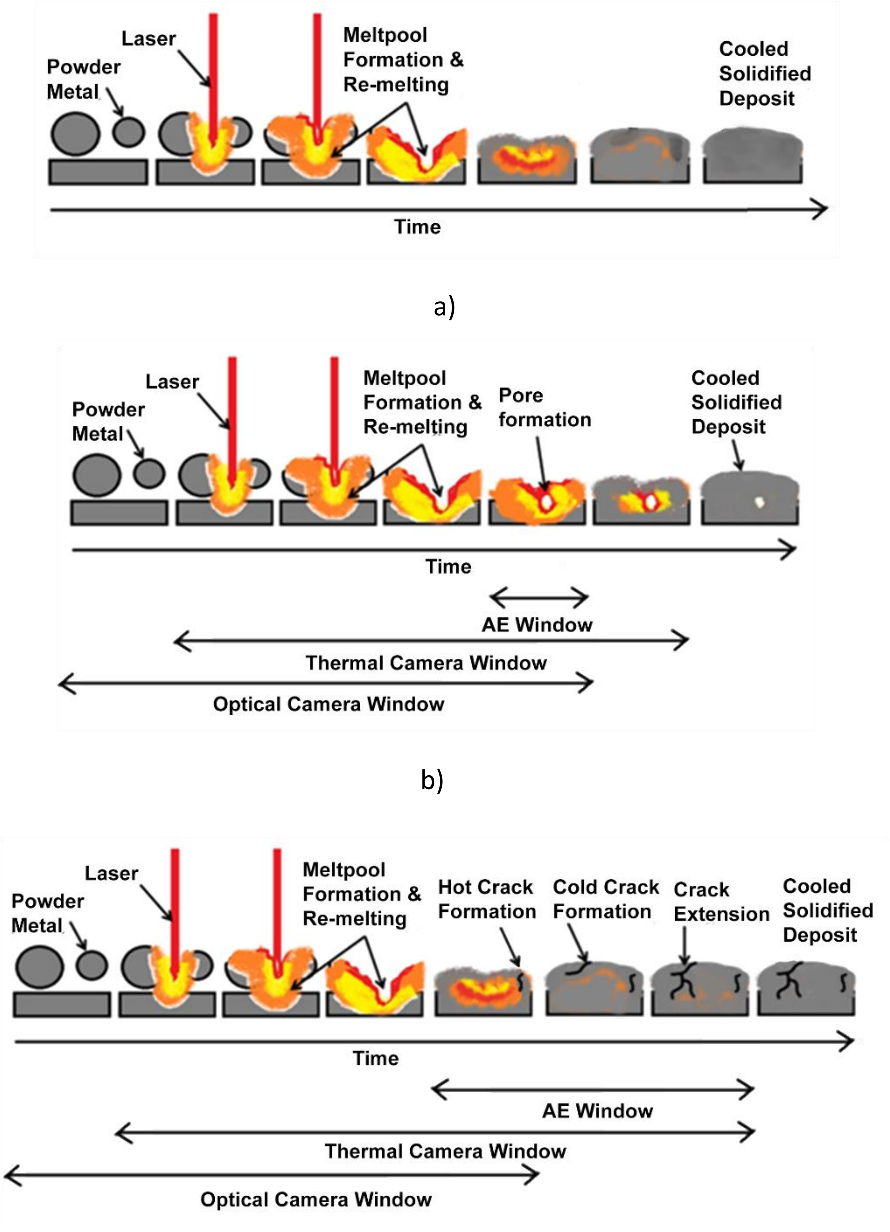

a)

b)

c)

Figure 24: Observation Window of different sensors during the LMD process

In terms of methodologies the common theme is to take worst case readings and compare them to best case readings and the deviations reveal the anomalies. Most systems will only output if a deposit contains or does not contain defects, but some reveal further details of the defect features. The features that exhibit defected traits can be identified in a few ways; Cooling curves can reveal anomalous melt pools, melt pool shapes can identify defected deposits, ultrasonic wavefront features can reveal the defect size and thermal spikes or concentrated thermal zones over defects can reveal their depth and size.

Machine learning algorithms within data fusion techniques can improve the reliability and accuracy of information (Meng & Xuyang Jing, A survey on machine learning for data fusion, 2020). Data fusion Models can be built using Artificial Neural Networks, K-means clustering, Self-organizing maps, and Logistic Regression and at time linear regression (relation of porosity with speed of ultrasonic waves) which can be used to predict defects in an online process. The methodology to develop these models take the aid of simulations models or carrying out experiments where detects are provoked though different methods. Signals collected from the simulated defects are used to build certain models that can be used to predict defect features. To link the signals to the defects, a post analysis study is often done though metallurgical analysis by cutting the sample up and observing it under a microscope or using XCT to observe defect position, size, and type. Each methodology is dependent on their goal, which can be simply detect defects or classify them or approximate their position and at times their size.

Data fusion for defect detection in laser metal deposition has little to no work on it except for the paper on (Clijsters, Craeghs, & S. Buls, 2014). With that being said, examples of multi-sensory systems that use data fusion to observe the process are found in the literature. But the goal of all of them is to monitor build height and maintain stable melt pool geometry. They mostly use a combination of thermal and optical cameras or multiple optical cameras or a combination of pyrometers and an optical camera. The majority of the multisensory research in LMD aims to create a control loop system to control build height and melt pool temperature. There is heavy focus on time stamping the data and having a very higher data acquisition rate. (Clijsters, Craeghs, & S. Buls, 2014) uses a custom DAQ system with a sample rate of up to 20KHz. As far as data fusion architectures are concerned most closed loop systems seem to be using the Waterfall model for data fusion however (Luo & Kay, 1989) model allows multisensory integration data fusion for data at different levels.

The investigation reveals that insufficient work is present on multisensory data fusion systems with the specific aim of defect detection. Single sensory systems exist but they are each observing different phenomenon that can be used to predict defects. Other than the difficulty in filtering and processing data regarding the change in a phenomenon or property of the melt pool, the phenomenon itself has limitations of what it can reveal about the defects e.g., Intensity of temperature spike can reveal information of crack depth whereas observing spectral radiance may not be able to do so. Even the timeline of when a change in an observable phenomenon or property occurs in relation to defect development varies. This is probably why research endeavors that utilize single sensory approaches can only ascertain certain details about the defect. It is also learnt that LMD system observations require highspeed sensory and data collection systems, and the required sampling rate can be calculated using the information regarding the plausible defect generation times. Lastly, it is understood that control systems that use a multisensory approach with data fusion are much more successful in achieving their goals. Hence designing a multisensory data fusion methodology using an existing data fusion architecture may be fruitful idea in a defect detection system.

Chapter 4: Research Design and Methodology

4.1. Specific gaps and Objectives

From the literature review it can be concluded that there is a very large gap in terms of reliable and efficient defect detection systems in laser metal deposition. Even though the concepts of NDT in LMD to detect defects using specific phenomenon and properties is well established in terms of which sensor signal properties may reveal defects, they all come with their limitations in revealing the type, level, and reliability of information. The type of information being Thermal, Spectral, Geometric, and structural while the level of information is what can be deciphered from the type of information e.g., Defect Type, Defect quantity, Defect Size, Defect position etc. The reason why level of Information is important in LMD is because it is the need of the industry to be able to establish their own acceptability standards contrary to the Bad or Good sample approach. The reliability of information here is the accuracy of the information e.g. A pyrometer can relate the position of a crack to the time when a temperature spike is observed, and multiple AE sensors can be used to locate the position of the crack as well. However, the accuracy of one from the other may vary depending on multiple factors and hence one sensor alone may not be able to provide reliable information. On top of this the sensors that detect them have their limitations in terms of what parts of the defect development process they are capable of viewing (Observation Window Figure 24) and their sampling rates. Not only this but there are inherent problems in processing their data e.g., emissivity calculations, direction emittance, signal classification (e.g., whether an AE signal belongs to a pore or crack), boundary detection etc. details of which are mentioned in Chapter 3. With that being said, the state of the art presents many novel solutions to improve these problems, but they cannot compensate for the shortcomings of the phenomenon being observed, the speed with which the melt pool properties change and of course the level of information that can be deciphered from specific methodologies of defect detection. A multisensory approach could be the solution since it makes up for the shortcomings of the level of information collected; however, it does not solve the problem that each sensor data represents a different observable phenomenon, and that each sensor must be fast enough to keep up with the changing phenomenon and properties. Even though each sensor may tell overlapping stories about the LMD process they tell them in very different languages i.e., each views a different phenomenon and outputs different signal types. Hence there is a need for a solution that could bridge the disconnection between a multisensory system so that they may tell the same story and this solution must be capable of high-speed data handling.

A data fusion approach can solve this problem where all sensor data can be processed and fused to tell the same story and compensate or correct others in places where their data may be lacking or weak. As far as sampling rates of the sensors are concerned, they can be approximated by the defect development times given in the literature. But this would mean that a custom platform that is capable of handling such highspeed sensors must be developed. Practically speaking all sensors will not be at the same sampling rate and hence the system must time stamp each sensor stream using a single clock or at least have the record of the lag or lead between the sensors internal clocks. As for the level or amount of information received from the fusion process, it can be used to create a model capable of predicting defects with some quantified level of reliability. This approach of a multisensory defect detection system that utilizes data fusion and predicts the properties of the defects detected can solve the shortcomings mentioned above. Hence the specific objective from this point onwards are as follows:

1. Design and develop a system architecture for a platform capable of online monitoring of the LMD process at very fast rates. This includes high speed data handling and processing.
2. Design experiments to provoke defects during the LMD process and collect signal data during these experiments using the developed platform.
3. Based on the signal data collected, develop a method that can detect and predict specific features of the defects using data fusion.

4.2. Research Methodology

The problem being tackled here is that the current state of the art defect detection solutions does not provide all types of information, does not provide a high level of information, and does not provide information with reliability. This being due to the type of phenomenon being observed, the sensor with which the phenomenon is being observed and how quickly the properties of the phenomenon change. The solution to the level and type of information is a multisensory approach, the solution to quick change in the properties of the phenomenon is the high-speed sampling rate approach and the solution to the reliability of the information is data fusion. In conclusion the overall solution proposed is the development of an Online Defect detection methodology using a high-speed multisensory data fusion system. As shown in Figure 25, The four main steps of the methodology are as follows: Development of System Architecture, Collection of Training Data, Training the system and testing the system.

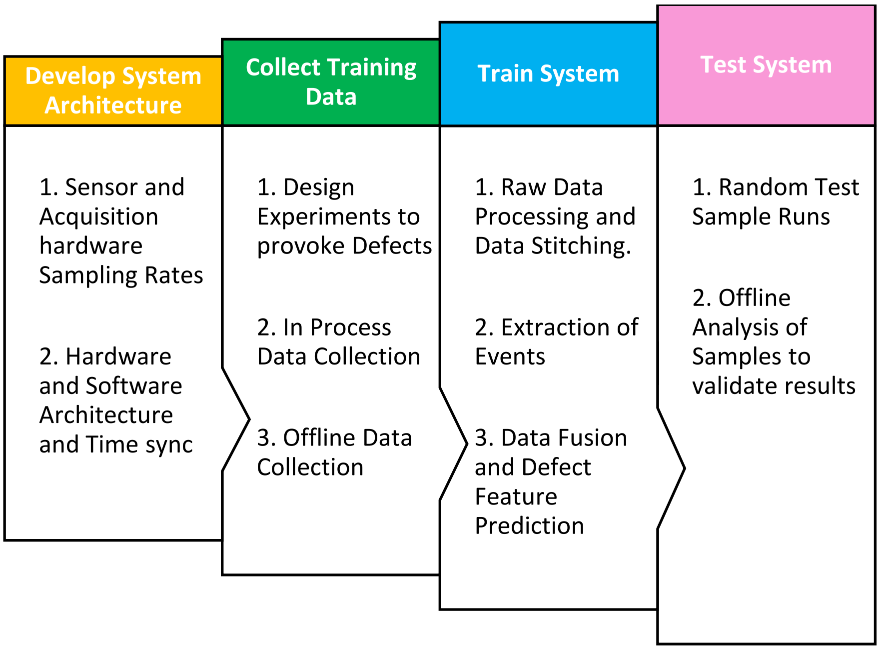

Figure 25: Overall Research Methodology

4.2.1. Development of System Architecture

This part of the research methodology involves the design and development of hardware and software capable of syncing data collection times of the sensors and representing them on a single timeline with respect to the deposition being monitored. Chapter 5 goes into detail regarding the design and implementation of the system architecture however this section discusses the methodology of the development and justifies the design choices.

The system uses three sensors: High Speed Optical Camera or HS Camera, a Thermal Camera and 2 Acoustic Emission Sensors. These three types of sensors are chosen since the research aims to catch as much of the deposition cycle (Figure 24 a) with the help of multiple sensors. The deposition cycle in this research is the time window of the entire deposition process where the powder charts a trajectory towards the melt pool, the laser melts or remelts the melt pool, the powder interacts with the laser and the melt pool, the laser moves off the melted zone and allows that part of the deposition to cool down and solidify. The HS optical camera as per the research aims to capture the part of the deposition cycle where powder flies towards the melt pool, interacts with the melt pool and then captures the phase where the melt pool cools down to a certain extent. The Thermal camera captures the part of the deposition cycle where the powder interacts with the melt pool and the phase where the melt pool cools down and solidifies. The Acoustic emission sensors are chosen to capture any part of the deposition cycle during which the material undergoes major and sudden structural changes i.e., when defects develop. It is known from the literature that these develop during certain temperature ranges and are classified as hot and cold cracks. For pores it is known that they develop during the melting and remelting phases of the deposition cycle and form or get trapped in the solidification phase. All these capture windows can be seen in Figure 24 a & b during the deposition cycle.

These sensors are also chosen since they capture the major phenomenon whose properties are indicators of a defect being present. The phenomenon are the Heat flow and structural changes of the deposited melt pool. The thermal imager can capture the thermal intensity, the Highspeed optical camera will capture the spectral Radiance of the powder particles and the melt pool and AE sensors will capture the acoustic waves generated when defects are formed. The details of exactly what features of these signals are captured that would indicate the presence of defects are discussed in Section 4.2.3.

The sampling rate of each sensor is decided on the minimum time it would take to pick up a certain detail of the deposition cycle that could indicate a defect. Based on the sampling rate chosen, sensors with sampling rates in similar vicinity are chosen. The minimum time it takes for a sensor to pick up a certain detail is calculated using pore generation times, residence time of particles and typical cooling rates found in the literature. The sampling rate of DAQ unit is calculated using the Nyquist Theorem considering the fastest sensor in a multi sensor array. The calculations for this are detailed in Chapter 5 where the implementation of the system is discussed.

The General system Architecture is represented by Figure 26 where A_n are the accessories for a specific sensor e.g. Lenses and Filters, S_n represents the Sensor and C_n represents the respective conditioning units for each sensor. All this data is received by the highspeed data bus in sequential order at the DAQ’s sampling rate. The processing Unit does any necessary user defined operation of raw data processing and time stamping and stores it in the buffer memory. The time it takes for the data to be collected from each sensor, processed, stored in the buffer memory and then transferred to the CPU unit is known as the acquisition time.

The time data is not being collected from the sensors due to the processing, storing, and transferring is known as a dead band in this application. When acquisition is complete all the data is transfer to the CPU unit for high level processing and then the cycle repeats itself. High level processing would be running a machine learning algorithm and data fusion operations. The reason why this is not carried out in the processing and Acquisition unit is because it adds to the overall acquisition time and will increase the dead band. This highspeed bus is controlled by the processing units and it is responsible for the scheduling and the ordering of the data collection, processing, storage, and transfer. However due to practical reasons the final system did not use the exact same structure, but it uses the general structure as guideline and is discussed in detail in Chapter 5. This is because of limited availability of equipment and how the available modules fit together.

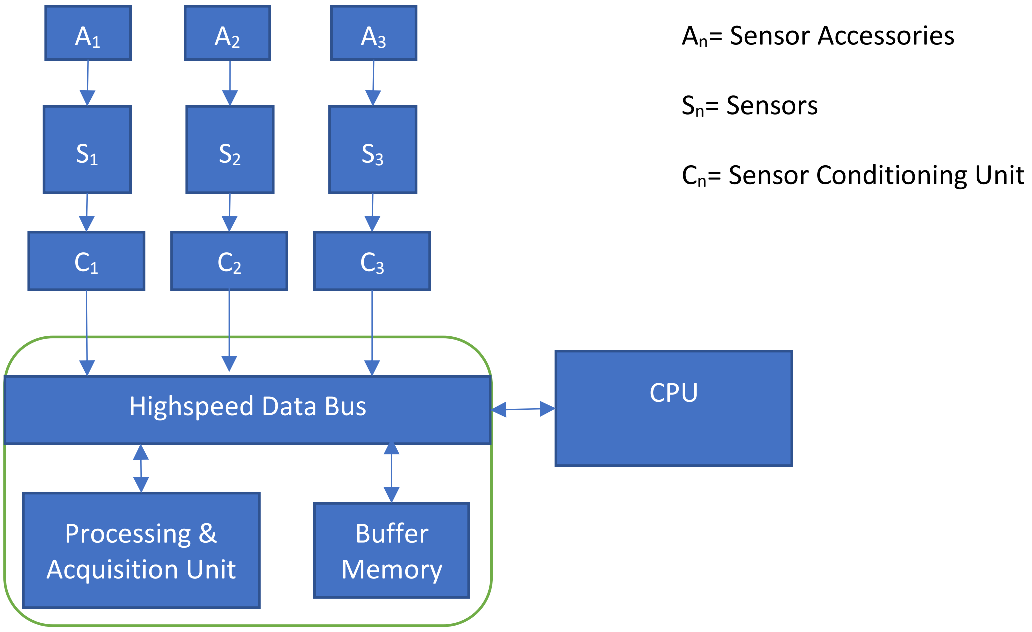

Figure 26: General System Architecture

The Timing system is very critical to the system and uses two types of clocks: Internal Clock and a Universal Clock. A universal clock is a separate clock which starts when the detection system is turned on and is used as the initial trigger for all sensors to turn on at the same time. The internal clocks of the system are the sensors own clocks. When data is acquired, it is already time stamped by its own clock but when it gets to the processing unit it is given another time stamp that records what time the data reached the DAQ unit and is then stored.

The difference in these times determines the lag and lead of the sensor and is used to sync all sensor data time to one timeline.

4.2.2. Collecting Training Data

This part of the methodology is where the defect provocation experiments are developed, and the experimentation is carried out. During these experiments data is collected and stored as training data. The deposited sample is observed using XCT to identify details regarding the defects and the physical dimensions of the deposits themselves. The implementation and details of this phase are discussed in Chapter 6.

The defect provocation methods are designed based on the critical analysis carried out in the literature that details the conditions under which defects are generated. These range from machine parameters to powder quality and contamination, deposition on physically deformed areas as discussed in Section 2.5 and Section 3.9. Four provocation techniques are utilized to provoke defects: Contaminated powder, Surface finish, machined deformities, and machine parameters. The surface finish and physical deformities are very similar, but Surface quality provocation technique gives a very rough surface quality whilst the physical deformities are machined into the work piece e.g., holes and machined lines of certain depth. Deposited samples are produced using all 4 methods and online data is collected during each deposition. The reason for using all defect provocation methods is because each defect provocation experiment technique should theoretically generate different types, amounts and sizes of pores and cracks. A system that is trained on all possible signals from a variety of defects will be capable of catering to a multitude of defect types, variations, and their resultant signals. The reasoning for the selection of these four experiments is further discussed in 6.1 with respect to what type of variation each experiment is intended to produce, and details of these experiments are discussed in Chapter 6.

Two types of Post Analysis measurements are made on the deposited samples for which data is collected: Physical Measurements and XCT measurements. The Physical measurements include the length of the deposit and the average width of the deposit in mm using a Vernier caliper tool. These measurements should help convert the scale of the measurements of XCT images into mm. The XCT measurements involves calculating the number of the XCT images that only show the deposited track length and the width of the deposit in pixels. XCT images are further used to identify defects and further calculate their position and size.

For physical measurements the Vernier is used to measure the length of the track of the deposited track in mm. The width of the deposit is calculated by taking physical measurements of the deposited track at 3 points along the length of the deposited track; 25% of the length, 50% of the length and 75% of the length (Figure 27). The average width of these points represents the physical width of the deposited track in mm. The reasons for taking three measurements are that at times the width of the tracks may slightly very along the length and to get a more uniform measurement an average of the readings at different points is taken.

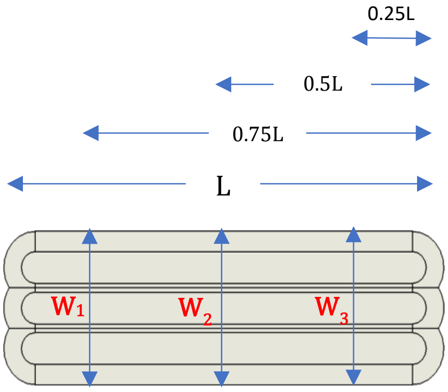

Figure 27:Method of measuring physical width

XCT images are vertical slices or cross-sectional images of the deposit at certain depths along the length of the deposit. From these 2D cross sectional images of the deposited tracks, defects can be identified and the area and position of the 2D projections of these defects can be calculated. Firstly, from the entire set of XCT images the XCT images that only represent that deposited track are isolated. This is done by establishing a reference line which is at the surface level of the deposited piece and then identifying the first image before which the build height crosses the reference line. The end of the deposit is identified by the first image where build height of the deposited track falls below the reference line (Figure 28). The total number of images in between these identified images represent the XCT for the deposited track being analyzed. This total number also represents the length of the deposited track in XCT images or number of frames. To convert this length from frames to mm the physical measurements of the deposited track are used to calculate the depth in mm for each frame it represents. The image analysis tool Image J is used to measure the width of the deposited track in pixels at 3 points along the length of the deposited track; 25% of the length, 50% of the length and 75% of the length. The average width of these points represents the width of the deposited track in pixels. The physical width of the deposited track can be used to calculate the mm per pixel of the XCT image.

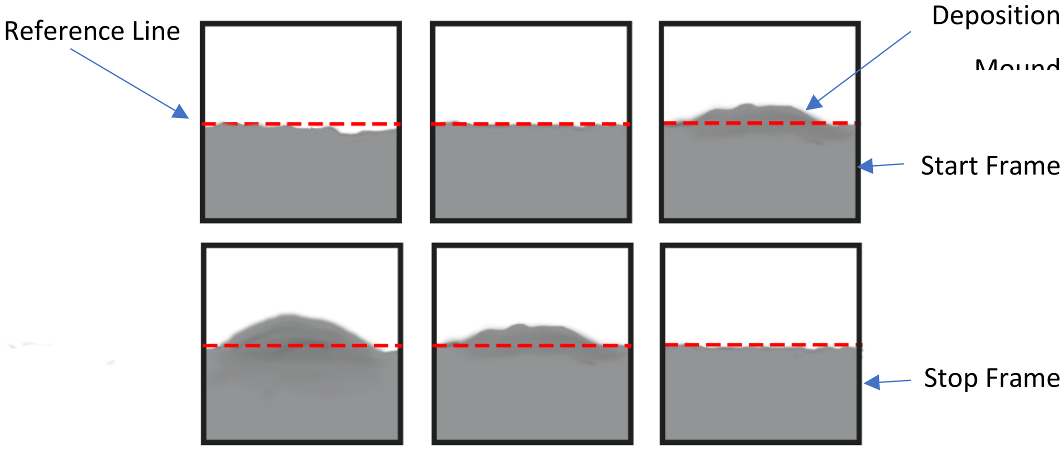

Figure 28: XCT deposit Identification Method

Now that scales have been established, defects and their type can be identified and their position along the length of the deposited track in the direction of how the deposition was laid down can be measured. Through edge detection the boundaries of the defects and the deposit are made prominent. Based on (ISO 13919-2, 2001) and the XCT voxel size a criterion is formulated based on which pores, cracks and other defects are identified (Table 19). After identification the frame at which the defect first appears and the frame after which it disappears is recorded. Using this the center frame is calculated and based on this frame the length along the deposition in the direction of the deposition is calculated in mm for the defect. This is the position of the defect relative to the length of the deposit (Figure 29). Another assumption here is that the epicenter of all defects is their center which may not be true for all defects. The max size of the defects can be measured in pixels by the Image J measurement tool and then converted to mm later.

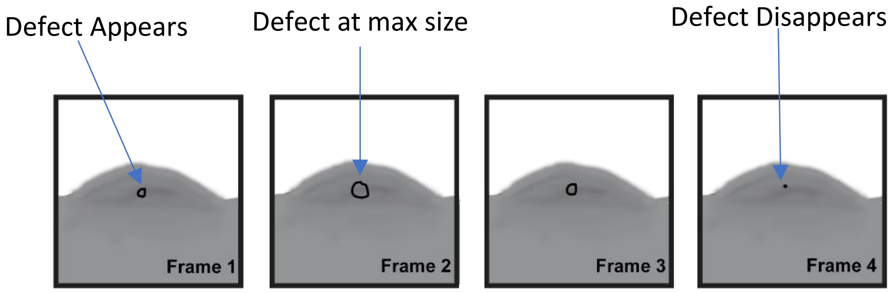

Figure 29: Defect Position and sizing method

An essential calculation here is to identify the position of these defects in terms of the time they come into existence relative to the total time of deposition. This calculation assumes that the time of generation of a defect is dependent on their epicenter position.

The total time of deposition can be calculated using 3 sources; a) laser on and off times seen using the highspeed camera and b) the time that the machine recorded when the laser was turned off then on and lastly the time recorded by the Universal Clock of the developed defect detection system.

4.2.3. Training the System

The overall training method of the system involves combining the online sensor data and offline defect data into spatial and time domain data sets, extracting *"Events"* from these combined data sets, clustering the Events for each sensor, analyzing and processing the distribution of data in each cluster which will allow prediction of a range within which a specific feature of a detected defect lies. At this point a data fusion algorithm is developed which outputs a range of values for a particular feature of a defect. The actual defect feature value should be within this range. Along with this it calculates the percentage confidence of the predicted range based on how many sensors picked up the defect and how far away did it lie from its appointed cluster center in the clustering algorithm.

The combination of the online and offline data sets is also known as data stitching which is a method by which data sets are combined revealing a deeper insight into the information relayed by the combined data set (Stark, et al., 2017) (Sjoedahl & Oreb, 2002) (Zhu, 2012). During this combination the information of the data sets is not changed, rather the data sets are overlayed on each other as they have a common independent variable. In this case the sensor data is mostly in the time domain and the offline data is in the spatial domain. Using machine parameters and physical measurements of the deposit, the data that exists in the spatial domain can be converted into the time domain and data that exists in the time domain can be converted into the spatial domain. After this conversion the sensor data can be stitched onto the XCT defect data which will generate 2D graphs that will allow the detection of sensor data trends and features that are indicative of defects in relation to defect data in both time and spatial domain. From the literature the signal features and trends that indicate the presence of defects are called “Events”. The reason why this method of data analysis is chosen is because data signals on their own without their relation to defect data may be misleading i.e., an Event is observed but no defect developed at that time or position. It is also because when the Event data is placed in the clustering algorithm, clusters formed will have considered defect data as well as signal data which is how it allows for a predictive algorithm to be developed. It is important to mention that the reason why both time and spatial data sets are constructed is because some events rely on time and others on position. For example, a sudden spike in the thermal gradient as per literature is indicative of the presence of a defect. The position of this spike in the melt pool can reveal defect position and the magnitude of the spike can reveal the depth of the defect hence this event must be recorded in the spatial domain.

Figure 30 shows the Data fusion Methodology used to create the model which enables the online fusion algorithm to predict ranges for specific features. This developed methodology takes influence from (Luo & Kay, 1989)’s data fusion architecture. The main sources of data for the multi-sensory data fusion system are the data from the Sensors, the XCT data, the physical measurements and machine parameters. This data can be representing the lowest level of data i.e., signal and pixel level. The XCT and Physical measurements are used in combination to create data sets that represent defect size relative to the position of the defect along the length of the deposit in the direction that the deposit was laid down and defect size relative to the deposition time. This is done so that defect size can be viewed in reference to when it was generated during the deposition and where along the length of the deposit it lies. This step also prepares the data so that it can be integrated with the sensor data later to form stitched data which can allow for sensor data to be analyzed in relation to the defects. Notice that the research only takes into consideration the position of the defects along the length of the deposition and not along the width of the deposit. This is because of the nature of how deposited tracks are laid down. Each deposit is formed by overlapping a certain number of tracks. The deposits in the experiments are made up of 3 tracks at 30%

overlap (Figure 69 b) and the post analysis of the defects does not allow the distinction between the track and hence it is near impossible to tell which track the defect was generated in.

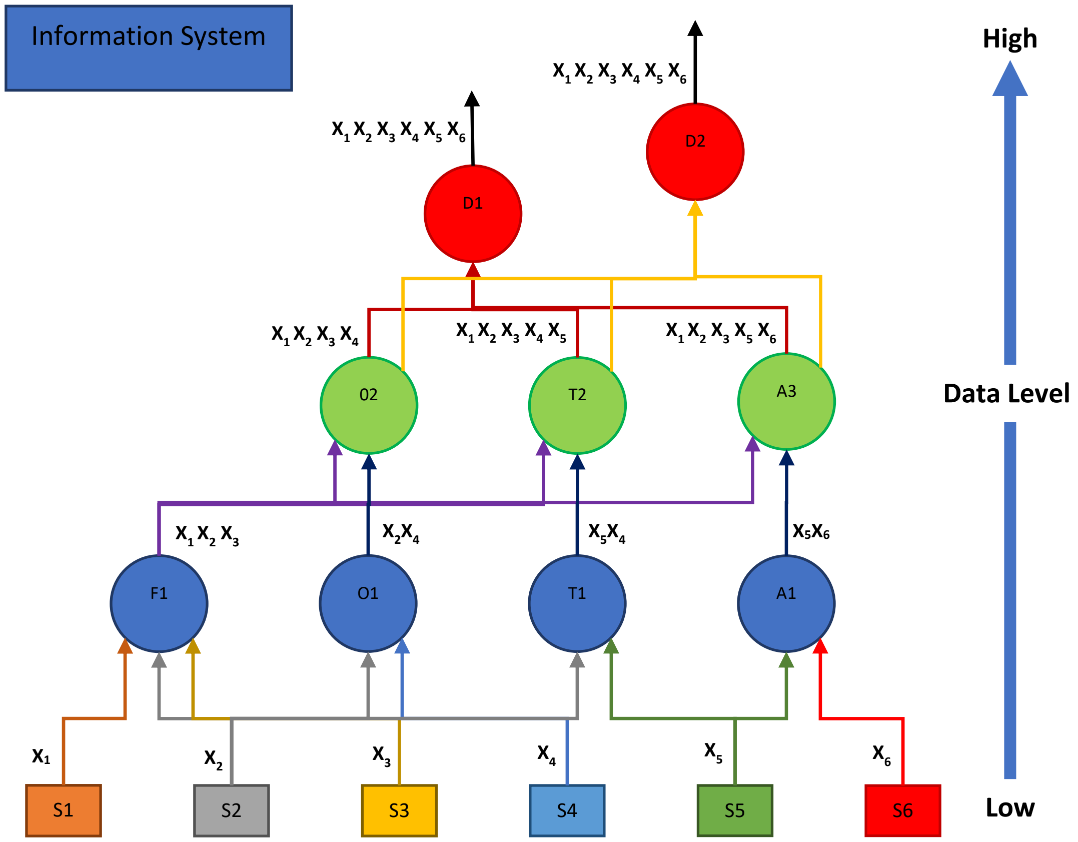

S1= XCT Measurements,
S2=Physical Measurements,
S3=Machine Parameters,
S4=Optical Sensor,
S5=Thermal Sensor,
S6=AE Sensor

F1=Defect Size and position in spatial and time domain

O1= Optical Data in spatial and time domain

T1= Thermal Data in spatial and time domain

O2= Optical Camera Cluster
T2= Thermal Camera Cluster
A3= AE Sensor Camera Cluster
D1= Feature Range Prediction
D2=Percentage Confidence

Figure 30: System Training Data Fusion Methodology

The data from the Optical Camera is processed and converted in intensity data. This data is already in the time domain but is not synced to the start and end time of the deposition of each track. This time can be identified by visually detecting laser on and off times from the captured image. To generate a data set of the optical images that represents pixel intensity in relation to the position along the length of deposition (spatial Domain), once again the physical measurements data is utilized. The intensity mentioned here is the pixel intensity of the CMOS sensor which in fact is just a voltage output based on the number of photons incident on that CMOS pixel sensor. The number of photons will be converted to charge which is then read out as voltage. This voltage is then represented as a digital number from 0 to 255 for an 8-bit image. Even though the spectral radiance is not directly being read, the value represented by the pixel intensity is heavily dependent on the phenomenon and the exact magnitude of irradiance represented by pixel intensity is not important since this study is interested in change in pixel intensity or change in patterns of pixel intensity. With the optical camera, reflection from approaching spherical particles and their interaction with the deposition can be seen. The radiance due to excessive temperatures in the melt pool is also registered by the optical camera.

Similarly, the data captured using the thermal camera represents thermal images in which each pixel represents thermal intensities i.e. This is radiation of the IR spectrum converted to voltage and represented by pixel intensities and once again this is non calibrated to emissivity values, so it does not show correlated temperatures however each pixel intensity shows the thermal intensity being received by a point in the image. In a similar manner the thermal intensities for each track can be isolated through the thermal images of when the laser is turned on and when it is turned off and hence can be viewed in sync with deposition time. Just like the Optical camera data, a data set is generated which represents the thermal intensities in relation to position along the length of the deposit. I.e., Thermal Data represented in the spatial domain. This can be calculated by using the physical measurements of the deposit.

Since AE data continuously collects data, the AE data for each track needs to be isolated from the main AE data stream. This can be done using the time each deposition started and where it stopped. For this the Universal Clock time stamps, the start and stop times recorded by the Thermal camera and the AE data internal clock time stamps are used to calculate time windows in which the deposition was taking place. This way AE data in relation to the deposition time for each track can be viewed. Even though most Events (data that indicates an anomaly) can be extracted from the time and frequency domain for the AE signal, for the sake of investigation AE signal position is also calculated using TOF calculation from the two AE Sensor signals. This in essence can generate an AE data set that displays the position of the signal in spatial domain i.e., relative to the length along the deposition.

At this point all data is processed and converted into time and spatial domain and can now be individually stitched with the Defect data. This is mainly done to correlate defects to the signals being observed. From this stitched data Events are extracted which represent anomalous behavior in the signals. In the scope of this research Events are data sets which contain information regarding values for certain signal features and defect data that correlates to signal features. Defect data includes Total Defects, Total Cracks, Total Pores, Total Defected area, and Max Defect size. The signals that represent a possible anomaly are taken from the elaborate single sensor research in the literature.

For the optical camera data, for every 2mm of deposition length Max Intensity and Intensity Spike frequency is extracted. If the intensity crosses a certain threshold it is recorded as an Event and the Max Intensity, Intensity spike frequency and Total Defects, Total Cracks, Total Pores, Other Defects, Max Defect Size, and total defected area under this event is recorded (Figure 31). The Event for the thermal data is determined when the thermal intensity see a sudden rise and then sudden fall in temperature forming a peak. For this event rise time (Time taken to reach max amplitude), fall time (time taken to fall below threshold after max amplitude is reached), Heating Rate and Cooling Rate, Variance in amplitude, peak thermal intensity, and average thermal intensity are recorded. Along with this all the defect features that are associated with this event (Figure 32). For the Acoustic emission when a certain threshold is crossed it is considered an Event. For this event its Amplitude, Rise Time, Ring Counts, Energy, Duration and Max Frequency for every 200Khz bands up to 1Mhz are recorded. The above-mentioned defect features that lie within the times of these signals are also recorded as a part of these events (Figure 33). The methods to establish threshold values for each sensor are discussed in detail in Chapter 7.

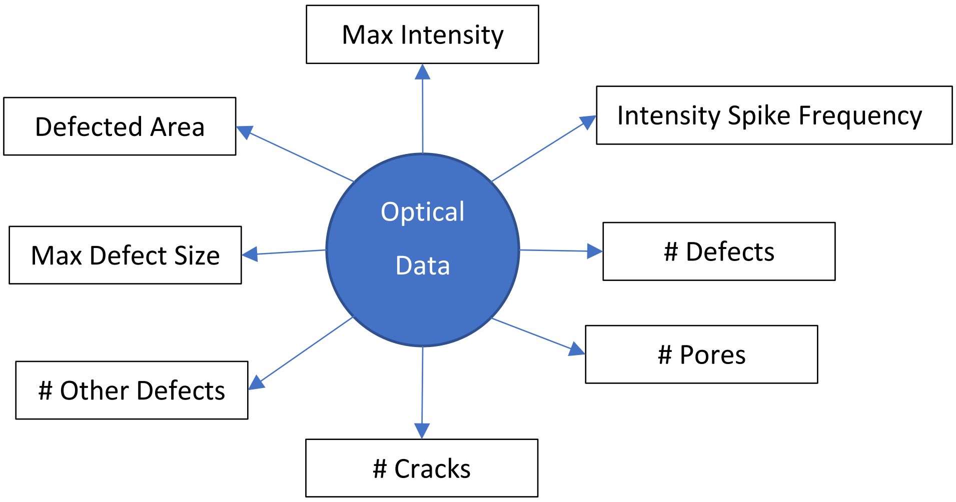

Figure 31: Optical Event and its features

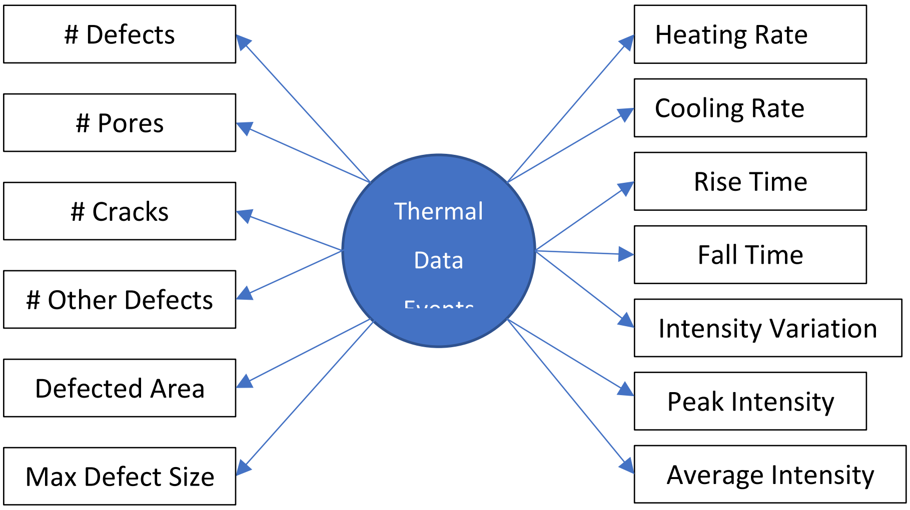

Figure 32:Thermal Event and its features

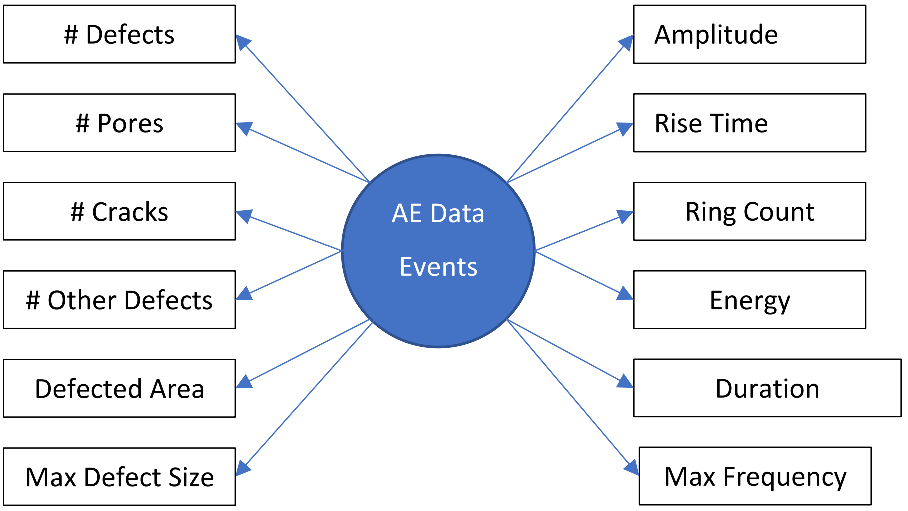

Figure 33: AE Event and its features

All these collected Events for each sensor are then put through a machine learning algorithm called K means clustering. This algorithm groups Events with like data into clusters based on their Euclidean distance from their appointed clusters centers also known as cluster centroids. The distribution of the data of the events of each cluster is analyzed using box and whisker plots which allows for outliers to be omitted. Max and min extremes of the distribution are calculated using interquartile ranges for each data type (Figure 34). These Max and Min values for each feature for each sensor serve a predictive range.

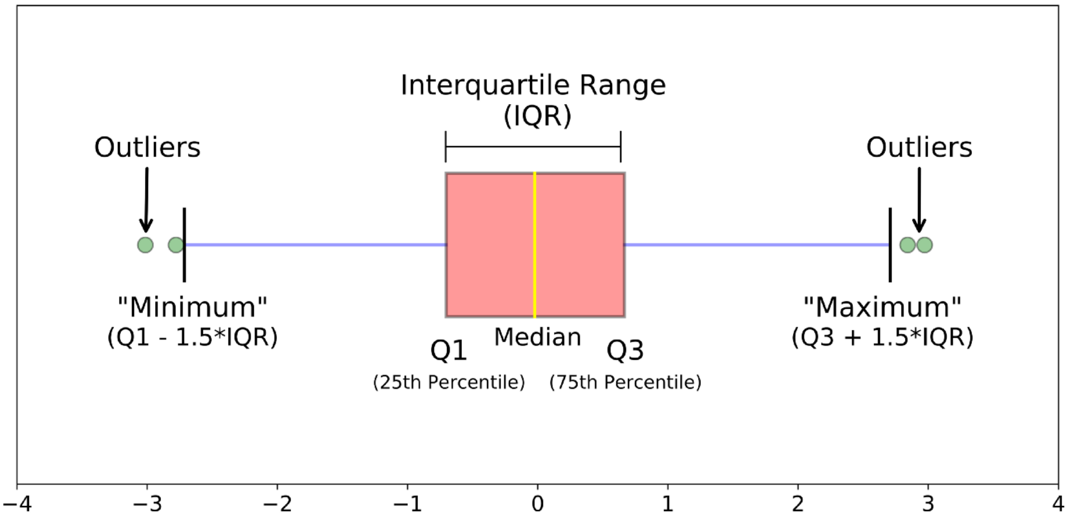

Figure 34: Box and Whisker plot working (Galarnyk, 2018)

Figure 35 shows the algorithm which outputs a singular range and % confidence value for each feature. Each sensor data cluster outputs individual predictive ranges for each feature i.e., Max and Min values within which the actual feature value should lie. The algorithm scans all three sensors continuously to see if a Hit is received within a specific time window. A Hit means that an event has been detected. For each hit received within that time window, its Individual predictive ranges and individual confidence scores are added to the data fusion equation. If within that time window all 3 sensors receive a hit, then the system does not wait for any more hits and just outputs a combined range and confidence value. An example of the scanning window is shown in Table 9.

Time Window	**AE Sensor Hit** $(\boldsymbol{AE_{Range}})$	**HS Camera Hit** $(\boldsymbol{HS_{Range}})$	**Thermal Camera Hit** $(\boldsymbol{Th_{Range}})$	**Add to Fusion Equation**
100ns to 200ns	Yes	Yes	Yes	$AE_{Range}, HS_{Range}, Th_{Range}$

200ns to 300ns	No	Yes	Yes	HS_{Range}, Th_{Range}
400ns to 500ns	No	No	Yes	Th_{Range}

Table 9: Scanning Window Example

Along with this a value called % confidence is calculated and is outputted to allow for the manufacturer to know how confident they can be in this predicted range. This % value is based on how far the Events lie from their respective cluster centers. Once the system receives a hit on a particular sensor the Euclidean distance of the event from its appointed cluster is compared to a criterion based on the 68–95–99.7 rule, also known as the empirical rule. Using this criterion, a score is given to each Hit called the individual confidence score. All the individual scores for a sensor Hit within a certain time window or when all three types of sensors catch data within that time window are combined using a custom algorithm and a % confidence value is generated. The logic being that the further an event lies from its respective cluster centroid the less alike it is to the events closer to the cluster centroid and hence their data will also be different. This process is explained in detail in Section 7.3 where the data fusion algorithms implementation is discussed.

Figure 35: Data Fusion algorithm

4.2.4. Testing the System

Testing the system involves taking a random sample and passing it through the system and later validating the results using post sample analysis (XCT analysis). The only difference will be that the algorithm does not use defect data as a source input in the data fusion algorithm as shown in Figure 36. Since the system has already been trained the output of the system should correctly predict the range if a defect signal is found. S2 in Figure 36 represents the Target Measurements or Dimension of the deposit. This is the target dimensions fed into the LMD machine or based on these dimensions the LMD operator will set his machine settings. After the comparison of the system results with the actual defects found in the deposit using XCT, the accuracy of the system can be calculated. The output of the system and its accuracy are compared with other methodologies and models of defect detection in the state of the art along with statistical tests to validate the hypothesis regarding accuracy.

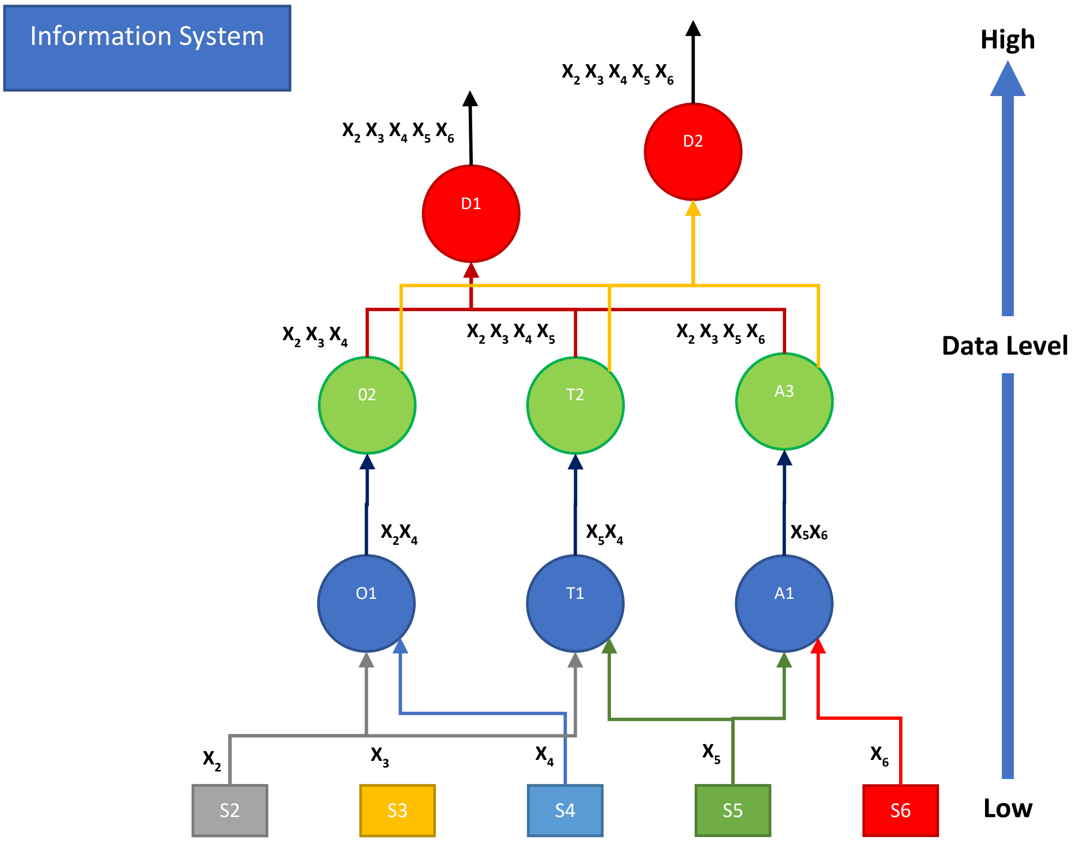

S2=Target Measurements,

S3=Machine Parameters,

S4=Optical Sensor,

S5=Thermal Sensor,

S6=AE Sensor

O1= Optical Data in spatial and time domain

T1= Thermal Data in spatial and time domain

A1= AE in spatial and time

O2= Optical Camera Cluster

T2= Thermal Camera Cluster

A3= AE Sensor Camera Cluster

D1= Feature Range Prediction

Figure 36: Online Data Fusion Methodology

The major metric of verification of the systems output is its accuracy of the predicted features compared to the state-of-the-art research. Since the system takes influence from the literature and uses most if not all “Events” with respect to each of the sensors, the same signal data can be used in the models and accuracy measurement methods of other researchers. This should allow for a level playing field when comparing accuracies of methodologies as data used in them is the same. The multi-sensory data fusion system predicts Total number of Defects, Total Number of Pores, Total Number of Cracks, Max Size of defect and Total Defected Area which is more features than any single state of the art method, however, the major difference is that it outputs a range instead of a single value for a predicted feature unlike the state-of-the-art research. There are two methods using which a single value can be produced for the sake of comparison. First method is where the average of the predicted range is taken and a multi regression equation is used to produce a single value for each detected Event. The second is where an equivalent look up table is formed where if the predicted value lies within the actual range, it is given a score of 1 (100% accuracy) and if the value lies outside the range, it is given a score of 0 (0% accuracy). Using the first method a value for a certain feature will be produced. For example, for Total Defects detected a single value is generated and this value can be put into the accuracy verification method presented by (Khanzadeh & Bian, 2016) and then the calculated accuracy can be compared with their result. The same can be done to compare with the output accuracy of (Barua & Frank Liou, 2014)'s model and (Gaja & Liou, 2018)'s model. The Accuracy calculated from the first method is also verified via the Wilcoxon Signed Rank test to determine if there is a probability that a more extreme result might be possible based on the sample set. The reason for choosing the Wilcoxon signed Rank test is because of the nature of the distribution of the data. This is discussed in further detail in Section 8.2.3 explained why a one sample T test was not used instead. For the second method the Binomial Test is utilized to verify whether a more extreme results than the calculated accuracy is probable. The Binomial test is used because the data being analyzed is non-parametric and dichotomous since the equivalence table is used.

4.3. Discussion

The methodology chapter explains the overall outline of how the research was carried out and provides justification for the research design choices. The methodology chapter does not go into elaborate details as there are dedicated chapters explaining these steps.

The specific gaps were identified as limitations in the type of information, level of information and reliability of information in the state of the art. The limitations are found in single sensor approaches since they only observe a single phenomenon which can only provide a single type of information and limited level of information and a low level of reliability. It is also important to mention that each sensor is observing a certain window in the deposition cycle and the phenomenon being observed are very quick to change. This adds another dimension of problems since the sensor observing the phenomenon must be quick enough to collect sufficient information that can indicate the development or presence of a defect and must be observing a window of the deposition cycle in which signs of the development of a defect can be captured.

The solution presented is a high-speed multisensory online defect detection system which uses data fusion to detect and predict features of the detected defects. This includes Total Defects, Pores, Cracks, Max defect size and defected Area. The multiple sensors are there to solve the problem of type, level, and reliability. The highspeed system caters for the quickness of the LMD process itself and the sampling data from multiple high-speed sensors. To combine all types of data streams into single type, a custom data fusion method is implemented. The data fusion method also improves the reliability of output of the system. The research methodology involves first developing a system capable catching defects at fast rates and managing the high-speed sensor array. After this system it used to capture signals from experiment where defects are purposely provoked. The samples from these experiments are analyzed using XCT where defect position, type and size is determined. Using machine settings and physical measurements of the experimental samples the defect size can be observed in reference to deposition time and position along the deposition length in the direction of how the deposition was laid down.

The system can be trained with the defect data from the defect provocation experiments to predict defect features. The data for each sensor needs to be converted into spatial and time domain and then defect data is stitched onto it. Using the stitched data for each sensor the Events which indicate defects can be extracted. These events contain features of the signal which display anomalous data and are recognized using the literature of the state of the art. Each of these events are then fed into the K-means clustering algorithm which groups events with like features. The K means groups data based on their Euclidean distance from cluster centers. The data for each cluster is analyzed using box and whiskers plot and the outliers are omitted and a new max and min range is established for the distribution for each feature. These ranges serve as predictive ranges for each feature depending on the sensor cluster, they lie in.

The clustering algorithm then detects events that lie within a certain time window and fuses them using a data fusion equation to output a single predictive range for each feature. The reliability in the predictive ranges is measured by % confidence value. This value uses the Euclidean distance from the cluster centers as a criterion to establish whether the predictive range will be precise or not. This is based on the fact that Events that lie further away from their appointed cluster centers have less similar data compared to the events closer to the cluster centers.

The online defect detection algorithm uses the trained data and target deposition dimension to accomplish the same goal as the method used to train the system. A random sample is put through the online defect detection algorithm and XCT is used to compare the systems output to the actual defects in the sample. This accuracy and system output is also compared to other methodologies and models utilized in the state of the art for further validation. The details regarding the systems design, implementation and development is explained in Chapter 5, The Experimentation and its details are explained in Chapter 6 and the details regarding the data processing and fusion methodology are explained in Chapter 7.

Chapter 5: System Architecture and Development

5.1. Sensors Specifications

The three sensors chosen for the system were High Speed optical Camera, Thermal Camera and 2 acoustic emission sensors. These sensors are chosen based on the observation windows that they are capable of viewing in the deposition cycle. The combination of these 3 sensor types allows the monitoring of much of the deposition cycle from powder trajectory to deposit cooldown. Sensor specifications need to be decided accordingly so that the maximum amount of data regarding the deposition and defect development can be collected. Hence deciding on sampling rates for each sensor is critical but very high sampling rates are accompanied by a multitude of issues which cause further complications in a multisensory system. This means as sensor speeds increase other problems start propping up which includes Overexposure issues, Data size, data streaming issues, online Data transfer limitations, Time stamping issues, Environmental Noise and increase in DAQ's dead band time. The solution to all these is to find a sweet spot for sampling speeds where the above-mentioned problems can be reduced but the systems detection capability is not compromised.

Five properties are found in the literature which can be used to estimate the time required to pick up a phenomenon or property and specifications on the capability of the sensor with regards to temperature and the number of defects it can pick up under certain conditions. These four properties are Powder velocity, Powder Residence Time, Pore Generation Time, Cracks Generation Temperature Zones and Typical Cooling Rates. The quickest, Average and bare minimum timing values for these properties are used to calculate Best, Average and Worst-Case scenario values where best case catch the most amount of detail, Average Case is where relatively good amount of detail is captured and worst case is the bare minimum to capture enough detail. Based on these values as shown in Table 10, sampling rates closest to or less than the Best Case timing values are utilized in this research. As mentioned earlier very quick sampling rates can cause further issues hence the aim is to keep a sampling rate using timing values within the Best Case and Worst Case. To understand these additive problems that occur due to very high sampling rates, how these sensors work must be understood.

	Best Case	Average Case	Worst Case
Particle Velocity	5 m/s at 12mm Standoff distance $t_{1mm} = 220\mu s$	3.5 m/s at 12mm Standoff distance $t_{1mm} = 285.7\mu s$	2 m/s at 12mm Standoff distance. $t_{1mm} = 500\mu s$
Residence Time	32 µs	307 µs	1210 µs
Pore Generation	11 µs	48 µs	85 µs
Crack Generation	42 - 54.3% of Cracks in 200°C window at cooling Rate of 10^4 °C/s. $t_{200°C} = 20000\mu s$	75% of Cracks in 600°C window at cooling Rate of 10^4 °C/s. $t_{600°C} = 60000\mu s$	100% of Cracks in 1200°C window at cooling Rate of 10^4 °C/s. $t_{1200°C} = 120000\mu s$
Cooling Rates	10^7 °C/s $t_{1°C} = 0.1\mu s$	10^4 °C/s $t_{1°C} = 100\mu s$	10^3 °C/s $t_{1°C} = 1000\mu s$

Table 10: Best, Average and Worst-Case values

The Highspeed camera used in this research is a Photron FastCam SA-X2 which is capable of recording at frame rates of up to 120000 FPS coupled with and Nikkon AF-P DX Nikkor 18-55mm F/3.5-5.6G Focus Lens upon which a natural density filter (ND 1000) is fixed. High Speed Cameras take images at very high rates and hence the time the image sensor is exposed to light decreases with increase in Frame Rates. This time is called shutter duration and is related to shutter speed. This means at higher frame rates the amount of light required to capture a visible or reasonably lit image also increases. This presents a unique challenge since in LMD process the amount of light reflected by the melt pool fluctuates between extremes at different parts of the melt pool which can cause the image sensor to either capture no image due to the lack of light or completely saturate under standard aperture settings. Using hit and trial the right combination of Frame Rate, Camera aperture, ND filter F stop values and distance of an illumination source are discovered which present an acceptable highspeed image. An acceptable high-speed image is where the image does not get over saturated during high temperature region formation and images are not completely dark due to low temperatures. Enough of the melt pool should be visible but differentiable from the background to capture extreme events. Using image J software, the overall image pixel intensity can be seen as shown in Figure 37 and this can be used as reference to find the right settings. Images where maximum pixel intensity is below 35 are chosen as reference images since the do exhibit excessive activity and the melt pool is visible along with powder particles without being very bright. The Images should be able to show contrasts in spectral radiance compared to other parts of the melt pool. Using this method, the Frame rate was set at 10,000 frames per second, aperture set f/11, Natural Density filter with an f stop reduction of 10 chosen and an 85W CFL[9] as an illumination source of 5386 Lumens is placed approximately 20 inches from the work piece. Another major issue faced with the Optical camera is the resolution since it increases the data size which causes streaming and downloading issues. It was seen that anything below 256 x 256 did not show the trajectory of powder particles. The HS data at 10000Frames/s and 256 by 256 resolution for a 3 track 11mm deposition which takes about 5 seconds can be as large as 15GBs. Using a single Gigabit ethernet port with a CAT 7 Cable this would theoretically take 120 seconds not including overhead times. The photon SA-X2 has dual channel Gigabit Ethernet interfaces hence two ports CAT 7 cable which can support 10Gbps is used to download the video. Theoretically the dual channels should allow download of an entire clip in 60 seconds not including overheads. The video is temporarily stored in a buffer memory in the camera and download to the PC when needed for analysis. However, due to some technical issues video data transfer during the deposition was corrupted at times and for the sake of reducing experimental time the Video data was download after the deposition was completed and video data time synced using that start time and stop time recorded by the HS Data acquisition script detailed in Section 5.3.

The thermal camera utilized is a NIT Tachyon 16K Uncooled MWIR 128x128 pixels infrared camera with high-speed frame rates up to 4000 FPS. The camera detects the IR region which ranges from 1.0µm to 5µm. Thermal Camera presents a different issue due to high frame rate selections. This is because with frame rate the random noise in the thermal images increases. This is unacceptable as the system is supposed to be sensitive to small changes even at the pixel level and noise could be interpreted as an event which would be misleading. Hence a tradeoff is made by setting the Thermal cameras frame rate to a 1000 frames per second. At this setting noise goes down significantly.

---

[9] Compact Fluorescent Lightbulb

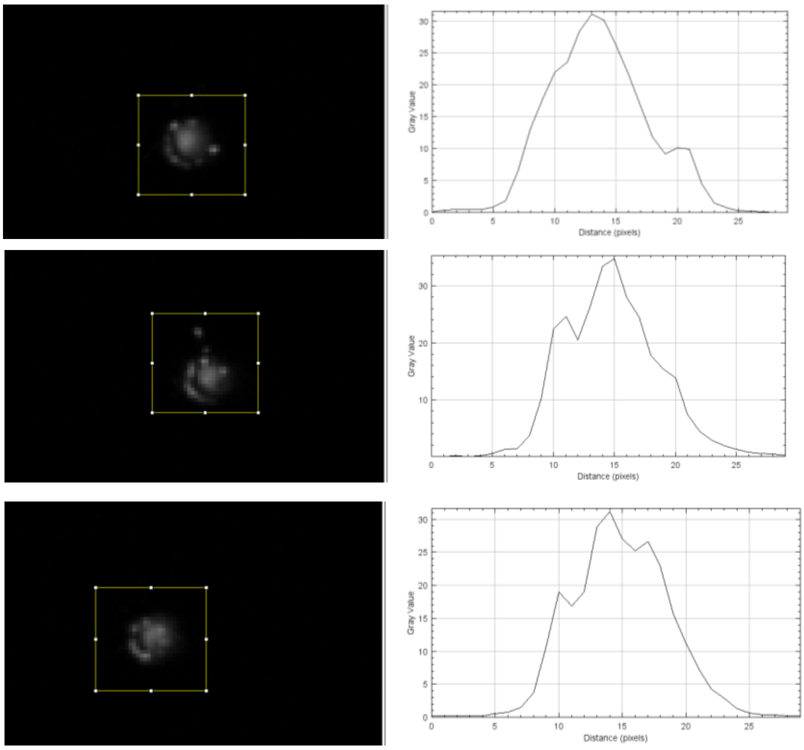

Figure 37:HS Camera Calibration method

AE sensors used are Kistler Type 8152C AE piezo electric sensors made for high temperature environments. This was coupled with a Kistler Type 5125C Piezotron coupler or conditioning unit. The rate at which AE data is sampled depends on the sampling rate of the data acquisition unit collecting the data. From Table 10 it is known that the quickest time for a best-case timing value is that of a cooling rate of 10^7 °C/s where change of 1°C takes 0.1μs. To collect a sample at every 0.1μs a sampling rate of 10,000,000 Samples/s or 10 MS/s is required. According to Nyquist theorem the sampling rate should at least be twice that of the minimum sampling rate. But it is a common practice to keep a sampling rate 4 times that of the minimum sampling rate to get better results. Hence two times the minimum sampling rate would be 20 MS/s and four times would be 40MS/s. Hence, a Digitizer unit (DAQ) which is capable of sampling at 50MS/s is chosen. The AE hardware collects 1024 data points per sensor or 2048 data points in total at a sampling rate of 50 Mega sample per second or 50MS/s. This means that 1 data point is collected per 0.00000002s hence to collect 2048 data points will take a total time of 40.96μs. Once 2048 data points are collected, they are then transferred to the temporary buffer storage. In other words, the acquisition unit continuously collects data for 40.96μs then stops recording, transfers data to temp storage and then resumes data collection. As explained earlier the time in which data is not being collected is called a dead band.

The sensor configuration and sampling rates are compared to the Best, Average and Worst-case timing values as can be seen in Table 11. The pore generation times, and residence times are collected from literature as they were presented. The time it takes for a powder particle to move 1mm is calculated by the particle velocity times found in the literature and nozzle standoff distance in experiments in this research. Crack generation times for a % of total cracks in a certain temperature window with a specific cool down rate are calculated from data collected from literature. Lastly, using the different cooling rates provided in the literature, the time it takes to observe a change of 1°C can be calculated. All the values collected from literature are discussed in detail in Section 2.5 and 3.9. It can be seen that most sampling rates fall between best case and worst case except that the HS and Thermal camera sampling rates are not quick enough to capture pore generation times. The HS camera sampling rate lies within the best-case timing values to capture Particle Velocity movement and Crack Generation. They lie within an Average Case for Residence Time and Cooling Rates. From these values it can be concluded that the HS camera can track a particle with a velocity 5m/s every 1mm of its movement. It can track any particle with a residence time of over a 100µs and observe any change that happens when temperature changes by 1°C if the cooling rate is 10^4°C/s. The HS camera just falls shy of the worst-case capture time for pore generation since single pore develops quicker that the time it takes to capture a single frame. However, this means that it is still capable of capturing the effect of multiple pores in a single frame. The thermal camera is incapable of catching powder trajectory as explained in the literature but meets the bare minimum for residence time and cooling rates. This means that if a particle is resident on or in the melt pool for greater than or equal to 1000µs there is chance to capture a defect caused by this particle. For cooling rate, it shows that the thermal camera can capture a change of 1 °C with a single frame if the cooling rate is 10^3 °C/s. It shows that it capable of capturing crack generation of 42% to 50% of cracks within 200°C window at a cooling rate 10^4°C/s. It shows a best-case capture time for crack generation times but is slower than the worst case for the pore gen times. The AE sensor shows best case capture times for pore generation, crack generation times and cooling rates.

		Particle Velocity	**Residence Time**	**Pore Generation Time**	**Crack Generation Time**	**Cooling Rates**
High Speed Camera	10000 FPS or 100µs/Frame	Best Case	Average Case	Greater than worst Case	Best Case	Average Case
Thermal Imager	1000 FPS or 1000 µs/Frame	N/A	Worst Case	Greater than worst Case	Best Case	Worst Case
Acoustic Emission Camera	Continuous sampling for 40.96 µs and 1 sample is collected at 0.02 µs	N/A	N/A	Best Case	Best Case	Best Case

Table 11: Sensor Best, Average and Worst Case

5.2. Hardware Architecture

The ideal practical implementation of the general architecture (Figure 26) would implement 5 modules: PC, Gigabit Ethernet Card, FPGA with Digitizer and High-speed Raid Array (Storage). All these modules would be sharing a single Highspeed full duplex data bus in a single Chassis (Figure 38). This system along with its advantages is discussed in detail in Chapter 9. However due to unforeseen circumstances and budget constraints the exact practical implementation of the general system architecture could not be implemented. This research does however implement a similar hardware architecture except for the part where all modules share a single High speed data bus and a single chassis. Even though the system is connected in a different way it's still follows the same guidelines provided by the General System Architecture. As seen in Figure 39 the system is divided in 4 general parts as seen in the general architecture (Figure 26) Pre–Condition Units, Sensors, Post Conditioning Units, Processing and Acquisition Units, buffer Storage and PC.

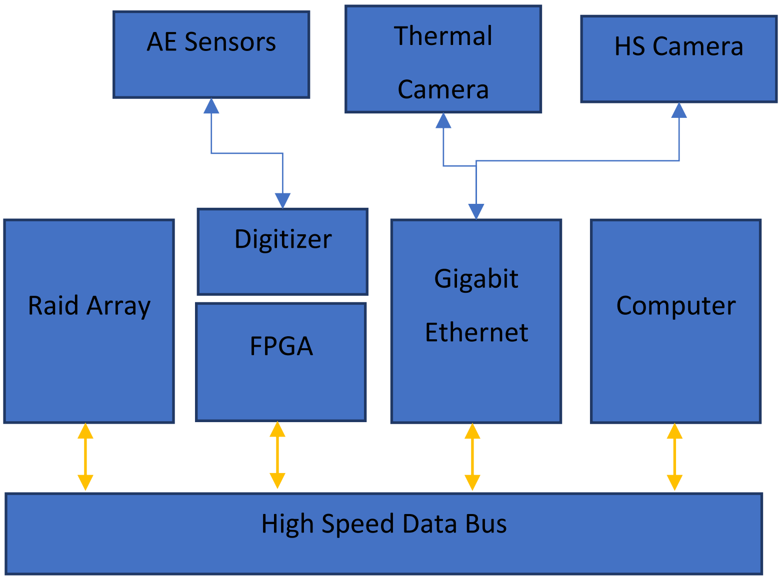

Figure 38: Ideal Hardware Architecture

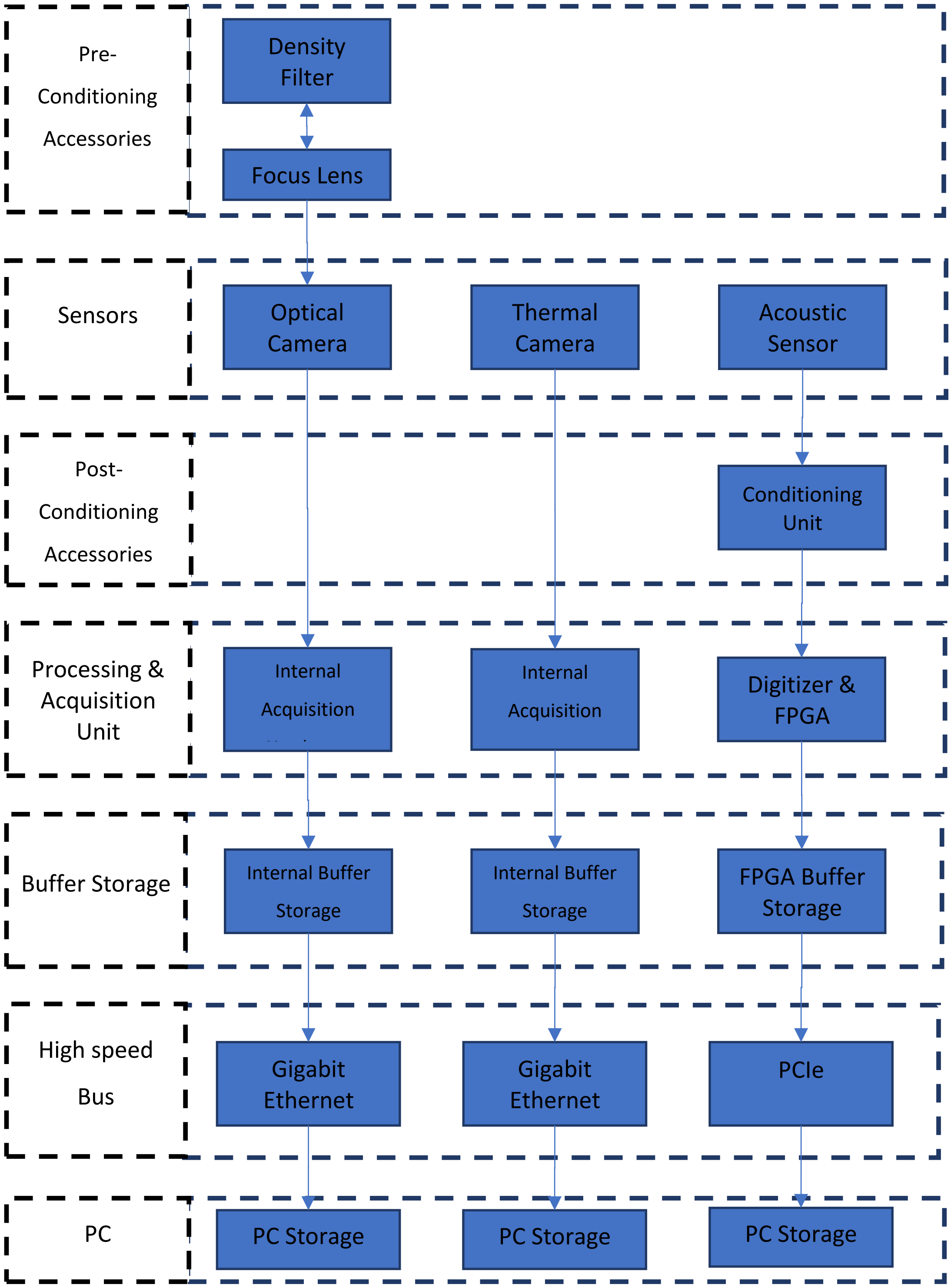

Figure 39: System Architecture Parts

Figure 40 shows the hardware architecture for the system used to collect data during experimentation. Data from the Highspeed Optical camera is transferred to the PC via two

CAT 7 cables plugged into a Dual Gigabit ethernet Card. This card is plugged into the PC's motherboards PCIe Slot. Likewise, the thermal Camera transfers data via a CAT 5 cable into another Gigabit ethernet port plugged into the motherboard's PCIe slot. The PCIe in modern computer architecture are meant for high-speed peripherals e.g., High Speed graphics arrays. Even though CAT 7 cables are capable of through putting 10000Mbps the NIT Thermal Imager was not compatible with CAT 7 Cables and hence a CAT 5e cable was used which is capable of through putting 1000Mbps. The AE sensors are connected to their Kistler Type 5125C units which condition and digitize the analog data and then output it to a Digitizer attached to an FPGA module via SMB accessory. The FPGA captures and stores it in a temporary memory buffer later to be transferred to the PC when the system collection cycle is complete. This is discussed in detail in the software section. Using DMA technology, the AE data is transfer via the PCIE controller to the PC which is capable of through putting 40Gbps in each direction simultaneously. The PCIE controller, the FPGA and the Digitizer module are all fitted into a single Highspeed data bus Chassis. Table 12 shows a list of the modules and parts used to implement the above-mentioned architecture. A large part of the system was implemented using National Instruments hardware due to its modular nature and the fact that LabView is a part of the conglomerate of software's used to write the Acquisition software. Figure 41 shows the picture of how the actual hardware was connected and used.

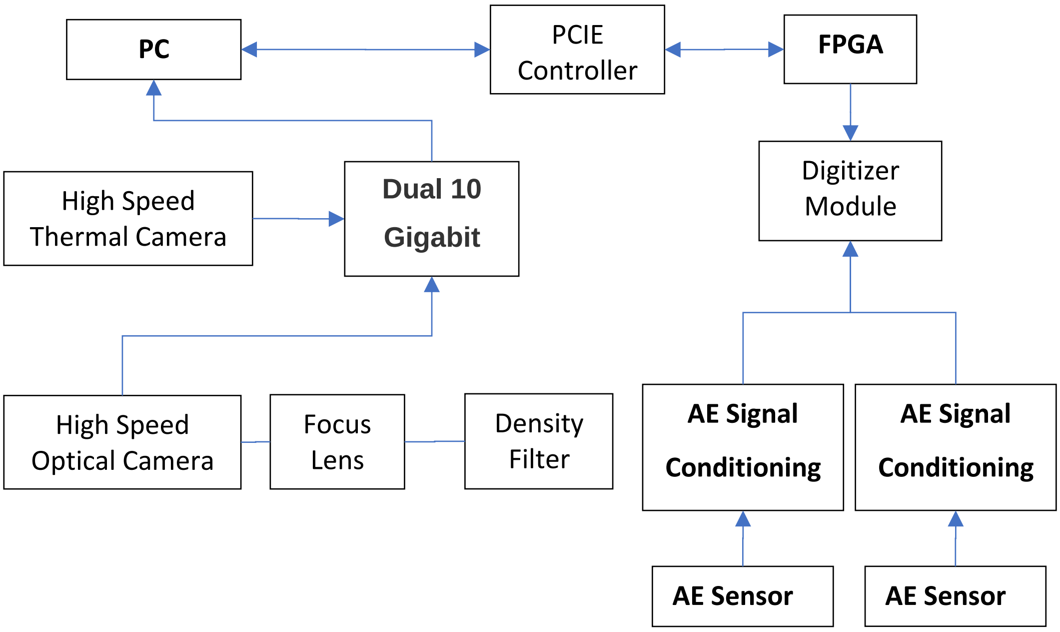

Figure 40:Hardware Architecture

#	Hardware	Name
1.	**High Speed Data Bus Chaisis**	NI PXIe-1082, 8-slot 3U PXI Express Chassis
2.	**FPGA**	NI PXI-7954R FlexRIO FPGA Module
3.	**Analogue Signal Interface**	NI 5752 32-Channel Digitizer Module for FlexRIO
4.	**Dual Gigabit Ethernet Card**	Gigabit PCIE Network Card for Intel E1G42ET - 82576 Chip
5.	**PCIE Interface**	NI PXIe-PCIe8381, x8 Gen2 MXIExpress for PXI Express Interface, 3m

Table 12: List of Hardware Modules

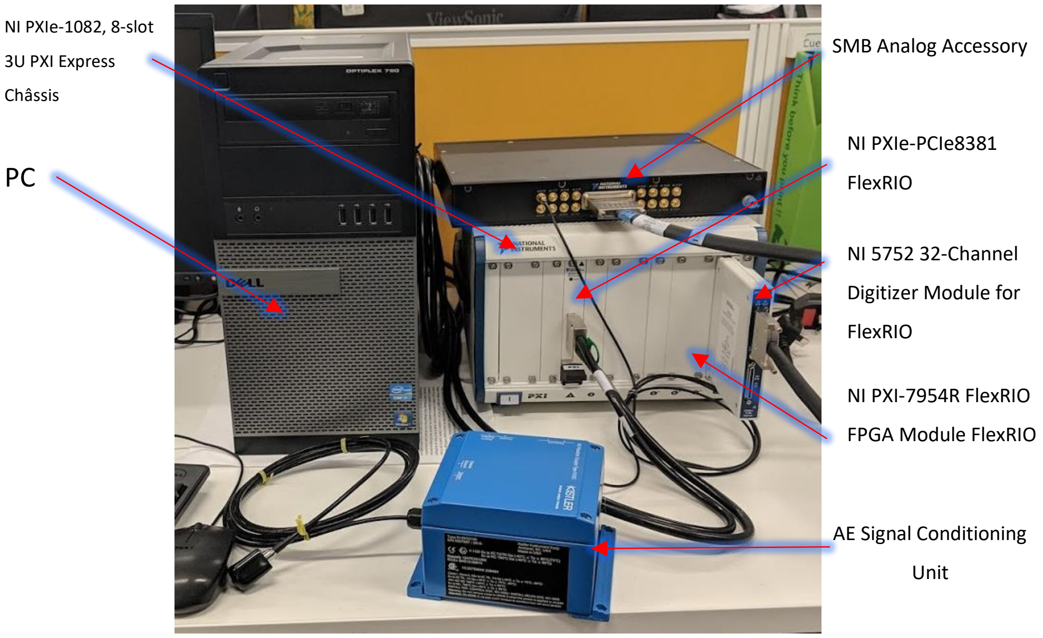

Figure 41: Highspeed Multisensory System

5.3. Software Architecture

Figure 42 shows the Software Architecture developed for the system hardware discussed above. The software uses Scripts written in LabView, C#, SDKs for the sensors and 3rd Party Software for the sensors communicating with each other for time stamps. A total of 6 Scripts are written: Acquisition VI, High Speed Camera SDK VI, Universal Timer Script, Thermal

Camera Interface Script, DMA IP Core VI and AE VI. Two scripts (AE and DMA IP Core) are implemented in the FPGA using LabVIEW and four scripts (Thermal Camera Interface, acquisition script, Highspeed Camera SDK and Universal Timer Script) are implemented on the PC using LabVIEW and C# Scripts.

Figure 44 shows the flow chart for the Acquisition script which is the main script that manages all the sensors and is written in LabView. This turns on the Universal Timer at the Start of the program and then starts the sensors in the order of Thermal, High Speed and AE. After this it goes into the AE acquisition loop which receives data from the AE VI and time stamps it using the universal timer. The data received by the acquisition loop is the data from the AE sensor bundled into a single datagram. The datagram is unbundled and 1024 data points for each sensor are separated, time stamped and stored in TDMS file format. If the deposition is completed a stop button is pressed and the timer script is turned off and all programs are stopped.

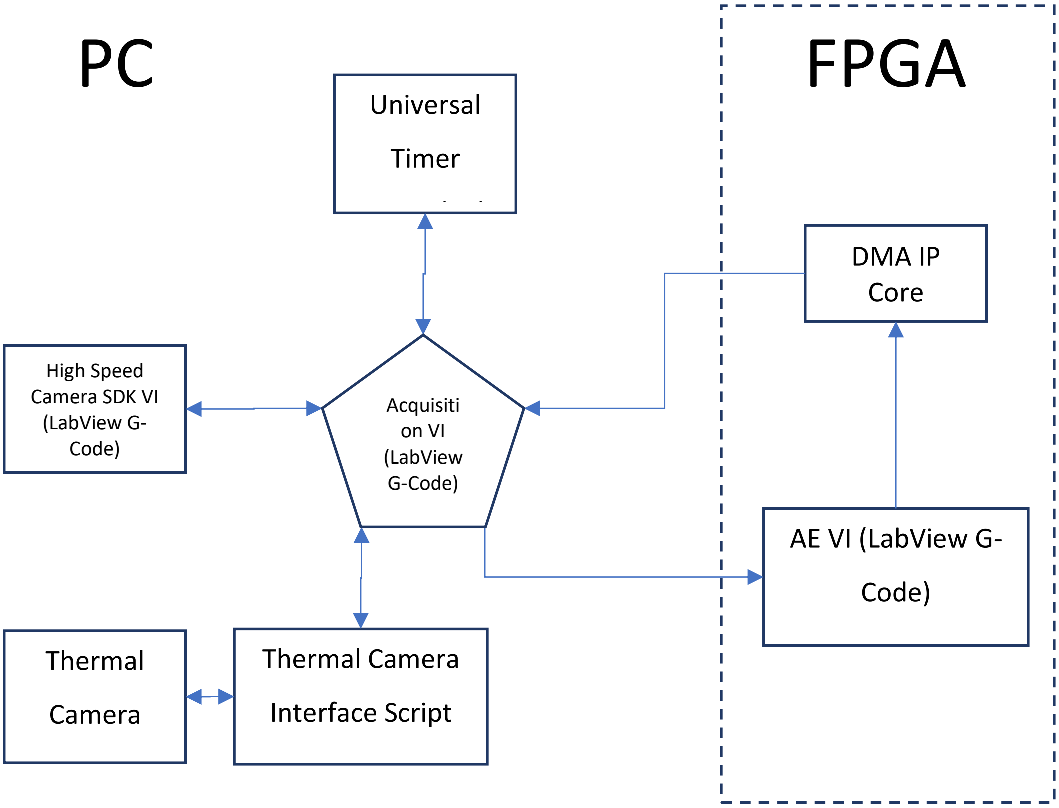

Figure 42: Software Architecture

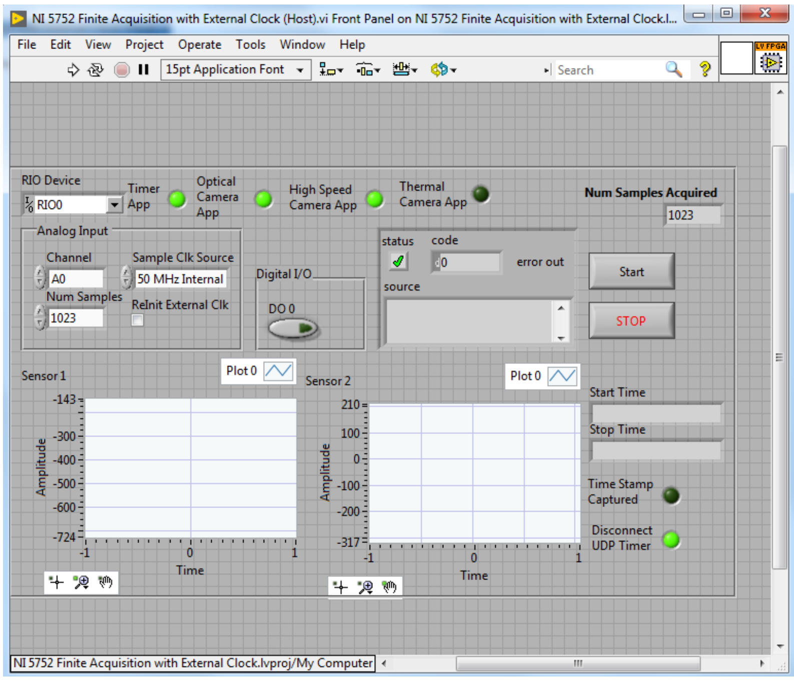

NI 5752 Finite Acquisition with External Clock (Host).vi Front Panel on NI 5752 Finite Acquisition with External Clock.l...

RIO Device: RIO0

Channel: A0

Num Samples: 1023

Sample Clk Source: 50 MHz Internal

Num Samples Acquired: 1023

error out: code 0

NI 5752 Finite Acquisition with External Clock.lvproj/My Computer

Figure 43:Acquisition VI

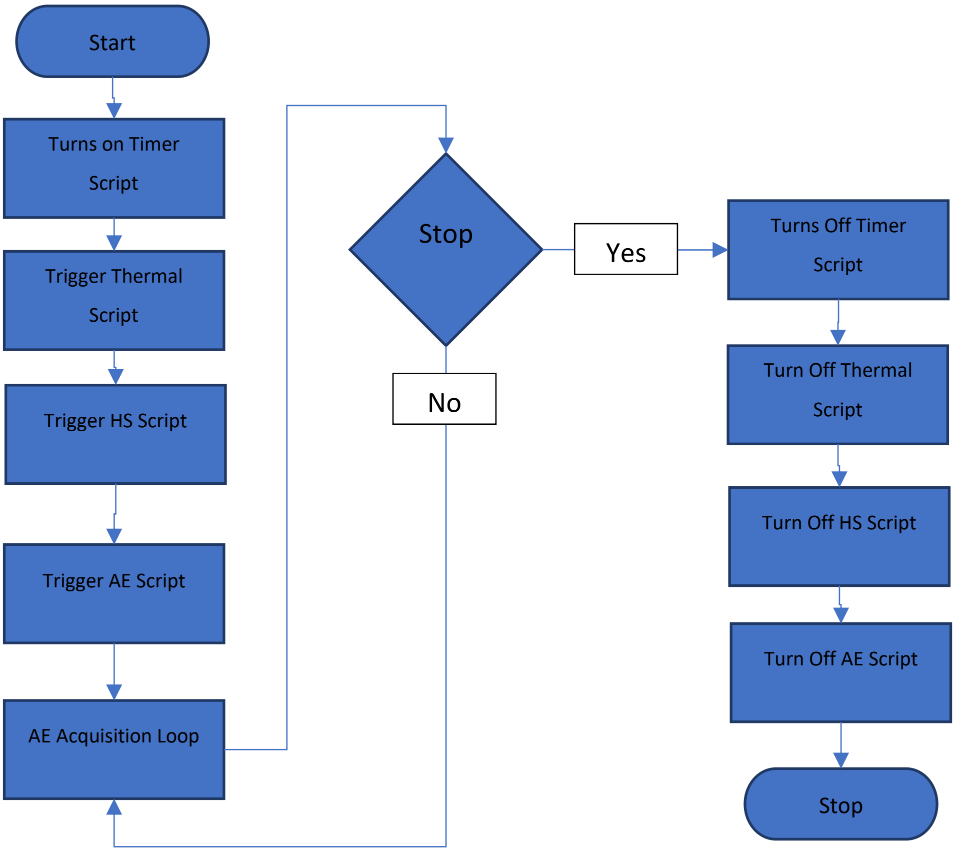

Figure 44:Acquisition Flow Chart

The Universal Timer script is the universal Clock which broadcasts a high precision timer to all other scripts. This script is the first to be activated by the acquisition script so that it becomes a reference to all other scripts. The universal timer utilizes an API called QPC or Query Performance counter which utilizes the CPU frequency (Ticks) to calculate time elapsed with high precision. For the PC that this script was running at the frequency 3312832 Hz and hence the interval between each tick is 301.85ns. Typical access time for the script from the QPC register is 30 ns which makes the overall tick time to 330 ns. Data is broadcasted over a dedicated virtual port on the PC machine using Universal Datagram Protocol or UDP and its multicast capability. UDP is a lossless low latency protocol often used in time sensitive applications. Figure 45 shows the flow chart for the Universal Timer Script.

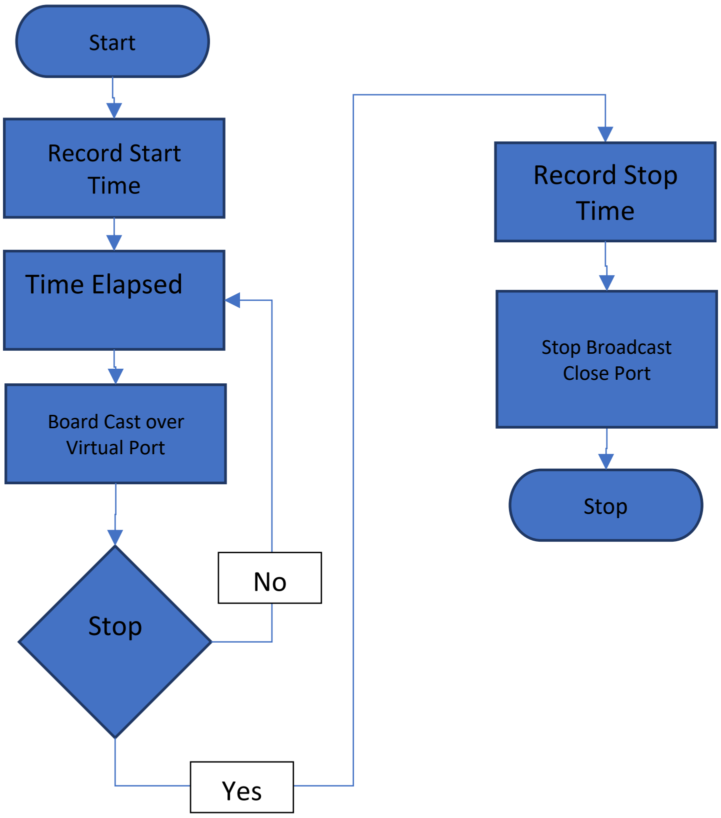

Figure 45:Universal Timer Script Flow Chart

High Speed VI is written in LabVIEW utilizes the prewritten SDK supplied by Photron. The SDK VI is modified to have a UDP listener which is used to time stamp start and stop times as well as used to receive start and stop instructions. Figure 46 shows the flow chart for the High-Speed VI Script.

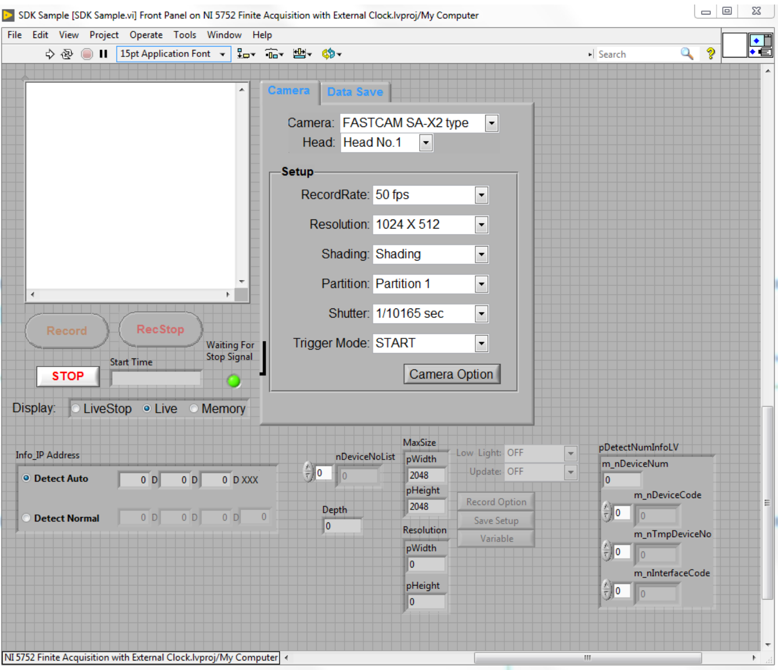

Camera: FASTCAM SA-X2 type
Head: Head No.1

Setup

RecordRate: 50 fps
Resolution: 1024 X 512
Shading: Shading
Partition: Partition 1
Shutter: 1/10165 sec
Trigger Mode: START

Start Time
Waiting For Stop Signal

Display: ○ LiveStop ● Live ○ Memory

Info_IP Address
● Detect Auto 0 D 0 D 0 D XXX
○ Detect Normal 0 D 0 D 0 D 0

nDeviceNoList 0 0
Depth 0

MaxSize
pWidth 2048
pHeight 2048

Resolution
pWidth 0
pHeight 0

Low Light: OFF
Update: OFF

pDetectNumInfoLV
m_nDeviceNum 0
m_nDeviceCode 0 0
m_nTmpDeviceNo 0 0
m_nInterfaceCode 0 0

Figure 46: High-Speed Camera SDK VI

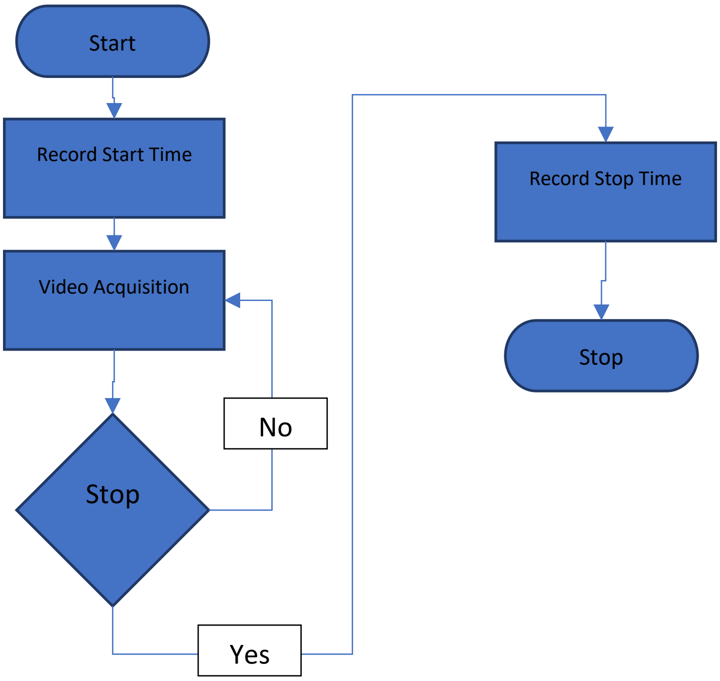

Figure 47: High Speed VI Flow Chart

The Thermal Camera Interface Script is written in C#. The NIT Tachyon 16 does come with a LabView SDK rather a software which controls the Thermal Camera. The thermal interface script is a clever hack for the NIT software where it records the start and stop of the software once again using a UDP listener as shown in the flow chart of the script in Figure 49.

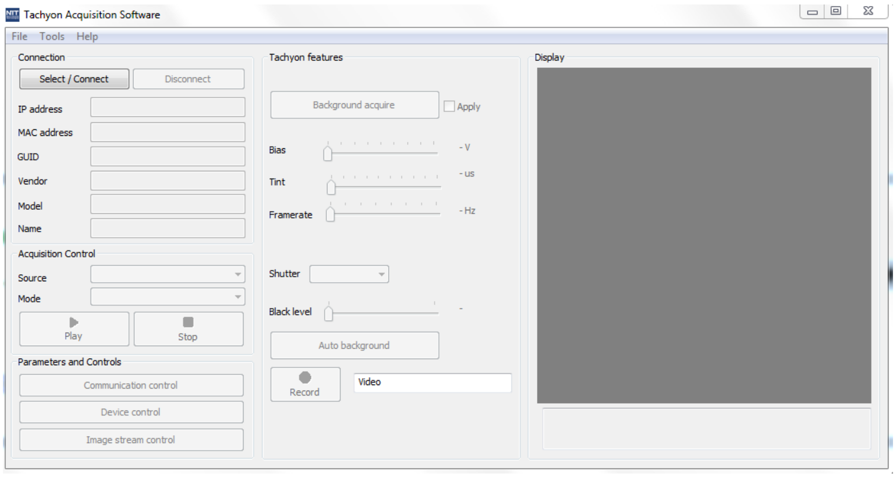

Figure 48: NIT Tachyon Application Software

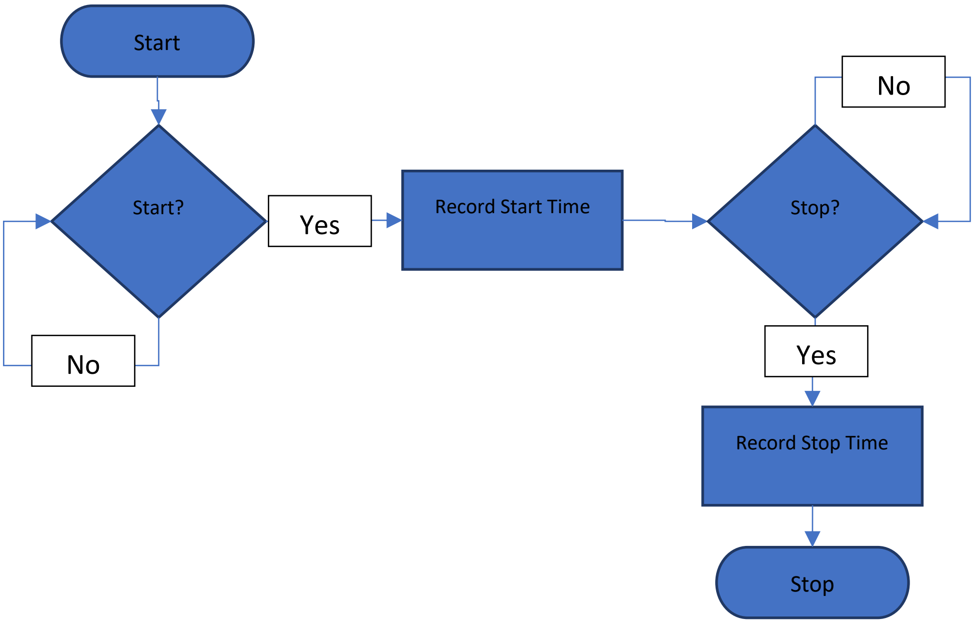

Figure 49: Thermal Script Flow Chart

The AE VI is written in LabVIEW and implemented in the FPGA. 1024 Data points are collected continuously for each AE sensor at 50MS/s and bundled into one package and stored in the dedicated DMA IP core of the FPGA. The Direct Memory Access or DMA Engine is a system that controls data transfer from the FPGA buffer storage to the RAM of the PC. This is done by developing a FIFO buffer at both ends i.e., HOST PC and FPGA as shown in Figure 50. Since the DMA controller handles data transfer this allows for the FPGA to collect data instead of spending valuable time transferring data when the host computer is free to collect it. This effectively reduces the dead time of the data collection system.

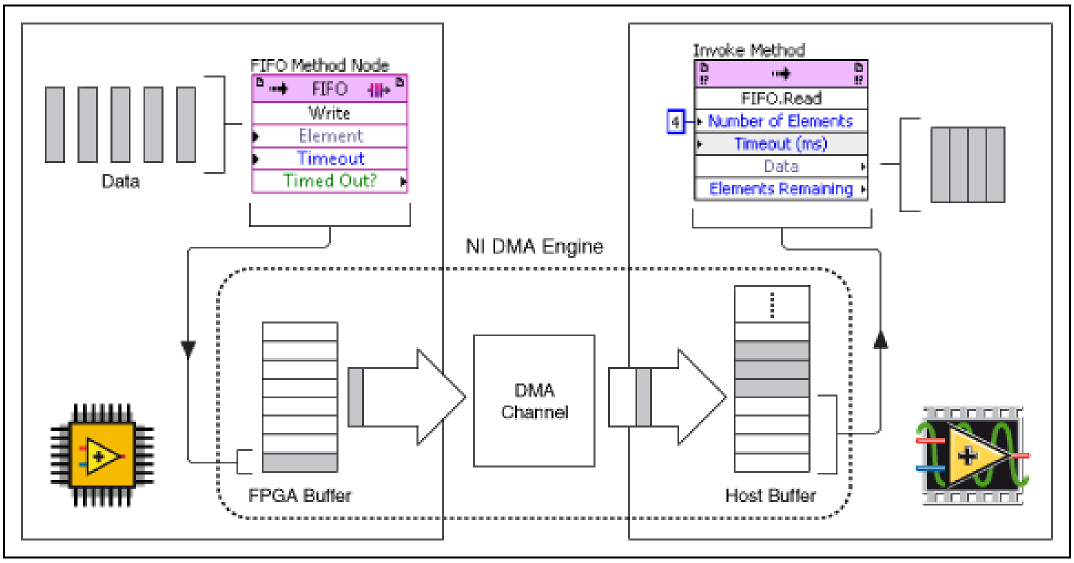

Figure 50: Workings of DMA Engine in LabView

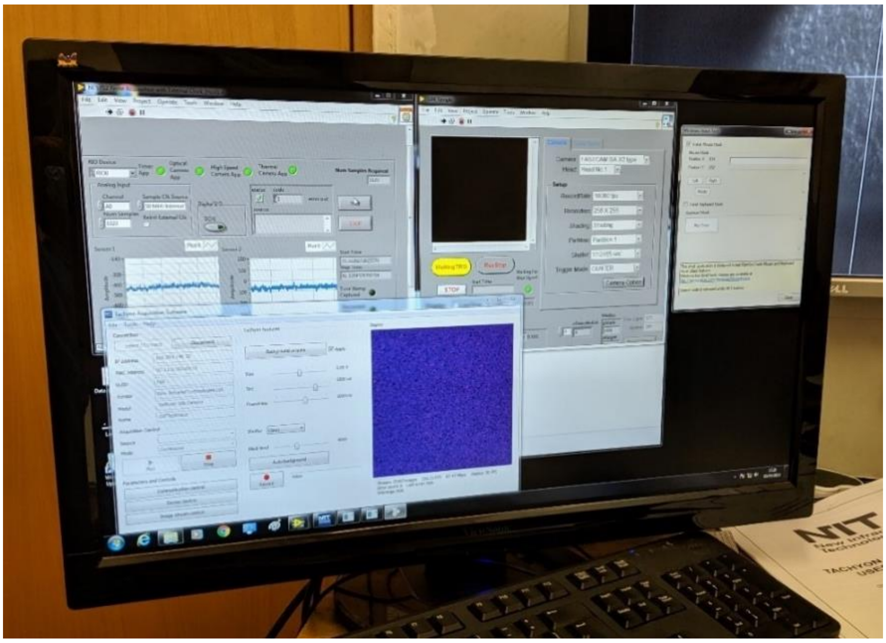

Figure 51: All Software Scripts during deposition

5.4. Discussion

This chapter explains in detail the system architecture which is a combination of hardware and software. The hardware includes the sensors and its accessories along with the actual acquisition hardware. To decide the frame rates which will allow sufficient information to be gathered that reveals the presence of defects a criterion is developed. This criterion establishes 3 values: best, average, and worst-case timing values for detecting certain deposition or defect properties. These properties include Particle velocity, Particle Residence time, Pore Generation Times, Temperature windows in which defects develop and cool down rates. Particle velocity which allows for the tracking of particles movements per 1mm. This is used as a precursor to detect the interaction of the powder particle with the melt pool. E.g., a particle which displays low intensity approaches the melt pool then interacts with it and causes a large spike in intensity in the melt pool. A spike as per the literature is a sudden very high temperature zone which has developed due to a disturbance in the heat flow cause by an anomaly. Hence if particles can be tracked their anomalous interactions can be tracked too. The second property based on which timing values are calculated is Particle residence time. The particle residence time is the time a particle spends on or in the melt pool before being melted. This once again is a window in which powder interaction with the melt pool occurs and from the literature, It is known that the longer the residence time the greater chance the particle will stay un-melted which causes defects to develop. Pore generation times are the time it takes for a pore to develop and as pores develop the heat flow in its surrounding is disturbed and hence it is vital for this window to be detected. Temperature windows in which a certain number of defects develop is also important to be observed. This is dependent of the total temperature window and the cooling rate with which the temperature window cools down. The literature also provides an approximate range in % of cracks developed in these windows. Lastly the cooling rates are used to calculate the time it takes for the melt pool temperature to change by 1°C. This means an increase or decrease in temperature can be detected with a precision of 1°C, this is of course depended on cooling rates. It is important to mention that temperature changes often do not increase until the defect is large enough to affect the heat flow and consequently to create high temperature zones.

It would be intuitive to choose sensor sampling rates that are based on the best-case timing of the five properties mentioned above however extremely high sampling rates bring unique challenges with them which include over exposure of image sensor, large data size, large dead bands and time stamping issues. To overcome this issue of over exposure in the HS camera the right combination of frame rate, aperture setting, Natural Density Filter and an illumination is chosen. Data size is managed by keeping resolution of images by 256 x 256 and data transfer rates are increased by using dual Gigabit ethernet capabilities of photron Fast Cam being used to capture high speed video. The noise in the thermal camera is lowered by reducing the sampling rate of the camera. It is important to mention that even though NIT tachyon 16K thermal camera is already being utilized in LMD monitoring in other projects its data transfer capabilities are limited to Cat 5 cables only. The AE outputs data continuously however due to the nature of how all data acquisition units work it can only be listened to for a certain time (40.96µs) and then the acquisition unit stops listening to complete the task of data storage or transfer and then it goes back to collecting samples. The main objective is to reduce the dead time by keeping the buffer size small (1024 data points) and using DMA engine. This decreases the overall time of dead time and a high sampling rate of the digitizer 50MSps further decreases the dead band.

The sampling rates are compared with the Best, Average and worst-case timing values and it is found that the sampling rates for the thermal camera and HS Camera are too low to capture the generation time for a single pore. However, this does not mean that both sensors are incapable of catching the effects of multiple pores all together. More so the HS speed camera is just shy of the worst-case pore generation times. Another major advantage of having a multisensory system is that AE sensor covers for blind spots of the other sensors i.e., it is fast enough to collect data faster than the best-case timing for pore generation.

Figure 52a shows the electromagnetic spectrum and the corresponding wavelengths. Figure 52b shows the spectral response with respect to wavelength with reference to temperature. Figure 52c shows the spectral response of the monochrome HS Camera. In between the HS camera and Thermal Camera, they cover a wavelength range of 0.4µm to 5µm however the spectral response varies. The HS camera shows highest response around 0.7um and these are the region where the melt pool temperature is up to (4726.85°C)5000K. This is good in the sense that extremely high temperature zones will show exceptional spectral radiance. Thermal IR camera covers 1µm to 5µm which show high spectral response over temperature regions from 226.85°C (500K) to 4726.85°C (5000K). These are all temperature regions where either defects are generated or where the effects of defect development are reflected in temperature changes and consequently spectral radiance.

It is worthwhile mentioning that the hardware architecture that was implemented is not the exact as is implementation of the general system architecture (Figure 26) but still uses the same general structure i.e. preprocessing units attached to sensor, sensor attached to post processing unit, post processing unit attached to Processing and acquisition unit, Processing and acquisition unit is attached to buffer memory and buffer memory is attached to high speed data bus which is connected to a PC (Figure 39). Ideally all these modules should have been fitted into a single chassis connected via a single full duplex data bus.

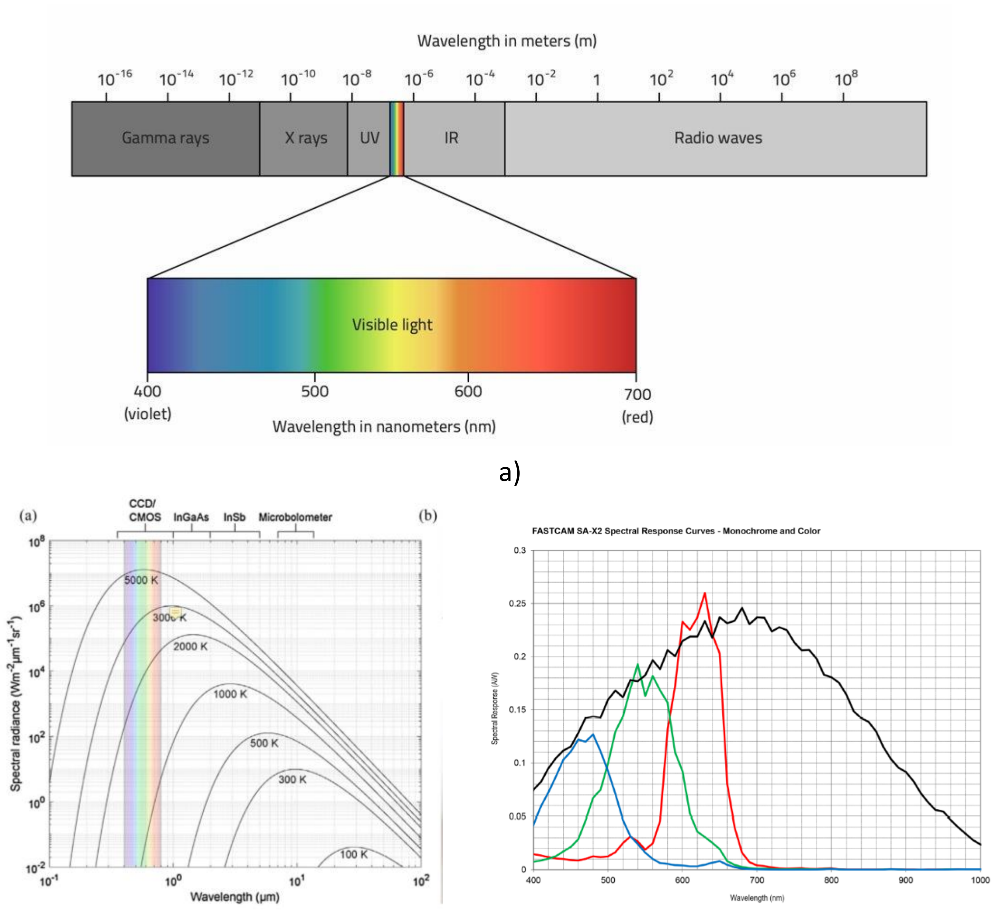

a)

b)

c)

Figure 52: a) Electromagnetic Spectrum b) Spectral Response c) Specteral Response Photron FASTCAM SA-X2

The software architecture is a conglomerate of scripts written in C# and LabView which are communicating with each other for triggering and time stamping purposes. These scripts include Thermal Camera Interface Script, Acquisition Script, HS Camera Script, AE Script, and Universal Timer script. Acquisition script turns on and off all sensors along with the Universal timer Script. The Universal timer uses a physical hardware timer which measures ticks at intervals of 330ns including the QPC register access time. This time is broadcasted to all scripts using a virtual port and UDP multicast ability. All scripts record start and stop time which can be used to sync data for all sensors.

Chapter 6: Experimentation

The experimentation chapter includes specific details and experimental design and experimentation. Here the defect provocation experiments their design are discussed in detail and along with that the details of the experimental setup and few calibration and configuration techniques are also discussed.

6.1. Defect Provocation Experiments

The main objectives of defect provocation experiments are to generate a variety of defects through different methods so that the system can be trained on a variety of signals. Four main types of defect provocation experiments are designed and carried out as shown in Table 13. The reason for the selection of these four experiments is that each provokes a specific type of pore or crack with varying quantities and sizes. Since their source mechanism varies, each type of defect should theoretically provide a slightly varied change in phenomenon which should produce a varied signal picked up by the sensors. Along with this the four types of provocation experiments should produce different sizes of defects. For example, the contaminated powder experiments should primarily produce gas pores and some lack of fusion pores, The surface finish experiment should produce cracks and pores due to lack of fusions specially in the bonding regions, the Machined deformities experiment should mainly produce cracks due to the sudden change in thermal distribution disrupting uniform heat flow and lastly, The Machine parameters experiments should produce both cracks and pores with varying quantity and size. The details of these experiments is explained in section 6.1.1, 6.1.2, 6.1.3, 6.1.4 and they leverage or adapt provocation methods discussed in Chapter 2.

Two types of powder are used for the experiments Ferrium S53 and TI 6Al 4V depending on the experiments. The work pieces upon which the deposit is laid down are rectangular blocks (150mm x 64mm x 40mm) made up of Titanium and Stainless steel (SS) depending on the experiment. Upon each block AE sensors are placed and fixed at a known distance from the center as shown in Figure 54. This allows for lateral distance measurements to be made from the AE sensors which are later used in TOF calculations. All depositions were made from left to right (facing the deposit) and all Deposits are mostly 3 tracks overlaid on each other with a 30% overlap with a Target measurement of 11mm by 2.5mm as shown in Figure 53. The reason why single-track deposits are not studied in these experiments is because 3 track deposits are a more realistic application of LMD since when using LMD to build a structure either tracks are overlapped or deposited on each other layer by layer. Defects may develop in remelting of previous tracks which is the point of the defect provocation experiments i.e., produce plenty of varying defects with different provocation methods to get a variety of signals.

In general, there is no need for a control experiment for each provocation experiment since defect provocation methods are very well established however, control experiments are still added to observe any contrasts. In the literature and Machine process settings for Contaminated Powder, Surface Finish Experiments are the same (Table 17) except for the Machine parameters experiments whose machine process parameter vary with each deposit as shown in (Table 14). Machined deformities are induced in the block by cutting a 1mm wide and 1mm deep grove (Figure 53) into the work piece upon which a deposit is laid.

	Title	**Brief Explanation**	**Work Piece**	**Control**	**Powder**
1	Contaminated Powder	Defects are induced using contaminated powder	Stainless Steel	Non-Contaminated Powder	Ferrium S53
2	Surface Finnish	Defects are induced by deposition on EDM finished surface	Titanium	Milled Surface	TI 6Al 4V
3	Machined Deformities	Defects are produced by depositing over Indented feature machined into the sample	Titanium	Non - Deformed Surface	TI 6Al 4V
4	Machine Parameters	Defects are induced varying machine parameters	Titanium	Optimum Machine Parameters	TI 6Al 4V

Table 13: Summary of Experiments

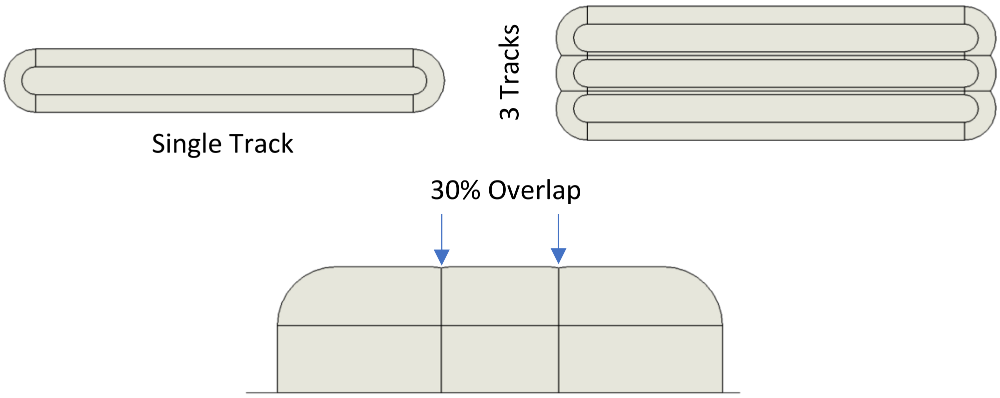

Figure 53: Deposition Tracks

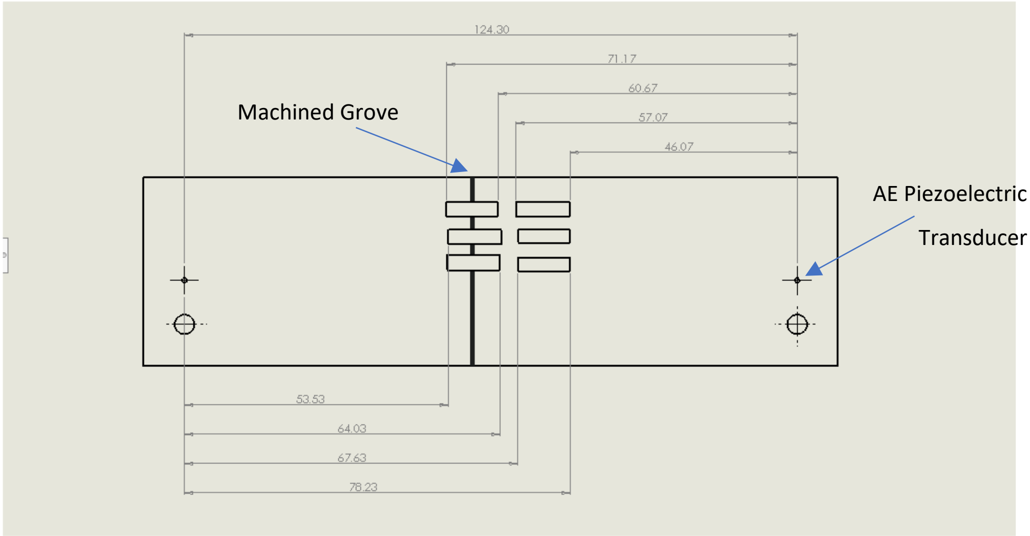

Figure 54: Deposition Diagram

6.1.1. Contaminated Powder Experiment

The objective of this experiment is to provoke gas and lack of fusion porosity in the deposition itself. It is established in the literature that impurities in the powders tend to induce these defects. A simple way of acquiring this contaminated powder or "dirty powder" is to collect unburnt/ un-melted powder from a previous deposition by ramping up the powder feed speed and lowering the laser power on the LMD machine. The un-melted powder is mixed with the pure "Virgin" powder and this mixture of powder is used to construct the deposition in this experiment.

The un-melted powder develops an oxide layer and in essence changing its chemical composition. This disrupts the melting process of the powder metal and in theory should increase residence time which causes powder particles to remain un-melted within the deposit which can cause defects to form. The change in chemical composition can cause further gases to be formed which may get trapped in the deposit.

As shown in Figure 55 the experiment only has one independent variable in the context of the experiment which is the contaminated powder. The dependent variables are the cracks and pores generated and constant independent variables are the machines process parameters. A total of 5 deposits are laid down with the contaminated powder experiment and 5 deposits are laid down using the virgin powder.

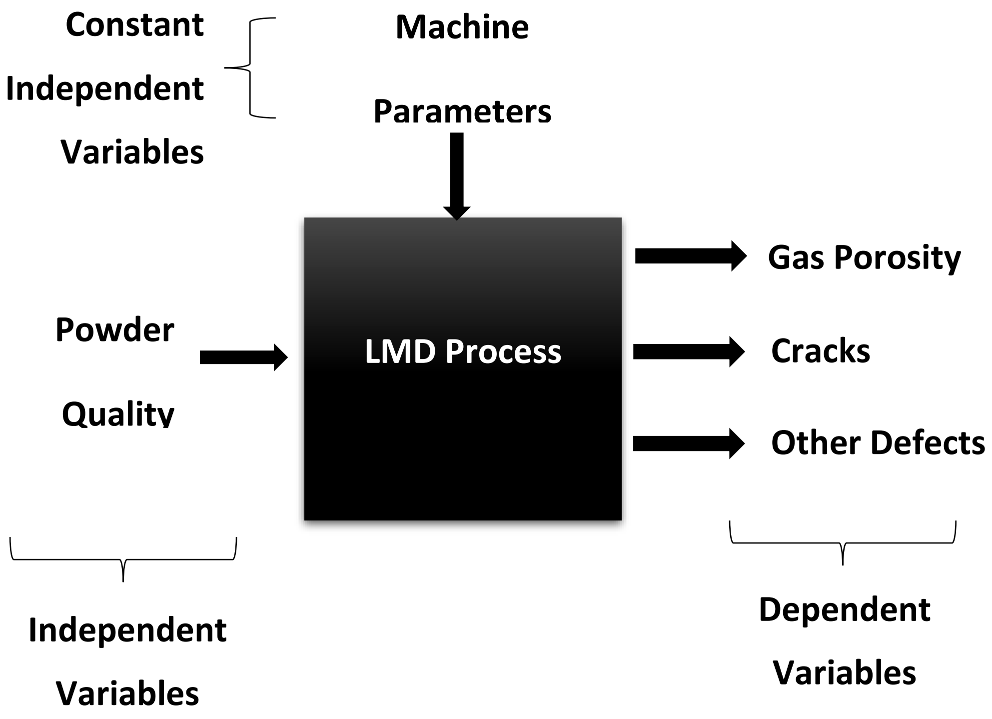

Figure 55: Contaminated Powder Experiment

6.1.2. Surface Finish Experiment

The objective of this experiment is to induce defects by depositing over a work piece whose surface is prepared using Wire Electrical discharge machining. Wire EDM surface becomes an ideal for producing defects due to two factors a) Poor surface finish can be achieved using certain process parameters b) A thin protective layer forms on the surface due to certain process parameters. In their investigation (Prathipati, 2019) shows that by manipulating pulse on time and peak current can change surface roughness and a thin protective layer consisting of carbides and oxides can be induced on the surface. These two properties make it an ideal breeding ground for defect development. This can be seen in Figure 56a where the surface finish of wire EDM is rough compared to that of the milled surface in Figure 56b. Even though these images are not obtained using a microscope rather XCT scan their scales are displayed on the images.

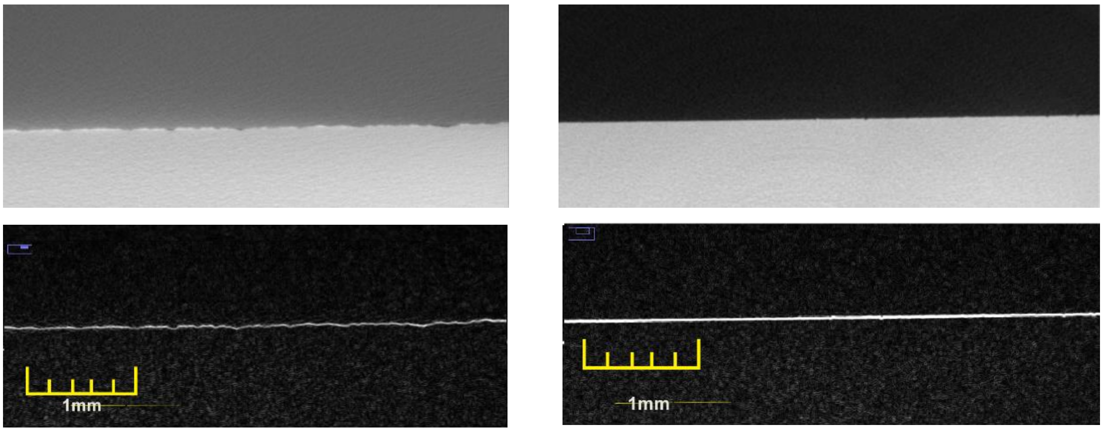

a) b)

Figure 56: a) Surface Finish EDM b) Surface Finish Milled

As shown in Figure 57 the experiment only has one independent variable in the context of the experiment which is the Surface Finish. The dependent variables are the cracks and pores generated and constant independent variables are the machines process parameters. A total of 3 deposits are laid down with the on the Wire EDM finish workpiece and 3 deposits are laid down on the milled surface work piece as this serves as the control.

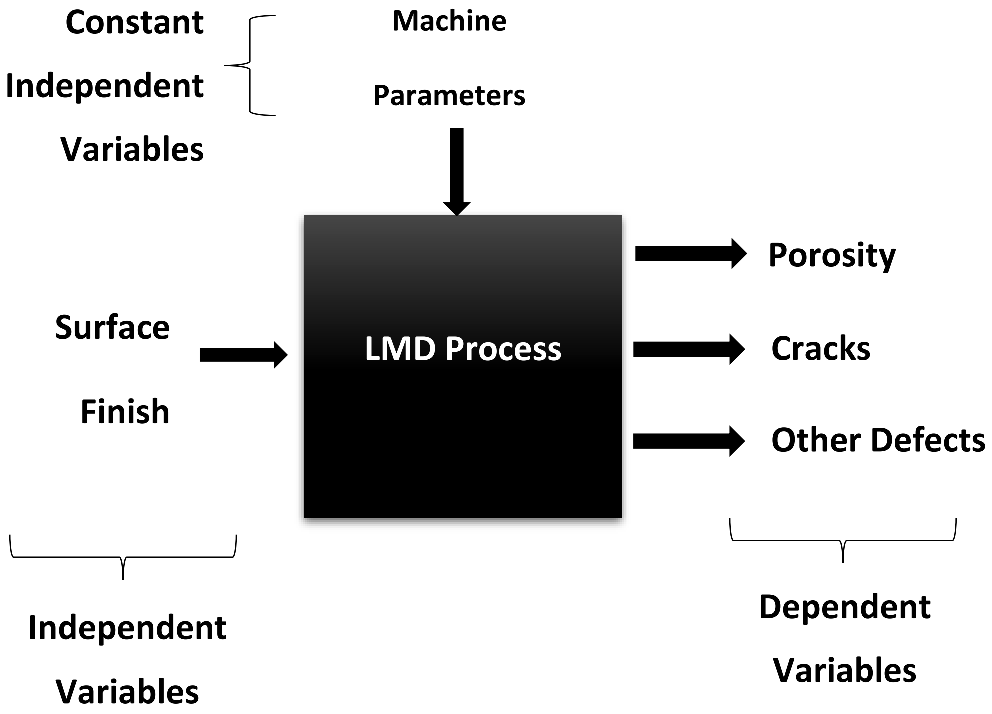

Figure 57: Surface Finish Experiment

6.1.3. Machine Deformities Experiment

Similar methods to (Barua & Frank Liou, 2014) are used to provoke and simulate cracks during the LMD process by introducing a physical feature on the workpiece itself upon which a deposition is made. As mentioned earlier this is 1mm width by 1mm depth slit machine on to the work piece. In this case the deposit is laid over both EDM workpiece and Milled Workpiece. Depositing over EDM in theory should produce more defects due to the nature of the EDM surface as explained above and the slit/grove upon which the deposit is laid.

As shown in Figure 58 the experiment only has one independent variable in the context of the experiment which is the Machine Deformities. The dependent variables are the cracks and pores generated and constant independent variables are the machines process parameters. A total of 3 deposits are laid down the on the Wire EDM finish workpiece and 3 deposits are laid down on the milled surface work piece.

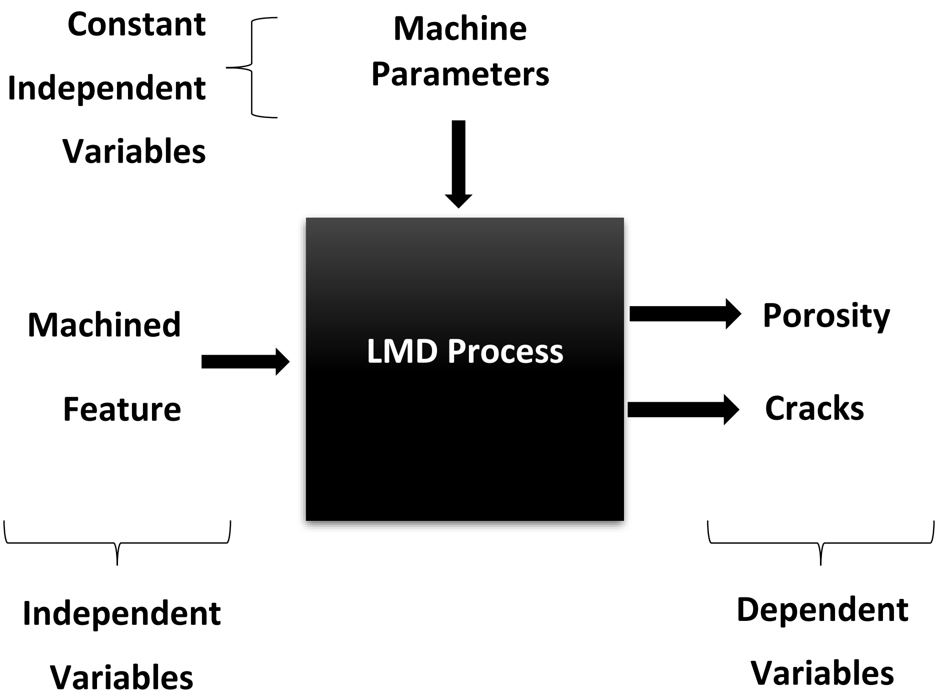

Figure 58: Machined Deformities

6.1.4. Machine Process Parameters

This experiment is carried out to provoke defects using machine process parameters which is well established in the literature. Even though by manipulating Laser Power, Powder Feed Rate, Scanning Speed, Shield Gas Rates defects can be generated, it is also true, any random combination will not generate a realistic deposit with specific dimensions. Too low a powder feed rate leads to a nonrealistic deposit which don't allow for sufficient build height and volume. It is known from the literature that a combination for a low powder feed rate and low laser power can cause defects to generate. As shown in Table 15 different combinations of powder feed rate and laser power is used until a sufficient volume is achieved which represents the target dimensions. The melt pool develops sufficient volume at 6.5% of the established powder feed rate and at Laser Power from 500 to 300W it is seen those deposits start developing defects (Figure 60).

As shown in Figure 59 the experiment only has two independent variables in the context of the experiment which is the Machine Process Parameters. The dependent variables are the cracks and pores generated and controlled independent variables are the Powder feed rate and laser power. The constant independent variables are powder Quality (Unused powder), Surface Finish (EDM cut work piece), Scanning Speed(10mm/sec) and Shield Gas Rate (41 lpm

@1.5bar). A Total of 13 deposits are laid down however only 5 pieces showed sufficient build volume that could be analyzed later.

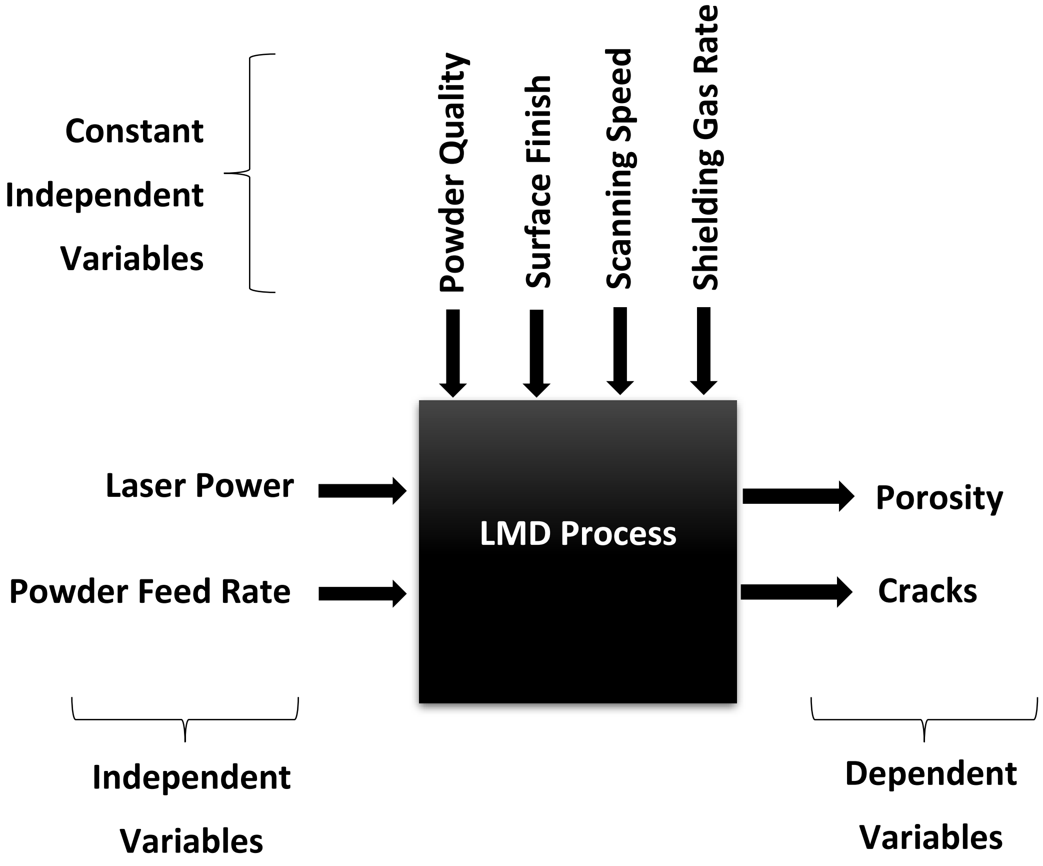

Figure 59: Influence of Machine Parameter

Laser Power	**Scanning Speed**	**Powder Feed rate** **10 lpm @2bar**	**Shielding Gas Rate**	**Nozzle standoff distance**
250 -550W	10mm/sec	4 -7.5%	41 lpm @1.5bar	12mm

Table 14: Machine Process Parameters

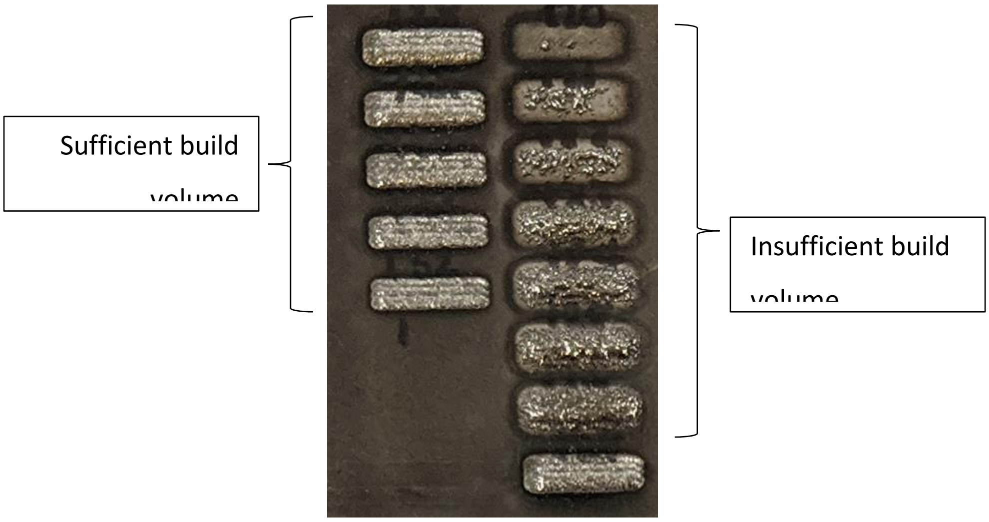

Figure 60:Powder Feed Rate and Laser Power Sample

#	Laser Power	Powder Feed rate (10 lpm @2bar)	Sufficient build height
1	250	4%	No
2	275	4%	No
3	300	4%	No
4	375	5%	No
5	425	5%	No
6	425	6%	No
7	425	7%	No
8	550	6.5%	No
9	500	6.5%	Yes
10	450	6.5%	Yes
11	400	6.5%	Yes
12	350	6.5%	Yes
13	300	6.5%	Yes

Table 15: Defect Provocation using Machine Parameters experimental Runs

6.2. Experimental Setup

As shown in Figure 61 the experimental setup is so that all cameras are at a certain distance from the deposition on a tripod at different levels. The Acoustic Emission sensors are attached at a known distance on both sides of the substrate block.

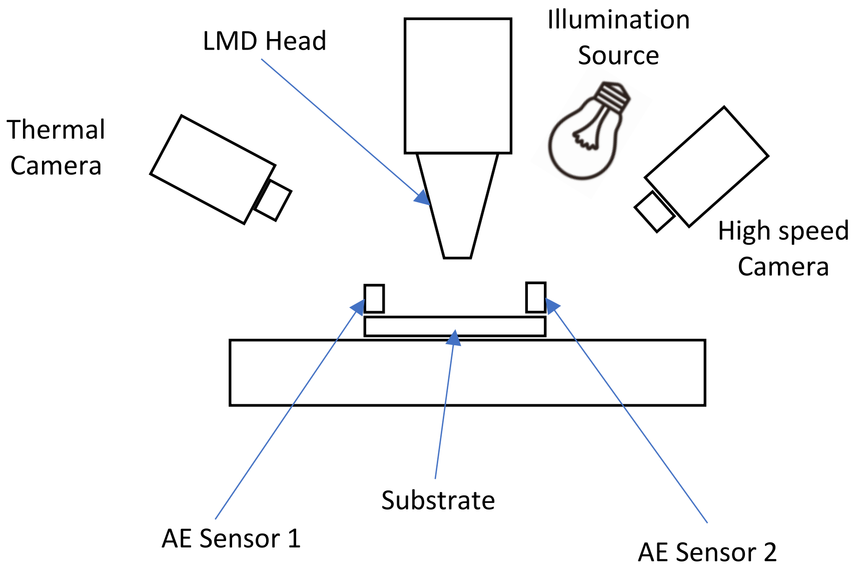

Figure 61: Experimental Setup diagram

The AE sensors are clamped on to the substrate using bolts after the coupling silicone gel is applied in between the AE piezoelectric sensor and the workpiece as shown in Figure 63. Cameras are focused on to the area where deposition is to be made using a technique where the actual target dimensions are drawn on a piece of paper and place on the work piece (Figure 62). This helps establish the position of where the deposit will be made using the internal optics LMD Machine along with allowing the researchers to establish sufficient focus and FOV that the entire deposit is captured during deposition. The Camera angles, positions and focus lengths are set based on hit and trial along with the distance of the illumination source (Figure 64).

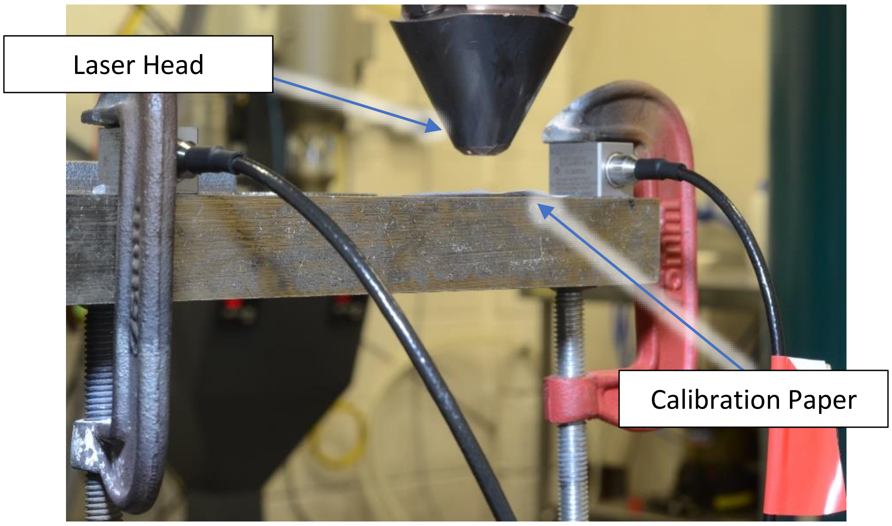

Figure 62: Calibration and Paper

Figure 63: (a) AE Clamping (b) LMD Head

Figure 64: Experimentation Setup

The substrate plates are first washed with water, dried, and then degreased with acetone. After this the plates are pre-heated before deposition begins. Along with the plates the powder is also preheated by setting the hopper jack temperature to 40ºC.

Since post analysis is being carried out by a XCT and the materials used are Titanium and Stainless Steel the pieces need be to cut up to a thickness of 2.5 mm to allow for XCT to image the piece with sufficient accuracy.

6.3. Discussion

As shown in Figure 65 four types of experiments are carried out to provoke defects. The defect provocation methods utilized different factors found in the literature that may cause defects to occur. Contaminated powder uses the change in chemical composition and oxide layers around the powder particles. The EDM surface finish takes advantage of the additive oxide layer and uneven surface finish which causes lack of fusion defects. Machined deformities take advantage of depositing over a machine groove upon which deposition is made. This causes lack of fusion on the sides of the deposit inside the groove. The last is the process parameters which are manipulated to provoke defects. Low powder feed rate and low laser power causes the powder to stay un-melted and causing the deposit too cool quickly causing pores to get trapped inside and cracks to develop. To find the ideal provocation parameters is not within the scope of this research and any conditions which may produce defects are utilized.

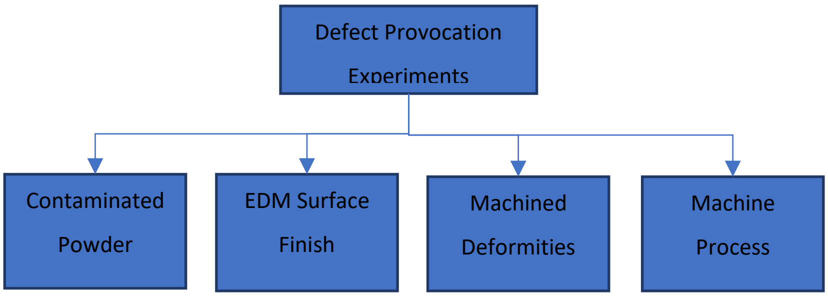

Figure 65: Defect Provocation Experiments

The experiment uses two AE sensors fixed onto the work piece on both side at known distance, so time of flight maybe used to calculate position of AE signal origin. In hindsight two sensors only take into consideration the horizontal distance and vertical distance from the deposits to the AE sensors is not measured. This may cause inaccuracies in calculating position however in the context of AE signal the position calculation is not important since other sensors cover for it. Thermal Camera and HS Camera are mounted on tripod and angled to view the deposition from a relatively safe distance. The distance of the cameras is based on whether the deposits are within FOV of the camera and are in Focus since a blurry image is not acceptable. This can be done by placing a paper with images of where the deposits will be laid down on the work piece. Using these images, the laser head is aligned and Camera angles, Camera distance, Camera focus and Illumination source distance is determined.

Figure 66 shows the block upon which depositions were made. Notice that there are a few single-track deposits in Figure 66c. This is because single track deposits do not yield sufficient defects and are also not practical since in real deposition applications layers are built over each other or at least with a certain % overlap in single layer coating applications.

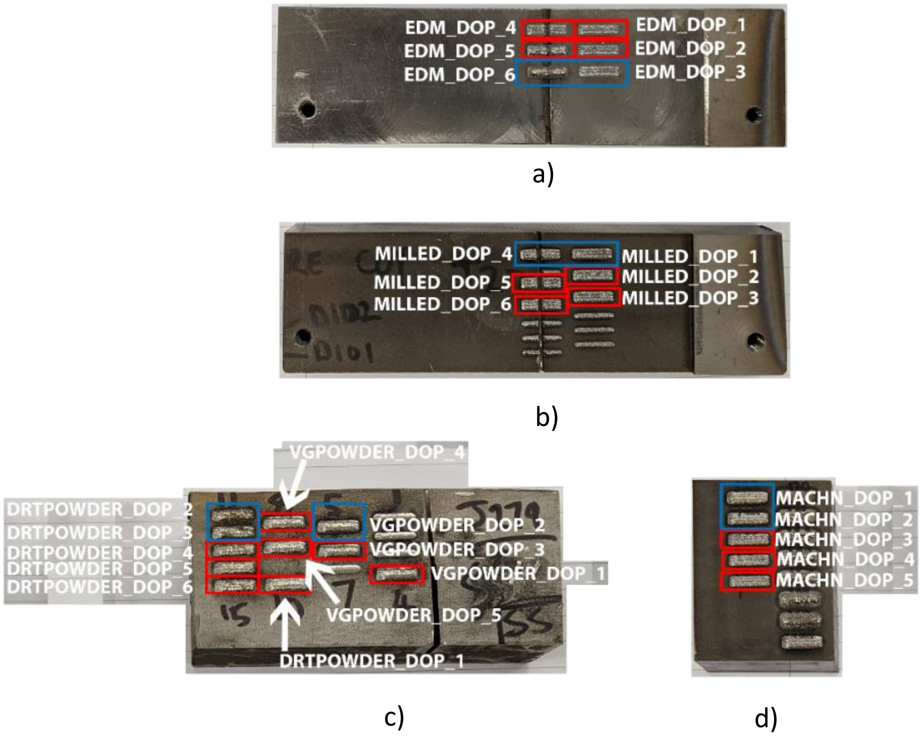

Figure 66: Work Piece with deposits

Figure 67 shows the deposited sample after they are cut up to be placed in the XCT machine to be scanned. The samples must be as thin as possible for accurate images to be extracted in which defects can be distinguished. Cutting pieces to such a thin thickness specially with materials like titanium is the special cutting tools required and if they are cut too thin, they start bending due to the heat. A solution is to cut them at lower speed and with sufficient cooling liquid. Due to this issue sample deposits were cut in a manner so that two may stay connected and are differentiated from within XCT images.

A valid discussion maybe why microscopic analysis was not carried out like other research since it provides a valid zoom scale and pixel to mm conversion is not required. However, to be observed under the microscope the piece needs to be cut up and observed at certain interval of depths underneath the microscope. The grinding process may cause further defects or cracks to develop due to residual stresses. The depth to which the pieces are grinded must also be selected carefully since some defects may be grinded away during that process.

Figure 67: Samples cut to thickness

Chapter 7: Data Analysis

This chapter discusses the details of the processing of the data collected from the experiments discussed in the previous chapter. The end goal of the data analysis chapter was to process the raw data and observe it in the *Time Domain* (Data w.r.t time) and *Spatial domain* (Data w.r.t the length of the deposit in the direction of deposition) using a custom data processing methodology as shown in Figure 68 to extract *Events* that will be used as inputs to the Clustering Algorithm. This is discussed in detail for each sensor and how each signal features from different sensors reveal about the defect that causes them.

Data is observed in Time Domain to observe the signals for each sensor in relation to deposition time. To sync the time of all three sensors 2 types of clocks are used: The internal clock of the sensor and the universal clock of the Data Acquisition System (DAQ).

Data observed in the Spatial Domain aims to see how data varies with the length of the deposit in the direction of the deposition. This can be calculated using *machine parameters* and the *physical measurements* of the sample itself. The machine parameters are the settings of the LMD machine and physical measurements are dimensions of the physical deposit taken using a Vernier Caliper.

The position of the defects relative to the deposit length in the direction of the deposition is calculated using from the X-ray Computed Tomography (XCT) of the samples from these experiments. The Defect position can also be calculated in the Time Domain using machine parameters.

The Defect data is stitched on to the processed Sensor data for each sensor. This stitched data allows for trends in the signals to be observed in relation to the defects in the Time and Spatial domain. Signal trends and features known as *Events* are then extracted from the Stitched Data and used in K means clustering analysis to identify Events with like features. The collective features for each cluster for each sensor are statistically analyzed and predicted feature value ranges are established with respect to clusters. The average of the 3 sensor’s predicted ranges is considered as the overall predicted feature Range. The *% Confidence* of the predicted value are established based on their Euclidian distance from their respective cluster centers. A *Confidence Score* for Sensor is added together to give the overall % Confidence.

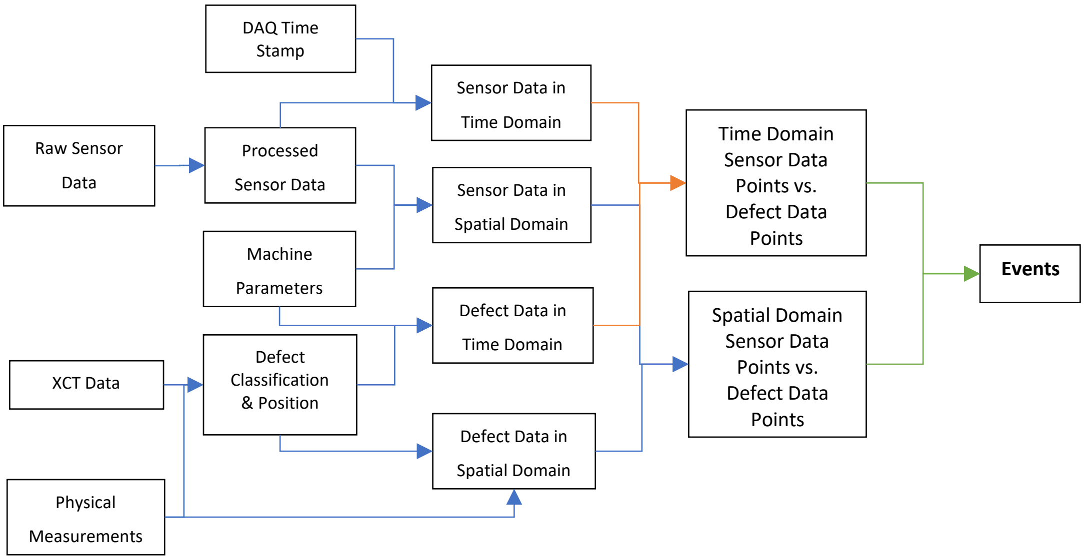

Figure 68: Data Processing and Event Extraction Method

7.1. Data Processing

Data the sensors is recorded in a raw format where the High-Speed Optical camera displays Gray Scale Images, the Thermal Camera outputs Thermal Images and the Acoustic Emission sensors output voltage signal in mV. All this data must be filtered and processed for it to be converted into a more useful format from which *Events* can be extracted which can be used as inputs for the clustering algorithm. There were multiple challenges that are faced when processing data for this PhD Thesis which include the Range of data types due to multiple sensors, loss of data during processing and the sheer amount of data due to high sampling rates for the sensors used. Table 16 contains the list of software used for data extraction and processing.

#	**Software**	**Operation**
1	MATLAB	Feature calculations, extraction, and Raw processing
2	MATLAB Signal Analyzer App	AE feature extraction and data processing
3	ImageJ	XCT, High Speed Optical and Thermal Image Processing
4	NIT Visualization Software	Thermal Data Processing and feature extraction

5	MATLAB Classification learner App	Clustering Analysis and Data fusion algorithm

Table 16: Software Used for Data Processing and Extraction

7.1.1. Machine Parameters

The machine parameters of the LMD (Laser Metal Deposition) deposition are not only essential in the scope of this PhD Thesis to provoke defects but also in the derivation of essential measurements and calculation of errors. Table 17 displays the machine parameters used in the 3 types of defect provocation experiments.

Provocation Method	Laser Power W	Scanning Speed mm/s	Nozzle Gas l/min	Carrier Gas l/min
Contaminated Powder	550	10	10	4
Surface Finish	850	10	10	4
Machined Deformities	850	10	10	4

Table 17: Laser Metal Deposition Machine Parameters

7.1.2. Physical Measurements

The deposits are physically measured using an electronic Vernier Caliper with resolution of 0.1mm and accuracy of $\pm 0.2mm$. As shown in Figure 69 a single deposit is comprised of 3 tracks with a 30% overlap. The length and width of each deposit is recorded for spatial calculations. The width taken of the deposit is the average of 3 points along the length. The first measurement is taken at 20% of the length, the second at 50% of the length and the third at 80% of the length for all samples. An average of all three width measurements is taken and this width is used for further calculations.

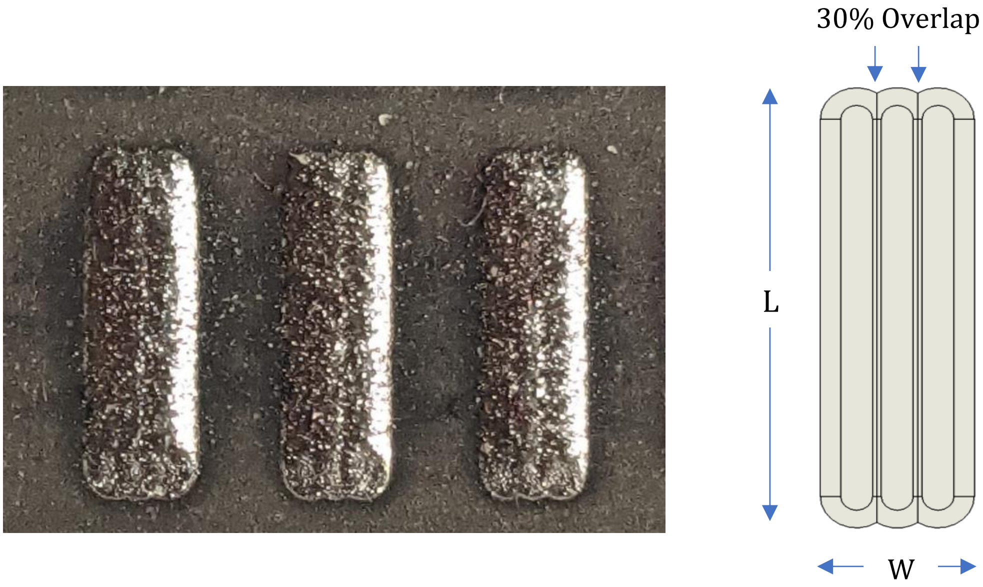

(a) (b)

Figure 69: (a) Deposited tracks (b) Measurements Diagram

7.1.3. X-Ray Computed Tomography (XCT) Data Analysis

As shown in Figure 70 (a) the sample to be tested is placed on a rotary stage and is rotated through a fixed angle step. At each Step, X-Rays are passed through the sample which are then caught at a Detector plate behind the sample also called the Matrix Detector. The Matrix Detector records these patterns as 2D radiographs. Using a reconstruction algorithm (Commonly known as *filtered back-projection*) the 2D radiographs are utilized to create a 3D data set consisting of horizontal reconstructed tomographic slices stacked together along the z axis in grey scale value as shown in Figure 70 (b). The XCT was carried out at the AMRL lab at the University of Strathclyde using a Nikon XT H 225 LC X-ray computed tomography system fitted with a Debeb CT 10kN cell. The XCT machine parameters used to carry out the XCT on the samples are given in Table 18.

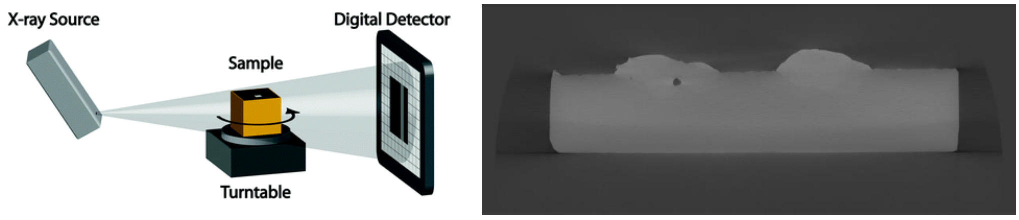

(a) (b)

Figure 70: (a) XCT Imaging method (Kastner J., 2018) (b) XCT Image Slice

Photon Energy (KV)	Exposure Time (S)	Image Resolution(pixels)	Voxel Size (mm)	Angular Step (Deg)
140KV	1415.00	2000x2000	0.00805779	0.1145882

Table 18: XCT Machine Parameters

7.1.3.1. Detected Defect Types

The defects identified in the XCT data slices are based on the Literature reviewed in Chapter 1. Even though many types of defects can be identified and classified as described in (ISO 13919-2, 2001), for the sake of simplicity in the scope of this research defects are classified as 3 types as shown in

Table 19.

Defect Group	**Criteria**	**Description**	**Measured Features**
Pores (Figure 71 (a))	1. Must be spherical. 2. Diameter must be significantly greater than voxel size(0.008mm)	All gas and lack of fusion pores are considered as pores.	1. Diameter 2. Projected Area
Crack (Figure 71 (b))	Identified based on EN ISO 13919-2 Standards criteria for cracks.	Defects that are shaped lines and have an area of less than 1mm^2 .	1. Avg Length 2. Avg Height 3. Projected Area
Other Defects (Figure 71 (c))	Voids, Crater Cracks, Shrinkage Cavity etc.	All other defects that do not come under the classification of Cracks of Pores are to	1. Avg Height 2. Avg Width 3. Projected Area

		be considered in this group.	

Table 19: Defect Classification Criterion

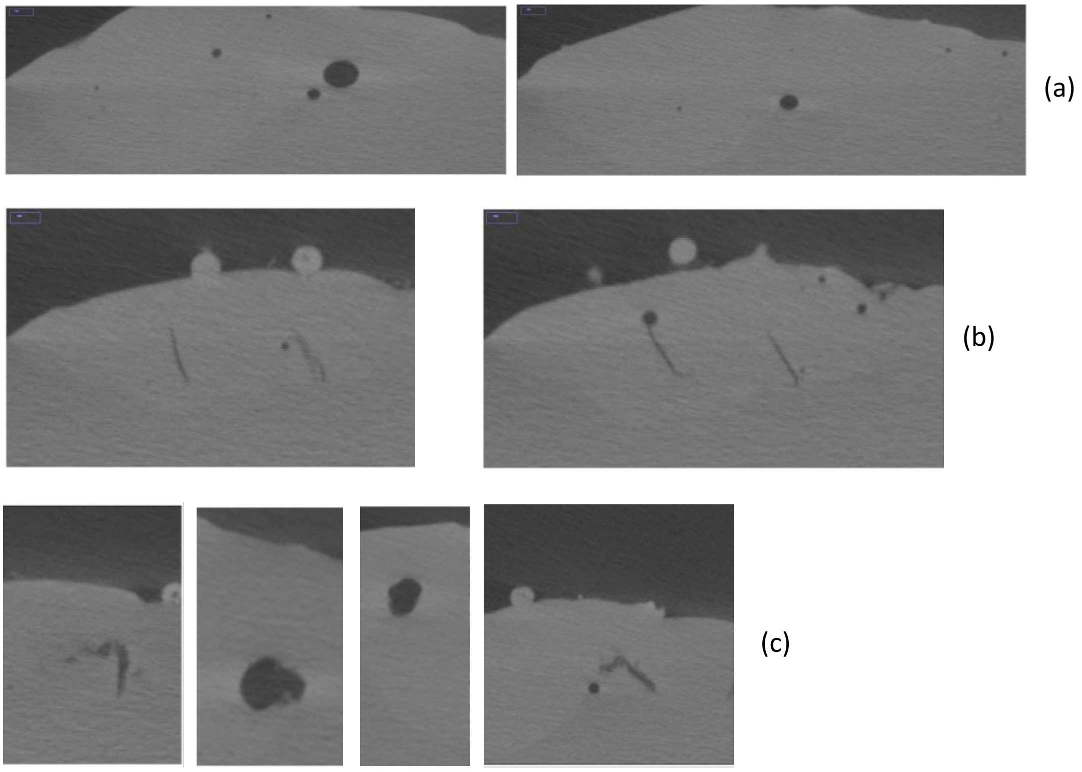

Figure 71: (a) Pores Identified in XCT Images (b) Cracks in XCT Images (c) Other Defects in XCT Images

Some of the Interesting facts determined by the research is defect propagation or how one defect begets other defects. The Literature in Chapter 1 does elaborate the study of crack propagation, but it does not mention 2 other phenomena observed in the XCT data; 1. Cracks can cause other pores (Figure 72 (a)), 2. Pores can cause other pores (Figure 72 (b)).

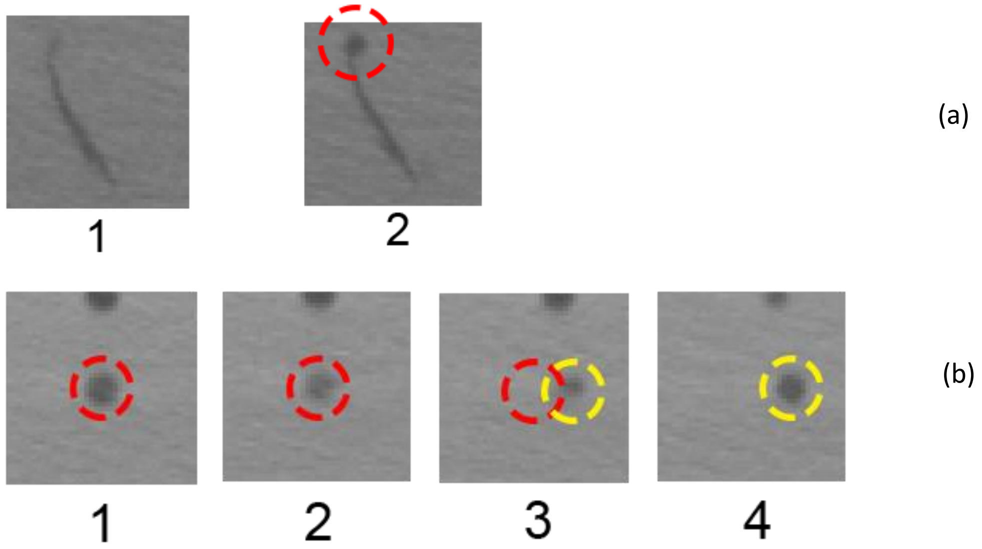

Figure 72: a) Cracks causing Pores b) Pores causing other pores

The following are the steps taken for the quantification of the defects and their features:

1. **Feature Recognition:** As shown in Figure 73 (a) the *Sobel edge detection* method is applied to the entire image sequence to outline features. This outlines all the defects and allows for defect types to be identified and measured.

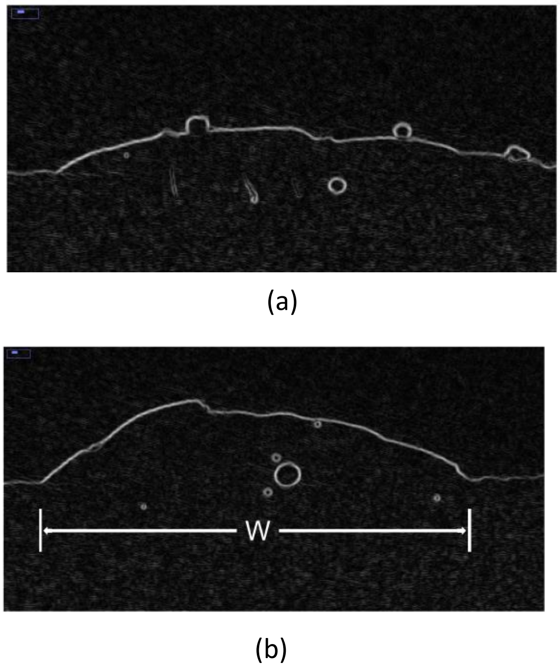

Figure 73: a) Edge Detection for feature recognition b) Deposit width measurement

2. **Identify Depth of each XCT Image Slice (Frame):** Manually Identify from the Images where the deposit starts and where it ends. Record the number of frames of the deposit and use the physical measurement of the deposit to calculate the depth of each frame in mm using the following equations:

$$F_T = F_E - F_S$$ (Equation 6: Total Length of the Deposition in frames)

$$D_F = \frac{l}{F_T}$$ (Equation 7: Depth each frame represents in mm)

$F_T = Total\ Number\ of\ Frames\ within\ the\ Deposition\ Length$

$F_S = Frame\ where\ the\ deposit\ starts$

$F_E = Frame\ of\ the\ deposit\ ends$

$D_F = Depth\ per\ frame\ in\ mm$

$l = Physically\ measure\ length\ of\ the\ deposit\ in\ mm$

3. **Establish measurement scale:** Defect features are measured from the XCT images, and their measurements are made in Pixels. To convert this to mm the measurement scale is calibrated using the physical measurement of the avg width of that deposit. As shown in Figure 73 (b) the width measured in pixels along with the physically measured width are used to calculate the length each pixel measures in mm.

4. **Identify all classifiable defects**: All defects are identified based on the criterion mentioned in Table 19 and sorted into groups.
5. **Measure Features:** Measure features for all identified defects are based on the criteria mentioned in Table 19 from the processed XCT images.
6. **Position of Defects w.r.t to deposition length:** For each defect, the frame at which the defect first appears (F_s) and the frame at which it disappears (F_E) is recorded. The origin point of this defect is considered the median frame (F_m) in between F_s and F_E . Using D_F from (Equation 7 the length at which the defects origin lies with respect to

the deposition length can be calculated. This length can be observed in Figure 75 as L_o. A fundamental assumption in this calculation is that the epicenter of all defects are their center points. This however may be true for most defects but in the cases of cracks this may not be true.

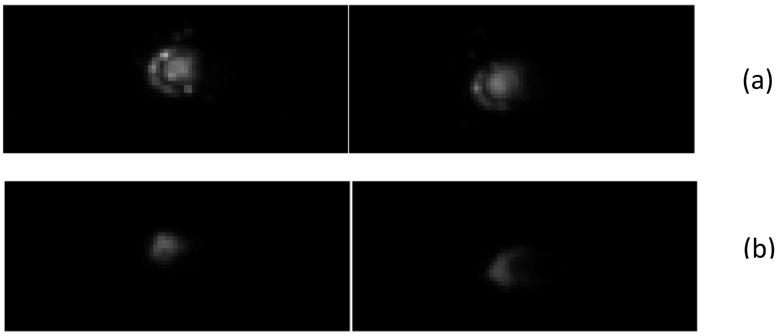

Figure 74: a) Laser On Images b) Laser Off Images

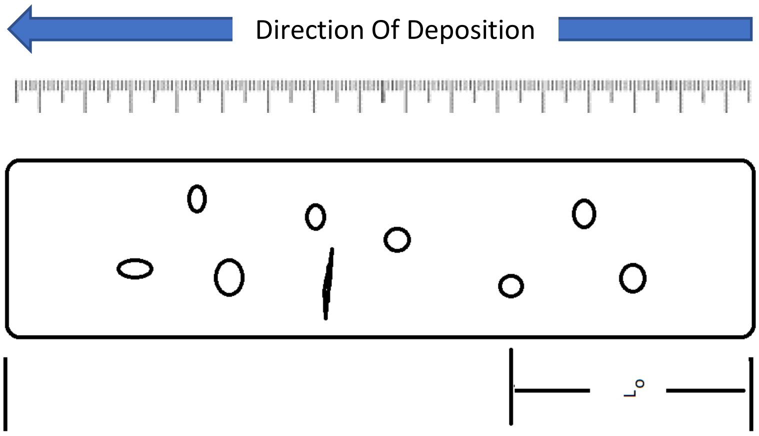

Figure 75: Defect Origin with respect to deposition length

7. **Calculate Defect position in time domain:** To calculate when the defect must have occurred during the deposition cycle the position of the defects are used along with the *Laser On* and *Laser Off* times detected using the High Speed Camera sensor and the Laser Scanning speed of the Laser Metal Deposition Machine mentioned in Table 17.

    a. **Total Laser On Time:** The Laser on and off time can best be identified from HS (High Speed) optical images as shown in Figure 74. When the laser is on it causes a circular dark ring feature to appear around the deposit and when the laser is turned off this ring feature disappears. (Equation 8 shows the calculation for total laser on time.

b. **Defect Time w.r.t Total Deposition time:** Using defect position, the time at which the defect appear during the deposition can be calculated using (Equation 9.

$$F_{Total\ On} = F_{OFF} - F_{ON}$$ (Equation 8: Total Laser On Frames)

$$Te_{On} = \frac{F_{Total\ On}}{HS_{FPS}}$$ (Equation 9: Experimentally calculated Total Laser On Time)

$F_{Total\ On} = Total\ Frames\ for\ which\ the\ laser\ is\ on$

$F_{OFF} = Frame\ at\ which\ the\ laser\ turns\ off$

$F_{ON} = Frame\ at\ which\ the\ laser\ turns\ on$

$Te_{ON} = Total\ Time\ for\ which\ the\ Laser\ is\ on$

$HS_{FPS} = High\ Speed\ Optical\ Sensor\ Frame\ Rate$

$$Tc_{On} = \frac{l}{V_l}$$ (Equation 10: Total Deposition Time)

$Tc_{ON} = Total\ Deposition\ Time$

$V_l = Laser\ Travel\ Speed$

$l = Physically\ measure\ length\ of\ the\ deposit\ in\ mm$

$$E = Tc_{ON} - Te_{ON}$$ (Equation 11: Error between Laser On Time Calculated

from HS Frames and Laser
On Time calculated from
Laser Scan Speed)

$E = Calculated\ Error\ in\ Time$

$$D_t = \frac{D_p \times Te_{ON}}{l}$$ (Equation 12: Defect Position in Time Domain)

$D_p = Position\ of\ Defect\ relative\ to\ deposition\ length\ in\ mm$

$D_t = Time\ of\ Defect\ relative\ to\ total\ deposition\ time\ in\ s$

$Te_{ON} = Total\ Time\ for\ which\ the\ Laser\ is\ on$

$l = Physically\ measure\ length\ of\ the\ deposit\ in\ mm$

Figure 76 show the Defect Size vs Defect Position relative to the deposit in the direction of the deposition while Figure 77 shows The Defect Size vs time during the deposition when they were generated. The graphs allow for further extraction of two more important bits of information; a). How closely these defects are packed together over a specific length; b). The type of defects along with the time at which they were generated during the deposition. These later become important when the signal data is overlayed on to these graphs to correlate what the effect of the above-mentioned parameters have on the signal data.

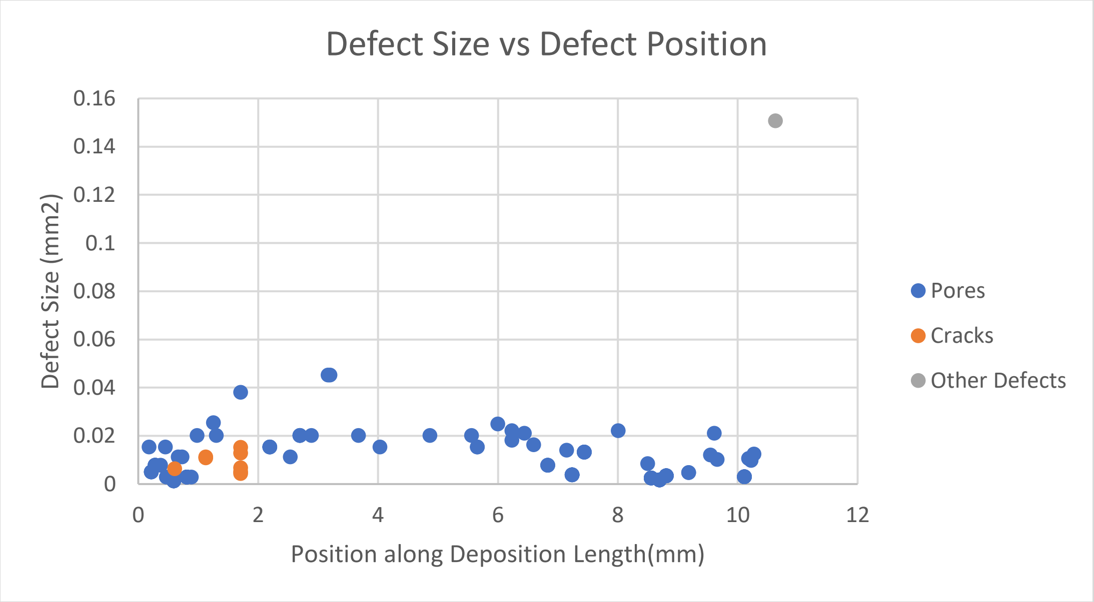

Figure 76: Defect Type and Size Spatial Domain

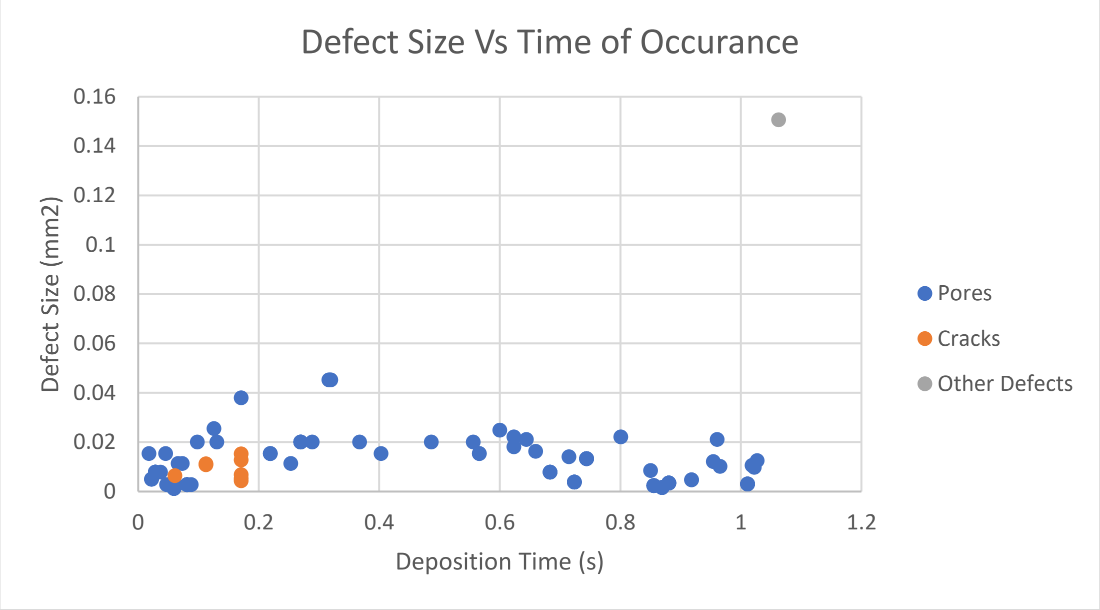

Figure 77: Defect Size and Type in Time Domain

Table 20 shows some of the basic statistics of the types of defects found in the samples for all 3 defect provocation methods. This also might give an insight on the effect provocation techniques have on the Size of the defects. Largest Pore and Crack are seen with provocation technique of Surface Finish. The most consistency in the size of Pores can be found in Contaminated Powder provocation technique and for cracks it would be Machined Deformities technique. All techniques utilized to provoke defects agree with the literature and were successful at creating sufficient amounts and variety of defects.

Provocation Method	**Stats**	**Contaminated Powder (mm)**	**Surface Finish (mm)**	**Machined Deformities (mm)**
Pores	Average	0.009866	0.025283	0.011927
	Max	0.045239	0.693978	0.237583
	Min	0.001257	0.000314	0.000127
	StdDev	0.009866	0.025283	0.034464
Cracks	Average	0.0091	0.008183	0.006138

	Max	0.0152	0.0189	0.008526
	Min	0.0044	0.003225	0.003525
	StdDev	0.0091	0.008183	0.002066
Other	Average	0.150674	0.02279	0.143398
	Max	0.150674	0.056019	0.7462
	Min	0.150674	0.004761	0.004428
	StdDev	0.150674	0.02279	0.297043

Table 20: Defect Size Statistic

7.1.4. High Speed Optical Sensor Data Processing & Feature Extraction

High Speed Data Images were captured 256 by 256 in 8-bit gray scale images. These images capture the light intensity from the melt pool in other words it captures the Incandescence of the melt pool. As the temperature of the of the melt pool increases its spectral radiance also increases. The value of each pixel is linearly related to the intensity of light received by the sensor (Barua & Frank Liou, 2014). When a defect is created it changes the thermal conductivity at the point due to which heat dissipation is disturbed hence increasing the temperature and radiation at that point. By the image sensor this is registered as a single or group of high intensity cluster of pixels as shown in Figure 78.

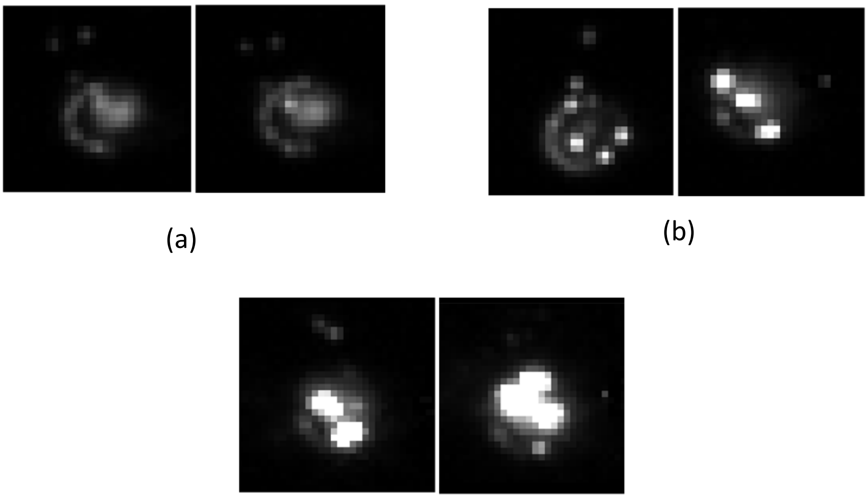
(a)
(b)
(c)

Figure 78: a) Stable Melt pool b) Segregated Small Events c) Big Event.

From the HS image data, two types of phenomena are observed; groups of merged high intensity pixels (Figure 78 (c)) and then groups of segregated high intensity pixels (Figure 78 (b)) are observed which pop up from time to time. In the scope of this research these will be called *Events*. The generation of these Events can often be seen when powder particles are absorbed into the melt pool (Figure 79 (a)) or when a powder particle is rejected from the melt pool (Figure 79 (b)). It is also seen that smaller events can merge or grow into bigger events (Figure 78 (c)). Sometimes powder particles are absorbed into the melt pool without causing an event; This is called a *clean fuse (*Figure 79 *(c))*. It should also be mentioned some of the high intensity reflection received from the melt pool at the start of the deposition is due to the angle between the melt pool and the Optical sensor itself. At times of light captured by the image is also due directional emittance phenomenon mentioned by (Robert Sampson, 2020).

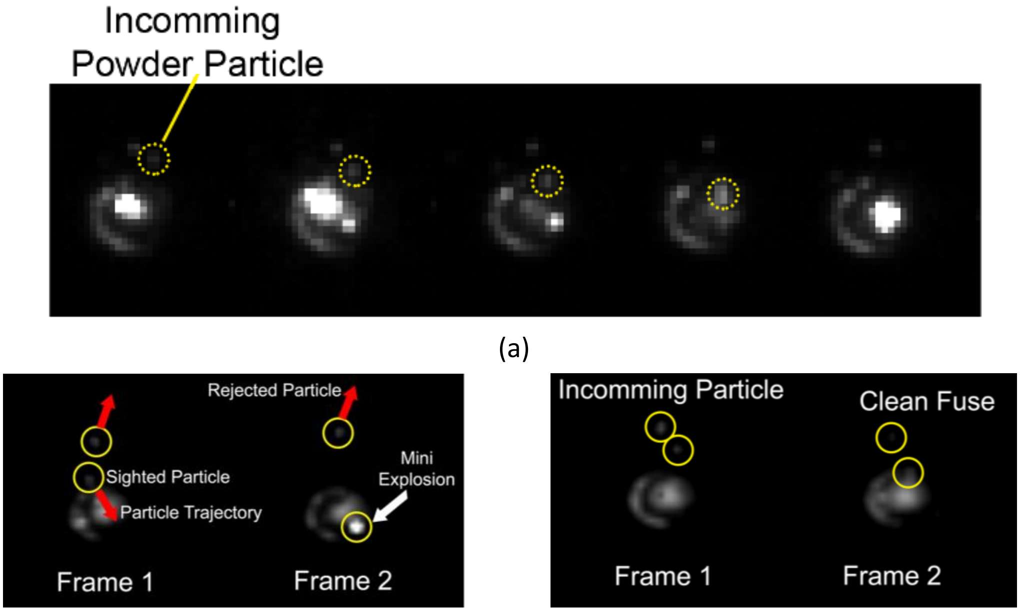

(a)

(b)

(c)

Figure 79: a) Powder Impact Event, b) Powder Particle Rejection, c) Powder Particle Clean Fuse

The following are the methods used to process these images into useful data:

1. **Thresholding:** To extract useful data from these images a threshold value for stable melt pool must be first established. This can be done by extracting stable melt pool images (Figure 78 (a)) from the entire sample and taking its maximum value for each sample and then taking the avg of that set. A *stable melt pool* in the context of the HS Optical Images of the melt pool is an image with no high intensity pixels or pixel groups. Since this is an 8-bit image each pixel can represent an intensity from 0 -255. The threshold of each sample is usually the same (102).
2. **Z projection:** Melt pool images are overlayed for each track using a method called Z projection. Since the objective is to only find the high intensity pixels and specially at points on the image where high Intensity pixels re-appear, the Summation method of Z projection is implemented as shown in Figure 80 (a).

3. **Angle Correction:** The deposition is at a certain angle to the Optical Sensor. To profile the Z projected image correctly, the image must be made parallel to the viewing plane as shown in Figure 80 b.
4. **Sharpening Filter**: A Sharpening Filter is then applied to the image (Figure 80 c) so that regions with high intensity pixels are highlighted further. This filter uses a 3 by 3 spatial convolutions where each pixel is replaced by a weighted average of its neighbors within this spatial matrix. (Equation 13 shows the 3x3 Weighing factors for the sharpening filter.

$$\begin{matrix} -1 & -1 & -1 \\ -1 & 12 & -1 \\ -1 & -1 & -1 \end{matrix}$$

(Equation 13: Weighted Average Coefficient Matrix)

5. **ROI Isolation:** A ROI (*Region of Interest)* is established around the deposit to isolate the track from the environment as shown in Figure 80 d.

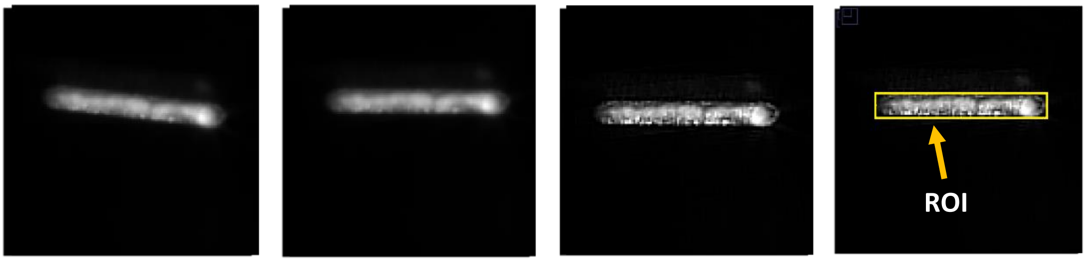

(a) (b) (c) (d)

Figure 80: a) Z Projection b) Angle Correction c) Image Sharpening d) ROI

6. **Set Spatial Scale:** To convert from measurements from pixels to mm the measured physical length of the deposit is used to set the scale to convert measurement from pixels to mm.
7. **Surface Profile:** A 3D surface plot is generated (Figure 81 (a)) which enables the visualization of the high intensity pockets along the length and width of the deposit. This further reinforces the hypothesis that high intensity areas only form around defected regions.
8. **Profile Plot:** For the simplification of data processing since the end goal is data fusion, a profile plot is generated (Figure 81 (b)) which basically averages each column

in the width direction in the ROI. This does however introduce the probability of losing data of isolate single events.

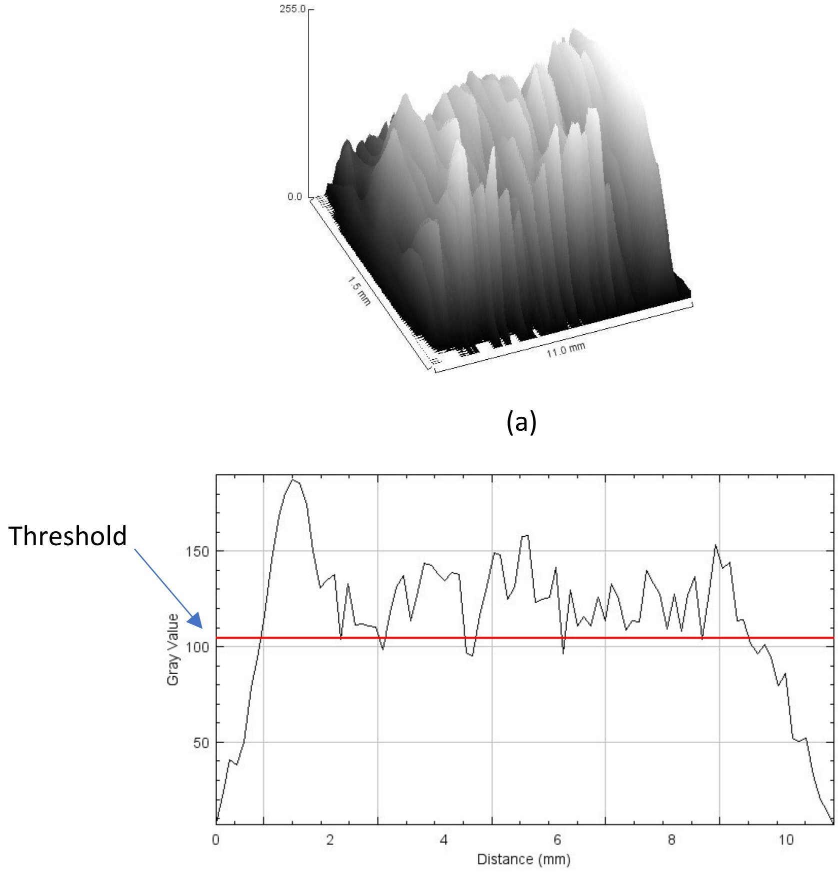

(a)

(b)

Figure 81: a) 3D Surface Intensity Plot b) 2D Intensity Profile Plot

The profile graph for each track is then overlayed on the same graph as defect size in both time (Figure 83) and spatial domain (Figure 82). This will now allow for the extraction of useful data in relation to the defects which will be called Events which will serve as input for the clustering algorithm. The intensity values considered are the ones above the set threshold value. Table 21 shows the features extracted from the graphs above for every 2mm of deposition length.

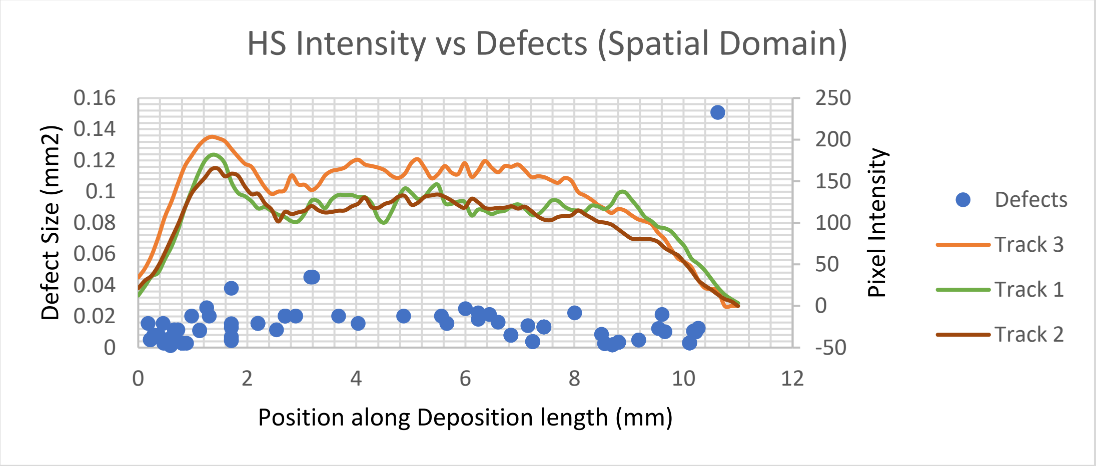

Figure 82: HS data stitched onto Defect data in Spatial Domain

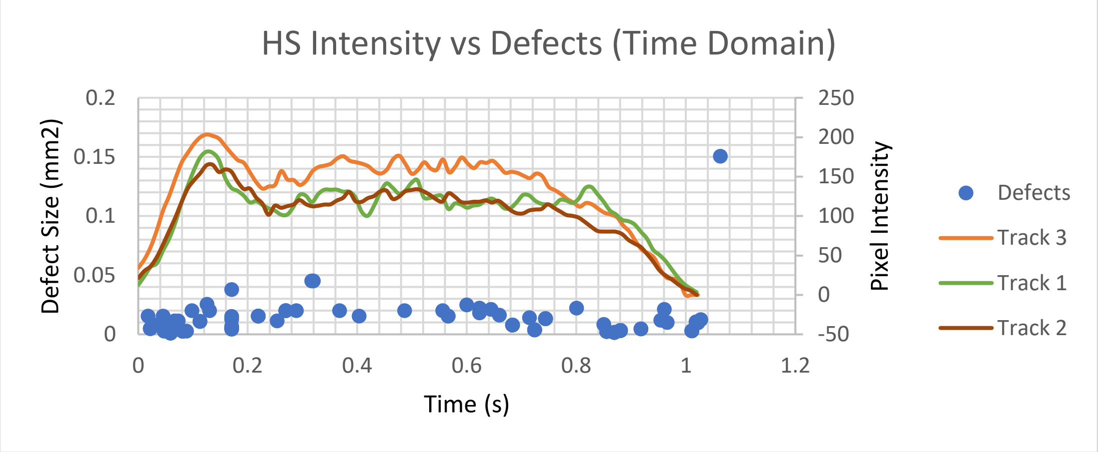

Figure 83: HS Data stitched on to Defect data in Time Domain

	Feature	**Explanation**	**Extraction Source**
1	Max Intensity	Over 2mm of deposition length the max Intensity observed.	Spatial Domain
2	Intensity Spike Frequency	Over 2mm, the frequency of Intensity spike is observed. An intensity spike here is defined as a change in intensity whose total duration is less than 0.05s.	Time Domain
3	Total Number of pores	Total number of Pores within this 2 mm of length	Spatial Domain

4	Total Number of cracks	Total number of Cracks within this 2 mm of length	Spatial Domain
5	Total Defected Area	The sum of projected area of all the defects within this area.	Spatial Domain
6	Max Defect Size	Max size of defect detected within in this area.	Spatial Domain
7	Defect Spatial Density	This is the measure of how closely packed the defects are to each other within this area. This is the variance of the defect position within the area and is hence a dimensionless value.	Spatial Domain

Table 21: HS Data Event Feature Extraction

7.1.5. Thermal Sensor Data Processing & Feature Extraction

The thermal camera captures 8 Bit, 128 x 128 Thermal Intensity images at 1000 Frames per second as shown in Figure 84 a. As explained by (Barua & Frank Liou, 2014) and (Ulf Hassler, 2016) in thermal cameras the cooling rates and intensity are affected in regions where defects are formed. Since the thermal camera picks up IR and the thermal conductivity is disturbed when a defect is generated the temperature fluctuations in this region increases along with how quickly and uniformly the melt pool cools.

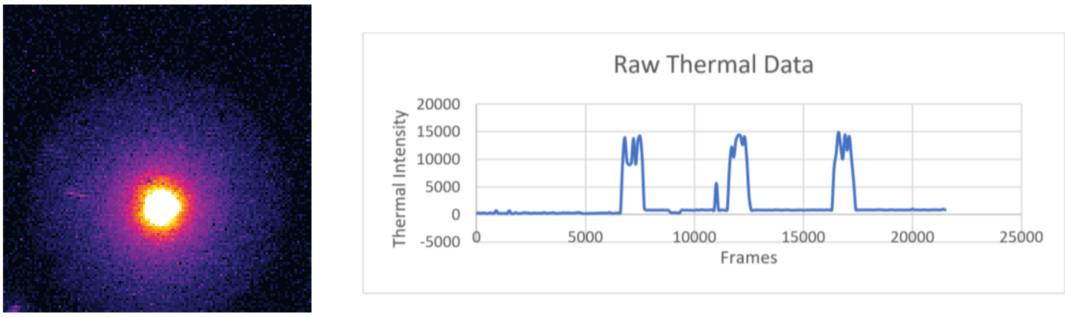

Figure 84: a) Raw Thermal Image b) Raw Thermal Profile

In the following are the steps taken to convert the thermal Data Images into useful data from which signal features can be extracted:

Calculate Thermal Data points in Spatial Domain: In this specific case the thermal data is time stamped by two sources; The DAQ Universal Time stamp and the calculated time stamp stitched into the Thermal Data Image Frames.

Identifying Track Specific Data: Thermal data captures a continuous data during the deposition of all 3 tracks as shown in Figure 84 b. The thermal Intensities observed during the deposition can be clearly distinguished from the track is not being deposited since the values cross a threshold value. At the average threshold value in all samples and tracks is 58.94. Thermal data for each track is extracted based on when the min threshold was crossed and when the amplitude falls back below the threshold. This threshold value is to isolate thermal intensities for a single track during the deposition of multiple tracks and is not to be confused with the thresholding value to extract events.

Track Deposition Time: Total Data Frames for each track can be established using (Equation 14 were the frame in which the amplitude drops below threshold is subtracted by the start frame at which the threshold amplitude was crossed. Using the cameras Hardware sampling frame rate, the collective total time for the deposition of the track is calculated as shown in (Equation 15.

$$TF_{Total} = TF_{End} - TF_{Start}$$

(Equation 14: Total Frames for the deposition of a single track)

$TF_{Start} = Frame\ atwhich\ Thermal\ amplitude\ first\ crosses\ threshold$

$TF_{End} = Frame\ at\ which\ Thermal\ amplitude\ falls\ below\ threshold$

$TF_{Total} = Total\ frames\ for\ the\ deposition\ of\ a\ single\ track$

$$Tt_{Total} = \frac{TF_{Total}}{T_{FPS}}$$

(Equation 15: Total Deposition time for a single Track)

$Tt_{Total} = Total\ Time\ for\ the\ deposition\ of\ a\ single\ track$

$T_{FPS} = Thermal\ Camera\ sampling\ rate$

Thermal Data in spatial domain: The Thermal Data points are converted into spatial domain i.e., position of data points along the deposition length by using the physically measured length. The thermal data points are interpolated over the entire physically measured length of the deposit. This can however reduce the accuracy of thermal data point in the Spatial Domain, but it is better than the method used in HS data processing where Data Images are used to determine deposition length. The reason the former method being more accurate is because the thermal image captures ambient temperatures of the region around the track as well as shown in Figure 84 a. Hence it becomes near impossible to distinguish temperature regions that lie within the boundaries of the track itself as a result this will skew any spatial measurement taken from the Thermal Data Image.

This data is then overlayed on to the defect data to stich the two data sets together in Time (Figure 86)and Spatial domain (Figure 87). Using this stitched data, certain anomalous trends can be identified, and key features are extracted from these Events.

From the thermal data it is known from Figure 86 that in the defected regions the cooling rates and temperature amplitude rise very quickly. It is also observed that in non-defected depositions temperatures are relatively stable as shown in Figure 85. Hence for the thermal data set, the sudden change in amplitude greater than 10^3 $\mathrm{Thermal\ Intesity/s}$ followed by a dip in temperature gradient is considered an event and the Table 22 shows the features extracted for each event.

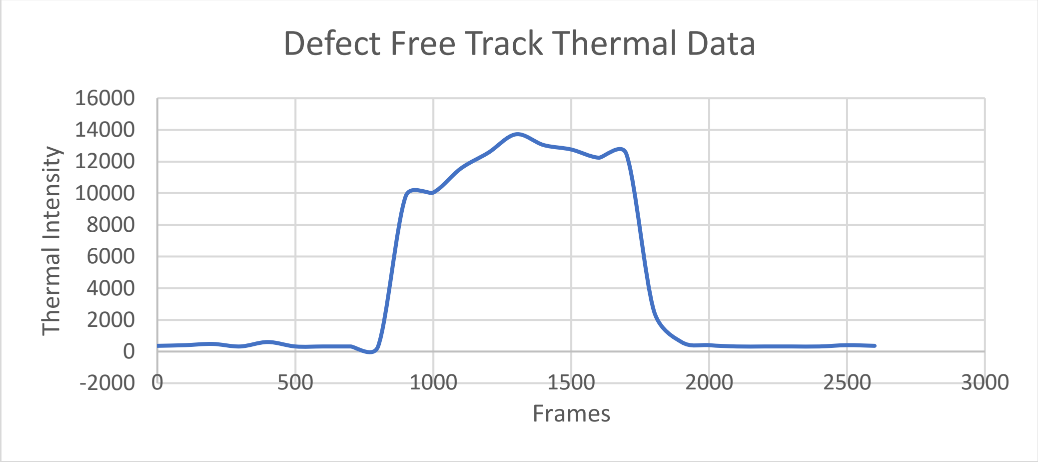

Figure 85: Raw Data for a defect free deposition Track

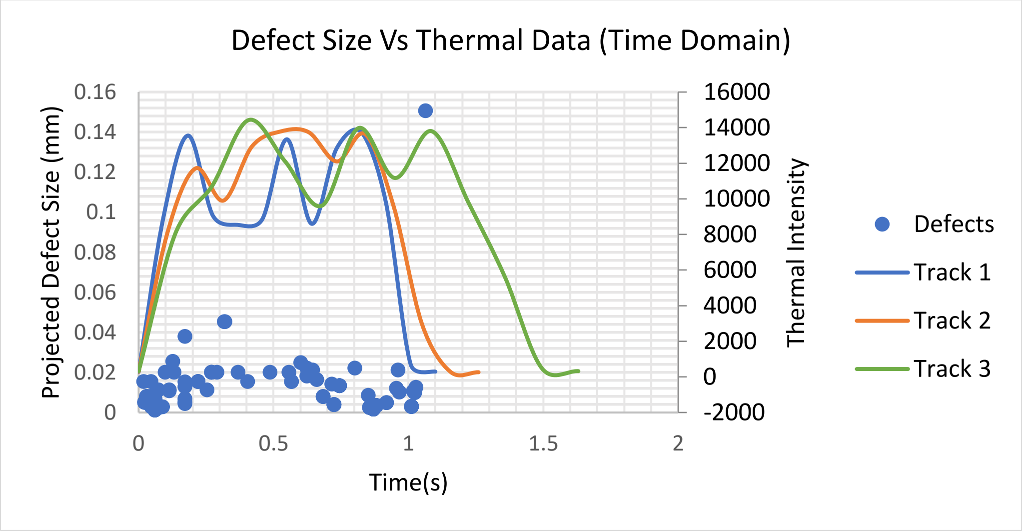

Figure 86: Thermal Data in Time Domain

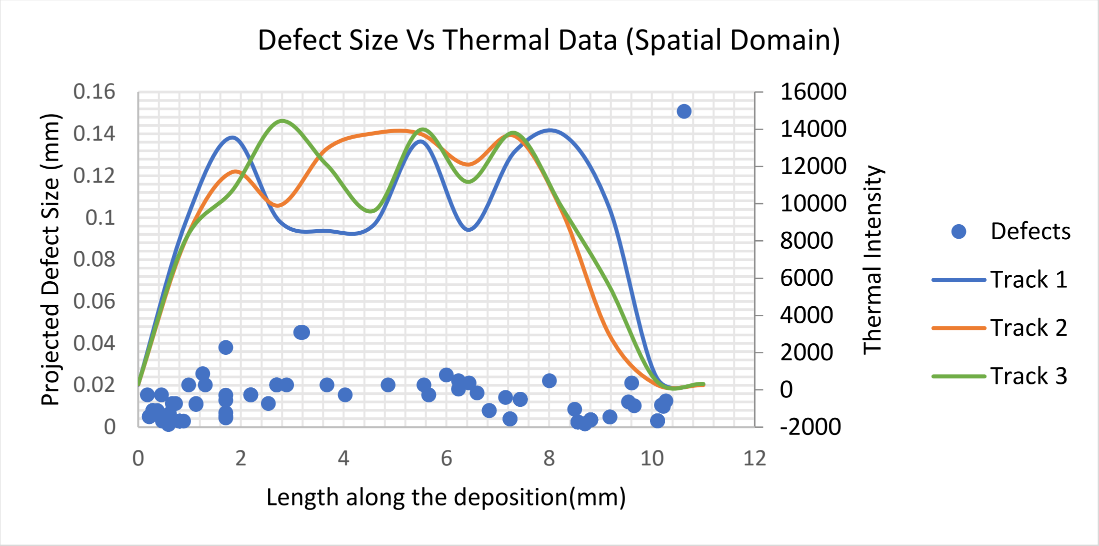

Figure 87: Thermal Data in Spatial Domain

#	Feature	Explanation	Extraction Source
1	Length	This is length in mm of this event with respect to the length of deposition Track.	Spatial Domain
2	Duration	This is the time the event crosses threshold and falls back below it.	Time Domain
3	Rise Time	The time it takes for the event to reach max amplitude	Time Domain
4	Fall Time	Time taken for the event to drop down below threshold from max amplitude	Time Domain
5	Heating Rate	The thermal gradient of the part of the event to reach max amplitude	Time Domain
6	Cooling Rate	The Thermal gradient of the part for the event to reach min amplitude	Time Domain
7	Peak Amplitude	Maximum amplitude of this event	Time Domain
8	Avg Amplitude	Average amplitude of the entire event	Time Domain
9	Standard Deviation	This determines the variation of temperature in the event around its avg temperature.	Time Domain

3	Total Number of pores	Total number of Pores within this event	Time Domain
4	Total Number of cracks	Total number of Cracks within this event	Time Domain
5	Total Defected Area	The sum of projected area of all the defects within this area of this event	Time Domain
6	Max Defect Size	Max size of defect detected within in this area.	Time Domain
7	Defect Spatial Density	This is the measure of how closely packed the defects are to each other within this area. This is the variance of the defect position within the area and is hence a dimensionless value.	Spatial Domain

Table 22: Thermal Data Event Feature Extraction

An interesting observation in Figure 88 in the data for Track 3, a large defect spike is seen corresponding to large defect of an area of more than $0.15mm^2$. This increases the time it takes for the sample to cool down.

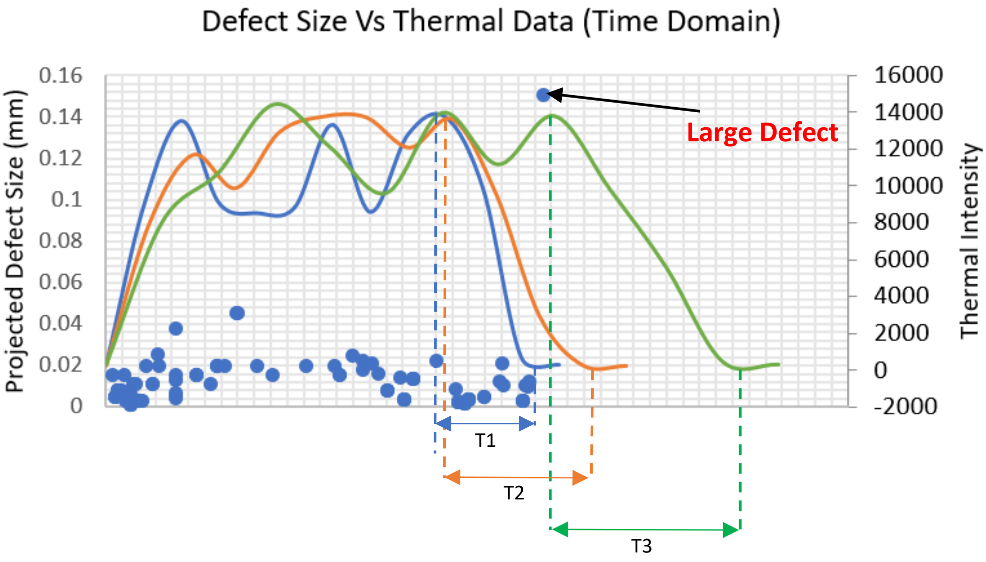

Figure 88: Cooling rates being affected due to large defect

7.1.6. Acoustic Emission Sensor Data Processing & Feature Extraction

The AE sensors pick up Acoustic signals during the changing of the material in form of bursts and continuous signals. The data received lies within the range of 100Khz to 1Mhz and the system is looking for “Events” as shown in Figure 90. An event is a signal whose amplitude crosses threshold amplitude and returns to near zero after a certain duration.

Before processing AE signals, it is important to differentiate machine and powder noises. Figure 89 show the FFTs (Fast Fourier Transform) and Spectrograms for the Machine only deposition run (Figure 89 (a)), Powder only Figure 89(b) deposition run and Raw data collected during the deposition for a Sample run of defected sample Figure 89(c). The objective of the Machine only test was to record the AE data when the motor and arm is turned on and the data for the Powder only Test is to record the AE Data for the when the powder is jetted on to the substrate. From the FFT graphs it can be concluded that an actual deposition creates a significantly higher number of Event signals with high power specially between the frequencies of 100Khz - 200Khz and 600 Khz -850 Khz. Therefore, the Powder and Machine test between these frequencies ranges exhibits a lot less activity compared to the data collected during the defected sample deposition run as shown in Figure 89 (c) in the frequency domain. From the spectrograms in Figure 89 it can be observed that at the above-mentioned frequencies that the maximum power and average power of the signal is also higher for the defected sample deposition run compared to the Powder and Machine Test as shown in Table 23.

Deposition Run	100 to 200Khz		600Khz- 850Khz	
	Max Power(dB)	Avg Power(dB)	Max Power (dB)	Avg Power(dB)
Machine Test	6	1.26	-1.8	-4.1
Powder Test	7	8.9	-1.1	-3.6
Deposition Test	8.1	11.23	-0.1	-2.06

Table 23: Frequency and Power Comparison

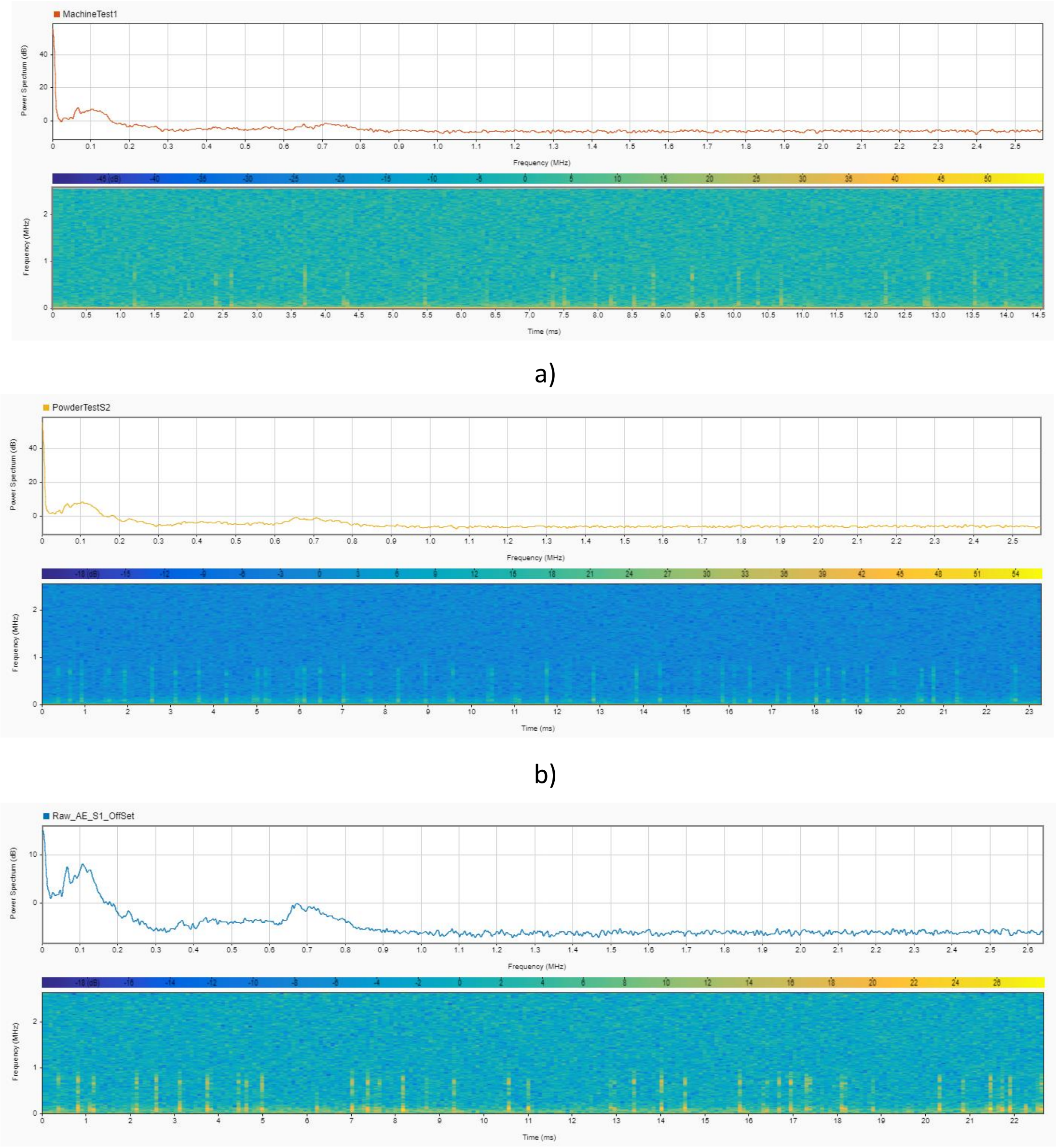

a)

b)

c)

Figure 89: a) Machine Only AE FFT and Spectrogram b) Powder only AE FFT and Spectrogram c) Track Deposition AE FFT and Spectrogram

The following are the steps taken to condition the data:

1. **Data Offset:** Raw Data offset is calculated for each sensor so that the no zero value for both AE sensors is the same.
2. **Bandpass Filtering:** The data is subjected to a digital Bandpass filter from 100Khz to 1Mhz to remove any other noise that might have creeped into the signal. Even though as per (Gaja & Liou, 2017) the signal noise in AE is much lower than the event

signals themselves, this step is to make sure noises of another nature do not creep into the signal.

3. **Moving Mean:** Even though this may cause some data loss in the signal it makes it easier for data to be extracted from the signal itself.
4. **Fast Fourier Transform:** FFT is applied to the signal for observation in the Frequency domain.
5. **Spectrogram:** A spectrogram is derived to observe the signal Time-Frequency domain i.e. observe the Signal Frequencies in relation to time.

Since the AE sensor is continuously picking up data, the points at which the deposition starts and the points at which the material has cooled down to temperatures lower than 100 Deg C need to be identified. This is because according to (Fujun Wang, 2008) it is known that majority of defects develop and propagate above 200 Deg C hence the AE monitoring should stop for temperatures lower than that. This can be determined by the start and stop frame of each thermal Data for each track. The important thing here is to sync the acoustic emission time and thermal data times first using the DAQ Universal Clock. Using (Equation 16 the lag between the time at which the thermal camera starts recording and the time at which the AE sensor starts recording is calculated. After this the time at which the deposition of a single track starts and ends can be calculated using the start and stop frames obtained from the thermal data using (Equation 17 and

(Equation 18. Now the time delay between the two sensors is added to sync their times ((Equation 19 and

(Equation 20).

$$t_{sync} = tT_{Universal\ Daq} - tA_{Univsesal\ Daq}$$

(Equation 16: Thermal and Acoustic signal Time Difference)

$$tT_{start} = \frac{TF_{Start}}{T_{FPS}}$$

(Equation 17: Time at which deposition Starts)

$$tT_{end} = \frac{TF_{end}}{T_{FPS}}$$ (Equation 18: Time at which deposition Ends)

$$tA_{start} = tT_{start} + t_{sync}$$ (Equation 19: Time Synced Deposition Start time)

$$tA_{end} = tT_{end} + t_{sync}$$ (Equation 20: Time Synced Deposition End time)

$tT_{start} = Time\ at\ which\ Thermal\ deposition\ for\ single\ track\ starts$

$TF_{start} = Frame\ at\ which\ Thermal\ deposition\ for\ single\ track\ starts$

$T_{FPS} = Framerate\ for\ the\ Thermal\ Sensor$

$tT_{end} = Time\ at\ which\ Thermal\ deposition\ for\ a\ single\ track\ ends$

$t_{sync} = The\ value\ of\ time\ for\ which\ the\ Thermal\ Camera\ lags\ behind\ Acoustic\ Camera$

$tT_{Universal\ Daq} = Time\ Stamp\ recorded\ when\ Thermal\ Camera\ Sensor\ data\ is\ collected$

$tA_{Universal\ Daq} = Time\ Stamp\ recorded\ when\ Acoustic\ Emission\ Sensor\ data\ is\ collected$

Data between the tA_{start} and tA_{end} for each track is Isolated from the continuous AE data for further data extraction. After this a threshold is identified for each sensor using the Hsu-Nielsen source which also known as pencil lead break method (Ramin Madarshahian, 2019). From the AE data for each deposition track, Events are identified as shown in Figure 90. These events can be identified by isolating signal envelopes that cross the determined threshold values (25). By analyzing the isolated signals in Time Domain and Frequency domain (Figure 91) use full features are extracted for each event as shown in Table 24.

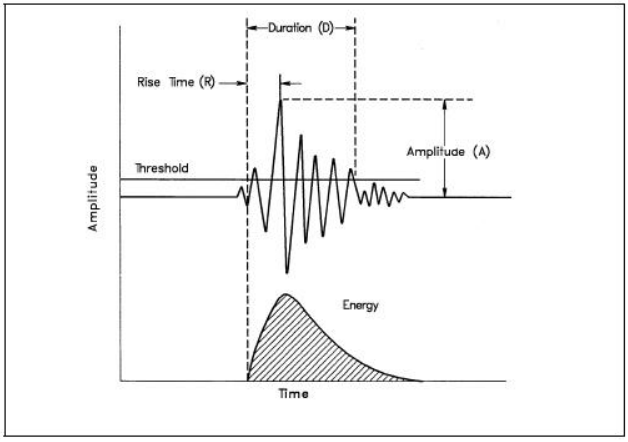

a)

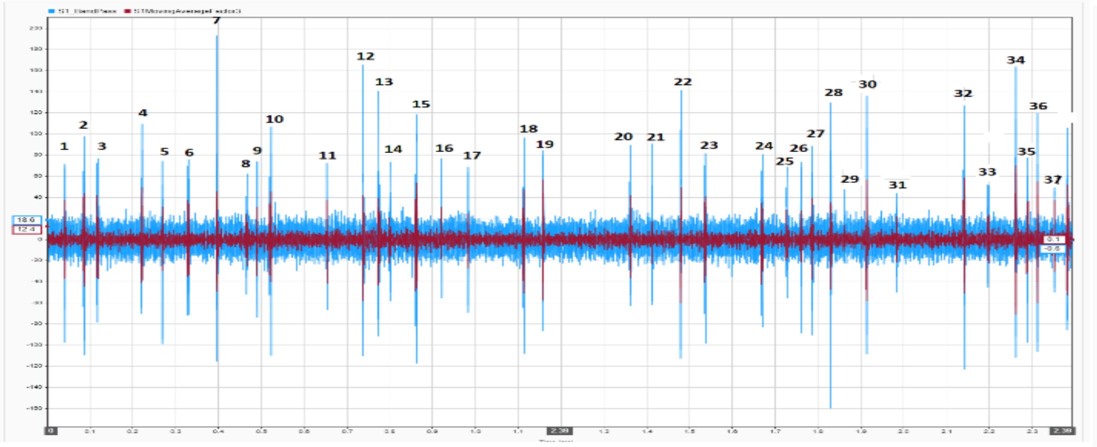

b)

Figure 90: a) AE Event Features b) AE Events

	Feature	Explanation	Extraction Source
1	Amplitude	The maximum amplitude of the Event. This is picked up from raw data to avoid data loss.	Time Domain
2	Rise Time	The time taken for the amplitude to rise to Max amplitude from when it first crossed the threshold value	Time Domain
3	Ring Counts	After the threshold has been crossed the number of times the signal crosses the threshold until falling below it once again	Time Domain

4	Energy	Time taken for the event to drop down below threshold from max amplitude	Time Domain
5	Duration	It is the total time the signal stays above the threshold value after it crosses it for the first time.	Time Domain
7	Position of Source	Using 1D Time of flight(TOA) analysis from both sensors the position can be calculated.	Time Domain
6	Max Frequency band Amplitudes	This is the Max amplitude of the frequencies (per 100Khz) within that signal. This is determined using the Spectrogram and FFT analysis.	Frequency and Frequency Time Domain.

Table 24: AE event Feature Extraction

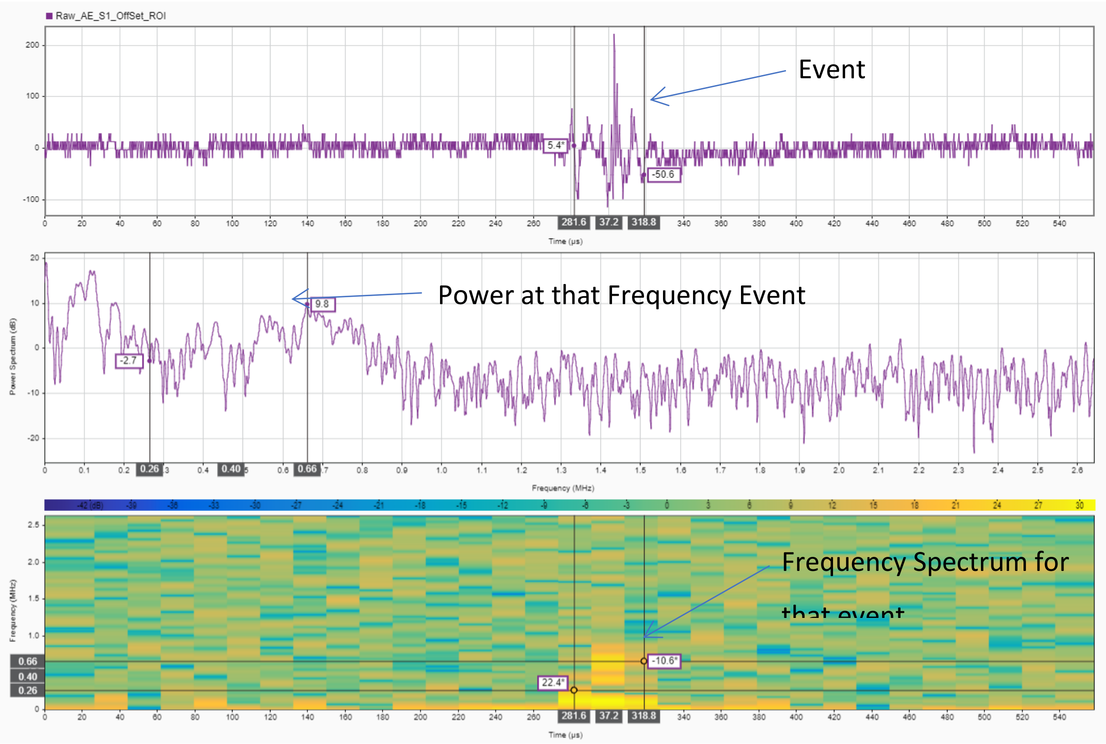

Figure 91: Signal Event Analysis

As per Mohamed (Shehadeh, 2006) and (Kaphle, 2012) the position of the source of the AE wave can be calculated using multiple sensors. In Truss like or cylindrical structures or structures whose length is significantly shorter than their width, 1 D Time of Flight method can be used to locate the position of the source. Since the objective is to determine the defects along the length of the deposit, this method is sufficient for this research as shown in Figure 92(a). (Equation 21 is used to calculate the position of each defect using the data of the of two features.

$$L_1 = c.T_1$$

$$L_2 = c.T_2$$

$$L_1 - L_2 = c.(T_1 - T_2) = -c\Delta t$$

$$L_1 + L_2 = D$$

$$L_1 = \frac{1}{2}(D - \Delta t.c)$$

(Equation 21: AE Source Position using TOA method.)

$L_1 = length\ to\ sensor\ that\ signal\ reached\ first$

$L_2 = length\ to\ sensor\ that\ signal\ reached\ second$

$\mathrm{D} = length\ between\ the\ two\ sensors$

$c = speed\ of\ sound\ in\ material$

$T_1 = Time\ at\ which\ the\ signal\ reaches\ the\ sensor\ that\ recives\ the\ signal\ first$

$T_1 = Time\ at\ which\ the\ signal\ reaches\ the\ sensor\ that\ recives\ the\ signal\ second$

$\Delta t = Time\ diffence\ between\ when\ the\ two\ sensors\ recive\ their\ signals$

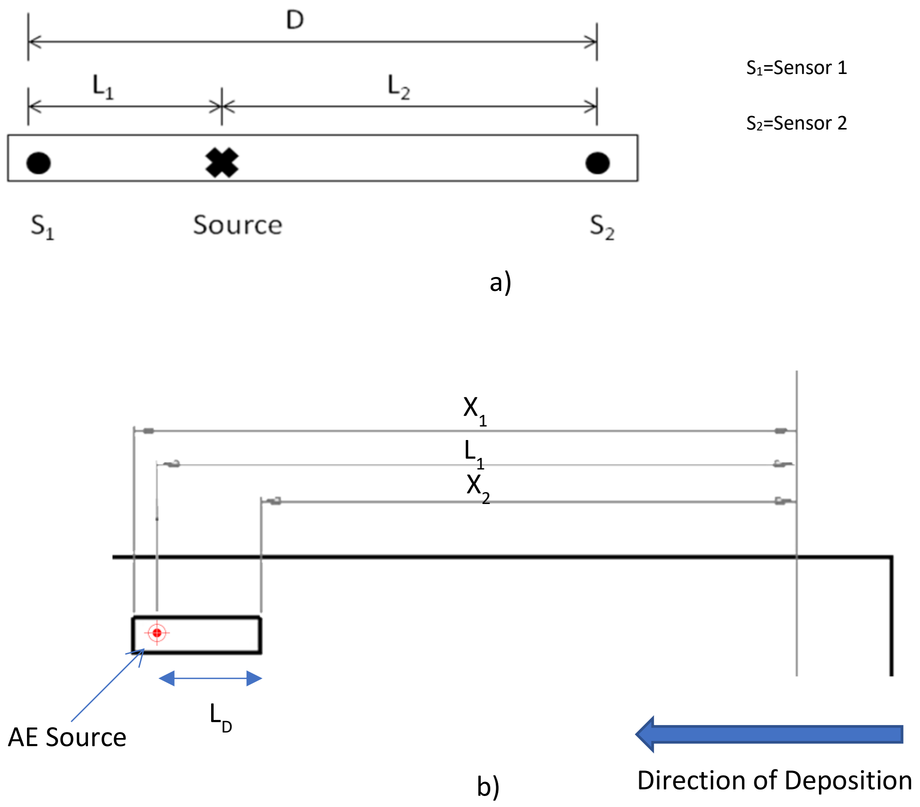

a)

b)

Figure 92: AE Source Position Calculation

The final step is to calculate the position of the defect relative to length of the deposition which can be achieved using (Equation 22. All deposits are laid from Left to Right as shown on Figure 92 (b).

$$L_D = L_1 - X_2$$

(Equation 22: AE Source Position along the length of deposition)

$L_D = length\ from\ the\ start\ of\ the\ deposit\ to\ the\ Defect$

$X_2 = length\ from\ the\ sensor\ to\ the\ start\ of\ the\ deposit$

Figure 93 shows the AE data for each track stitched on to the defect position with respect to time. It can be observed that the main events occur around the area where defects are densely populated, and the amplitude of the defects agrees with the defect sizes.

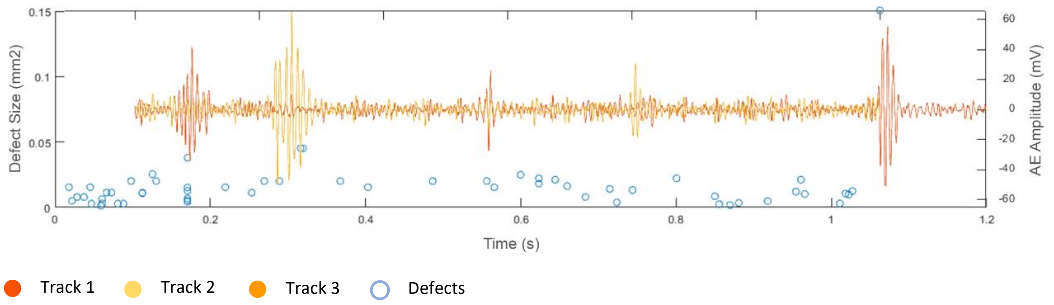

Figure 93: AE Data stitched onto Defect Data in Time Domain

It is important to mention the AE Data when stitched on to defect data it was out of sync and was manually adjusted 0.1s which also means the data for the first 0.1s of the deposition is lost. The time domain AE graph shows that the amplitude of the event varies with the size of the defects and there is peak at the point of the defect. This could also mean that the rise to max amplitude could be considered a precursor to a defect being formed.

Figure 94 shows AE event source positions stitched onto defect data in the spatial domain. Some event sources seem to be within 0.5 mm of the areas with densely populated defects or some large defects, but some data points calculated originate from outside the deposition. This inaccuracy might be caused by the 1D TOA methodology or due to AE wave type or due to AE signal attenuation explained by (Shehadeh, 2006).

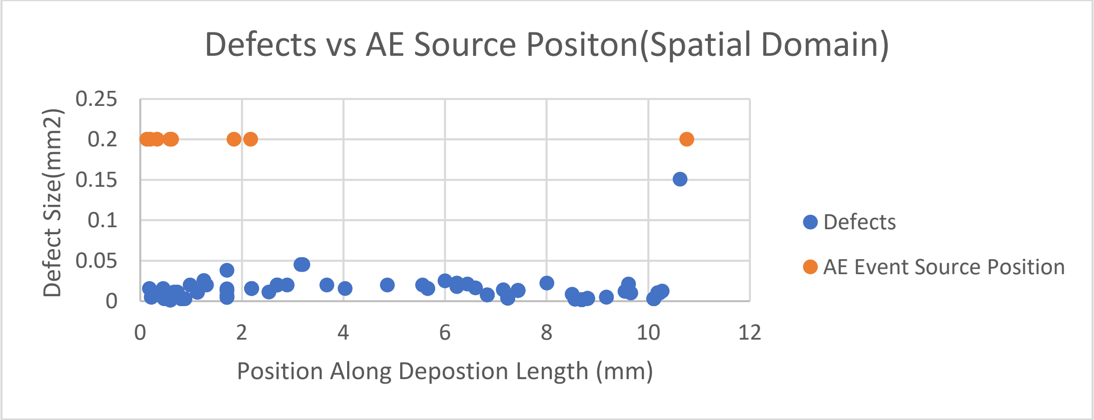

Figure 94: AE Sources Stitched onto Defect Data in Spatial Domain

It is also important to be mentioned here that sometimes one sensor might cross the threshold and the other might not. In this case due to the uncertainty of the source of the signal, this signal is not considered as an event.

7.2. Machine Learning

After *Events* are extracted from the stitched data, the data is prepared to be fed as input into an unsupervised learning algorithm called K means clustering as training data. The conclusions drawn from the Clustering Analysis will form the bases for the defect detection algorithm which can be seen in Figure 95 along with procedure that leads up to it.

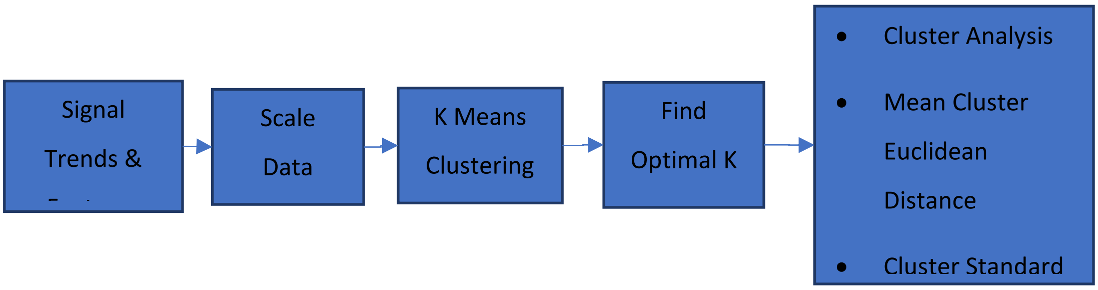

Figure 95: Machine Learning Procedure

7.2.1. Scaling Data

Since the objective is to cluster multiple variables with different ranges which at times can be drastically different from each other, the data set needs to be normalized. This is mainly since K-Means clustering algorithm utilizes the calculation of distances and if ranges are not the same, some variables might influence the results more than others. In this case z scaling is used for the normalization method which is governed by (Equation 23.

$$Zscore = \frac{Value - \mu}{\sigma}$$

(Equation 23: Z-Score Calculation)

Z scaling caters for outliers but does not put each feature data set of an Event on the exact same scale. For the data set it is understood that some sensors will respond to what might be considered outliers since they do represent extreme defects. But it is also known that the K-means clustering algo is heavily dependent on the Euclidian distances and that data sets with different ranges can affect how data is clustered. Choosing this scaling method then becomes a balancing act for catering for the outliers yet not having drastically different scales in features. Table 25 shows the minimum and maximum z score of each feature in their respective data sets.

HS Sensor Events Scaling

Z Score	**Max**	**Min**
Max Intensity	2.066	-1.775
Spike Frequency	2.786	-1.649
Max Defect Size	2.403	-0.706
Total Defected Area	2.283	-1.008
Defect Spatial Density	3.027	-0.891
# Total Defects	2.361	-1.512
# Pores	2.422	-1.476
# Cracks	2.535	-0.475
#Other Defects	2.175	-0.648

Thermal Sensor Events Scaling

Z Score	**Max**	**Min**
Total Time/s	2.377176	-2.07055
Rise Time	1.825285	-0.84258
Fall Time	1.285444	-1.59725
Rise Rate	2.278414	-0.99746
Cool down Rate	0.867352	-1.78013
Max Amplitude	1.484784	-0.90098
# Total Defects	1.810366	-1.33702
# Pores	1.827115	-1.4014
# Cracks	3.859186	-0.29339
Other Defects	2.759893	-0.58103
Max Defect Size	2.814012	-0.7062
Total Defected Area	3.118105	-0.96367
Defect Spatial Density	2.537594	-2.0098

AE Sensor Events Scaling		
Z Score	**Max**	**Min**
Amplitude mV	2.246979	-2.15615
Rise Time/us	1.556022	-1.21182
Duration/us	2.013733	-1.9261
Energy	2.283653	-1.29982
Ring Counts	1.816553	-2.16023
Max Amplitude of any frequency band /dB	3.605616	-1.28701
Max Frequency above threshold/Khz	1.234209	-2.29284
Median Frequency	1.717752	-1.57687
Mean Frequency Khz	1.89425	-2.0853
100Khz - 200Khz	0.615177	-3.21635
200 Khz - 300 Khz	1.106976	-1.36497
300 Khz - 400 Khz	2.611538	-0.40568
400Khz - 500Khz	1.219099	-1.26817
500Khz - 600 Khz	1.813193	-0.68938
600Khz - 700Khz	1.16923	-0.87679
700Khz - 800Khz	0.936537	-1.27535
800Khz - 900	2.446727	-0.40903
900-1Mhz	5.003702	-0.19245
# Total Defects	2.803539	-1.1544
# Pores	2.969018	-1.19748
# Cracks	3.475652	-0.33909
Other Defects	2.589614	-0.58855
Total Defected Area / mm2	4.188766	-0.55736
Max Defect Size/ mm2	4.234336	-0.46508

Defect Spatial Density	2.715908	-1.12782

Table 25: Z-Score Scaling of Event Features

7.2.2. K-means Clustering

K-means clustering is an unsupervised machine learning algorithm which allows for the grouping of *Events* based on the similarities in their features for each sensor. It is very important to understand the internal workings of the K-means Clustering Algorithm as it plays a very vital role in the data fusion algorithm.

The K means clustering algorithm has 3 major steps as shown in Figure 96. It iterates through steps 2 and 3 to divide the data into K number of groups.

1. **Initialization of Centroids:** Randomly Initialize K number of Centroids with random position. MATLAB does this by using K means ++ algorithm. In K means ++ the first centroid is placed at a random point and the following centroids are placed on a probability proportional to the squared distance away from the nearest centroid. The aim is having the initial centroids as far away from each other as possible (Arthur & Vassilvitskii, 2007).
2. **Cluster Assignment:** Calculate the Euclidean Distance from each data point to each centroid and assign to the Cluster of the Centroid to which the calculated Euclidean distance is the least.
3. **Move Centroids:** Once data points have been assigned to a cluster, Calculate the mean of all these points and move the centroid to this mean.

Steps 2 and 3 are iterated until the centroids stop moving position i.e. the iteration at which K means algorithm converges.

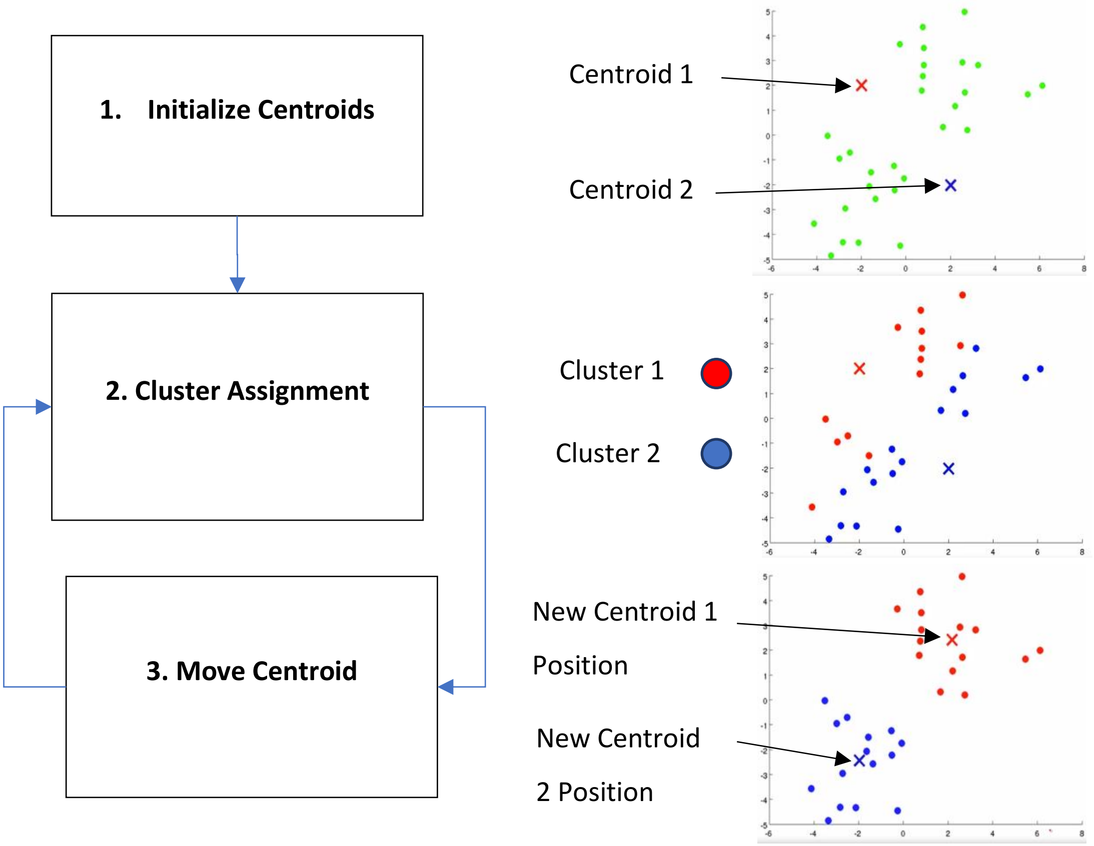

Figure 96: K-means Clustering Algorithm

The number of Clusters must be manually chosen before running the K means Algorithim. There are multiple techniques to select the optimal number of K (clusters) but the one utilized here is “Calinski-Harabasz Index” also known as Variance Ratio Criteria. The criterion calculates the ratio between clusters dispersion and inter cluster dispersion for all clusters. This is calculated over a range of K values and the K value at which the highest Calinski-Harabasz score achieved is chosen.

Figure 97 shows the Calinski-Harabasz Index Score over a range of K values for each sensor Data set and based on those graphs, Table 27 shows Optimal K for each Sensor.

	High Speed Data	Thermal Sensor Data	Acoustic Emission Data
Smallest Distortion	225.98	164.258	383.62

Table 26: Smallest Distortion for each sensor for K means runs

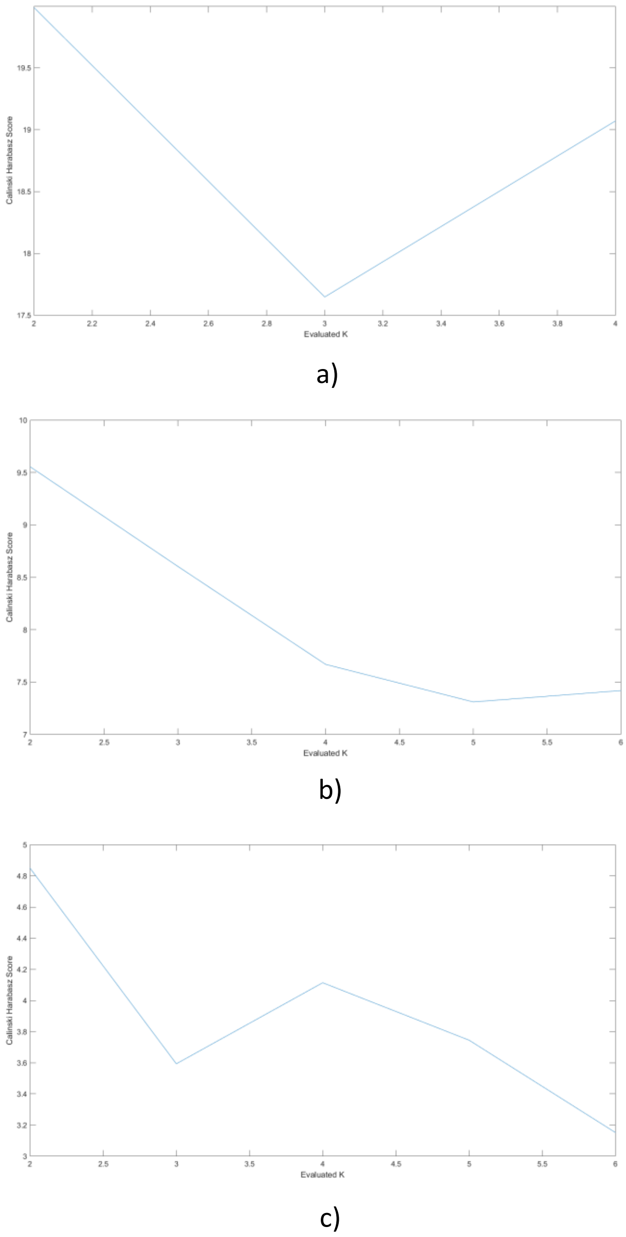

Figure 97: a) Calinski-Harabasz Index for HS data Events, b) Calinski-Harabasz Index for Thermal data Events, c) Calinski-Harabasz Index for AE data Events

	High Speed Data	Thermal Sensor Data	Acoustic Emission Data
Optimal K	2	2	2

Table 27: Optimal Number of K Cluster for all sensors

Often with a high dimensional data set Principal Component Analysis is applied to reduce the data sets dimension before applying K-means Clustering to it. In this case PCA is not applied before implementing K means due to the inherent issues that come with dimensional reduction; a) After PCA components are put though K means it is difficult to read back the original feature set which is a major concern when making the feature predictions and b) Dimensionality reduction means loss of data which cannot be afforded since the Raw data values have already gone through so much processing and filtering. Often higher dimensional data can cause relatively less accurate clusters compared to when dimensionality reduction techniques like Principal Component Analysis are applied to them. But this is a tradeoff this research is willing to make due to the above-mentioned reasons and the dimensions of the data sets are not considered to be significantly high.

The Sum of Squared Distances to the centroid aka Distortion is calculated each time the entire K means algorithm is implemented. Running the K means algorithm multiple times can give a wide range of Cost Functions. By choosing the K means Clustering run that gave the lowest Cost Functions ((Equation 24), the best Clustering results can be achieved. For each sensor K- means cluster is run 1000 times and the K means run that has the smallest Distortion is chosen as shown in Table 26.

$$J(c,\mu) = \sum_{i=1}^{m} ||x^{i} - \mu_{c^{(i)}}||^{2}$$ (Equation 24: Cost Function)

$c^{(i)} = Index\ of\ the\ cluster(1,2..K)\ to\ which\ x^{i}\ is\ assinged$

$x = data\ point$

$\mu_{c^{(i)}} = Cluster\ centeroid\ of\ cluster\ to\ which\ x^{i}\ is\ assinged$

$m = Number\ of\ Points$

$K = Total\ Clusters$

Often Clusters of higher dimension data sets can be visually misleading in terms of cluster centroid positions and cluster overlap since they only show a few dimensions. Figure 98(a) shows a 3-dimensional scatter plot and Figure 98 (a), (b) and (c) show 2D projections of the scatter from different angles. When only observing the 2D projections they may appear to be altogether different clustering scatter graphs but mathematically the cluster assignment of data and centroid position is justified and based on the K means Euclidean distance calculations for multiple dimensions. Figure 98(a),Figure 99 and Figure 100 show the

Clustering results for the High-Speed Data Events, Thermal Data Events and AE Data Events respectively.

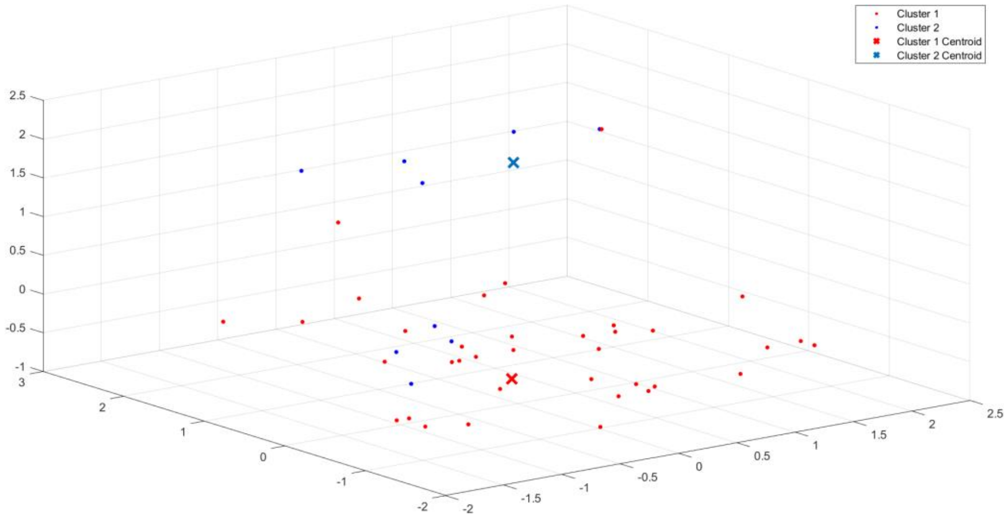

a)

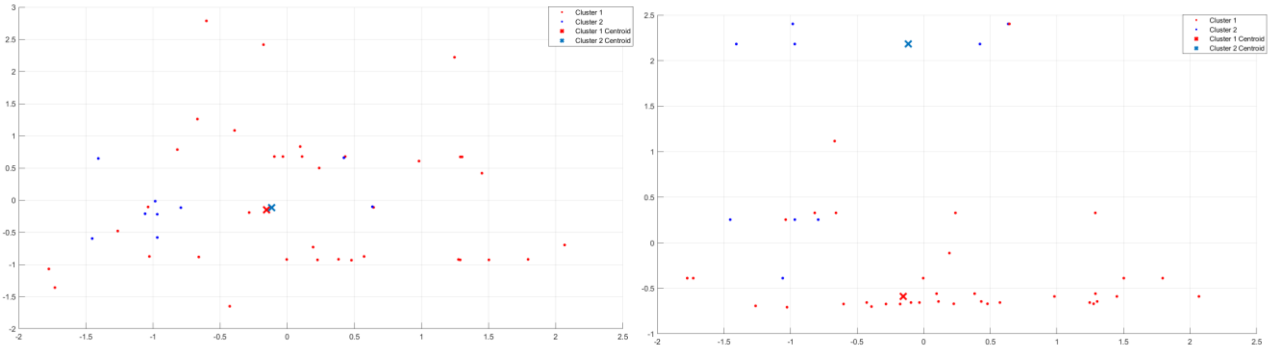

b) X-Y View

c) X-Z View

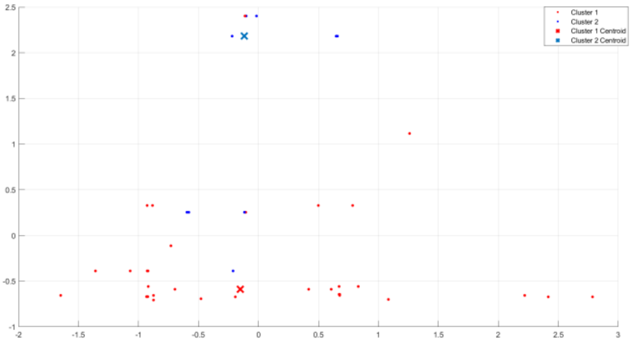

d) Y-Z View

Figure 98: a) HS Data Clustering plot in 3D b) XY Projection HS Data Clustering, c) XZ Projection HS Data Clustering, b) YZ Projection HS Data Clustering

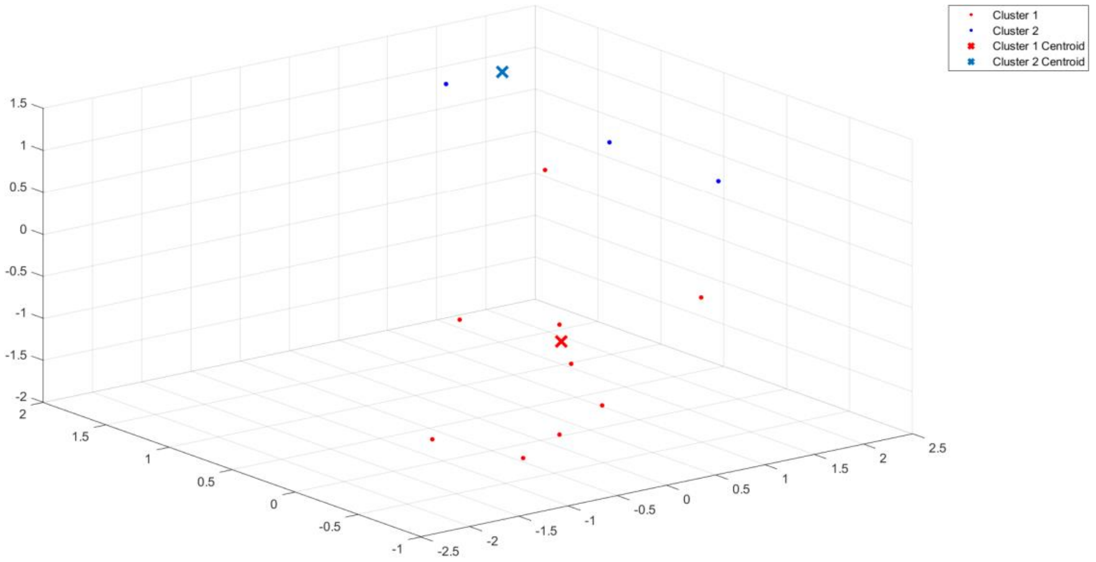

Figure 99: Thermal Data Clustering

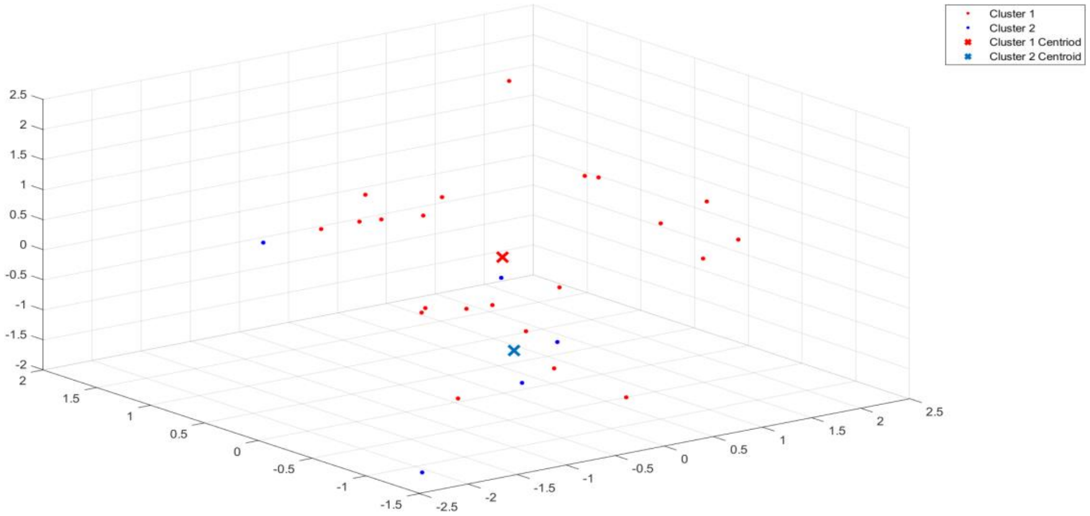

Figure 100: AE Data Clustering

7.3. Defect Detection Algorithm

The defect detection algorithm utilizes the Clustering Graphs of all three sensors to predict the features and % confidence (In the prediction) for a new point introduced into those trained cluster models. Using the produced cluster models, predictive ranges can be derived for a feature of a particular Cluster that should be able to justify representing any new point that is assigned to that Cluster. A confidence score that estimates the accuracy of this prediction can also be assigned to this predictive range. All these ranges take into consideration all three Sensor Cluster Models and Fuse their data to come up with a single output of a Feature Range and its % Confidence. Figure 101 shows the Data Fusion Algorithm which is discussed in detail in the following sections.

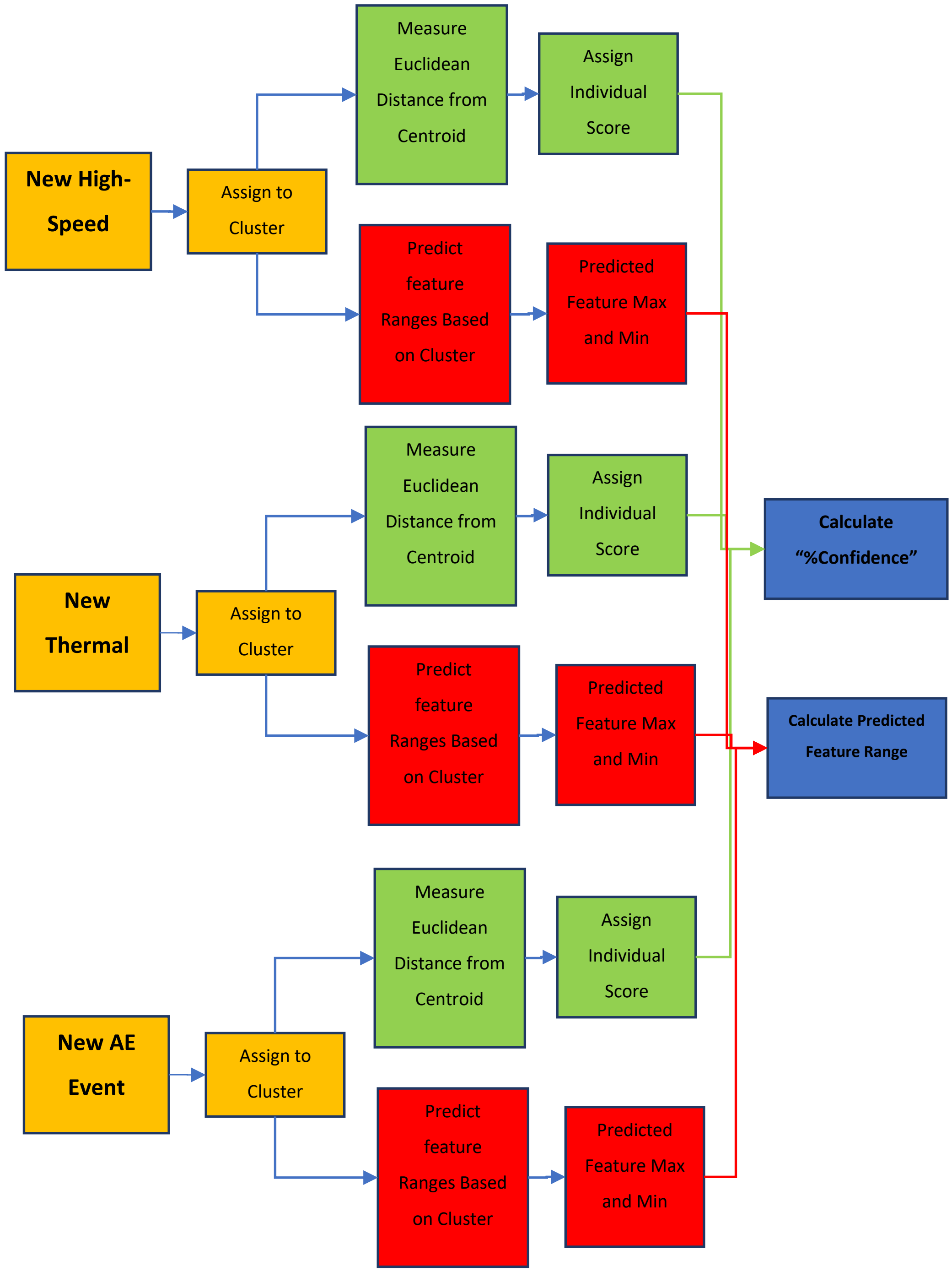

Figure 101: Data Fusion Algorithm

7.3.1. Feature Range Prediction

The distribution of some feature sets may be considered normal however the majority does not fit any distribution and hence drawing any conclusion based on a known distribution is not possible on all feature sets. Another approach would be to statistically analyze the distribution of the collective values for each data feature set using Box Plots as shown in

Figure 102, Figure 103, Figure 104, Figure 105 and Figure 106 . These plots display what is known as the “five number summary” in descriptive statistics which should allow an understanding of the distribution of the feature sets. The five number summary includes the Maximum, Minimum, Upper Quartile, Lower Quartile and Median values for that feature set. The maximum and minimum values of the box plot are calculated using the interquartile range. The interquartile range (IQR) is the distance between the upper quartile and lower quartile range. The largest point in the data set within a distance 1.5 times the IQR from the upper quartile range is consider the maximum. Similarly, the smallest point in the data set within a distance 1.5 times the IQR from the lower quartile in the opposite direction is the minimum. Any other points that lie outside the Max and Min are considered outliers.

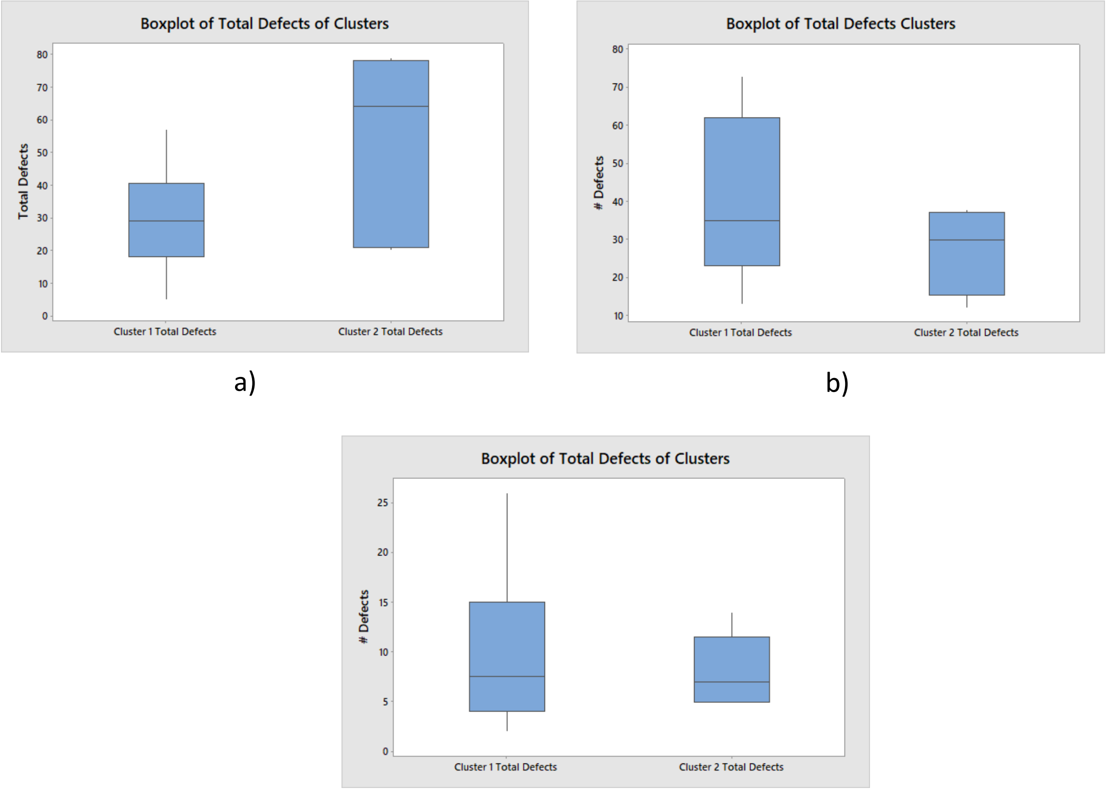

a) b)

c)

Figure 102: Box and Whiskers plot for Total Defects for a) HS Cluster Events, b) Thermal Cluster Events, c) AE Cluster Events

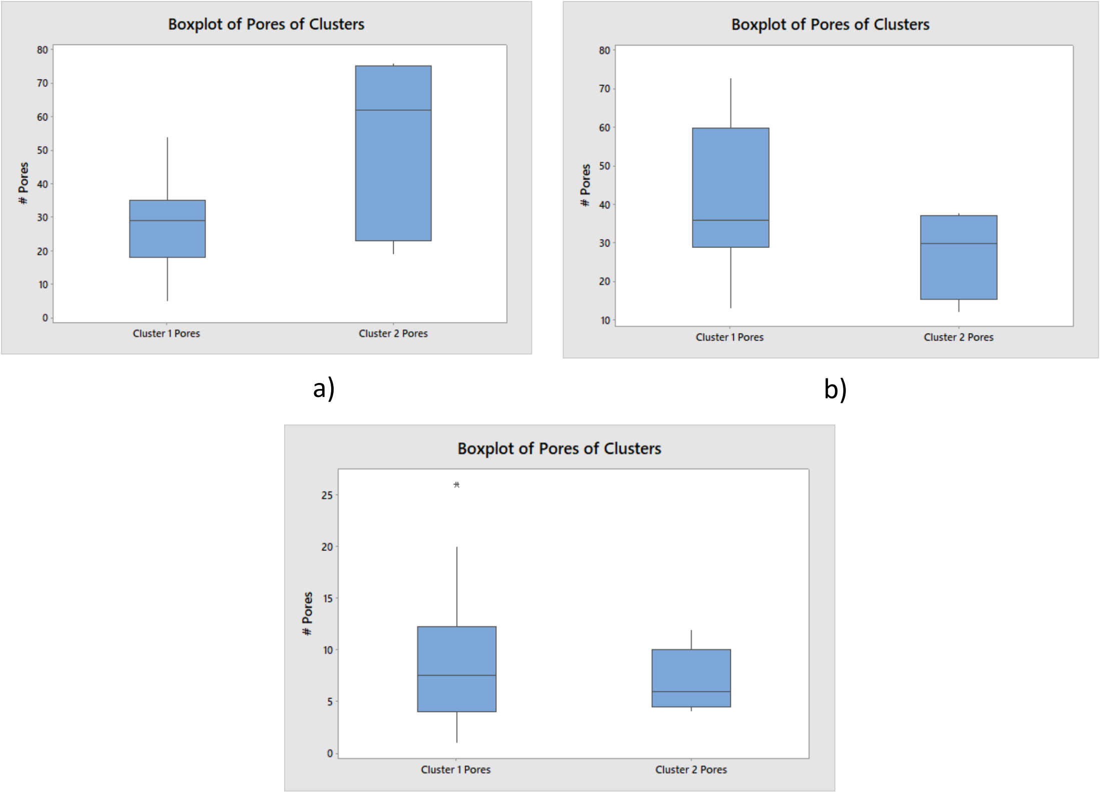

a)

b)

c)

Figure 103: Box and Whiskers plot for Total Pores for a) HS Cluster Events, b) Thermal Cluster Events, c) AE Cluster Events

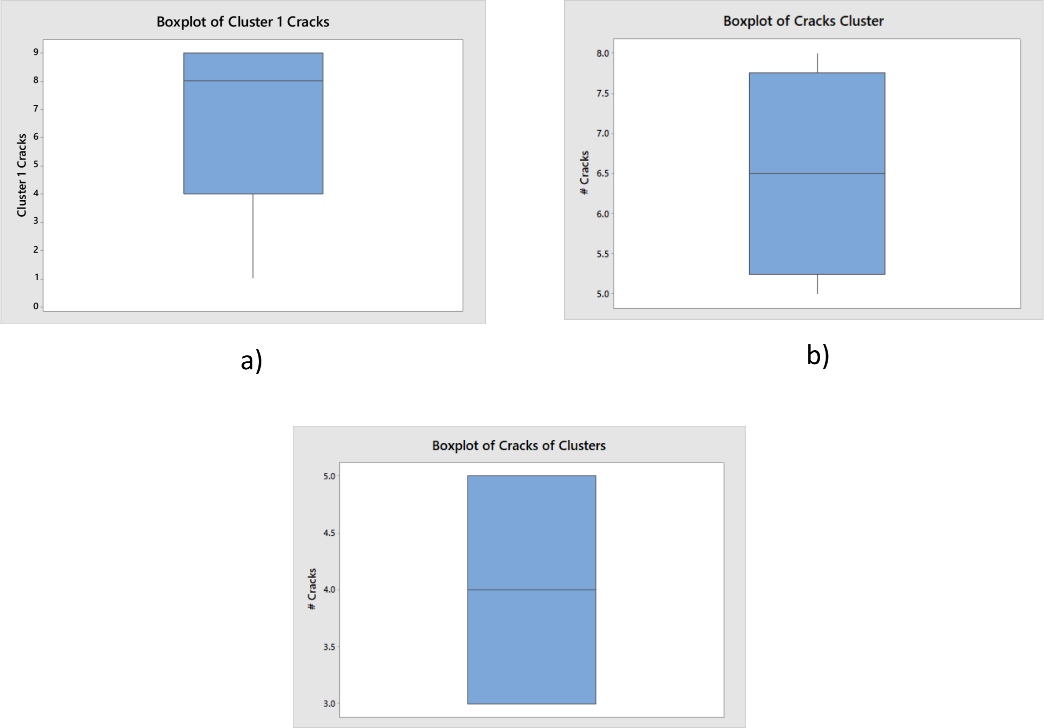

a)

b)

c)

Figure 104: Box and Whiskers plot for Total Cracks for a) HS Cluster Events, b) Thermal Cluster Events, c) AE Cluster Events

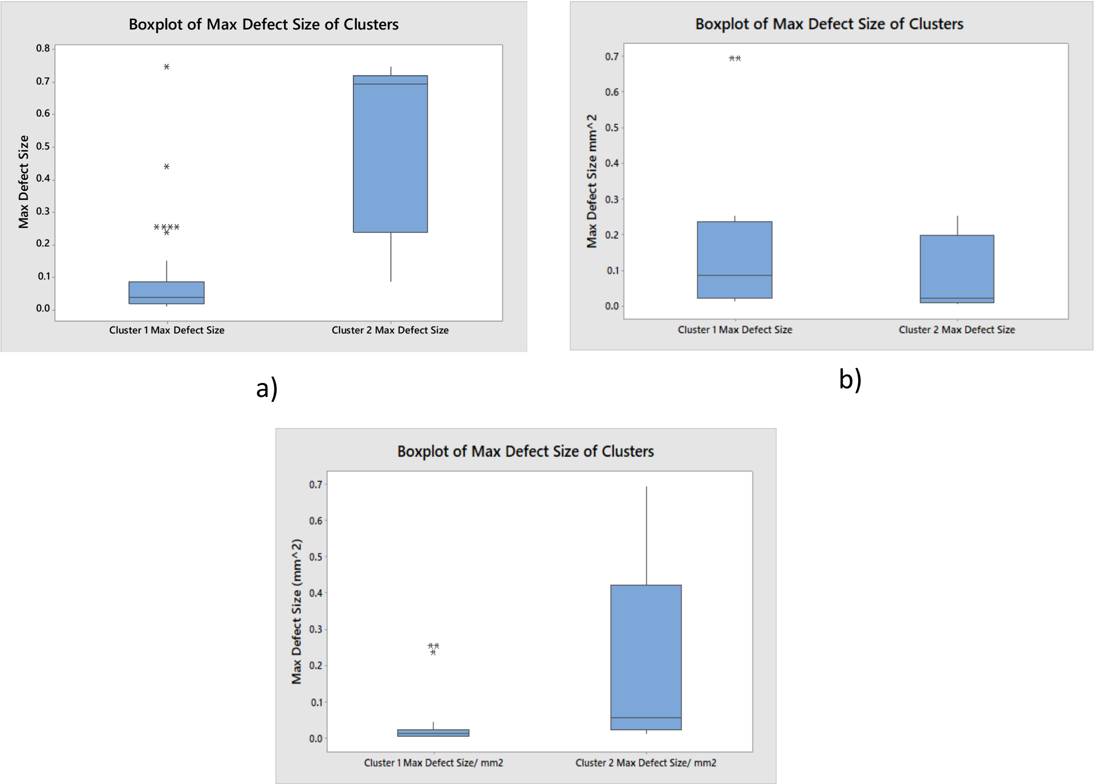

a)

b)

c)

Figure 105: Box and Whiskers plot for Max Defect Size for a) HS Cluster Events, b) Thermal Cluster Events, c) AE Cluster Events

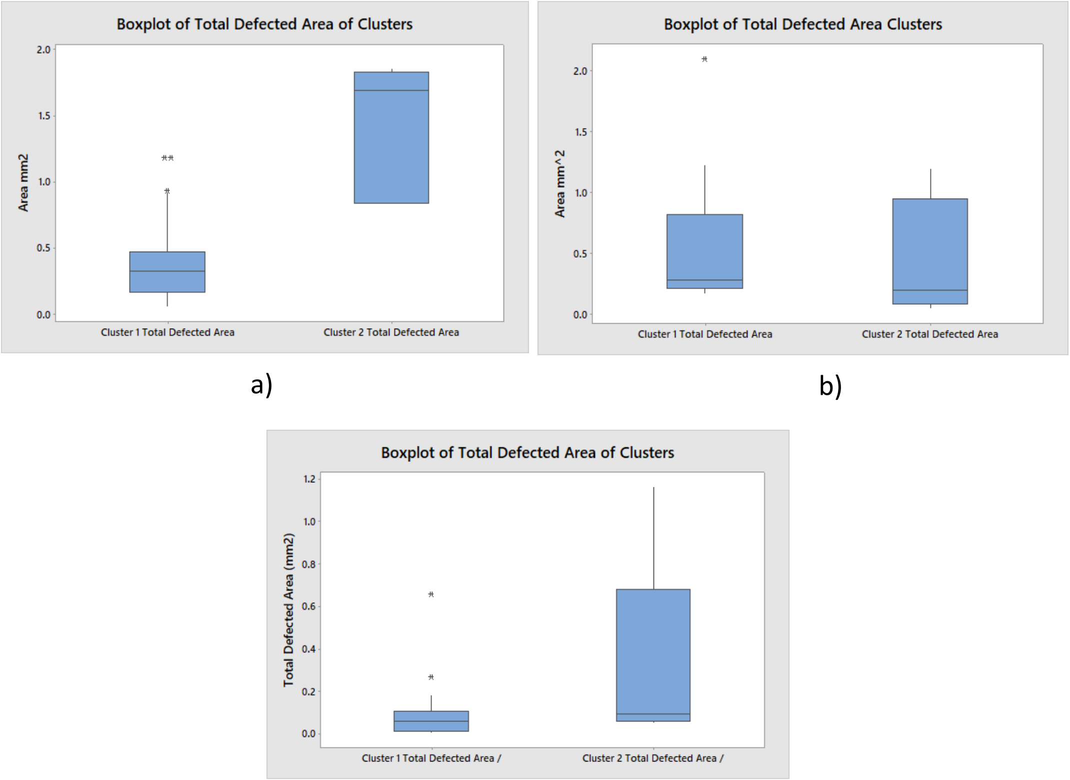

a)

b)

c)

Figure 106: Box and Whiskers plot for Total Defected Area for a) HS Cluster Events, b) Thermal Cluster Events, c) AE Cluster Events

Once the outlier for each feature is eliminated, the min and max values from their respective Box plots are chosen to form predictive ranges for each Sensor and each sensor Cluster shown in Table 28. Interesting observations can be made by analyzing the individual box plots, but this will be discussed briefly in the discussions section and mostly left to further works.

	Cluster 1									
	Total Defects		Pores		Cracks		Defect Size		Total Defected Area	
	Max	Min	Max	Min	Max	Min	Max	Min	Max	Min
HS	57	5	54	5	9	1	0.7462	0.01	1.1871	0.0529
Thermal	73	13	73	13	8	5	0.694	0.0117	2.096	0.166
AE	26	2	26	1	5	3	0.6574	0.0051	0.2552	0.0036
	Cluster 2									
	Total Defects		Pores		Cracks		Defect Size		Total Defected Area	

	Max	Min	Max	Min	Max	Min	Max	Min	Max	Min
HS	79	20	76	19	0	0	0.7462	0.0855	1.853	0.836
Thermal	38	12	38	12	0	0	0.2552	0.0055	1.195	0.048
AE	14	5	12	4	0	0	1.163	0.05	0.694	0.011

Table 28: Predictive Ranges for Sensor Clusters

The Following equations are a rudimentary way to fuse data from each sensor and come up with a final predicted range for a new point introduced into the Data fusion Algorithm.

$$F_{Max} = \frac{FHS_{Max} + FTh_{Max} + FAE_{Max}}{n}$$

(Equation 25: Predicted Feature Max Value)

$$F_{Min} = \frac{FHS_{Min} + FTh_{Min} + FAE_{Min}}{n}$$

(Equation 26: Predicted Feature Min Value)

$$F_{Range} = F_{Max}\ to\ F_{Min}$$

(Equation 27: Predicted Feature Range)

$F_{Range} = Predicted\ Feature\ Range$

$F_{Max} = Predicted\ Feature\ Max\ Value$

$F_{Min} = Predicted\ Feature\ Min\ Value$

$FHS_{Max} = High\ Speed\ Feature\ Range\ Max\ Value$

$FTh_{Max} = Thermal\ Feature\ Range\ Max\ Value$

$FAE_{Max} = Acoustic\ Emission\ Range\ Max\ Value$

$FHS_{Min} = High\ Speed\ Feature\ Range\ Minimum\ Value$

$FTh_{Min} = Thermal\ Feature\ Range\ Minimum\ Value$

$FAE_{Min} = Acoustic\ Emission\ Range\ Minimum\ Value$

$FAE_{Min} = Acoustic\ Emission\ Range\ Minimum\ Value$

$n = Number\ of\ Sensors$

7.3.2. Percentage Confidence

Theoretically the clustering algorithm groups Events with similar features based on their distance from their respective cluster centroids. Based on this, each cluster group should have similar feature values but the further they move away from their respective cluster centroids the more dissimilar the features will get compared to those closer to the centroid. The Defect detection algorithm aims to predict an estimated range for the Total Number of Defects, Pores, Cracks and Max Defect Size. The variance trends for these features in the Clustering output for the training data of the HS Cluster 1, HS Cluster 2, Thermal Cluster 1, Thermal Cluster 2, AE Cluster 1, AE Cluster 2 can be seen in Figure 107,Figure 108,Figure 109,Figure 110,Figure 111 and Figure 112 respectively. The graphs display a general trend that as the events move away from their cluster centers, the dispersion of their features compared to the ones closer to the cluster center increases. The variance trends are calculated using the variance for each feature set at μ, $\mu + 1\sigma$ and $\mu + 2\sigma$. Sometimes it is seen that even though some features may have an increasing trend they seem to have a variance change of lower than 0.1 across the range.

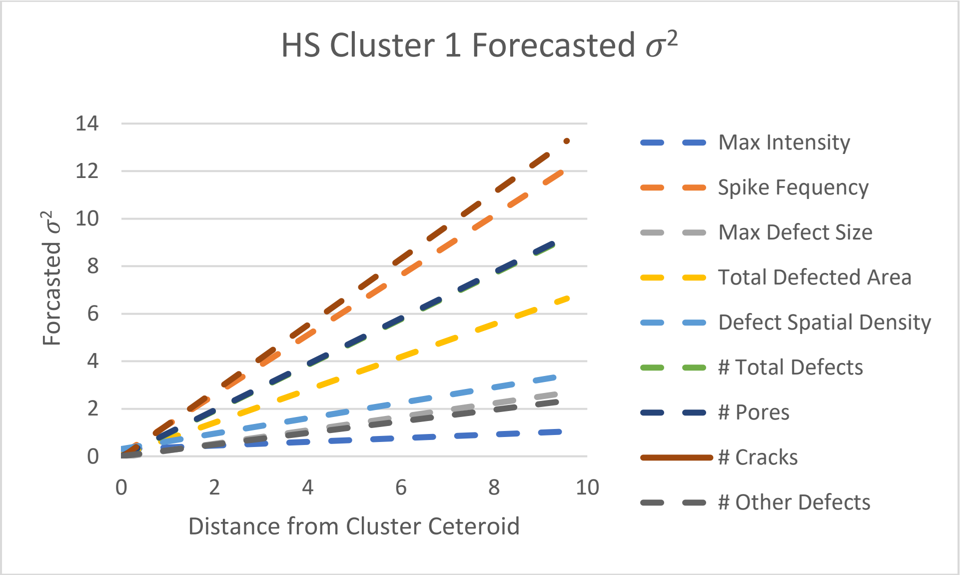

Figure 107: HS Cluster 1 Variance vs Distance from Cluster Centroid

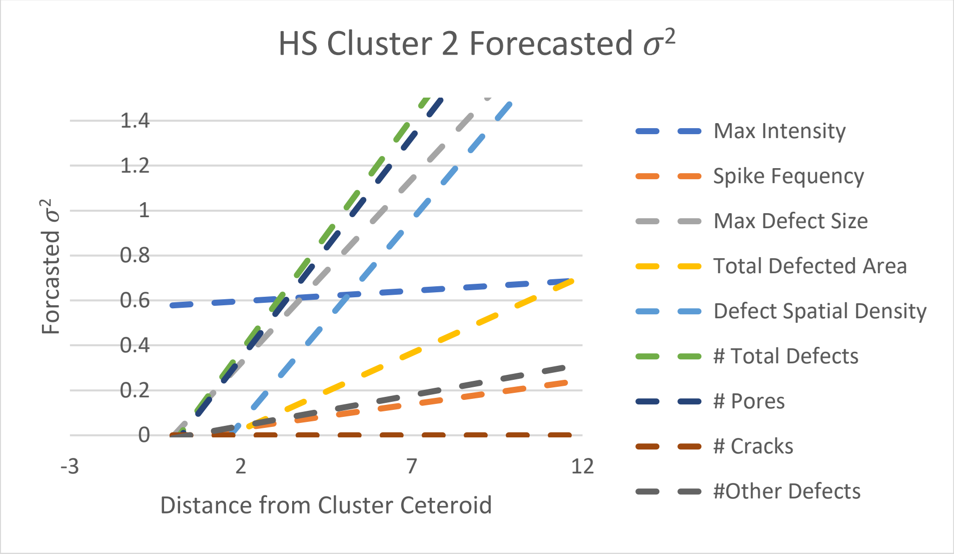

Figure 108: HS Cluster 2 Variance vs Distance from Cluster Centroid

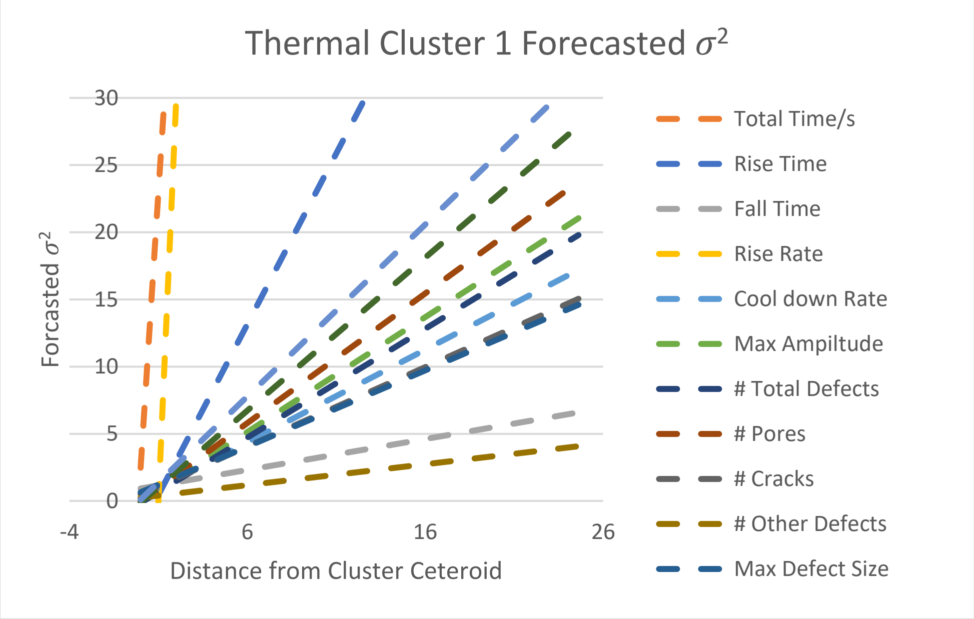

Figure 109: Thermal Cluster 1 Variance vs Distance from Cluster Centroid

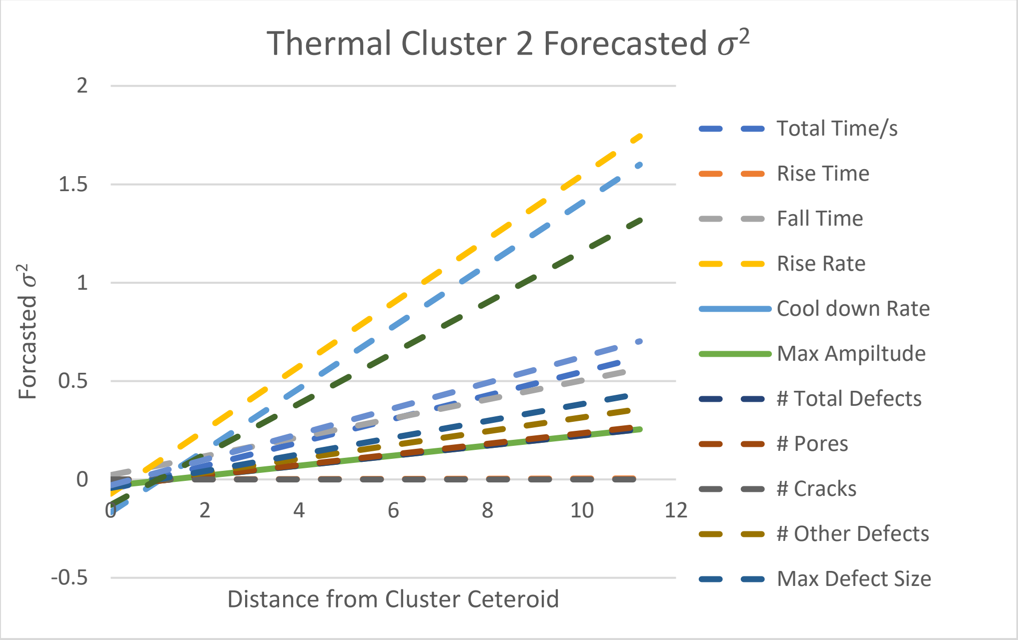

Figure 110: Thermal Cluster 2 Variance vs Distance from Cluster Centroid

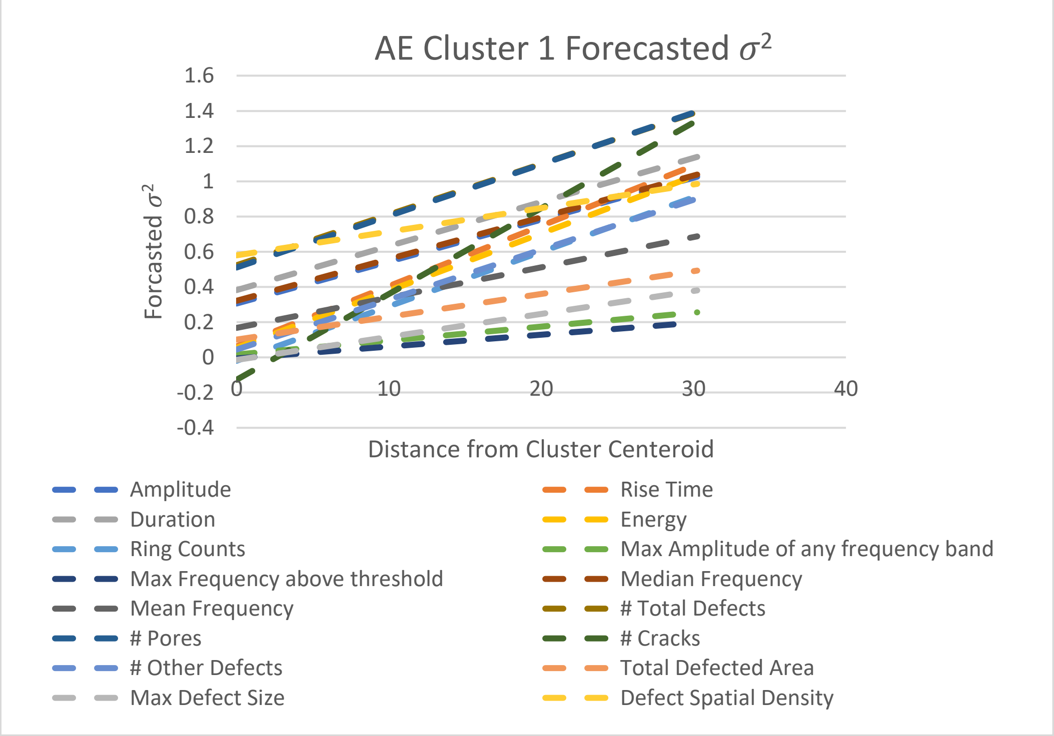

Figure 111: AE Cluster 1 Variance vs Distance from Cluster Centroid

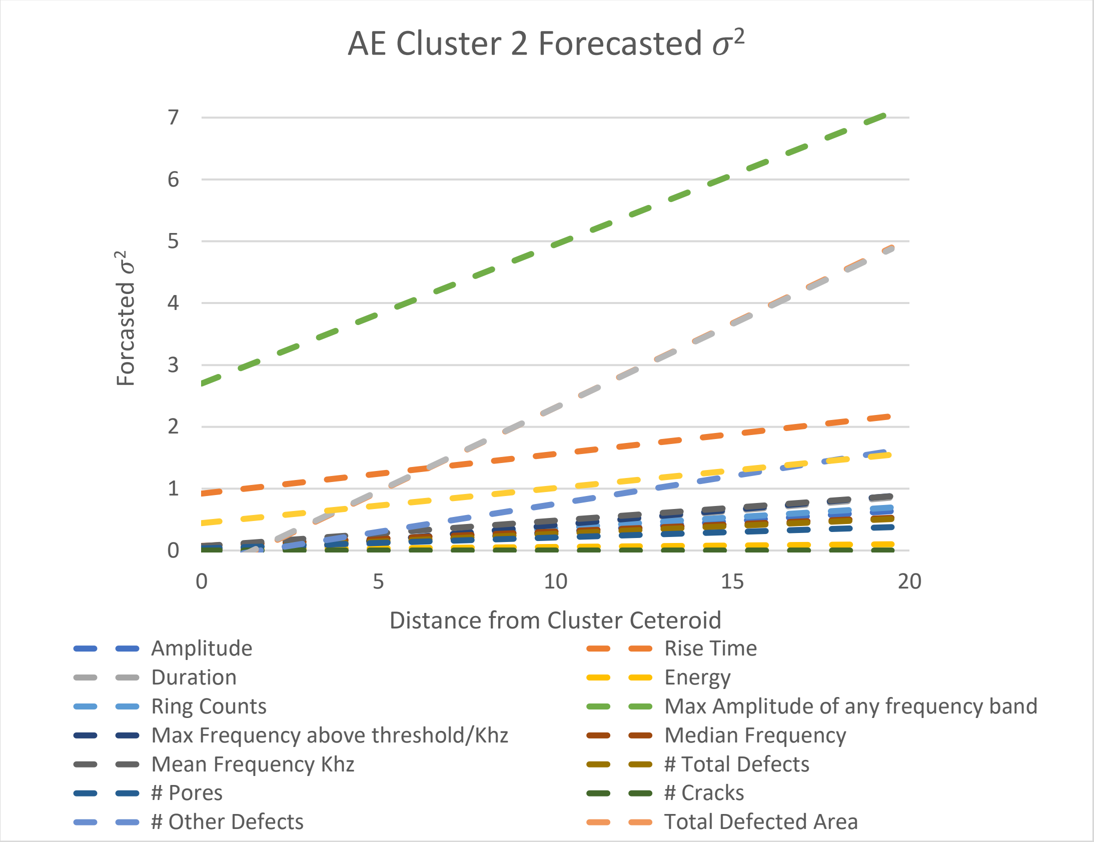

Figure 112: AE Cluster 2 Variance vs Distance from Cluster Centroid

Based on the conclusion that within a cluster the further a point moves from the cluster centroid the more dissimilar features it will have compared to the ones closer to the cluster center, a confidence score system can be developed that will predict how dissimilar a new point will be compared to the predicted Feature Range for that cluster. To establish how much further away from the cluster centers do the feature predictions stop becoming reliable, the distribution of the Euclidian Distance from the Centroid for each event/point appointed to the Cluster must be observed. The answer to; what % of the training data lies within what range of its distribution will help determine the intervals based on which score can be given to a point.

It can be concluded from Figure 114 that the Euclidean distances of the training data clusters from the respective centroids in all; High Speed Data, Thermal Data and AE data is roughly normally distributed. From the probability plot or QQ plots (Quantile-Quantile plots) it is seen that most data roughly lie on or in the very close proximity of the best fit line and within 95% confidence intervals.

The Null Hypothesis here (Data is normally distributed) is not rejected for the Alternative hypothesis (Data is NOT normally distributed) as P> 0.05(α=0.05) for all the data sets.

If data has a ideal Standard Normal Distribution often the "3 Sigma Rule" can be assumed. It states that 99.73% of the data should lie within 3 standard deviations of the sample set. When considering that the sample set under discussion is Euclidean distance (X) from the centroid, the data points closest to the centroid and the vast majority are the ones that lie within 1 standard deviation of the mean ($0 > X \leq \mu + 1\sigma$). 27% of the points should lie between 1 Std Dev and 2 Std Dev of the mean ($\mu + 1\sigma < X \leq \mu + 2\sigma$) which is a bit further away from the centroid and 5% of the data points lie above 2 Std Dev of the mean ($X > \mu + 2\sigma$).

As can be recalled in the K means clustering algorithim aims to group data points with similar features based on their Euclidean distance from the centroid of that Cluster. The Feature Range Prediction methodology proposed in this research utilizes the majority of the data within the min and max of the box plots and eliminates the outlier I.e. does not take into consideration some of the data. The distribution shows that roughly 68% of the data lies within $0 > X \leq \mu + 1\sigma$, and 95% within ($\mu + 1\sigma < X \leq \mu + 2\sigma$). It is also known that majority of the data should lie closer to the center of the Cluster by the internal mechanisim of K means clustering. Based on these points, it seems to be correct to assume that the interval range shown in Figure 113 will serve as a good criteria for defining ranges where an individual confidence scoring system can be established.

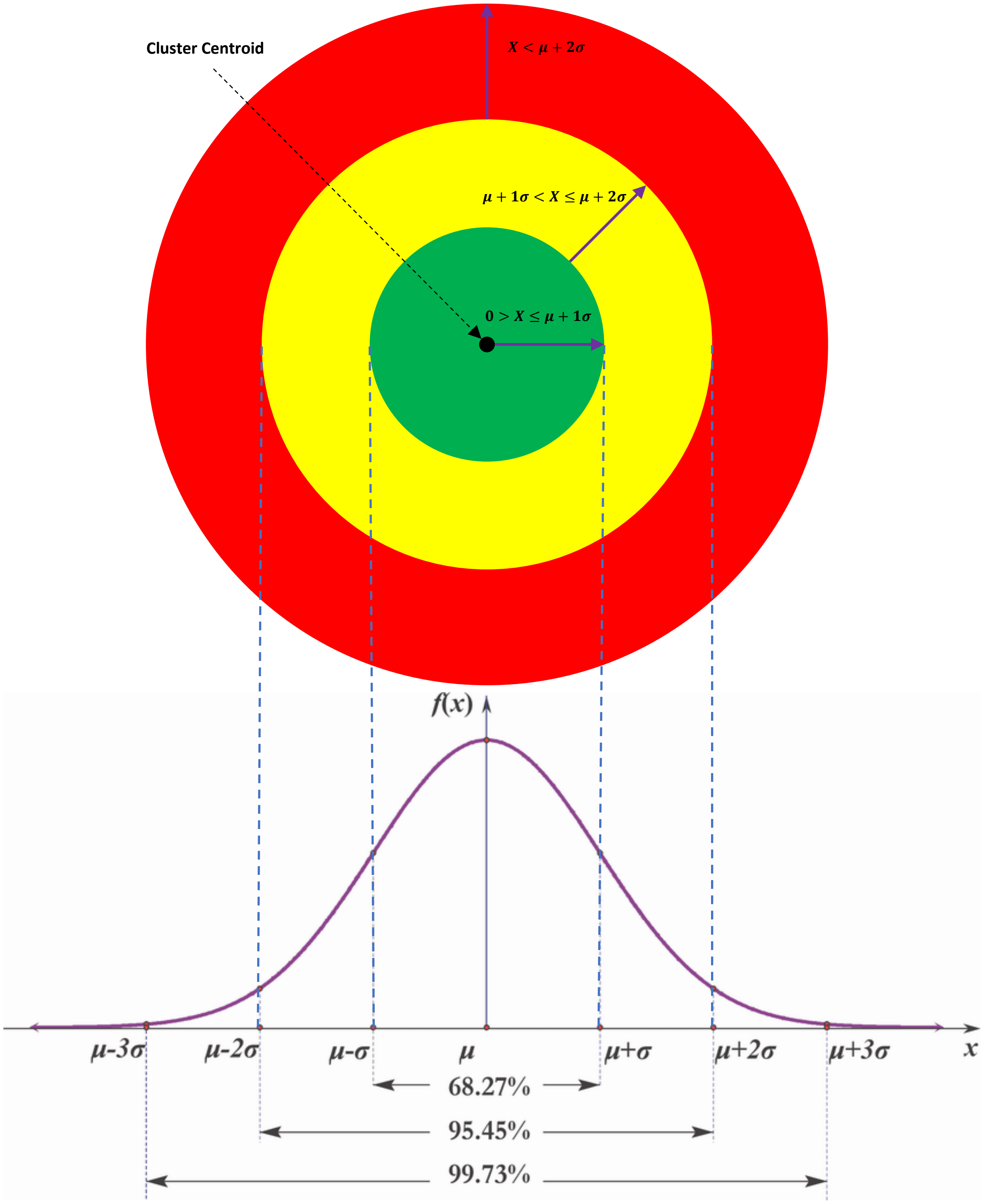

Figure 113: Confidence Interval Range based on "3 sigma rule"

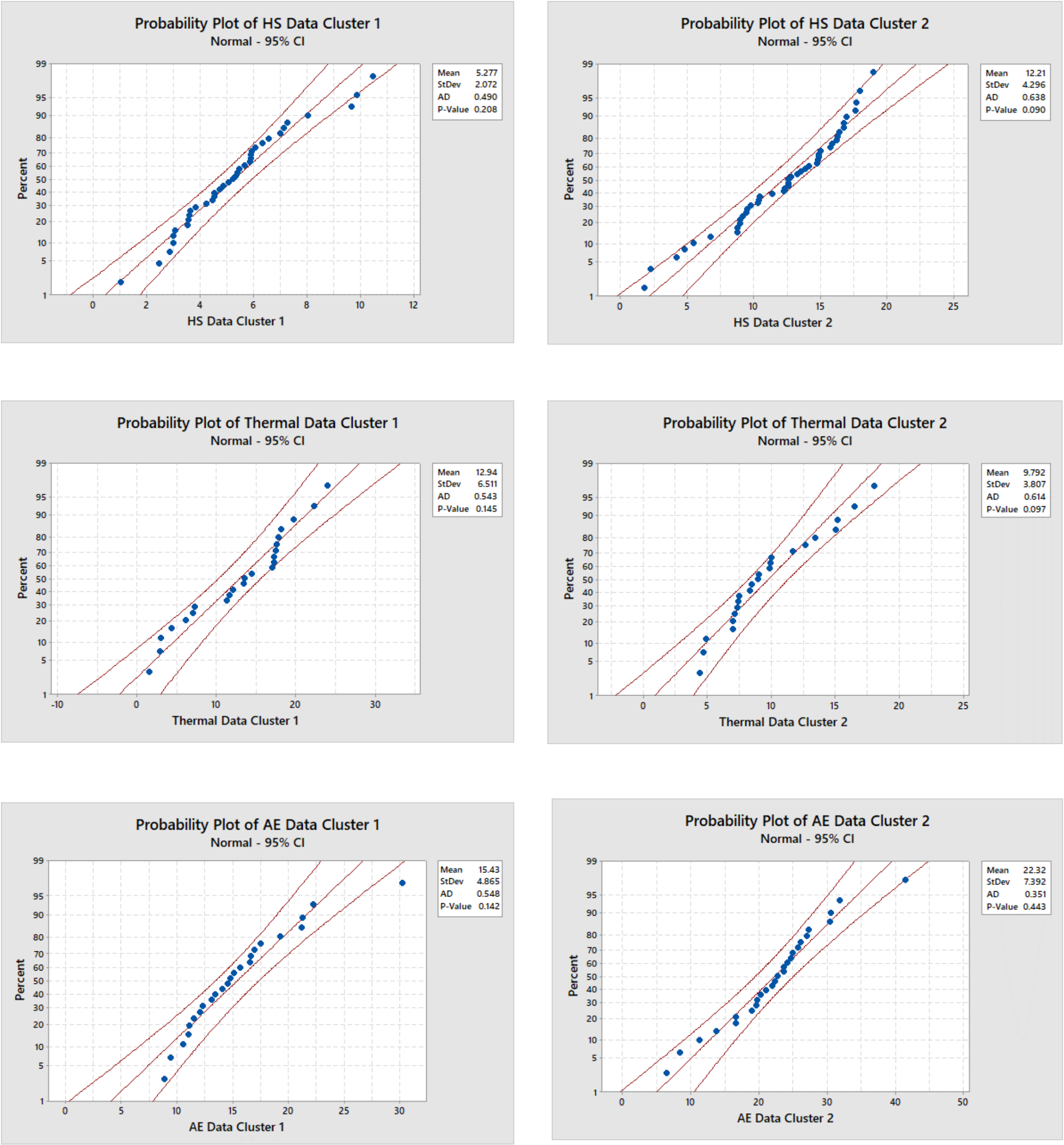

Figure 114: Normality Test for Euclidian Distances

Table 29 shows the individual score given for each sensor. When the data point lies within $(0 > X \leq \mu + 1\sigma)$ it is the closest to the centroid and is given a score of 1,if it lies within $(\mu + 1\sigma < X \leq \mu + 2\sigma)$ it is given a score of 0 and finally if more than $(X > \mu + 2\sigma)$ its given a confidence score of -1. As it is evident 1 is the highest confidence score (Closest to centeroid) and -1 is the lowest (Furthest from the centeroid. Once all three sensors are alloted a individual confidence score, using (Equation 28 a collective confidence score is calculated. This Collective Confidence score is used to calculate the % Confidence by mapping the Collective Confidence Score on to % Confidence Scale (0 to 100%) using Linear mapping as shown in Figure 115 . It should be noted that the %confidence is a measure of how well the fusion algorithm worked.

Standard Deviations	$0 > X \leq \mu + 1\sigma$	$\mu + 1\sigma < X \leq \mu + 2\sigma$	$X > \mu + 2\sigma$
Individual Score	1	0	-1

Table 29: Individual Scoring System

$$p = p_{HS} + p_{Th} + p_{AE}$$

(Equation 28: Collective Confidence Score)

$p = Confidence\ Score$

$p_{HS} = High\ Speed\ Cluster\ Confidence$

$p_{Th} = Thermal\ Data\ Cluster\ Confidence$

$p_{AE} = Acoustic\ Emission\ Cluster\ Confidence$

$$\%\ Confidence = (p - A) \times \left(\frac{D - C}{B - A}\right) + C$$

(Equation 29: % Confidence Score)

$A = Confidence\ Score\ Range\ Start$

$B = Confidence\ Score\ Range\ End$

$C = \%\ Confidence\ Range\ Start$

$D = \%\ Confidence\ Score\ End$

Figure 115: % Confidence Scale

7.4. Discussion

This Chapter explains the step-by-step detail on how the system is trained and how it outputs its prediction ranges for specific features. It explains how raw data is processed converted to time and spatial domain and stitched with defect data collected offline. It further explains the steps of extracting Events out of these stitched data sets and then clustering them and using the data distribution of the data in each cluster to construct a prediction table. It also explains how the working of the K means clustering algorithm can be leveraged into approximating how reliable or precise the predicted values will be. At the end it shows how the fusion equation works and how % confidence scoring system is developed and implemented.

Firstly, the defect data is extracted from the XCT scan images and using specific criteria and scaling techniques the type, position and size of the defects can be established with respect to the direction of how the deposition was laid down. This data is also converted into the time domain by the aid of the laser head scanning speed i.e., how fast the laser head moves over the deposit and physically measured length of the deposit. The limitation of this method is that the research assumes that the defects are created at the same time as the laser head is over that position along the length of the deposit where the defect developed. It also assumes that the epicenter of the defects lie at their geometric centers. While this may not always be true, the fact that the melt pool size at instant is very small for a single track and the extremely quick cooling rates would dictate that these defects would not develop that far off from the laser beam spot. Figure 116 show the avg size of defects generated during the defect provocation. It is seen that largest avg cracks are created in the contaminated powder experiment and largest avg pores are generated in the surface finish experiments. Figure 117 shows the same graphs compare to avg size found in the literature and it can be seen that it is much larger than the defects generated in the experiments of this research. This may be a good thing since it may go to show that the proposed system can catch smaller defects.

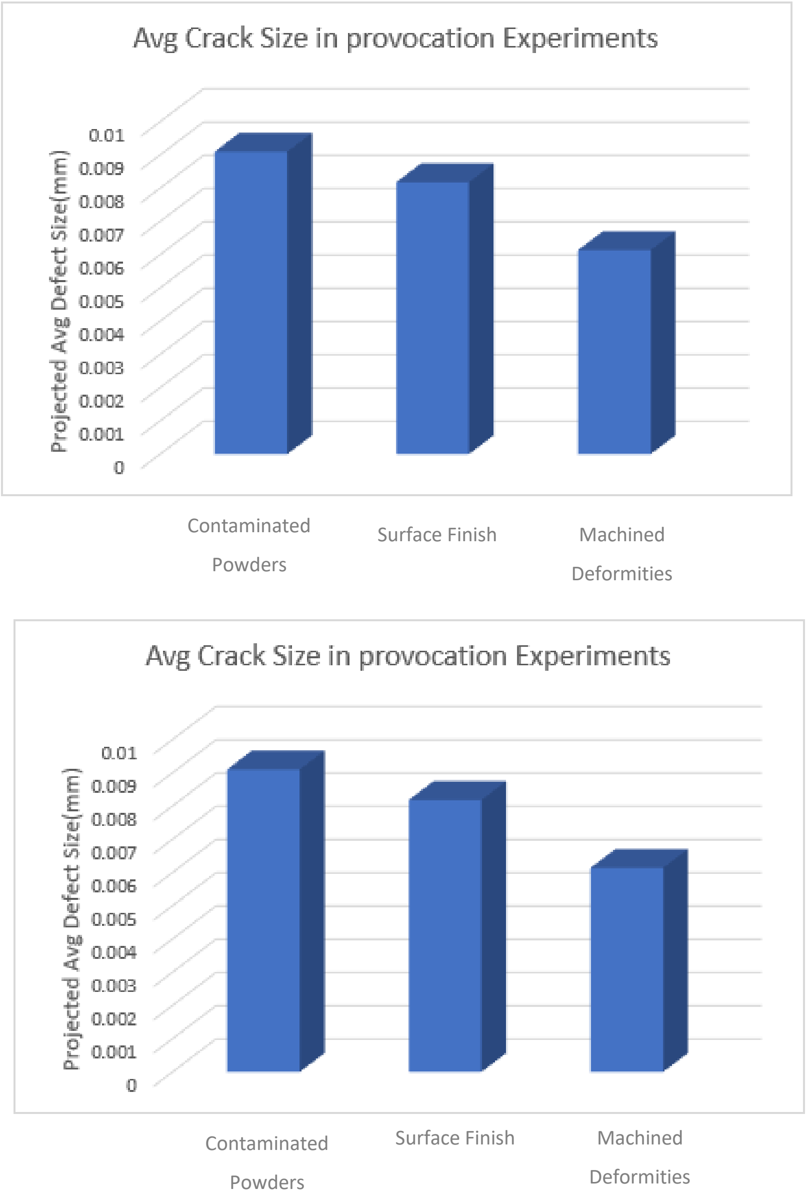

Figure 116:Avg Defect Size in defect provocation Experiments

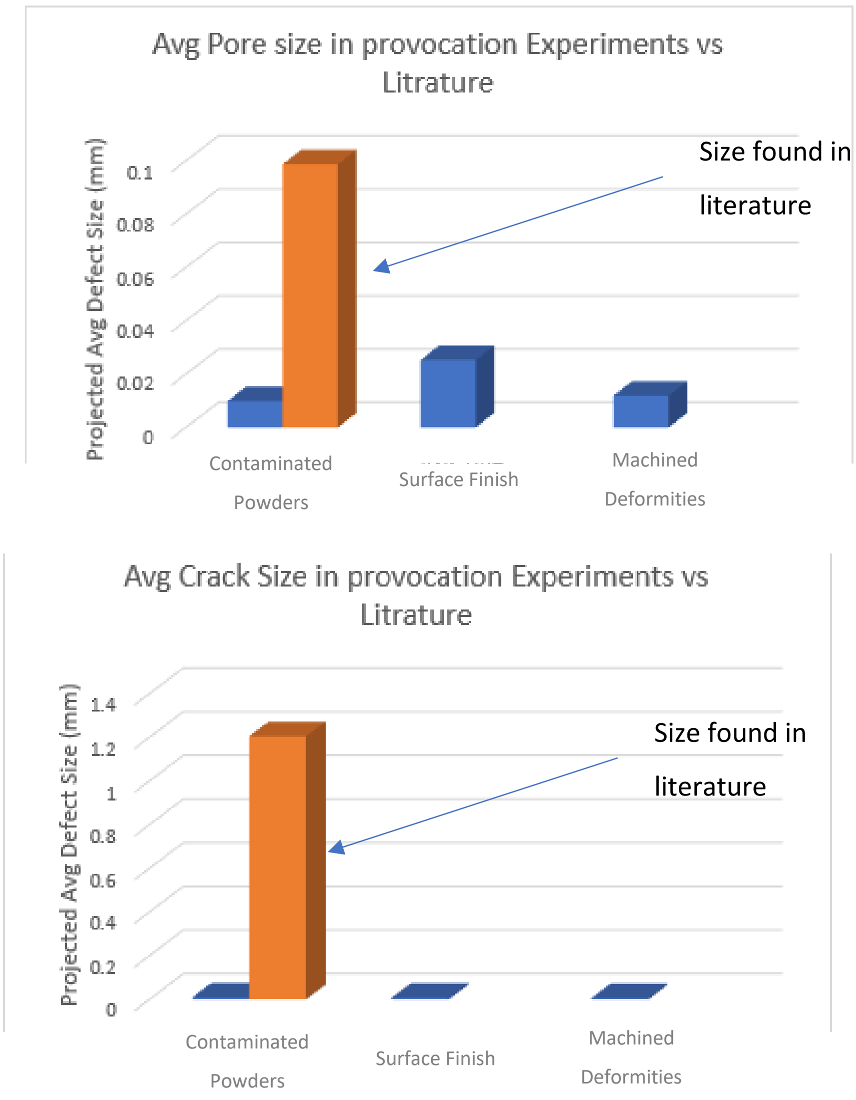

Figure 117: Avg Defect Size compared to Avg size found in literature

The HS speed camera data is processed, and a reconstruction is made of the images using a technique called Z projection. In this technique melt pool images are overlapped over each other. The overlap technique is such that is sums the pixels the image that overlap each other. This means that if a high intensity pixel overlaps one with a lower intensity the reconstructed image will display the intensity of the higher pixel at that point. The advantage of this can be seen in Figure 118 where if a previous frame displays high intensity pixels at a certain point they are not lost in the overlapping process and also show position along the length in the reconstructed image.

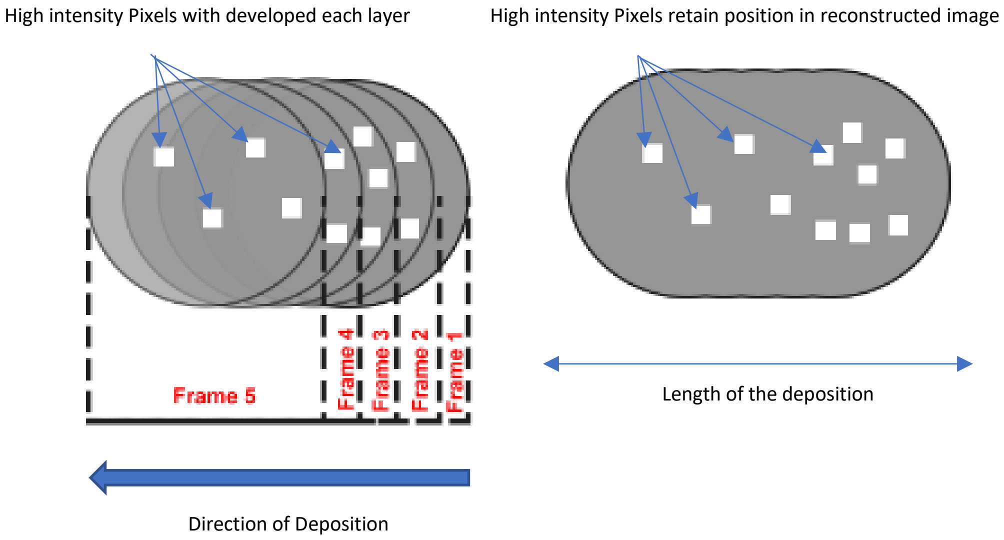

Figure 118: a) Frame by Frame overlap using z projection b) Image reconstruction retaining high intensity pixel positions

An intensity plot is used to construct an intensity profile along the length of the deposit. As shown in Figure 119 this method takes each Column along the width of the deposit and takes the average intensity of that column. This yields a singular value which is used to construct and intensity profile which is then converted in time and spatial domain and stitched to defect data. Certain events are extracted using a thresholding technique from the stitched intensity profiles. This technique establishes a threshold value using a melt pool image that is stable i.e., does not contain any high intensity pixel zones. The threshold establishes what levels of intensities need to be crossed so that the signal that crosses this threshold will be called an Event. The justification of the thresholding technique is intuitive since high intensity pixel zones equal high temperature zones and wherever high temperature zones develop there is a likely hood that a defect will develop. Events extracted from the stitched data are plugged into the clustering algorithm which groups events with like features.

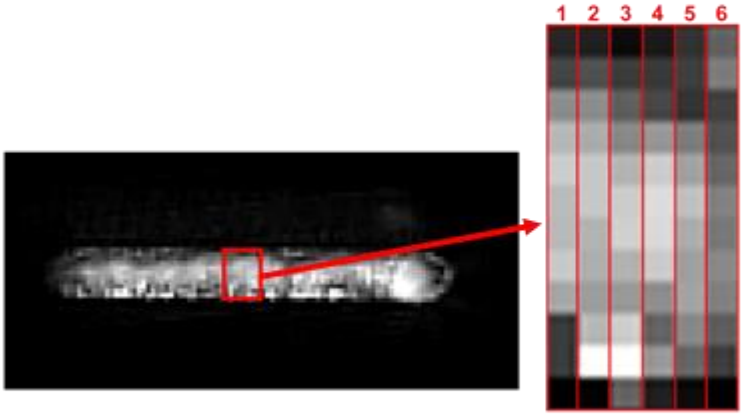

Figure 119: Method of intensity profile construction

For the thermal images a similar technique is used to develop temperature profiles which are converted into spatial domain. Both time domain and spatial domain data is stitched on to defect data to generate new data sets. From these data sets Events are extracted using a thresholding technique which looks for quick change in thermal intensities. Any signal that has a certain rise rate which is followed by a fall is considered an Event. Once again events are extracted and clustered to generate two distinct clusters. It is found that defect size increases cool down rate, and this is an agreement with literature which states that cooling is affected due to development of defects since they disturb the heat sync effect not allowing the heat to dissipate efficiently.

Even though AE data in time domain is sufficient to be stitched to defect data for events to be extracted, an attempt was made to stich calculated position of an AE Event on to the defect data. Position data was unreliable since only two sensors were used to calculate position and some events gave anomalous position data. The position for events that are caused by large defects only provide relative accurate position data. It is however found that signal amplitude might be related to defect size since large defects coincide with high amplitude AE events. AE data events are extracted from stitched data in the time domain and clustered to develop a prediction table. When analyzing spectrum of the AE signal it is found that a single event contains different frequencies of varying power. This may indicate that a single envelope may not represent a single event and could represent a superimposed wave containing the signal of multiple waves generated from different defect sources.

All Events for each sensor are clustered using a unsupervised learning algorithm called K Means clustering algorithm. K means uses the Euclidean distance to assign an event to specific cluster to which a point is closest. Using The Calinski-Harabasz scoring method the optimal number of K clusters are determined and it turns out the optimal number of cluster for all 3 sensor data was 2. This may be because the defects are of two types: Cracks and Pores and clusters formed are based on this. This theory is supported by the fact that for each sensor one cluster only contains cracks and the other contains pores and cracks. The distribution of each cluster of each sensor is analyzed and using a box and whisker plots out liers are eliminated and as result produces new max and min values. These values will serve as prediction range if a new event is appointed to a particular cluster.

After the prediction tables are established, it is placed in the data fusion equation which combines the results for all three ranges for a particular feature to form one single predictive range. The reliability of this fused range is determined by % confidence value. The % confidence value is formed by the individual confidence score of each sensor. This is established based on how far from the cluster center the new event lies. The further away from the cluster center the new Event lies the less likely it is to be like the events closer to the cluster center. Hence the distance of an event from the cluster center becomes a metric of how accurate the prediction value will be.

Chapter 8: Statistical Analysis and Verification

The system aims to predict a feature range for a single new Event (New point) or Group of Events for an entire sample (Group of points) during a deposition. It collects the data during the deposition, processes the data, Extracts events from the processed data and places them in the Sensor Cluster Models and assigns them to a Cluster closest to them. Based on the cluster appointed to them, the system predicts a range for the features and based on the distance from the cluster centroid, gives the prediction a confidence score. Predicted Feature Ranges from all 3 Sensors Cluster Models are “fused” using (Equation 27 and the final % Confidence is calculated (Equation 29.

8.1. Feature Prediction

The system predicts the ranges for Total number of Defects, Total Number of Pores, Total Number of Cracks, Max Size of defect and Total Defected Area. The accuracy/ functionality of the system is put through multiple statistical tests and compared to other methodologies of defect detection. Particularly it is tested for number for Total Defects and defect classification. As per the research carried out for this thesis, other systems are not capable of predicting Max defect size and Total Defected Area and hence it is verified using statistical tests.

8.1.1. Feature Range Prediction

The systems’ primary function is to predict a range in which the detected Events actual value lies. To verify the accuracy of the system the data from a random sample is analyzed whose XCT analysis is also available to us. Using Table 30, every time the system predicts the correct feature range for an event, the event is given a score of 1 (100% accurate) and every time the new points feature lies outside the predicted range the Event is given a score of 0(0% accuracy). Using this method, a table containing a binary data set of (Accurate and Inaccurate predictions) can be created from which the accuracy of the system can be judged.

	Within Predicted Range	Outside Predicted Range
Appointed Accuracy Score	1(100%)	0(0%)

Table 30: Binary Output Look Up Table

Table 31 shows a set of randomly selected events from a sample and their accuracy score calculated using the method mentioned above. Where D# is the Total Defects, # Total Pores, # Total Cracks, MDS is the max defect size and DA is the defected area.

Predicted Defect Feature Ranges										Actual Defect Features					Predicted Accuracy				
Total Defects		Pores		Cracks		Defect Size		Total Defected Area		Total Defects	Pores	Cracks	Max Defect Size	Total Defected Area	# D	# P	# C	MDS	DA
Max	Min	Max	Min	Max	Min	Max	Min	Max	Min										
57	5	54	5	9	1	0.7462	0.01	1.1871	0.0529	39.5	34	4.5	0.137038	0.680165	1	1	1	1	1
57	5	54	5	9	1	0.7462	0.01	1.1871	0.0529	33	29.3	3	0.094038	0.466118	1	1	1	1	1
57	5	54	5	9	1	0.7462	0.01	1.1871	0.0529	24	24	0	0.261699	0.721129	1	1	0	1	1
57	5	54	5	9	1	0.7462	0.01	1.1871	0.0529	29	29	0	0.474577	1.302605	1	1	0	1	1
57	5	54	5	9	1	0.7462	0.01	1.1871	0.0529	21.5	21.5	0	0.253133	0.593541	1	1	0	1	1
57	5	54	5	9	1	0.7462	0.01	1.1871	0.0529	29	29	0	0.441786	0.509223	1	1	0	1	1
57	5	54	5	9	1	0.7462	0.01	1.1871	0.0529	28	37.5	8	0.041647	0.465813	1	1	1	1	1
79	20	76	19	0	0	0.7462	0.0855	1.853	0.836	55	54	0	0.064105	0.691615	1	1	1	1	1
57	5	54	5	9	1	0.7462	0.01	1.1871	0.0529	32.3	30.6	0	0.101918	0.312673	1	1	0	1	1
57	5	54	5	9	1	0.7462	0.01	1.1871	0.0529	29	25.5	3.5	0.076361	0.468168	1	1	1	1	1

Table 31: Binary Accuracy Data fused Predictions for a random Sample

8.1.2. Single Feature Value Prediction

Most researchers have developed systems or used methodologies that predicts a single number for a feature e.g. (Khanzadeh & Bian, 2016) uses Self Organizing Maps to predict total number of defects. Even though the system is not designed to predict a single value, for the sake of having values to compare with other researchers the thesis will go a step further to devise a method by which the system can predict a single value.

For this average values ((Equation 30) are used of the predicted feature range for all the events and their actual average feature values ((Equation 31) taken from the stitched data.

$$F_{avg} = \frac{F_{Max} + F_{Min}}{2}$$ (Equation 30: Avg Feature Value Calculation)

$$D_{avg} = \frac{D_{HS} + D_{Th} + D_{AE}}{3}$$ (Equation 31: Average Actual Defect Value Calculation)

$D_{HS} = Actual\ Defect\ Value\ associated\ with\ High\ Speed\ Sensor\ Event$

$D_{Th} = Actual\ Defect\ Value\ associated\ with\ Thermal\ Sensor\ Event$

$D_{AE} = Actual\ Defect\ Value\ associated\ with\ Acoustic\ Emission\ Sensor\ Event$

$D_{avg} = Actual\ Average\ Defect\ Value$

$F_{avg} = Average\ Feature\ Value$

Using the tables constructed from (Equation 30 and (Equation 31 a multi variable regression models can be developed from the collection of events for each feature. Using Table 32, models are constructed for Total Defects, Total Pores, Total Cracks, Max Defect Size and Total Defected Area.

F_{avg} by HS Cluster Prediction ((Equation 30)	F_{avg} Thermal Cluster Prediction ((Equation 30)	F_{avg} by Acoustic Emission Cluster Prediction ((Equation 30)	Actual Average Feature ((Equation 31)

Table 32: Data Variables used to create single value predictions

(Equation 32 shows the Regression model used to predict single values for the Total Defects. It's important to mention that the data is normalized before the models are constructed and the model output is scaled accordingly to reflect real data values.

$$\text{Total Defects} = 26.9 + 9.98HS_{avg} + 3.53 * Th_{avg} + 6.3{HS_{avg}}^2 - 14.72HS_{avg}Th_{avg} - 0.15AE_{avg}$$

(Equation 32: Single Value Predictor Model using Multiple variable Regression)

The modeling data shows that Multi Regression Models are not efficient method of representing the system but a necessity for comparison with the other research. In places where the model gives negative values, they are considered 0. Table 33 shows the results of the Multiple Regression Models and the % Accuracy in their representation for a randomly selected sample of Events.

HS	HS Scaled	Th	Th Scaled	AE	AE Scaled	Total Defects	Regression Fit Prediction	% Accuracy
31	-0.01813	25	0.323149	0	-1.46987	39.5	27.26855	69.0343
31	-0.01813	43	1.196524	14	1.102404	33	30.19885	91.51168
31	-0.01813	0	-0.88987	14	1.102404	24	22.27695	92.82063
31	-0.01813	43	1.196524	0	-1.46987	29	30.5847	94.53553
31	-0.01813	0	-0.88987	14	1.102404	21.5	22.27695	96.38627
31	-0.01813	0	-0.88987	0	-1.46987	29	22.66279	78.14756
31	-0.01813	43	1.196524	0	-1.46987	28	30.5847	90.76894
49.5	1.440462	43	1.196524	1	-1.28614	55	32.4939	59.07982
31	-0.01813	43	1.196524	3	-0.91867	32.33333	30.50202	94.33613
31	-0.01813	0	-0.88987	11	0.551202	29	22.35963	77.10218
							Average %	84.37231

Table 33: Accuracy for single value prediction using Multiple Regression Model

8.1.3. Feature Prediction for an entire sample

For the entire sample the defects are calculated a little differently as recurring defects are taken into consideration due to 30% overlap between the three layers. Also, the methodology of calculating the Total Defect, Pores and Cracks is different from how the Max Defect Size is calculated. Total Defected area however cannot be calculated for the entire sample because the calculation cannot take % overlap into consideration since this feature is an Area and hence makes this a feature predicted only for single events.

The total number of defects, cracks and pores for each sensor data is calculated by first calculating the estimated Overlap compensation as shown in (Equation 33. This takes into consideration % Overlap (which in the case of the deposits produced during the experiments of this research is 30%) and the Number of Overlapping zones. The next step is to again the sum of that entire feature set for all events from the calculated approximate of the overlap compensation. The compensated sums for all 3-sensor data can now be plugged into the previous used (Equation 25 and (Equation 26 to calculate the final range prediction for the feature.

$$Z = \left(\left(\sum_{i=1}^{n} x_i \right) \times \%Overlap \right) \times N \quad \ldots$$

(Equation 33: Overlap Compensation Calculations)

$$F = \sum_{i=1}^{n} x_i - Z$$

(Equation 34: Calculating the feature for an entire sample)

$N = Number\ of\ overlaping\ layers$

$n = Number\ of\ total\ number\ of\ events$

$x = Feature\ Value\ for\ event$

$Z = Overlap\ Compensation$

$F = Feature\ value\ for\ the\ entire\ sample$

For the confidence score for the entire sample, the sum of all the individual scores of the events for each sensor data is calculated and then use the linear mapping technique to project the sum of score onto a range of -1 to 1. The range being projected is calculated by using the total number of events from which the score was calculated as shown in Table 34. Now it is simply put through the same process by plugging it in (Equation 28 and calculating the overall % Confidence using (Equation 29.

A (Original Min)	B (Original Max)	C (New Range Min)	D (New Range Max)
$Total\ \#\ Events \times (-1)$	$Total\ \#\ Events$	-1	+1

Table 34: Range of Each Sensor Data when calculating for entire sample

The singular value for the Max Defect Size is calculated by taking the Max and Min Range of Max size feature from the predicted ranges of all the events. The average is taken from the Max Defect Size from each respective sensor data sets and this becomes the predictor range. The results for the feature prediction for the entire sample are shown in Table 35 along with the actual defects and Max Defect size found in that entire sample through XCT. Intuitively taking the average of Max defect size may seem wrong but it is important to understand these are prediction values which may be over or underestimating hence to take largest number may be in accurate.

	Total Defects		Pores		Cracks		Max Defect Size		% Confidence Score
	Max	Min	Max	Min	Max	Min	Max	Min	
	224.6667	32	218.1333	30	27.46667	9.6	0.706394	0.016166	62.02%
mean	128.3333		124.0667		18.53333		0.36128		
Actual	158		144		9		0.693978		

Table 35: Results for Feature Prediction for an entire sample

For the entire sample it can be seen that predicted defect ranges are much larger (Values between Max and min) than the ones calculated for a single event. However, the actual values (values collected via Stitched data) do lie within the predicted ranges. The mean values of the ranges are much closer to the actual quantities of defects although it can be seen that mean value for the cracks for the sample has been over approximated. It can also be seen that the confidence score has dropped even lower to 62%.

8.2. Total Number of Defects

This section looks at the methodologies used to verify results for total defects and compare them to other researchers. It also uses Statistical Methods to verify the calculated results for the Total Defects predicted Range and

8.2.1. Precision Calculation

(Khanzadeh & Bian, 2016) suggest a verification method by calculating the precision of the system using (Equation 35 for an entire sample. The method divides the number of defects detected via the Self Organizing Maps method and the number of defects detected via the XCT during post analysis study of the deposit.

$$Precision = \frac{Defects\ via\ Methodology}{XCT\ Defects} \times 100 = 62.75\%$$

(Equation 35: Accuracy Verification Method by (Khanzadeh & Bian, 2016))

If the total mean number of total defects predicted (Table 35) is plugged into (Equation 35, it outputs an accuracy of 81.22% as far as predicting total number of defects in the entire sample is concerned. (Khanzadeh & Bian, 2016) computes their systems precision to be at 62.75% when it comes to predicting the total number of defects in the entire sample using their methodology. Hence it can be concluded that the total defects prediction using the Multi Sensor Data Fusion methodology yields a much higher precision using the proposed precision calculation methodology.

$$Precision = \frac{128.33}{158} \times 100 = 81.22\%$$

(Equation 36: Precision Verification using predicted total defects)

8.2.2. Linear Regression Model

(Barua & Frank Liou, 2014) use Sum of residuals (SOR) or SSR technique to verify their research statistically hence to use this technique some sort of regression model was developed. Since a similar vision-based technique was used in the methodology presented by this research, a model is generated using Regression Analysis on the High-Speed Data to predict Total Defects.

Term	Coefficients	Standard Error	P-Value
Constant	0.00	0.139	1
Max Intensity	-0.289	0.141	0.047
Spike Frequency	-0.277	0.141	0.056

$$y = \beta_0 + \sum_{i=1}^{n} \beta_i x_i$$

$$y = 0.00 - 2.89x_1 - 2.77x_2$$

$$x_1 = Max\ Intensity\ , x_2 = Spike\ Frequency$$

Max Intensity	Spike Frequency	Model Predicted	Model Predicted Non-Scaled	Actual	Accuracy
0.22559	-0.92855	0.322403	22.0508	41	0.537824
-0.65903	-0.88353	0.054278	19.55857	36	0.543294
1.288564	-0.92855	0.629603	24.90623	29	0.858835
-1.40759	0.647988	-0.58629	13.60452	20	0.680226
-1.77598	-1.06952	-0.217	17.03703	32	0.532407
0.478563	-0.9335	0.396884	22.74311	41	0.55471
-0.8186	0.785626	-0.45419	14.83232	36	0.412009
0.238261	0.499713	-0.06956	18.40747	29	0.63474
-0.96849	-0.21953	-0.21908	17.01769	21	0.810366
-1.73093	-1.35945	-0.12367	17.90452	31	0.577565
1.275667	-0.92259	0.624225	24.85624	41	0.60625
-1.03683	-0.10575	-0.27035	16.54114	35	0.472604

-0.66903	1.260516	-0.54251	14.01141	29	0.483152
0.422106	0.658937	-0.06054	18.49137	21	0.880541
-0.00376	-0.92199	0.254305	21.41783	23	0.93121
				Average Sample Accuracy %	63.43823

Table 36: Output of the Linear Regression Model

8.2.3. Wilcoxon Signed Rank test for Total Defects Accuracy

The precision verification methodology and linear regression model yield an accuracy of 62.75% and 63.43% respectively. Even though precision wise the multisensory system yields a higher accuracy a statistical verification needs to be carried out of the accuracy of the multisensory system in comparison to the two % accuracies mentioned above. A statistical method to validate this would be to use the Wilcoxon Signed Rank test for One Sample. Wilcoxon Signed rank test is meant to determine if a median of a population is equal to a theoretical value (Null Hypothesis) or the median of population is not equal to a theoretical value (Alternative Hypothesis). The reason for using Wilcoxon Signed Test for this purpose instead of One sample t test is because the Population distribution is non-parametric i.e., does not follow any known or well understood distribution. To use this test the population distribution of the data must be symmetric, and the sample being analyzed must be a random sample.

The Null Hypothesis here is that the median value in this set is 63.43 and claim i.e., the Alternative Hypothesis is that the accuracy produced by the proposed methodology is higher than 63.43. Table 37 shows the results from the Wilcoxon Signed Rank Test and a P value of 0.01. The P values are much lower than the significance level of 5% which means the null hypothesis can be rejected in favor of the alternative hypothesis that the median value is greater than 63.43. It is very important to mention that this only means that there is sufficient evidence to reject the null hypothesis NOT that there is no chance for the null hypothesis to be true.

$H_0 : \eta = 63.43\%$ vs. $H_A : \eta > 63.43\%$ where $\alpha = 0.05$			
N	Wilcox Statistic	P	Estimated Median
10	54	0.004	85.48

Table 37: Wilcoxon Signed Rank test for one Sample

8.2.4. Binomial Test for Total Defects Range Accuracy

The Multi Sensor Fusion Defect Detection Methodology is designed to predict a range within which the feature's values should lie. Hence the approach where the system outputs a single value isn't the best methodology to measure the systems accuracy. Table 31 shows a classification (1 or 0) method using which it could establish if the system gave an accurate range for an event or not. To verify this, Binomial Test is run on that same random collection of events to figure out whether this system gives a better accuracy at predicting defect ranges compared to the most accurate result (63.43%) in the LR model (Table 36).

A Binomial test can be used to statistically test a hypothesis for the non-parametric population where data is dichotomous (1-Accutrate or 2-Not Accurate). The test assumes the data is dichotomous and nominal, the sample size is significantly less than the population size, the sample is a fair representation of the population, and the data items are independent.

The Null Hypothesis in this case is that the capability of a system to get the right range is (Average Accuracy 63.43%) and consequently the Alternative Hypothesis is that the accuracy is greater than that number using the proposed system. Using (Equation 37 the probability which will help determine the chance to observe a more extreme result is calculated. Table 38 shows that a P value of less than 0.05 is produced and hence the null hypothesis can be rejected in favor of the alternative hypothesis.

$$P(X) = \frac{n!}{(n-X)!\,X!} \,.\, p^X \,.\, q^{n-X}$$ (Equation 37: Binomial Probability Formula)

$q = 1 - p = Probability\ of\ failure$

$X =$ The number of successful Samples

$n =$ The number of randomly selected items

$H_0: p = 0.6344\ (63\%)$ vs. $H_A: p > 0.6344\ (63\%)$ where $\alpha = 0.05$				
n	p	q	X	P Value
10	0.6344	0.3656	10	0.010559

Table 38: Binomial Test for total Defects

8.3. Defect Classification

Defect Classification in the proposed system is done based on the cluster that the new data points belong to and how close they are to their respective cluster centers. For verification of the logistic regression model, (Gaja & Liou, 2018)'s work is used as a reference. They use the same variables that are used in the clustering analysis for Acoustic Emission in this research. This allows for the multi–Sensor Data fusion process for defect detection in direct energy deposition's performance to be compared with the above-mentioned research.

$$y^* = ln\left(\frac{p}{1-p}\right) = \beta_0 + \sum_{i=1}^{n} \beta_i x_i$$

(Equation 38: Generic Logistic Regression Model)

$$y^* = ln\left(\frac{p}{1-p}\right) = -12.2 + 2.37x_1 - 4.78x_2 + 46.23x_3 + 0.11x_4 - 34.48x_5 + 4.91x_6 - 0.06x_7 \quad \cdots$$

… (Equation 39: Logistic Regression Model developed by (Gaja & Liou, 2018))

$x_1 = Rise\ Time$

$x_2 = Peak\ Amplitude$

$x_3 = duration,$

$x_4 = kurtosis,$

$x_5 = Ring\ Counts$

$x_6 = Energy$

$x_7 = Frequency$

The AE data for two samples is used as an input to this model and it classifies the defect for each event (Table 39).

Rise Time	Peak Amplitude	Duration	Kurtosis	Ring Counts	Energy	Frequency	y*	Model Defect Classification	
-1.1385	-1.05706	-0.82559	0	-0.83463	-0.67126	-1.9057907	-22.4158	Pore	
-1.12017	0.026233	-1.41986	0	-1.49743	1.192348	0.80643365	-23.1831	Pore	
-0.4053	0.386653	1.733102	0	0.49096	0.712826	-0.4880747	51.7135	Crack	

1.363556	0.026233	0.043817	0	-0.17184	-0.13482	-1.0460053	-1.74241	Pore	
-0.55194	1.470621	1.050785	0	1.153757	0.618254	-0.2412271	-8.69131	Pore	
-0.53361	0.386653	1.782625	0	1.153757	0.483892	-1.2324387	29.76623	Crack	
0.749497	0.026233	-1.03468	0	-0.17184	-0.50332	0.69793314	-54.9708	Pore	
1.097769	0.386653	0.186883	0	0.49096	0.587086	-0.429607	-16.8268	Pore	
-0.54277	-1.05706	-1.43637	0	-0.83463	-0.97703	-0.0160164	-50.8552	Pore	
-0.53361	-0.69664	-0.0002	0	0.49096	-1.07712	-0.0390773	-32.3588	Pore	
-1.17516	1.108756	0.896713	0	1.816553	-0.7565	-0.7717621	-45.1328	Pore	
-1.1385	-0.69664	-0.25882	0	-0.83463	-0.64888	-2.0853032	2.18351	Crack	% Accuracy
Pores/Actual Pores								9/144	6.25%
Total Cracks/Actual Cracks								3/9	33.3%
Total Defects								12/158	7.59%

Table 39: Logistic Regression Model Output

The Logistic Regression Model predicts that the sample has 9 pores, 3 cracks in a sample which contained 144 pores and 9 Cracks. (Gaja & Liou, 2018) and (Gaja & Liou, 2017) it is established that for a single event the Clustering method is good at classifying and detecting Pores and Cracks. They compare this to an artificial neural network and Logistic Regression Model. Even though it seems that the Logistic Regression Model correctly identifies defect types, it seems to be incapable of detecting all the pores and cracks. This may not be the methodology limitation rather the sensors inability to pick up all the signals. In comparison the multi sensor data fusion method seems to predict the number of total pores and Cracks with higher relative accuracy ((Equation 40 and … (Equation 41) however, it seems to over approximate cracks. In hindsight practically speaking over estimation of defects is better than underestimating defects. With multi–Sensor Defect Detection System it is seen that in a random sample of events, the system correctly classifies 10 pores but only correctly classifies 5 Cracks in 10 events. This is testament to the system inaccuracy in prediction of Cracks and is a plausible indication of underfitting of data as far as cracks are concerned. Underfitting is where training data shows high error in both test and training data.

$$Pore\ Prediction\ Accuracy = \frac{(198.6 + 113.2 + 60.4)/3}{144} \times 100 = \frac{124}{144} \times 100 = 86.11\% \qquad \cdots$$

… (Equation 40: Pore Prediction Accuracy)

$$Crack\ Prediction\ Accuracy = \frac{(24 + 15.6 + 16)/3}{9} \times 100 = \frac{18.53}{9} \times 100 = 205\%\ (Over\ estimation) \quad \cdots$$

… (Equation 41: Crack Prediction Accuracy)

8.4. Defect size and total Defected Area

The system can predict the size of Largest Defect in an event and the total defected area in an event. Total Defected Area is sum of areas of all the defects detected in an event and Max defect is the largest possible defect regardless of classification. The same Accuracy classification(Table 30: Binary Output Look Up Table) is applied to the entire training data for Max Defect Size and Total Defected area to see the overall accuracy of the system as shown in Table 40.

	Max Defect Size	Total Defect Area
Training Data Accuracy	94%	98%

Table 40: Accuracy of Max Defect Size and Total Defect Size for training data

8.4.1. Binomial Test for Max Defect Size and Total Defected Area Range Accuracy

Random data for a test sample is chosen and it is put through a binomial test to evaluate the hypothesis that the accuracy of the system is equal to the accuracy of the training data or less than the accuracy of the training data. The reason of why the alternative hypothesis is looking for probability that the accuracy is less than that of the training data is because it would be a matter of concern if the accuracy is lower since the accuracy training data is already very high. Table 41 shows the Binomial Tests and it reveal that for both test P values are greater than 0.05 which means the null hypothesis CANNOT be rejected in favor of the alternative hypothesis and there is not sufficient evidence to support that there is chance the data is lesser than the training data.

	Hypothesis	N	p	q	X	P Value
Max Defect Size Binomial Test	$H_0 := 0.94\ (94\%)$ vs. $H_A :< 0.94\ (94\%)$ where $\alpha = 0.05$	10	0.94	0.06	10	0.53861511
Total Defected Area Size Binomial Test	$H_0 := 0.98(98\%)$ vs. $H_A :< 0.98\ (98\%)$ where $\alpha = 0.05$	10	0.98	0.02	10	0.81707281

Table 41: Hypothesis Testing for Max Defect Size and Total Defected Area

8.5. Discussion

The Statistical analysis and Verification Chapter mainly aims to analyze the performance of the system by comparison to other methods and uses statistical methods that would imply that there is enough evidence for the hypothesis of the system accuracy. The system is made to predict data fused ranges for Total Number of defects, Total number of Pores, Total Number of Cracks, Max Defect Size and Total Defected Area.

For the sake of comparison, the systems range needs to be converted into single values. Even though this is NOT the output function of the original system this is the need so that the systems accuracy can be compared. For this purpose, a multiple variable regression model is generated using Minitab however this method will lower the systems original accuracy. The multiple regression model outputs single values for Total number of defects inputting the data from all three sensors predicted ranges.

The second accuracy measure is of the systems original function. I.e., output feature range. To calculate the accuracy per event a look up table is used which will give 100% accuracy score if the actual value lies within the predicted range and 0% accuracy score if it does not lie within that range. This way the systems performance can be rated. Table 42 shows the Accuracy of prediction feature values using different methods some of which are presented by other researchers. One of the reasons the multi sensor data fusion method show 100% accuracy is because the training data is very well fitted however the accuracy in predicting cracks is relatively lower. Majority methods aim to predict total number of defects and only one predicts defect type i.e., classifies defects. Most other methods do not predict Max size and total defected area. Even though AE Logistic Regression Model is pretty accurate in predicting whether an event contains pores or cracks it cannot predict total number of pores or cracks in the entire sample correctly. The same goes for optical and SOM methods which are accurate to some extent in predicting total number of defects. This might be testament that the single sensor approach has its limitations compared to the multisensory approach.

	Single Event or Entire Sample	Total Defects	Total Pores	Total Cracks	Max Defect Size	Total Defected Area
Multi Sensor Data Fusion Method (range prediction)	Avg per event	100%	100%	50%	94%	98%
Multi Sensor Data Fusion Method (Single Value Prediction)	Entire Sample	81.22%	N/A	N/A	N/A	N/A
	Avg per Event	84.37%	86.11%	205% (Over estimation)	N/A	N/A
Optical Camera Data Linear Regression Model	Avg per Event	63.34%	N/A	N/A	N/A	N/A
AE sensor Logistic Regression Model	Entire Sample	6.25%	6.25%	33.3%	N/A	N/A
Precision Calculation Method	Entire Sample	62.75%	N/A	N/A	N/A	N/A

Table 42: Methodologies and their Accuracies

The System carries out statistical test and are shown in Table 43 to test out hypothesis of accuracy. These statistical tests are only used to calculate whether there is a probability that accuracies more extreme than the ones calculated based on the sample set may be observed.

Feature	Test Type	Hypothesis	P Value	Rejected
Total Defects	Wilcox Statistic	$H_0: \eta = 63.43\%$ vs. $H_A: \eta > 63.43\%$ where $\alpha = 0.05$	0.004	H_0
	Binomial Test	$H_0: p = 0.6344\ (63\%)$ vs. $H_A: p > 0.6344\ (63\%)$where $\alpha = 0.05$	0.010559	H_0
Total Pores	N/A	N/A	N/A	N/A
Total Cracks	N/A	N/A	N/A	N/A
Max defect Size	Binomial Test	$H_0: = 0.94\ (94\%)$ vs. $H_A: < 0.94\ (94\%)$ where $\alpha = 0.05$	0.53861511	H_A
Total Defected Area	Binomial Test	$H_0: = 0.98(98\%)$ vs. $H_A: < 0.98\ (98\%)$ where $\alpha = 0.05$	0.81707281	H_A

Table 43: Statistical Tests

Chapter 9: Conclusion and Further works.

This chapter aims to conclude the research by providing a summary of the key findings of the research considering the research aims and objectives. It will explain what contributions the study makes to the current field along with the limitations of the study. Lastly it will present possible future works.

This study aimed to investigate and develop a solution capable of solving the limitations (type of information, level of Information, and reliability of information) of the single sensor approach in online defect detection systems in laser metal deposition. The type of information here is the phenomenon the system observes, the level of information is the feature that can be inferred or predicted from the phenomenon being observed and lastly the reliability of the information is how accurately a feature can be predicted from the information available.

The research presents a solution to the above-mentioned problems in the form of a methodology that can detect defects and generate prediction ranges for the total quantity, type, size, and defected area of the detected defects with relatively higher accuracy. Not only this, but the research provides a unique multi-sensory platform architecture that is an essential part of this methodology. The platform uses specific sampling times to pick up essential windows of the defect development cycle. Along with this it develops a unique data fusion algorithm which combines data from different sensors to present a singular prediction range along with a confidence value which is a metric for how reliable the generated prediction range is. When compared to the state of the art this system provides a higher accuracy in terms of predicted total defects and type of defects along with their quantities. The system also provides predictions for two other features: Max Defect Size and total defected area which are not seen in systems in the state of the art.

The system and its results show that it was successful in detecting defects and predicting the features of these results with relatively higher accuracy than the methods in the literature. The system can predict Total Defects, Total Pores, Total Cracks which some previous systems have been able to predict too (Khanzadeh & Bian, 2016), however as mentioned earlier the system also predicts Total Defected Area and Max defect size which is not seen in the state-of-the-art literature. The results show that the system has an accuracy of 81.22% in predicting total number of defects in an entire sample and an accuracy of 86.11% in predicting total number of defects per detected Event. Since the study takes a lot of its events from other literature it was possible to feed the same data into models that existed in the literature. The

Linear model used by (Barua & Frank Liou, 2014) yields an accuracy of 63.34% in detecting total number of defects and (Khanzadeh & Bian, 2016) methods yields and accuracy of 62.75%. Logistic Regression models used by (Gaja & Liou, 2018) yield an accuracy of 6.25% in predicting pores and 33.3% accuracy in predicting cracks. The relative higher accuracy can be attributed to many things that was done differently in this study which includes the multi-sensory system designed based on timing of the defect development cycle, Data Stitching technique, Training the system on a variety of provocation techniques and the unique Data fusion methodology.

The research extracts events from stitched data sets that contain both signal and defect data in both time and spatial domain. This approach allows for "Events" that indicate the presence of possible defects that exist both in time and spatial domain to be extracted. This is one of the reasons why the system yields a higher accuracy compared to "Events" extracted from single domain extraction methods seen in (Fujun Wang, 2008) (Gaja & Liou, 2017) (John A. Slotwinski & E.J. Garboczii, 2014) (Barua & Frank Liou, 2014). Along with the fact that these signals can be seen in reference to the defects which verifies previous literature in terms of signal change when a defect develops, and the relation of these signals to the properties of the defect (Wu, Cui, & Xiao, 2020). (Gaja & Liou, 2017) states that the number events roughly agree with the number of defects found in the post analysis microscopic study. However, they do not have any mechanism through which they can correlate an AE event to a specific defect or group of defects found in the microscopic analysis. This problem is solved by stitching data as this method allows for defects to be directly corelated to signals instead of assuming a certain signal trend is associated with a certain defect or group of defects. With regards to signal indicating certain properties of the detected defect, it is found that certain sensors will show signal change based on the size of the defect detected. For example, large defects increase cooling rates, and the AE Amplitude is also relatively higher.

Another reason for having higher accuracy is because of the highspeed multisensory approach and architecture mentioned in Chapter 5. A multisensory approach has allowed for the system to observe more than one phenomenon and an efficient data collection system makes sure that even if the sensor collects data at high sampling rate, the mutli-sensor data can be time stamped using a singular timeline. Therefore, the system architecture and consequently defect detection platform is an essential component of the methodology as without it the high data speeds become unmanageable. This is probably why (Clijsters, Craeghs, & S. Buls, 2014) emphasizes that a custom data collection system is essential for a multisensory defect detection system. The multisensory approach allows for the monitoring of different windows or phases of the defect development cycle. This should provide a more complete picture of before during and after of the defect development cycle. This study also attempted to understand the timing of the defect development cycle Chapter 3 and Chapter 5 which shows that the defects can develop as quickly as 0.1μs seconds and that certain sensors can only capture certain parts of the defect development cycle due to the phenomenon they are observing. When observed in the light of the accuracy this methodology presents it is evident that a single sensor approach (specially hardware that samples at slower rates) are incapable of capturing the entire defect development cycle leading to a lower level of information and lower accuracy.

At this point it is also important to mention that one of the reasons for the relatively higher accuracy is because the system is trained on a multitude of defects varying in type, quantity and size which produced by the variation in Defect provocation techniques utilized in this study. These provocation experiments discussed in Chapter 6 took influence from the studies of (Barua & Frank Liou, 2014), (Gaja & Liou, 2017) and (Rasheedat M. Mahamood, 2014) and designed experiments that use physical deformities on the sample, contaminated powder, surface finish and machine parameters to provoke defects. As discussed in Chapter 7 a comparison is made between the quantity and sizes of the defects found in the literature and this study. It is found that contaminated powder experiments generate larger sizes of cracks, and the surface finish experiments produces larger pores. Compared to the sizes found it in the literature the development system can detect smaller size of defects which is testament to the systems sensitivity and efficiency (Reliability).

The data fusion aspect combines the prediction ranges from different sensors to produce a singular range. The data fusion architecture developed takes influence from the (Luo & Kay, 1989)'s architecture for multi sensor integration. The range generated from the data fusion equation compensates for sensors who aren't as efficient at determining certain features e.g., AE data was proven to be inefficient at calculating the source position of defects however the HS camera due to its fast frame rate and frame overlapping technique used is quick to capture changes and the position of the defects rather accurately. Hence in the part of HS camera compensates for the weakness of AE sensor in the fusion equation. The reliability of the data is developed by a clever scoring system that relies on Euclidean distances from the cluster centers. This theory is validated by calculating the forecasted variance graphs of the data at certain distances from the Cluster and it is found that as data points move away from their cluster center, the variance in their features of the data points increases (Chapter 7). This also goes to show that using K means cluster may have an added advantage compared to other unsupervised machine learning methodologies if used in this manner.

The research heavily relies on previous literature and in a way validates previous works. Two plausible publications are a product of this research. The first one is “Defect Detection in LMD using Custom Data Fusion Algorithm” which details the unique data fusion methodology which uses stitching data from multiple sensors and extracting events from it which are clustered and based on these cluster prediction tables are formed. These prediction tables are used to predict the features of any new Event depending on which cluster it is assigned. The prediction of each sensor is combined using a data fusion equation. The reliability of the prediction range that the data fusion equation produces is determined by a % confidence value generated using a unique scoring system. The second publication “Multi-Sensory Defect detection architecture system for LMD” focuses on the architecture of the system and its timing specification to capture quick changes in defect development windows.

In the grand scheme of things this research lays the road map for multi-sensory defect detection systems in LMD. It lays down the foundation by establishing the basic specification required to build such a machine even if it is for control purposes. Since it is built on a National Instruments system, is modular and uses industrially approved equipment this can be readily adopted and modified by the industry. The ability to predict the features of defects will allow for manufactures to set their own quality standards and will cut down on down time during post analysis to see if a sample has defects. It is also known when different material powders are used to build a sample the machine process parameter are fine-tuned to find the optimum process parameters. This system could help in calibrating the process parameters so that the ones chosen to do not generate any defects.

One of the major limitations of this study is that the architecture uses two busses, and all its modules are not incorporated in a single chassis. A single chassis to house all hardware modules and a single full duplex bus for communication would have significantly increased the efficiency of the system. The data for just 10 deposits was over 4 terabytes which includes High Speed video, Thermal camera images, AE images and XCT. All this data had to be scanned through and processed and some of the samples weren't even utilized in the thesis. The analysis of each data type was done on different software's which further increases analysis time. Better and automated analysis tools for all data types would improve the quality, quantity of data that can be extracted and be utilized to improve system training.

Figure 120 shows the future works that can stem from this research. With multiple sensors integrated into a single LMD monitoring system a study can be carried out to observe the signal trends more closely. Since the system allows before, during and after monitoring of the defect development cycle, a Zero-defect manufacturing approach can be taken if a precursor signal to the development of a defect can be discovered. Once the precursor signal is discovered a corrective action to stop the defect from ever formulating can be taken. Second research that can be carried out is to use the system to observe all three phenomena in relation to each other e.g., what happens when there is a temperature spike observed in the thermal camera? What is observed in the AE or HS optical signal at this time. This will allow for a better understanding of the limitations of the signals collected from the melt pool.

An improved fusion algorithm can be developed using empirical modeling. This will allow for researchers to understand which sensor outputs a stronger information or accurate information on a particular defect feature. Further research that is required is improved defect position calculation whether it is through multiple AE sensors or a better image processing technique. Lastly a closed loop control system needs to be built for this system so that after defects are detected corrective action may be taken.

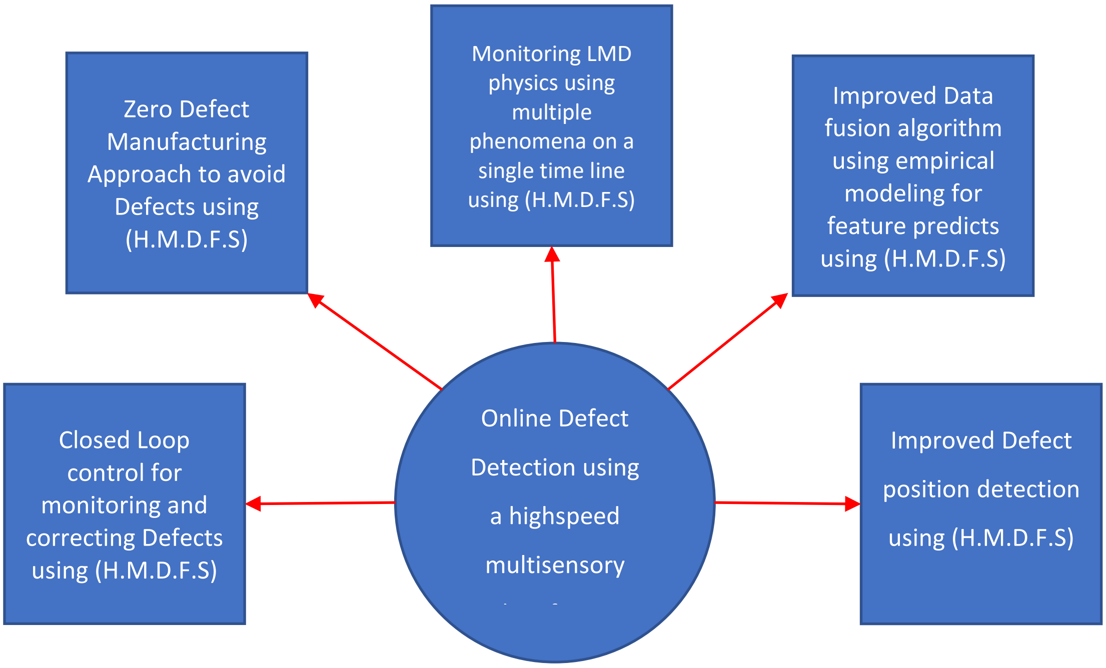

Figure 120: Future Works (HMDF stands for High Speed Data Fusion System)

References

(n.d.). Retrieved from http://www.pcb-manufacturer.net/.

3dpbm. (n.d.). *BigDataLMD project launches to improve quality of LMD processes*. Retrieved from www.3dprintingmedia.network: https://www.3dprintingmedia.network/bigdatalmd-project-launches-to-improve-quality-of-lmd-processes/

A. R. Nassar, T. J. (2014). Sensing defects during directed-energy additive manufacturing of metal parts using optical emissions spectroscopy. *25th Annual International Solid Freeform Fabrication Symposium, An Additive Manufacturing Conference, SFF 2014*, (pp. 278-287). Austin.

A. Ramakrishnan, G. D. (2020). Microstructural control of an Al–W aluminum matrix composite during direct laser metal deposition. *Journal of Alloys and Compounds, 813*. doi:https://doi.org/10.1016/j.jallcom.2019.152208

A.J.Pinkerton. (2010). 16 - Laser direct metal deposition: theory and applications in manufacturing and maintenance. In A.J.Pinkerton, *Advances in Laser Materials Processing* (pp. 461-491). Woodhead Publishing.

Arthur, D., & Vassilvitskii, S. (2007). k-means++: The Advantages of Careful Seeding David Arthur and Sergei Vassilvitskii Abstract. *Proceedings of the eighteenth annual ACM-SIAM symposium on Discrete algorithms*, (pp. 1027–1035). New Orleans, Louisiana.

Barua, S., & Frank Liou, J. N. (2014). Vision-based defect detection in laser metal deposition process. *Rapid Prototyping Journal, Vol. 20*, 77-85.

Barun Haldara, P. (2018). Identifying defects and problems in laser cladding and suggestions of some remedies for the same. *Material Today: Proceedings, 5*(5), 13090-13101.

Bridges, A. (2021, July 7). *High-Speed Video: Selecting a Slow-Motion Imaging System*. Retrieved from https://www.photonics.com/: https://www.photonics.com/Articles/High-Speed_Video_Selecting_a_Slow-Motion_Imaging/a25138

C Y Kong, R. J. (2010). High-rate laser metal deposition of Inconel 718 component using low heat-input approach. *Physics Procedia, 5*, 379-386.

Cerniglia, D., Scafidi, M., Pantano, A., & Lopatka, R. (2013). Laser Ultrasonic Technique for Laser Powder Deposition Inspection. Le Mans, France: 13th International Symposium on Nondestructive Characterization of Materials (NDCM-XIII).

Chabot, A., Rauch, M., & Hascoët, J.-Y. (2019). Towards a multi-sensor monitoring methodology for AM metallic processes. *Welding in the World*, 759–769.

Christopher B. Stutzman, A. R. (2018). Multi-sensor investigations of optical emissions and their relations to directed energy deposition processes and quality. *Additive Manufacturing, 21*, 333-339. doi:https://doi.org/10.1016/j.addma.2018.03.017

Clijsters, S., Craeghs, T., & S. Buls, K. K.-P. (2014). In situ quality control of the selective laser melting process using a high-speed, real-time melt pool monitoring system. *The International Journal of Advanced Manufacturing Technology*, 1089-1101.

Drachler, W., & Murphy, B. (1995, June -). New High-Speed, Low-Power Data-Acquisition ICs. *Analog Dialogue, 29*, pp. 3-6. Retrieved from https://www.analog.com/media/en/analog-dialogue/volume-29/number-2/articles/volume29-number2.pdf#page=3

Esteban, J., Starr, A., Willetts, R., & Hannah, P. B.-c. (2005). A Review of data fusion models and architectures: towards engineering guidelines. *Neural Computing and Applications, 14*(4), 273-281.

Fang, T., Jafari, M., Bakhadyrov, I., Safari, A., Danforth, S., & Langrana, N. (1998). Online defect detection in layered manufacturing using process signature. *SMC'98 Conference Proceedings. 1998 IEEE International Conference on Systems, Man, and Cybernetics* (pp. 4373-4378). San Diego, CA, USA: IEEE Xplore. doi:10.1109/ICSMC.1998.727536

Fujun Wang, H. M. (2008). Online study of cracks during laser cladding process based on acoustic emission technique and finite element analysis. *Applied Surface Science, 255*, 3267-3275.

Gaikwada, A., Yavaria, R., Montazeria, M., & Kevin Colea, L. B. (2020). Toward the digital twin of additive manufacturing: Integrating thermal simulations, sensing, and analytics to detect process faults. *IISE Transactions, 52*(11), 1204-1217. doi:https://doi.org/10.1080/24725854.2019.1701753

Gaja, & Liou. (2018). Defect classification of laser metal deposition using logistic regression and artificial neural networks for pattern recognition. *The International Journal of Advanced Manufacturing Technology*, 315–326.

Gaja, H., & Liou, F. (2017). Defects monitoring of laser metal deposition using acoustic emission sensor. *International Journal of Advanced Manufacturing Technology, 90*(1-4), 561-574.

Galarnyk, M. (2018, September 12). *Toward Data Science*. Retrieved from Understanding Boxplots: https://towardsdatascience.com/understanding-boxplots-5e2df7bcbd51

Gary K.L. Ng, G. B. (2008). An Investigation on Porosity in Laser Metal Deposition. *International Congress on Applications of Lasers & Electro-Optics.* Laser Institute of America.

Gawade, V., Singh, V., & Guo, W. “. (2022). Leveraging simulated and empirical data-driven insight to supervised-learning for porosity prediction in laser metal deposition. *Journal of Manufacturing Systems, 62*, 875-885. doi:https://doi.org/10.1016/j.jmsy.2021.07.013

Gibson I., R. D. (2015). Directed Energy Deposition Processes. . In R. D. Gibson I., *Additive Manufacturing Technologies.* (pp. 245-268). New York, NY: Springer.

Haythem Gaja, F. L. (2017). Defects monitoring of laser metal deposition using acoustic emission sensor. *The International Journal of Advanced Manufacturing Technology, 90*(1-4), 561-574.

Hossein Taheri, L. W. (2019). In Situ Additive Manufacturing Process Monitoring With an Acoustic Technique: Clustering Performance Evaluation Using K-Means Algorithm. *Journal of Manufacturing Science and Engineering, 141*(4), -. doi:10.1115/1.4042786

Hult, R. (2020, August 25). *The Evolution of High-Speed Data Transfer.* Retrieved from connectorsupplier.com: https://connectorsupplier.com/the-evolution-of-high-speed-data-transfer/

INTRAPID. (n.d.). *Innovative inspection techniques for laser powder deposition quality control*. Retrieved from http://www.intrapid.eu/: http://www.intrapid.eu/

ISO 13919-2. (2001). *Welding — Electron and laser beam welded joints — Guidance on quality levels for imperfections*. International Organization for Standardization.

ISO13919-2. (2001). Welding — Electron and laser beam welded joints — Guidance on quality levels for imperfections. *International Organization for Standardization*.

J.Yu, M. G. (2013). Cracking behavior and mechanical properties of austenitic stainless steel parts produced by laser metal deposition. *Materials & Design, Volume 45*, 228-235.

James C. Haley, J. M. (2018). Observations of particle-melt pool impact events in directed energy deposition. *Additive Manufacturing, 22*, 368-374.

John A. Slotwinski & E.J. Garboczii. (2014). Porosity Measurements and Analysis for Metal Additive Manufacturing Process Control. *Journal of research of the National Institute of Standards and Technology, 119*, 494-528.

John H. Martin, B. D. (2017). 3D printing of high-strength aluminium alloys. *Nature, 549*, 365–369. doi:https://doi.org/10.1038/nature23894

Jon Iñaki Arrizubieta, A. L. (2018). Hardness, grainsize and porosity formation prediction on the Laser Metal Deposition of AISI 304 stainless steel. *International Journal of Machine Tools and Manufacture, 135*, Pages 53-64.

JRPANEL. (2020, November 12). *What is a high-speed circuit? What is the difference between "high frequency" and "high speed"*. Retrieved from pcb-manufacturer.net: http://www.pcb-manufacturer.net/what-is-a-high-speed-circuit-what-is-the-difference-between-high-frequency-and-high-speed/

Jungeon Lee, H. J. (2021). Review on Quality Control Methods in Metal Additive Manufacturing. *Applied Sciences, 11*(4), -. doi:https://doi.org/10.3390/app11041966

Kai Zhang, W. L. (2007). Research on the processing experiments of laser metal deposition shaping. *Optics & Laser Technology, 39*(3), 549-557. doi:https://doi.org/10.1016/j.optlastec.2005.10.009

Kaphle, M. (2012). *Analysis Of Acoustic Emisson Data For Accurate Damage Assessment, PhD Thesis.* Brisbane: Queensland University of Technology.

Kastner J., H. C. (2018). X-Ray Tomography. In M. N. Ida N., *Handbook of Advanced Non-Destructive Evaluation.* Cham: Springer. doi:https://doi.org/10.1007/978-3-319-30050-4_5-1

Khanzadeh, M., & Bian, L. S. (2016). Porosity Detection of Laser Based Additive Manufacturing Using Melt Pool Morphology Clustering. *Solid Freeform Fabrication 2016: Proceedings of the 27th Annual International.*

Kim Vanmeensel, K. L.-P. (2018). 8 - Additively manufactured metals for medical applications. In K. L.-P. Kim Vanmeensel, *Additive Manufacturing: Materials, Processes, Quantifications and Applications* (pp. 261-309). Butterworth-Heinemann.

Lang, M. (2017, November 6). *The Fabricator.* Retrieved from TheFabricator: https://www.thefabricator.com/thefabricator/article/additive/an-overview-of-laser-metal-deposition

Liu, M., Kumar, A., Bukkapatnam, S., & Kuttolamadom, M. (2021). A Review of the Anomalies in Directed Energy Deposition (DED) Processes & Potential Solutions - Part Quality & Defects. *Procedia Manufacturing, 53*, 507-518. doi:https://doi.org/10.1016/j.promfg.2021.06.093

Liu, S., Farahmand, P., & Kovacevic, R. (2014). Optical monitoring of high power direct diode laser cladding. *Optics and Laser Technology, 64*, 363-376.

Lockwood, D. (2016). Rayleigh and Mie Scattering. In L. M.R, *Encyclopedia of Color Science and Technology.* New York, NY: Springer. doi:https://doi.org/10.1007/978-1-4419-8071-7_218

Luo, R. C., & Kay, M. G. (1989). Multisensor integration and fusion in intelligent systems. *IEEE Transactions on Systems, Man, and Cybernetics, 19*(5), 901-931.

Manin, J., Skeen, S. A., & Pickett, L. M. (2018). Performance comparison of state-of-the-art high-speed video cameras for scientific applications. *Optical Engineering, 57*(12), . doi:https://doi.org/10.1117/1.OE.57.12.124105

Markus Franz, J. B. (2014). Laser Metal Deposition Welding in the Field of Tool and Mould Making. *Procedia Engineering, 69*, 237-240. doi:https://doi.org/10.1016/j.proeng.2014.02.227

Meng, T., & Xuyang Jing, Z. Y. (2020). A survey on machine learning for data fusion. *Information Fusion*, 115-129. doi:https://doi.org/10.1016/j.inffus.2019.12.001

Meng, T., Jing, X., & Zheng Yan, W. P. (2020). A survey on machine learning for data fusion. *Information Fusion, 57* , 115–129.

Mohammad H. Farshidianfar, A. K. (2016). Effect of real-time cooling rate on microstructure in Laser Additive. *Journal of Materials Processing Technology, 231*, 468-478.

Prathipati, R. C. (2019). Corrosion behavior of surface induced by wire EDM on 316L stainless steel: an experimental investigation. *SN Applied Sciences*, 1-11.

R.Liu, Z. (2017). 13 - Aerospace applications of laser additive manufacturing. In Z. R.Liu, *Laser Additive Manufacturing: Materials, Design, Technologies, and Applications* (pp. 351-371). Woodhead Publishing.

Ramin Madarshahian, V. S. (2019). Hsu-Nielsen source acoustic emission data on a concrete block. *Data in brief*.

Rasheedat M. Mahamood, E. T. (2014). Characterizing the Effect of Processing Parameters on the Porosity of Laser Deposited Titanium Alloy Powder . *Proceedings of the International MultiConference of Engineers and Computer Scientists2014.* Hong Kong: IMECS.

RelativitySpace. (n.d.). *www.relativityspace.com/rockets*. Retrieved from www.relativityspace.com: https://www.relativityspace.com/rockets

Renken, V., & Stephan Albinger, G. G. (2017). Development of an adaptive, self-learning control concept for an additive manufacturing process. *CIRP Journal of Manufacturing Science and Technology, 19*, 57-61. doi:https://doi.org/10.1016/j.cirpj.2017.05.002

Richards, A. (2021, June 9). *The Promise, Advantages, And Challenges of High-Speed Infrared Cameras*. Retrieved from www.infradex.com: https://www.infradex.com/high-speed-infrared-cameras-2/#:~:text=The%20latest%20models%20of%20high,fps)%20to%20above%2030%2C000%20fps.

Robert Sampson, R. L. (2020). An improved methodology of melt pool monitoring of direct energy deposition processes. *Optics & Laser Technology,Volume 127*.

Royce, R. (n.d.). Retrieved from https://www.rolls-royce.com/.

Saad A. Khairallah, A. T. (2020). Laser powder-bed fusion additive manufacturing: Physics of complex melt flow and formation mechanisms of pores, spatter, and denudation zones. *Acta Materialia, 108*, 36-45. Retrieved from https://doi.org/10.1016/j.actamat.2016.02.014

Segerstark, A. (2017). *Laser Metal Deposition using Alloy 718 Powder: Influence of Process Parameters on Material Characteristics.* University West.

Shehadeh, M. F. (2006). *Monitoring of Long Steel Pipes using Acoustic Emission, PhD Thesis.* Edinburgh: Heriot-Watt University.

Sibisi, P. N., Popoola, A. P., Arthur, N. K., & Pityana, S. L. (2020). Review on direct metal laser deposition manufacturing technology. *The International Journal of Advanced Manufacturing Technology, 107*(3), 1163-1178. doi:10.1007/s00170-019-04851-3

SIEMENS. (n.d.). *https://new.siemens.com/global/en/company/stories/research-technologies/additivemanufacturing/additive-manufacturing-laser-metal-deposition.html*. Retrieved from https://new.siemens.com/.

Sjoedahl, M., & Oreb, B. (2002). Stitching interferometric measurement data for inspection of large optical components. *Optical Engineering*. doi:10.1117/1.1430727

Slotwinski, J. A. (2014). Porosity measurements and analysis for metal additive manufacturing process control. *Journal of Research of the National Institute of Standards and Technology, 119*, 494-528.

Song, L., Bagavath-Singh, V., Dutta, B., & Mazumder, J. (2012). Control of melt pool temperature and deposition height during direct metal deposition process. *Int J Adv Manuf Technol*, 247–256.

Stark, F., Rosenberger, M., Dittrich, P.-G., Celestre, R., Hänsel, M., & Notni, G. (2017). Geometrical and spectral data stitching for combining hyperspectral imaging systems. *Automatisierungstechnik, 65*(6), 381-395. doi:doi:10.1515/auto-2017-0027

Stebut, J. V. (1999). Acoustic emission monitoring of single cracking events and associated damage mechanism analysis in indentation and scratch testing. *Surface and Coatings Technology, 116-119*, 160-171.

Tang, S., Wang, G., Zhang, H., & Wang, R. (2017). An online surface defects detection system for AWAM based on deep learning. *Solid Freeform Fabrication 2017: Proceedings of the 28th Annual International Solid Freeform Fabrication Symposium – An Additive Manufacturing Conference* (pp. 1965-1981). Austin Texas: University of Texas at Austin. doi:http://dx.doi.org/10.26153/16919

Tao Liu, L. H. (2019). Real-time defect detection of laser additive manufacturing based on support vector machine. *Journal of Physics: Conference Series, 1213*(5).

Tiangang Zhang & Ronglu Sun. (2015). Study on Pores and Crack Sensitivity of Ni- based Composite Coating by Laser Cladding. *IOP Conference Series: Materials Science and Engineering* (p. Volume 87). IOP Publishing.

Torsten Petrat, B. G. (2016). Laser Metal Deposition as Repair Technology for a Gas Turbine Burner Made of Inconel 718. *Physics Procedia, 83*, 761-768. doi:https://doi.org/10.1016/j.phpro.2016.08.078

TrumpF. (n.d.). *https://www.trumpf.com/*. Retrieved from https://www.trumpf.com/en_GB/products/laser/disk-lasers/.

Ulf Hassler, D. G. (2016). In-situ Monitoring and Defect Detection for Laser Metal Deposition by Using Infrared Thermography. *Physics Procedia, Volume 83*, 1244-1252.

Vandone, A., & Stefano Baraldo, A. V. (2018). Multisensor Data Fusion for Additive. *IEEE ROBOTICS AND AUTOMATION LETTERS*, 3279-3284.

Verhaeghe, G., & Hilton, P. (2004). Laser Welding of Low-Porosity Aerospace Aluminum Alloy. *34th International MATADOR Conference* (pp. 241–246). Manchester: Springer, London.

Wang, F. M. (2008). Online study of cracks during laser cladding process based on acoustic emission technique and finite element analysis. *Applied Surface Science, 255*, 3267-3275.

Wei Feng, Z. M. (2022). Online defect detection method and system based on similarity of the temperature field in the melt pool. *Additive Manufacturing, 54*. doi:https://doi.org/10.1016/j.addma.2022.102760

Wei He, W. S. (2019). In-situ monitoring and deformation characterization by optical techniques ; part I : Laser-aided direct metal deposition for additive manufacturing. *Optics and Lasers in Engineering*, 74-88.

White, F. E. (1991). *Data Fusion Lexicon.* San Diego: Joint Directors Laboratories.

Wohlers, T. (2008). *State of the Industry Report: Rapid Prototyping & Tooling.* Colorado USA: Wohlers Associates Inc.

Wu, Y., Cui, B., & Xiao, Y. (2020). Crack Detection during Laser Metal Deposition by Infrared Monochrome Pyrometer. *Materials, 13*(24). Retrieved from https://doi.org/10.3390/ma13245643

Yun-Jeong Kim, J.-H. K.-J.-I. (2004). An 8-bit 1 Gsps CMOS pipeline ADC. *Proceedings of 2004 IEEE Asia-Pacific Conference on Advanced System Integrated Circuits*, 424-425. Retrieved from https://ieeexplore.ieee.org/document/1349520

Zavala-Arredondo, M., & Haider Ali, K. M. (2018). Investigating the melt pool properties and thermal effects of multi-laser diode area melting. *The International Journal of Advanced Manufacturing Technology*, 1383–1396.

Zhang, X. (2019). Online defect detection method of array optical sensorbased on watershed image processing algorithm. *Multimedia Tools and Applications*. doi:https://doi.org/10.1007/s11042-019-7340-y

Zhengtao Gan, H. L. (2019). Data-Driven Microstructure and Microhardness Design in Additive Manufacturing Using a Self-Organizing Map. *Engineering, 5*(4), 730-735. doi:https://doi.org/10.1016/j.eng.2019.03.014

Zhu, J. S. (2012). Stitching together Multiple Data Dimensions RevealsInteracting Metabolomic and Transcriptomic NetworksThat Modulate Cell Regulation. *PLOS Biology*, . Retrieved from https://doi.org/10.1371/journal.pbio.1001301